Theses - Daytona Beach   Dissertations and Theses

Summer 2006

An Investigation of the Dynamic Effects of Flap Deflection on the Aerodynamic Characteristics of an Airplane Wing Using Computational Fluid Dynamics

Alexander Moerchel

Embry-Riddle Aeronautical University - Daytona Beach

AN INVESTIGATION OF THE DYNAMIC EFFECTS OF FLAP DEFLECTION ON THE AERODYNAMIC CHARACTERISTICS OF AN AIRPLANE WING USING COMPUTATIONAL FLUID DYNAMICS

by

Alexander M. Moerchel

A Thesis Submitted to the

Graduate Studies Office

in Partial Fulfillment of the Requirements for the Degree of

Master of Science in Aerospace Engineering

Embry-Riddle Aeronautical University

Daytona Beach, Florida

Summer 2006

UMI Number: EP32096

INFORMATION TO USERS

The quality of this reproduction is dependent upon the quality of the copy submitted. Broken or indistinct print, colored or poor quality illustrations and photographs, print bleed-through, substandard margins, and improper alignment can adversely affect reproduction.
In the unlikely event that the author did not send a complete manuscript and there are missing pages, these will be noted. Also, if unauthorized copyright material had to be removed, a note will indicate the deletion.

UMI®

AN INVESTIGATION OF THE DYNAMIC EFFECTS OF FLAP DEFLECTION ON THE AERODYNAMIC CHARACTERISTICS OF AN AIRPLANE WING USING COMPUTATIONAL FLUID DYNAMICS

by

Alexander M. Moerchel

This thesis was prepared under the direction of the candidate's thesis committee chairman, Dr. Hany Nakhla, Department of Mechanical Engineering, and has been approved by the members of his thesis committee. It was submitted to the Aerospace Engineering Department and was accepted in partial fulfillment of the requirements for the degree of Master of Science in Aerospace Engineering.

THESIS COMMITTEE:
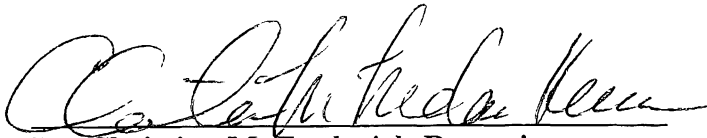
Dr. Hany Nakhla
Chairman

Dr. Eric Perrell
Member
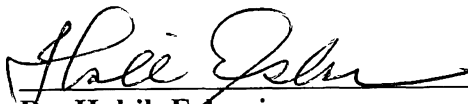
Dr. Axel Rohde
Member

Dr. Christina M. Frederick-Recascino   **Date** 8/10/06
Associate Provost

Dr. Habib Eslami   8/10/06
Department Chair, Aerospace Engineering   **Date**

ACKNOWLEDGEMENTS

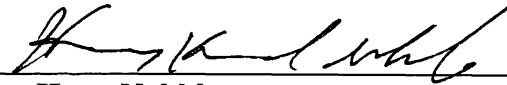# ABSTRACT

Author: Alexander Moerchel

Title: An Investigation of the Dynamic Effects of Flap Deflection on the Aerodynamic Characteristics of an Airplane Wing Using Computational Fluid Dynamics

Institution: Embry-Riddle Aeronautical University

Degree: Master of Science in Aerospace Engineering

Year: 2006

Flaps are used to increase an airplane's lift and to adjust its stability and maneuverability. This study shows an application of STAR-CD, a commercial computational fluid dynamics (CFD) software, to an investigation of the dynamic effects of flap deflection on the lift, drag and moment coefficients, as well as on the location of the center of pressure. For this study, a plain flap was modeled with a moving mesh and was attached to a NACA 0012 airfoil and a wing of a general aviation aircraft for a 2D and 3D investigation, respectively. In addition, the flap deflection rates were varied to investigate their effect on the flow field and the airfoil's stability characteristics. The results from the analyses were ultimately used to prove that commercial CFD software is a viable option to investigate the stability and control characteristics of an aircraft.

TABLE OF CONTENTS

LIST OF TABLES

LIST OF FIGURES

LIST OF SYMBOLS

A_b -   Wall cell face area

A_m -   Effects of convection and/or diffusion

a speed of sound

aa Highest vertex number in a given vertex set

C_j -   Contributions due to convection

C_L Lift coefficient

C_p Pressure coefficient

C_s Sutherland constant

c -   Airfoil chord

c_d -   Section drag coefficient

c_f Flap chord

c_l -   Section lift coefficient

$c_{m,c\ 4}$ -   Section moment coefficient about the quarter chord

$\overline{c}_p$ Mean constant-pressure specific heat at temperature T

c_p^0 Reference specific heat at temperature T

$c_{l,max}$ -   Maximum section lift coefficient occurring just before stall

D' -   Drag of a wing section or airfoil

D_i -   Induced drag

D_j -   Contributions due to diffusion

D_P -   Geometric coefficient

d -   Drag force acting on a surface cell

dm -   Function of the airfoil's profile dimensions

$dm2$ -   Function of the airfoil's profile dimensions

E - Empirical coefficient

ED Turbulent kinetic energy dissipation rate

$ENTH$ - Enthalpy

F_{hJ} Diffusional energy flux in direction x_j

g_m - Gravitational acceleration components

H_m - Heat of formation of constituent m

h - Static enthalpy per unit mass

h_t - Thermal enthalpy per unit mass

II_s - Second invariant of the rate of strain tensor

k - Turbulent kinetic energy

L Lift

L' - Lift of a wing section or airfoil

$LG1$ - Extrusion layer thickness

l - Lift force acting on airfoil surface cell

M Mach number

M'_{c4} - Moment about the quarter chord experienced by a wing section or airfoil

M_{LE} Moment about the leading edge experienced by a wing

M_x Moment due to drag experienced by airfoil

M_y - Moment due to lift experienced by airfoil

MAC - Mean aerodynamic chord

$Mass$ - Mass flow rate

m_x - Moment due to drag acting on an airfoil surface cell

m_y - Moment due to lift acting on an airfoil surface cell

$\overline{n}_b$ - Outward-pointing unit vector normal to the wall

$nyl1$ - Number of cell layers in extrusion direction

P	-	Pressure
p		Piezometric pressure: $p = p_s - \rho_0 g_m x_m$
p_s	-	Static pressure
q		Corrector level (i.e. $q = 1, 2, \ldots$)
R	-	Specific gas constant
Re	-	Reynolds number
S		Closed surface
S		Wing planform area
$\vec{S}$	-	Surface vector
S_j	-	Discrete cell face area
S	-	Wing span
s_l	-	Function of nodal velocity fields u_i^n and u_i^o and other quantities
s_h	-	Energy source
s_l	-	Momentum source components
s_{ij}		Rate of strain tensor
s_m		Mass source
s_ϕ		Source coefficient
T		Temperature
T_0	-	Absolute temperature
TE	-	Turbulent kinetic energy
t	-	Time
U	-	Velocity component in x-coordinate-direction
u		Tangential fluid velocity
$\bar{u}$	-	Fluid velocity

u'	-	Fluctuations of the absolute fluid velocity component about the average velocity
$\bar{u}_c$		Local coordinate velocity
u_i	-	Absolute fluid velocity component in direction x_i
u_j		Velocities normal to the cell faces
$\bar{u}_r$	-	Relative velocity
u_w	-	Tangential wall velocity
V		Volume
V		Velocity component in y-coordinate-direction
V_p	-	Volume of a computational cell
V_∞	-	Freestream velocity
$\bar{v}_{par}$	-	Velocity vector component parallel to the wall at the center of a near-wall cell
W		Velocity component in z-coordinate-direction
w	-	Downwash
x_{cp}	-	Horizontal distance between the airfoil's leading edge and its center of pressure
x_{cp}/c		Relative location of the center of pressure
x_i	-	Cartesian coordinate (i = 1, 2, 3)
x_m	-	Coordinates relative to a datum where ρ_0 is defined
Y_m	-	Mass fraction of mixture constituent m

Greek Symbols

ρ	-	Angle of attack
ρ_{eff}	-	Effective angle of attack
ρ_i		Induced angle of attack
$\rho_{L=0}$	-	Zero-lift angle of attack
ρ_{stall}	-	Stalling angle of attack

γ		Ratio of specific heats
γ, γ_f	-	Flap deflection angle
γL		Mean mesh dimension
γ_{ij}	-	Kronecker delta
γt		Time interval or step
γt_c	-	Smallest characteristic time step
γ	-	Turbulent kinetic energy dissipation rate
ϕ	-	Placeholder for dependent variable
γ	-	Von Karman constant
Γ_ϕ		Diffusion coefficient
μ	-	Molecular dynamic viscosity
μ_0	-	Dynamic viscosity at $T = 273.15$ K and $p_s = 101.325$ kPa
μ_t	-	Turbulent viscosity
γ_0	-	Integrand for the chordwise location
γ	-	Density
γ_0		Reference density (also referred to as freestream density)
γ_x	-	Freestream density (also referred to as reference density)
γ	-	Summation sign
γ_{ij}	-	Stress tensor components
γ_w	-	Wall shear stress

1. INTRODUCTION

1.1. Background

Today, modeling and simulation are popular research and development techniques in the engineering and science community. With ever-increasing computational power through the development of faster super computers and clusters and the emergence of more accurate simulation algorithms, computational methods continue to drive out experimental methods from the design process. Nevertheless, it should be noted that experiments will always continue to serve as a validation basis for the computational results, but their share in the design process will continue to decline.

One such modeling and simulation technique is computational fluid dynamics, or CFD. It benefited greatly from the improvements in computational performance of hardware and software because it is now applied to a wide range of applications. For example, CFD and wind tunnel testing are equal players nowadays in the design process of commercial transport aircraft [1]. Furthermore, CFD has its place in multidisciplinary approaches to design problems [2].

The application that is of particular interest in this investigation is airplane aerodynamics. This is a rather complex and interesting field due to the fact that an airplane consists of many components such as engines, wings and control surfaces on the wing and tail, whose effectiveness and efficiency greatly impact the overall success of the design. Furthermore, there is one specific component of the airplane system which is of

1

particular interest due to its substantial impact on the airplane's aerodynamics and stability and control characteristics: the flap. It is used during those parts of the airplane's flight regime with low air speeds, such as take-off and landing, because then the wings alone are unable to produce sufficient lift to support the airplane's weight. A deflected flap increases the lift coefficient of the wing and thereby improves the flight characteristics of the airplane at low airspeeds. That is why they are part of a group called high lift devices. In general, these devices increase flight safety and lower the overall risk of the mission. The introduction of flaps and other high lift devices, such as leading edge slats, improved the flexibility of the airplane by enabling it to improve its take-off and landing performance while simultaneously increasing its cruising efficiency. This, in part, led to the overall success of airplanes as a means of civil transportation, for example.

1.2. Statement of the Problem

One drawback of high lift devices, on the other hand, is their tendency to increase the airplane's overall drag. That is why an optimization of these devices is of particular interest to aircraft designers and manufacturers. This iterative process of aerodynamic optimization calls for the power of CFD since experimental methods, such as wind tunnel testing, cause higher costs due to the necessity to built new or modified scaled prototypes for each test. This indicates that airplane designers and manufacturers would benefit from a tool or methodology that allows them to analyze the effects of flap deflection on the aerodynamic characteristics of a wing. This methodology, however, should not be limited to either capturing the development of the flow field or analyzing the stability and control characteristics, but should incorporate both.

2

The subsequent chapters of this work develop a methodology for the analysis of the effects of flap deflection on the aerodynamic and stability and control characteristics. This is accomplished on the basis of a commercial CFD code called STAR-CD, which was developed by CD-adapco and has found a variety of applications in many branches of the engineering industry and research community. This underscores the necessity for a methodology based on commercially available software because it facilitates its implementation in the industry with the potential to directly affect the efficiency and success of the design process. The competitive market environment of today requires that development times of new aircraft become shorter [1].

1.3. Review of the Literature

The effects of flap deflection on the aerodynamic characteristics of a wing or airfoil have been studied numerous times since the beginning of aviation and aerodynamics research. This alone shows the significance of this topic, and it is needless to say that it should certainly not be missing in any introductory literature to aerodynamics, such as Fundamentals of Aerodynamics by Anderson [3]. Indeed, Anderson outlines the effects of flap deflection on the lift coefficient of an airfoil and even cites some experimental data to back up the assumptions. However, [3] deduces these assumptions from thin airfoil theory rather than any experimental or even computational data. Therefore, it serves well as an introductory reference, but is far from providing any kind of methodology which would enable a commercial user to investigate the problem with commercially available CFD software.

3

More recently, the application of CFD to the flow field around flaps, in particular, became more prevalent. In [4], the author applied a simple time-splitting algorithm to advance the Navier-Stokes equations in time and to compute an unsteady solution of the flow field around the flap edge. His primary goal, however, was to estimate the noise field created by the flap edge flow and not the effect of the flap on the aerodynamic characteristics of the wing as a whole. The author also did not consider the stability and control characteristics and their variation during flap deflection.

In another study of the flow field around a wing with a flap [5], the authors focus on the analysis of the accuracy of four different CFD approaches as compared to experimental data. In addition, this research incorporates flow control through a steady blowing device, which is located on the airfoil's upper surface at the leading edge of the flap. Throughout the comparison, this study does take a look at the lift-to-drag ratio and the pressure distribution on the airfoil's surfaces, but it lacks an emphasis on stability and control parameters. This could have been realized by investigating the lift, drag and moment coefficients as functions of the flap deflection angle. Besides, [5] does not provide a specific methodology in conjunction with a commercial CFD application and is limited to the 2D case.

As opposed to the preceding papers, the authors of [6] focus more on the stability and control characteristics of the effects of flap deflection. They develop a variety of physical models and compare the results to experimental data in order to attempt an improvement of the accuracy of their numerical simulation. The authors furthermore conclude that improper flow separation predictions cause the numerical hinge moment results to be inaccurate as compared to the experimental values. While this work does

focus on the aerodynamic effects of flaps and describes an application of CFD, it limits its analysis to two deflection angles at different angles of attack. This does not allow a complete transient interpretation of the effects of flap deflection on the aerodynamic characteristics of the wing, which, however, is the goal of this analysis.

The preceding citations showed that the effects of flap deflection on the flow field around the wing are an active research area. Furthermore, although the example studies above showed similarities to the work presented in this thesis, none of them contained a development of a methodology that would enable the user to capture both flowfield and stability and control characteristics subject to the effects of flap deflection. This observation leads to the conclusion that the work presented in this thesis is not redundant and that it does present a new analysis of an existing and already investigated physical phenomenon in the area of airplane aerodynamics.

1.4. Statement of the Hypothesis

Through the use of commercially available CFD software, namely STAR-CD, a methodology can be developed that has the ability to fully capture both the aerodynamics and the related stability and control phenomena that occur during flap deflection. This methodology has the ability to conduct a transient simulation of the process of flap deflection. In addition, the methodology is semi-automatic in order to reduce the number of inputs from the user and to shorten the time spent in the pre-processing phase of the analysis. Finally, the methodology has the capability to adapt to varying wing and airfoil geometries with a minimum of effort from the user.

The following chapters attempt to prove the above hypothesis by introducing STAR-CD, by developing the method and by presenting the results. More specifically, the methodology is divided into two parts. In the first part, a method for the transient simulation of flap deflection and its effects on a two-dimensional wing section is developed. The second part takes basic concepts from the method developed in the first part and extends the model, so that it can model the deflection of a three-dimensional flap and its effects on the aerodynamic characteristics of a complete aircraft. The presentation of the results has a similar structure as the methodology.

2. METHODOLOGY

2.1. An Introduction to Flaps and their Aerodynamic Effects

Before presenting the methodology developed to approach the problem stated in the previous chapter, a brief theoretical analysis of the background of the problem is undertaken. This involves a theoretical description of the process of flap deflection and a theoretical analysis of their aerodynamic effects. This should not only help the reader to understand the rationale of the approach developed in subsequent sections of this chapter, but should also serve as a reference point for a verification of the CFD results presented in chapter 4.

2.1.1. When Are Flaps Used?

As previously mentioned, flaps are only used during those parts of an airplane's flight regime, during which the airspeed is relatively low as compared to the normal cruising speed. This is particularly the case during take-off and landing because of the limited length of runways at most airports. According to the lift equation stated below (equation 2.1), the overall lift, L, of a wing with a specific planform area, S, is proportional to the square of the airspeed, V_∞.

$$L = \frac{1}{2} \cdot \rho_\infty \cdot V_\infty^2 \cdot C_L \qquad [2.1]$$

Since the freestream density, ρ_r, at takeoff is constant, the only practical way to counter the decrease in lift due to a reduction in air speed is an increase of the wing's lift coefficient, C_L. This, in turn, can be realized by increasing the angle of attack, ρ. This is a result from classical thin airfoil theory, which states that the section lift coefficient, c_l, is directly proportional to the angle of attack, ρ, of the airfoil. For a symmetric airfoil, this is expressed by equation 2.2.

$$c_l = 2\pi\pi \hspace{8cm} [2.2]$$

The above equation also shows that a symmetric airfoil does not produce any lift at zero angle of attack.

On the other hand, this direct relationship between the lift coefficient and the angle of attack has an upper limit in the sense that if the angle of attack is increased beyond a critical value, the lift coefficient will drop abruptly. The critical value for the angle of attack is also referred to as the stalling angle of attack, ρ_{stall}, because the abrupt decrease of the lift coefficient, which occurs at this angle, is called stall. The highest value for c_l that occurs just before stall is termed the maximum section lift coefficient, $c_{l\,max}$. Physically, stall is due to a separation of the airflow from the top surface of an airfoil. This, in turn, is a result of the inability of the airflow to overcome the increasing adverse pressure gradient as the angle of attack of the airfoil increases. Figure 2.1 on the next page shows a graph of the section lift coefficient, c_l, as a function of the angle of attack, ρ. This graph, however, is typical for a cambered airfoil due to the fact that the zero-lift angle of attack, $\rho_{L=0}$, is smaller than zero and not equal to zero as would be the case for the symmetrical airfoil.
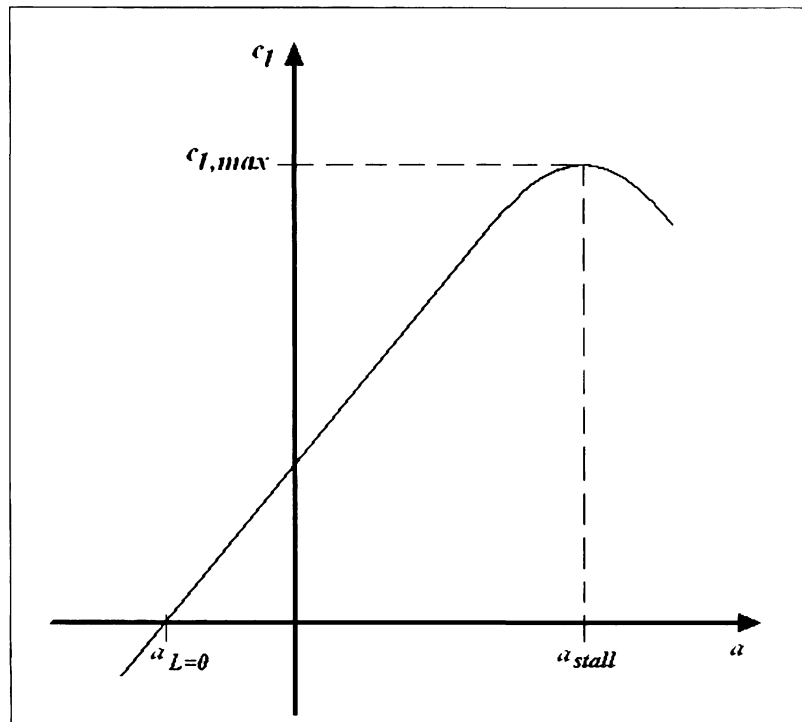
Figure 2.1: Graph of the lift coefficient, c_l, as a function of the angle of attack, α

Depending on the situation and aerodynamic characteristics of the airplane, an even higher maximum lift coefficient might be necessary than the wing can produce before stalling. In this case, flaps are deployed downward, which is defined as a positive flap deflection. Several types of flaps exist in practice; however, for the sake of geometric simplicity, only the plain trailing edge flap is considered in this investigation. This type of flap consists of part of the trailing edge section of a wing or airfoil and is hinged at some location within the contour. The hinge point is usually located at some point on the camber line that lies between 70% and 80% of the chord downstream of the leading edge of the wing or airfoil. Figure 2.2 on the next page visualizes the configuration of an airfoil with a plain trailing edge flap and clarifies the airfoil terminology just introduced.

9
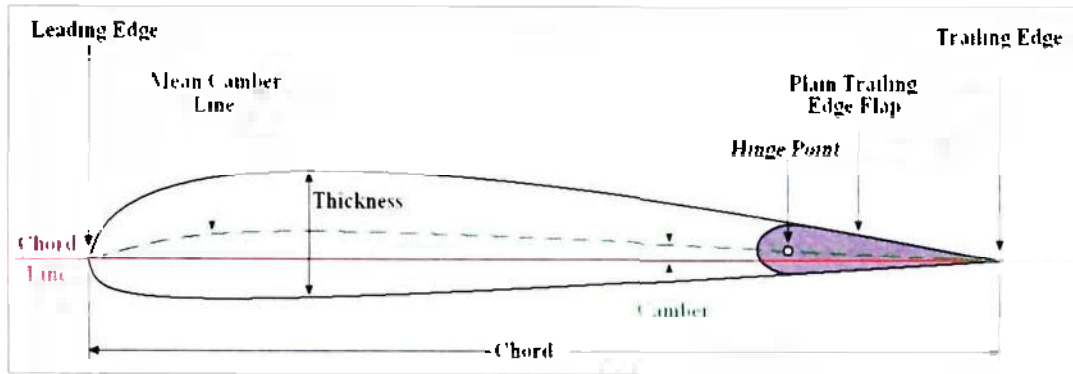
Figure 2.2: Sketch of a cambered airfoil with a plain trailing edge flap

2.1.2. What Are the Effects of Flap Deflection in the Case of an Airfoil?

Effectively, the deflection of a plain trailing edge flap increases the camber of the airfoil. This, in turn, decreases the zero-lift angle of attack, $\alpha_{l\ 0}$, and increases the lift coefficient, c_l. These two effects are obvious results from classical thin airfoil theory for cambered airfoils:

$$c_l = 2\pi \left| \alpha + \frac{1}{\pi} \int_0^\pi \frac{dz}{dx} (\cos\theta_0 - 1) d\theta_0 \right| \qquad [2.3]$$

In the equation above, dz/dx represents the slope of the camber line and θ_0 is the integrand replacing the chordwise location in the integration. Effectively, equation 2.3 reflects flap deflection and the consequent increase in the camber of the airfoil as an increase in the slope of the camber line, dz/dx.

Further effects of flap deflection have been investigated experimentally by the National Advisory Committee for Aeronautics (NACA) in the first half of the 20th century because classical thin airfoil theory proved to be inaccurate. This is mainly due to the fact that classical thin airfoil theory is based on the assumption that fluid flow is inviscid, which disregards friction, thermal conduction and diffusion within the fluid. In other words, the inviscid classical thin airfoil theory is incapable of capturing flow

10

phenomena such as separation and recirculation. which often occur on the surface of an airfoil at high angles of attack or with large flap deflection angles.

The NACA conducted a vast amount of experiments using different airfoil shapes and various flap configurations at different angles of attack and flap deflection angles. The results showed that. in general. the deflection of a plain trailing edge flap increases the maximum section lift coefficient. c_{lmax}. and decreases the stalling angle of attack. a_{stall}. Together with the results of classical thin airfoil theory. this means that the lift curve shown in figure 2.1 experiences a shift in both the positive c_l-direction and the negative a-direction. This is visualized in figure 2.3 below. in which the green curve represents a lift curve of an airfoil with a deflected flap
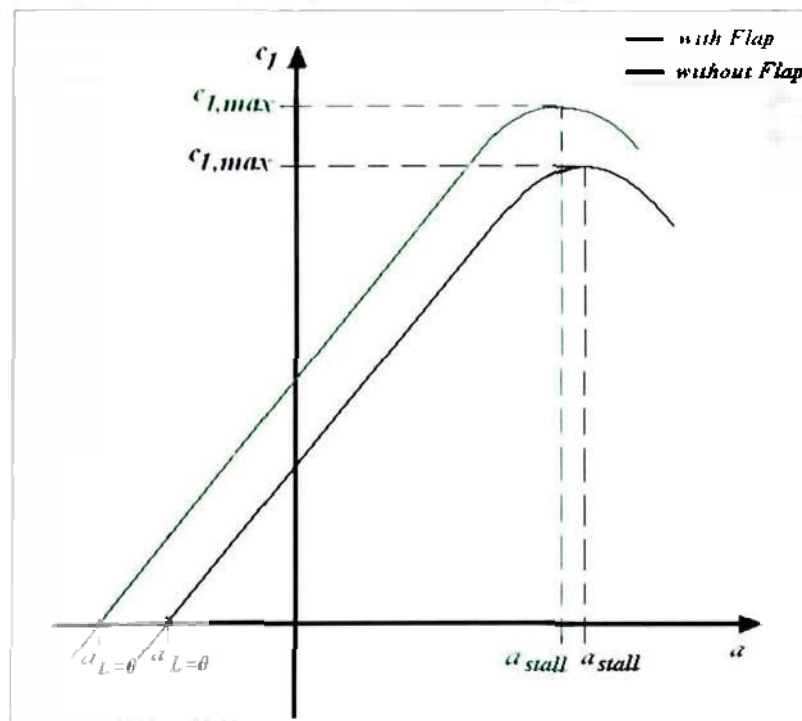
Figure 2.3: **Graph of the lift coefficient, c_l, as a function of the angle of attack, a, for both an airfoil with a deflected flap and one without**

11

Another effect of the deflection of a plain trailing edge flap is an increase of the airfoil's drag. This is due to the fact that flap deflection effectively increases the camber of the airfoil and consequently forces the flow over the top surface to accelerate. This, in turn, means that the flow on the top surface has to overcome a larger adverse pressure gradient as it continues to move downstream. Furthermore, a greater adverse pressure gradient promotes the transition of laminar flow to turbulent flow, which in turn increases the skin friction drag. If the flap deflection angle increases further, the flow at the upper surface of the flap will eventually separate because the flow will not have sufficient energy to overcome the ever increasing adverse pressure gradient. This separation bubble is an area with low flow velocities and reversed flow, which leads to an increase of the airfoil's pressure drag [3]. Overall, this means that during the process of flap deflection the airfoil initially experiences an increase of its skin friction drag and subsequently sees an increase of its pressure drag due to flow separation at sufficiently large flap deflection angles.

Flap deflection also changes the location of the center of pressure, which is the point at which the resultant forces of lift and drag would act on the airfoil. This is due to the fact that the deflection of a plain flap effectively changes the camber and the velocity distribution on the surface of the airfoil. This simultaneously affects the static pressure distribution, which implicates a shift of the center of pressure away from its initial position. The center of pressure is located at the quarter chord for a symmetric airfoil at zero angle of attack and with no flap deflection. Its position can be calculated using the following equation:

$$-\frac{c}{4}L' + M'_{c/4} = -x_{cp}L' \qquad [2.4]$$

12

In the above equation, c is the chord, L' is the lift of the airfoil, $M'_{c/4}$ is the moment about the quarter chord of the airfoil and x_{cp} is the location of the center of pressure measured from the leading edge. Equation 2.4 is a result of equating two equivalent force-and-moment systems on an airfoil, which are sketched in Figure 2.4 below.
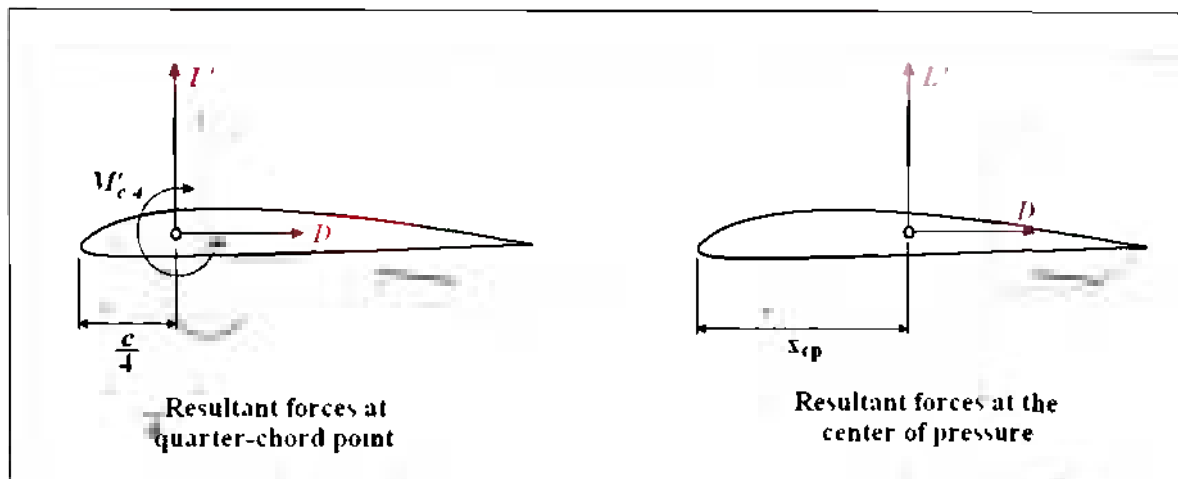
Figure 2.4: Equivalent force-and-moment systems on an airfoil

Solving equation 2.4 for x_{cp} and taking into account that cambered airfoils experience a larger nose-down pitching moment about the quarter chord, it is obvious that x_{cp} becomes larger as the camber of the airfoil increases. This means that the center of pressure must be located aft of its initial position during the deflection process of the plain flap.

In summary, the deflection of a plain trailing edge flap effectively increases the camber of an airfoil and thereby increases the lift and drag coefficient; it causes the nose-down pitching moment to increase and moves the center of pressure aft towards the trailing edge.

2.1.3. What Are the Effects of Flap Deflection in the Case of a Finite Wing?

Before investigating the effects of flap deflection on the aerodynamic characteristics of a finite three-dimensional (3D) wing, it is necessary to capture the aerodynamic differences between the airfoil and the finite wing. In the case of the latter, further aerodynamic phenomena exist that have an effect on the flow field around the wing as a whole. These aerodynamic phenomena are called downwash and induced drag. The latter is a result of the former.

In the case of a finite 3D wing, the air flow tends to leak from the bottom surface to the top surface of the wing around the wing tip. This is due to the lift-producing pressure differential between the bottom and the top of the wing. Furthermore, the leakage of the air flow around the wing tip creates a circulatory motion that continues to grow into vortices farther downstream of the wing tip. The trailing vortices at the wing tip cause a small downward velocity component, also called downwash, in the vicinity of the wing, which effectively deflects the freestream velocity vector downward. The angle between the deflected and the original velocity vector is called the induced angle of attack. This means that the wing perceives an effective angle of attack which is smaller than the actual angle of attack. Figure 2.5 on the next page consists of a two-dimensional (2D) sketch of a wing clarifying the relationship of downwash and effective angle of attack, and it shows the effect of downwash on the lift of the wing.
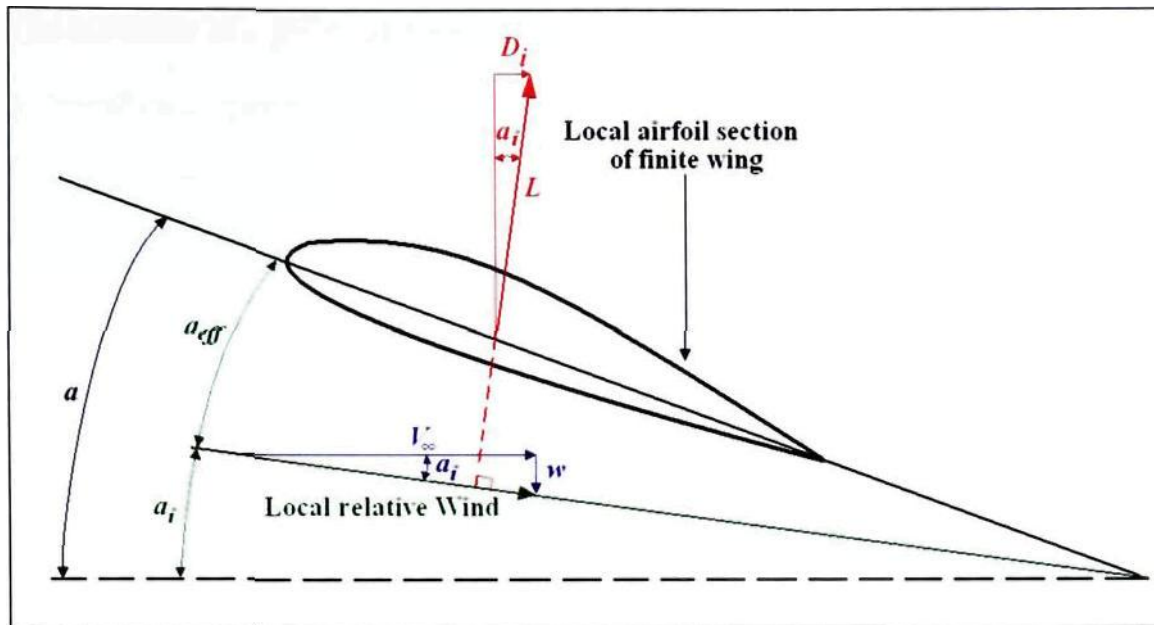
Figure 2.5: Effect of downwash on the flow over a local section of a finite 3D wing

In the figure above. α_i represents the induced angle of attack and α_{eff} marks the effective angle of attack. With this information. it is clear that the effective angle of attack can be computed using the following relationship:

$$\alpha_{eff} = \alpha - \alpha_i \qquad\qquad\qquad [2.5]$$

In addition. figure 2.5 shows the downwash. labeled as w. and its effect on the freestream velocity. V_∞. Also visible is the lift force vector. L. which is now perpendicular to the local relative wind. This means that it has a perpendicular and a horizontal component In this consideration, the horizontal component is of particular interest because it points in the direction of the freestream velocity and. hence. resembles a drag force In fact. it is called the induced drag. D_i. because it is an unwanted by-product of downwash and the induced angle of attack.

15

The deflection of a plain trailing edge flap on a finite 3D wing emphasizes the effects of downwash and induced drag. In practice, a plain trailing edge flap consists of only part of the wing's span. During deflection, the flap will create a gap at both span-wise edges, giving the airflow the opportunity to leak from the bottom surface to the top surface of the wing. This creates further vortices and the wing experiences an increased downwash in the vicinity of the flap. This, in turn, causes the induced drag to increase further. In addition, the wing sees a variation in the span-wise lift distribution. This is shown in figure 2.6.
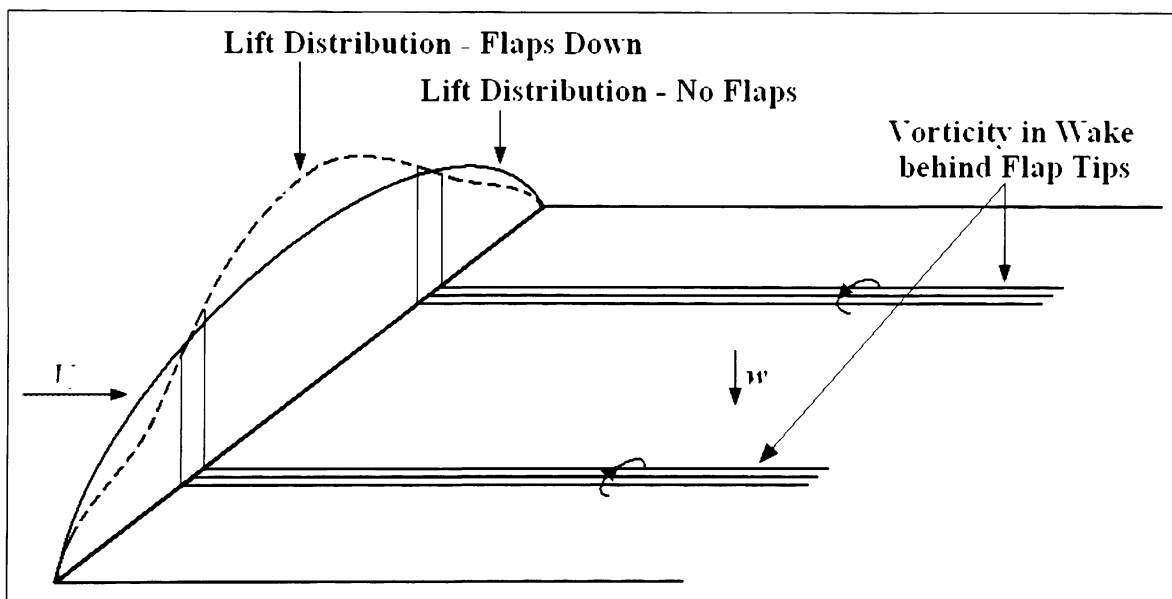
Figure 2.6: Sketch of the effects of part-span flap deflection on the span-wise lift distribution

This figure shows the lift distribution curve for both a wing with a deflected flap (dashed line) and a wing without a deflected flap (solid line). In the former case the lift distribution curve decreases at a much larger rate in the vicinity of the flap as seen from the center of the wing towards the wing tip. This is mainly due to the fact that the

additional leakage of air from the lower surface to the top surface of the wing magnifies the effects of downwash in the vicinity of the flap.

In summary, the deflection of a plain flap on a finite 3D wing increases the induced drag and alters the wing's span-wise lift distribution due to an additional leakage of air from the bottom to the top surface of the wing at the flap edges.

2.2. STAR-CD – The Computational Fluid Dynamics Software

STAR-CD is a commercially available software that was created by CD-adapco for the calculation of fluid flow, heat and mass transfer and chemical reactions in industrial and environmental applications. This section has the purpose to introduce the reader to the numerical solution techniques used to solve the mathematical models. In order not to go beyond the scope of this thesis, only those solution techniques of STAR-CD will be described that were actually used in the investigation. Furthermore, if appropriate, a brief explanation is presented of why a particular mathematical model or technique was chosen. Ultimately, this section should represent a transition into the methodology that has the ability to fully capture both the aerodynamics and the related stability and control phenomena that occur during flap deflection.

2.2.1. The Basic Conservation Equations

Just like any other fluid flow related computational software, STAR-CD solves the mass and momentum conservation equations, also called the Navier-Stokes (NS)

equations. These are presented below as equations 2.6 and 2.7, respectively, and are written in Cartesian tensor notation:

$$\frac{\partial \rho}{\partial t} + \frac{\partial}{\partial x_j}\left(\rho u_j\right) = s_m$$

[2.6]

$$\frac{\partial \rho u_i}{\partial t} + \frac{\partial}{\partial x_j}\left(\rho u_j u_i \, \partial \rho_{ij}\right) = \partial \frac{\partial p}{\partial x_i} + s_i$$

[2.7]

where t - time

x_i Cartesian coordinate (i = 1, 2, 3)

u_i absolute fluid velocity component in direction x_i

p piezometric pressure = $p = p_s - \rho_0 g_m x_m$ where p_s is static pressure, ρ_0 is reference density, the g_m are gravitational acceleration components and the x_m are coordinates relative to a datum where ρ_0 is defined

ρ - density

ρ_{ij} stress tensor components

s_m - mass source

s_i - momentum source components

In laminar flow, both Newtonian and non-Newtonian fluids are modeled in STAR-CD, if they obey the following constitutive relation:

$$\tau_{ij} = 2\mu s_{ij} \, \partial \frac{2}{3} \mu \frac{\partial u_k}{\partial x_k} \tau_{ij}$$

[2.8]

18

In equation 2.8, μ is the molecular dynamic viscosity of the fluid and δ_{ij} is the Kronecker delta, which is a 3-by-3 unit matrix. Furthermore, s_{ij} is the rate of strain tensor and is given by equation 2.9 below:

$$s_{ij} = \frac{1}{2}\left(\frac{\partial u_i}{\partial x_j} + \frac{\partial u_j}{\partial x_i}\right) \tag{2.9}$$

In the case of non-Newtonian fluids, STAR-CD distinguishes between pseudoplastic (shear-thinning) and dilatant (shear-thickening) classes. In both cases the fluid viscosity is dependent on the local value of the second invariant of the rate of strain tensor, II_s, defined by:

$$II_s \equiv \frac{1}{2}\left(s_{ij}s_{ij} \equiv s_{ii}s_{jj}\right) \tag{2.10}$$

The viscosity formula used for non-Newtonian fluids is the Ostwald-de Waele or 'power law' model, described by the following equation:

$$\mu = m\left|II_s\right|^{\frac{n-1}{2}} \tag{2.11}$$

m and n are fluid-dependent parameters. A value of $n < 1$ corresponds to pseudoplastic and $n > 1$ corresponds to dilatant fluids, respectively. If $n = 1$, then equation 2.11 reduces to the Newtonian case. STAR-CD allows access to the viscosity model and the II_s file, so

that the user can code alternative models. However, for this investigation, this option was not utilized.

In the case of turbulent flow, u_i, p, τ_{ij} and other dependent variables assume their ensemble averaged values. In this case, the stress tensor takes the following form:

$$\tau_{ij} = 2\mu s_{ij} \partial \frac{2}{3}\mu \frac{\partial u_k}{\partial x_k}\tau_{ij} \partial \overline{\tau u_i'u_j'} \qquad [2.12]$$

In equation 2.12, the u' are the fluctuations of the absolute fluid velocity component about the average velocity. The rightmost term in equation 2.12 represents the additional Reynolds stresses due to turbulent motion. These are linked to the mean velocity field via the turbulence models, which are presented in a subsequent section.

2.2.2. Heat Transfer Modeling

STAR-CD models heat transfer through the general form of the enthalpy conservation equation for a fluid mixture, which is given by equation 2.13 below. Again, this equation is presented in Cartesian tensor notation and the subscript j denotes a summation in the following manner: $\dfrac{\partial \rho u_j}{\partial x_j} = \dfrac{\partial \rho u_1}{\partial x_1} + \dfrac{\partial \rho u_2}{\partial x_2} + \dfrac{\partial \rho u_3}{\partial x_3}$

$$\frac{\partial \rho h}{\partial t} + \frac{\partial}{\partial x_j}\left(\rho h u_j + F_{h,j}\right) = \frac{\partial p}{\partial t} + u_j\frac{\partial p}{\partial x_j} + \rho_{ij}\frac{\partial u_i}{\partial x_j} + s_h \qquad [2.13]$$

In equation 2.13, h denotes the static enthalpy and is defined in the following way:

20

$$h \equiv \overline{c}_p T \equiv c_p^0 T_0 + \sum Y_m H_m = h_t + \sum Y_m H_m \qquad [2.14]$$

where T - temperature

                Y_m - mass fraction of mixture constituent m

                H_m - heat of formation of constituent m

                $\sum$ - summation over all mixture constituents

                $\overline{c}_p$ - mean constant-pressure specific heat at temperature T

                c_p^0 - reference specific heat at temperature T_0

                $F_{h,j}$ - diffusional energy flux in direction x_j

                s_h - energy source

                h_t - thermal enthalpy

The static enthalpy, h, in equation 2.14 is defined as the sum of the thermal and chemical components. This has been done to allow the solution of chemically reacting flows. However, since this investigation does not consider such flows, this term becomes irrelevant.

2.2.3. Thermophysical Properties

STAR-CD accounts for variation of all thermophysical properties of fluids, such as density, viscosity, thermal conductivity, species diffusivities and specific heats, as functions of temperature, mass fraction and other variables. In addition, it is possible to

insert user-specified property functions. However, those have not been utilized and, hence, are not elaborated in the following paragraphs.

As already indicated in the introduction, flap deflection takes place at low airspeeds when it is necessary to increase the lift coefficient of the airplane. Therefore, it was assumed for part of this investigation, that the flow is incompressible. This means that STAR-CD's built-in function for incompressible liquids and gases was chosen, which runs as follows:

$$\rho = \rho_0 \qquad\qquad\qquad [2.15\ a]$$

In equation 2.15, ρ_0 is a reference or freestream density and is constant. For the remainder of the analysis, for which it was not certain whether the flow is incompressible, it was assumed that the gas (air) is ideal. This means that the density of the flow is a function of pressure and temperature:

$$\rho = \frac{p_s}{RT} \qquad\qquad\qquad [2.15\ b]$$

In equation 2.15 b, p is the static pressure, R is the specific gas constant and T is the temperature. For further information regarding the calculation of the density, please refer to subsection 3.2.1. on page 104.

The variation of viscosity is modeled with the Sutherland equation, which expresses the viscosity as a function of the absolute temperature.

$$\mu = \left(\frac{T_0}{273.15}\right)^{\frac{3}{2}} \frac{273.15 + C_s}{T + C_s} \mu_0 \qquad\qquad\qquad [2.16]$$

In equation 2.16, μ_0 is the dynamic viscosity at 273.15 K and 101.325 kPa, C_s is the Sutherland constant and T_0 is the absolute temperature.

2.2.4. Turbulence Modeling in STAR-CD

The turbulence modeling capabilities of STAR-CD are divided into three categories: Eddy Viscosity, Reynolds Stress and Large Eddy Simulation (LES) models. All of these models represent approximations of reality, whose degrees of accuracy differ from each other. In general, however, an increase in accuracy is accompanied with an increase in required computational performance due to more complicated mathematical models or higher resolution in the discretization scheme. Furthermore, the STAR-CD methodology states that the accuracy of a turbulence model mainly depends on the nature of the problem to which it is applied. The ability to judge the suitability of a specific model is mainly based on experience.

The specific turbulence model used during this analysis is the k-ε/high Reynolds number model. An explanation for why this specific turbulence was used for this investigation is given in the next subsection. The k-ε/high Reynolds number model belongs to the Eddy Viscosity models and uses the turbulence kinetic energy, k, and its dissipation rate, ε, as typical turbulent velocity scale and length scale, respectively. In addition, the model comprises the high Reynolds number forms of the k and ε equations and a linear relationship between Reynolds stresses and strains. The following equation represents the transport equation for the turbulence kinetic energy, k:

$$\frac{\partial}{\partial t}(\rho k) + \frac{\partial}{\partial x_j}\left[\rho u_j k - \left(\mu + \frac{\mu_t}{\rho_k}\right)\frac{\partial k}{\partial x_j}\right] = \mu_t(P + P_B) - \rho\rho - \frac{2}{3}\left(\mu_t\frac{\partial u_i}{\partial x_i} + \rho k\right)\frac{\partial u_i}{\partial x_i} \qquad [2.17]$$

23

where
$$P \partial S_{ij} \frac{\partial u_i}{\partial x_j} \qquad [2.18]$$

$$P_B \partial \partial \frac{g_i}{\rho_{h,t}} \frac{1}{\rho} \frac{\partial \rho}{\partial x_i} \qquad [2.19]$$

$$\mu_t = f_\mu \frac{C_\mu \rho k^2}{\rho} \qquad [2.20]$$

In equation 2.17, the first term on the right-hand side represents turbulence energy generation by shear and normal stresses and buoyancy forces, the second viscous dissipation, and the third amplification or attenuation due to compressibility effects. Furthermore, equation 2.20 gives the turbulent viscosity μ_t, whereas f_μ in this case is equal to unity. S_{ij} is equal to $2s_{ij}$ from equation 2.9 and C_μ is given in table 2.1 on the next page.

To complete the description of the turbulence model, equation 2.21 represents the transport equation for the turbulence dissipation rate, ε:

$$\frac{\partial}{\partial t}(\varepsilon \varepsilon) + \frac{\partial}{\partial x_j}\left[\varepsilon u_j \varepsilon \right] \left[\mu + \frac{\mu_t}{\varepsilon_t} \right]\left[\frac{\partial \varepsilon}{\partial x_j} \right] =$$

$$C_{\varepsilon 1}\frac{\varepsilon}{k}\left[\mu_t P \right] \frac{2}{3}\left[\mu_t \frac{\partial u_i}{\partial x_i} + \varepsilon k \right]\left[\frac{\partial u_i}{\partial x_i} \right] + C_{\varepsilon 3}\frac{\varepsilon}{k}\mu_t P_B \left[C_{\varepsilon 2}\frac{\varepsilon^2}{k} + C_{\varepsilon 4}\varepsilon \varepsilon \frac{\partial u_i}{\partial x_i} \right]$$

$$[2.21]$$

In equation 2.21 ε_σ is the turbulent Prandtl number and $C_{\sigma 1}$, $C_{\sigma 2}$, $C_{\sigma 3}$ and $C_{\sigma 4}$ are coefficients whose values are also given in Table 2.1.

Table 2.1: Coefficients for the k-ε/high Reynolds number turbulence model

C_μ	σ_k	σ_ε	σ_h	σ_m	$C_{\varepsilon1}$	$C_{\varepsilon2}$	$C_{\varepsilon3}$	$C_{\varepsilon4}$	σ	E
0.09	1.0	1.22	0.9	0.9	1.44	1.92	0.0 or 1.44	-0.33	0.419	9.0

Table 2.1 indicates that the value of $C_{\varepsilon3}$ varies. In fact, if the value of P_B is greater than zero, $C_{\varepsilon3}$ will be equal to 1.44. Otherwise, $C_{\varepsilon3}$ will equal zero as well.

This concludes the description of the turbulence model used in this investigation. As mentioned earlier, the next subsection explains why this turbulence model was chosen.

2.2.5. Turbulence Model Selection

Next to grid generation methods and solution algorithms, turbulence models represent an important part of all CFD software. This is mainly due to the fact that the majority of flows which appear in nature or in any engineering or science experiment contain turbulence somewhere in the flowfield. In fact, turbulent flow occurs if the inertial forces within a fluid become stronger than its viscous counterpart, which is usually accompanied by large velocity and pressure gradients.

This subsection has the goal to provide further justification for the choice of turbulence model that was presented and explained in the previous subsection. This is done by listing the advantages and disadvantages of all three classes of turbulence models that are available in STAR-CD and by evaluating their applicability to this investigation. As a reminder, the three classes of turbulence models are eddy viscosity, Reynolds stress and large eddy simulation models [7]. The eddy viscosity models can be further

subdivided into zero-, one- and two-equation models. The number of equations indicates how many additional differential transport equations need to be solved on top of the conservation of mass, momentum and energy equations [13].

The zero-equation turbulence model, also referred to as algebraic or mixing length model, has the advantage that its implementation is simple and that it shows a strong numerical stability. However, by definition this model is incomplete, which practically means that it is very specific in its application. In other words, it needs to be calibrated for different types of cases. Besides, the zero-equation model provides relatively inaccurate results for detached boundary layers as compared to one- and two-equation models. This proves unsuitable for this investigation due to its transient nature, changing geometry and suspicion of flow separation at large flap deflection angles.

Two-equation and advanced one-equation turbulence models, on the other hand, are complete, which means that they do not require fine-tuning for each type of analysis and therefore are applicable to a wide variety of flows. Examples for the one-equation turbulence model are the Baldwin-Barth and the Spalart-Allmaras models. The former showed worse results in terms of accuracy in the presence of an adverse pressure gradient than the latter [13]. Examples for the two-equation model are the k-ε and the k-ε model, whereas the former was used in this specific investigation due to its widespread applicability. Wilcox, however, indicates that the k-ε turbulence model showed inaccuracies for separated flow and that it has shortcomings in responding to adverse pressure gradients.

Reynolds stress models, which directly calculate the Reynolds stresses, have several advantages as compared to the models previously discussed. They are applicable

whenever it is necessary to investigate non-isotropic effects in the flowfield. Furthermore, this turbulence model shows improvements in the results for cases in which streamline or wall curvature is prevalent. The downside of the Reynolds stress model, however, is the complexity of their implementation, their numerical instability and high computational demands [14]. These disqualify the Reynolds stress model from this application because the goal of this analysis is to prove the feasibility of a methodology as efficiently as possible.

Finally, the large eddy simulation (LES) models compute the large eddies in the flowfield and model the smallest eddies on a subgrid scale (SGS). LES is a relatively young turbulence model as compared to those discussed above, and it still contains deficiencies such as the SGS stress model. In addition, the LES model tends to be time intensive from a computational point of view. Nevertheless, Wilcox indicates that the research in this area has a promising future.

The above considerations showed that all turbulence models have their advantages and disadvantages. For this investigation, it was necessary to choose a turbulence model that is numerically stable, has a history of widespread successful application and does not exhibit high computational demands. Considering these characteristics, it turned out that the k-ε turbulence model seemed to be the best compromise. Certainly, this turbulence model has shortcomings regarding its accuracy for flows with large adverse pressure gradients, but the fact that it has successfully been applied to a large number of cases outweighs this shortcoming.

2.2.6. Geometry and Computational Mesh Capabilities

Mesh generation plays a central role in CFD analysis because of its potential to affect the quality and accuracy of a simulation. Furthermore, a mesh has the purpose to fit the boundary surface of a computational domain and divide its volume into smaller subdomains, also called cells. These are then used to solve the differential conservation equations of the mathematical model. In other words, the mesh bridges the gap between the geometry and the computational model. The purpose of this section is to introduce the reader to those meshing capabilities of STAR-CD that were especially useful to complete this study. Brief examples will be taken from the model created for this study. However, this section will not elaborate on the mesh development itself because this is the main subject of section 2.3.

STAR-CD has built-in geometry and mesh generation tools that allow the user to either develop a mesh from scratch or to import a geometry from a computer aided drawing (CAD) tool. For this investigation, pro-STAR was the primary mesh generation tool. In addition, the advanced meshing module, pro-am, was used to save mesh geometry elements, such as the flaps, in databases in order to integrate them into a single model. As already mentioned, further details about how the meshes were created are given in section 2.3. when the actual mesh generation process is described.

Embedded mesh refinement played a significant role in the generation of the mesh geometry for this study. This feature allows the user to subdivide existing cells into smaller cells. In the case of a wing, for example, this is especially important in the region close to the surface. There, it is particularly important to increase the density of the mesh in order to properly model the boundary layer and related aerodynamic phenomena, such

as turbulence. Figure 2.7 below shows embedded mesh refinement in the region around the aircraft model used in this analysis.
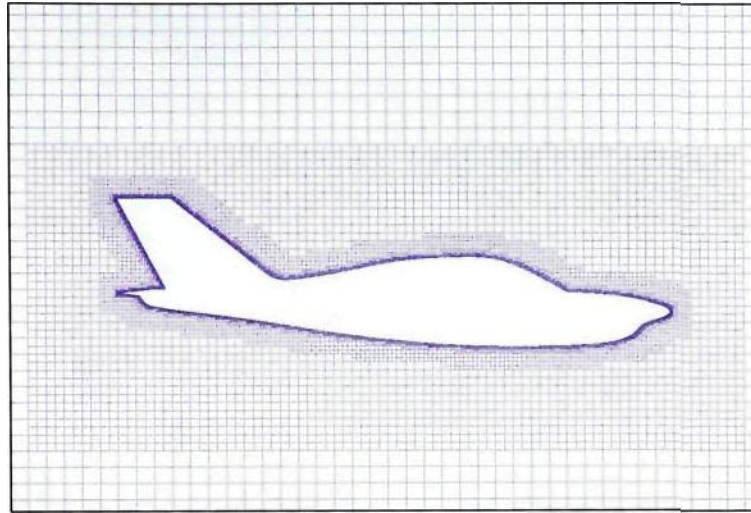
Figure 2.7: Embedded mesh refinement shown in a section view of a 3D airplane model

Another feature of STAR-CD's pre-processor pro-STAR that found application in this study was the capability to create arbitrary mesh interfaces, which allow a discontinuity across the common interface between adjacent mesh blocks. This feature was particularly useful when the movable 3D trailing edge flap section was attached to the wing of the general aviation airplane model for this analysis. The movable 3D trailing edge flap section was generated within a structured mesh block exclusively consisting of hexahedra. The mesh block that contains the general aviation aircraft was generated using an unstructured mesh consisting of polyhedral cells. For clarification, refer to figure 2.8 below.
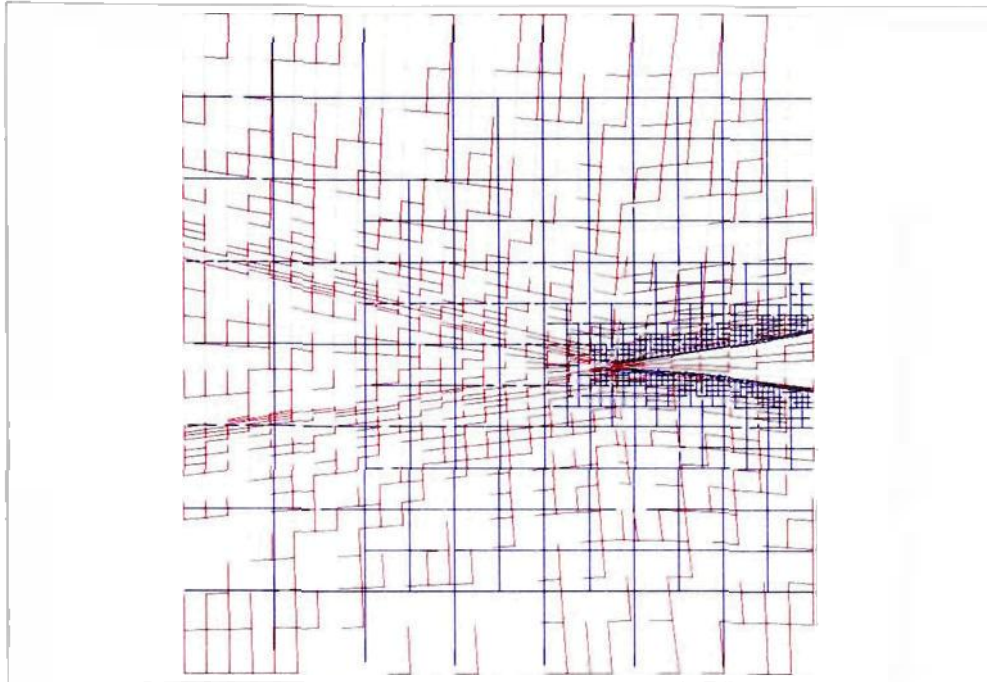
Figure 2.8: Arbitrary mesh interface between the flap mesh block and the airplane mesh block

The most important feature for this analysis is STAR-CD's capability to model moving meshes. This option allows the user to distort the entire mesh or portions thereof in a prescribed time-varying fashion to accommodate boundary motion, such as a moveable flap. Figure 2.9 on the next page shows three 2D plots of the mesh in the vicinity of the flap at three different deflection angles. All three pictures show the same mesh at different stages of the deflection process. Again, a detailed description of the method used to move the mesh is presented in section 2.3.
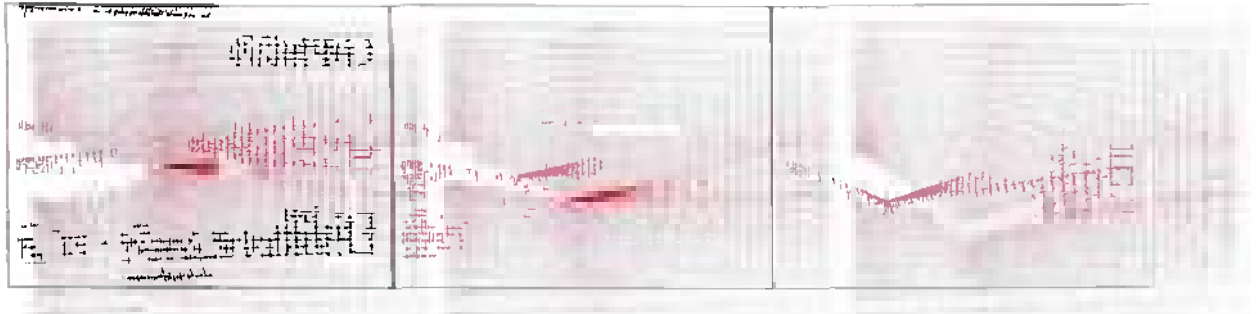
Figure 2.9: **2D moving mesh of the flap section at deflection angles of 0°, 16° and 30°, from left to right**

2.2.7. Discretization Practices

After an introduction of the physical discretization of the computational domain in the previous section, it seems meaningful to continue with a description of the discretization practices used for the mathematical model. STAR-CD uses the finite volume (FV) method to discretize the governing conservation equations of mass, momentum and energy, which were mentioned in subsections 2.2.1. and 2.2.2. More specifically, the governing equations are first integrated over the individual computational cells and over a finite time increment, in the case of transient problems, and then approximated in terms of the cell-centered values of the dependent variables. This approach has the merit of ensuring that the discretized forms preserve the conservation properties of the parent differential equations [7].

With regards to the FV discretization scheme, STAR-CD utilizes a special form of the conservation equations. This special form is coordinate-free and is given below:

$$\frac{\partial}{\partial t}(\rho\phi) + div\left(\rho \vec{u}_r \phi - \Gamma_\phi grad\phi\right) = s_\phi \qquad [2.22]$$

31

In equation 2.22, $\bar{u}_r = \bar{u} - \bar{u}_c$ is the relative velocity between the fluid, $\bar{u}$, and the local coordinate velocity, $\bar{u}_c$. Furthermore, ϕ acts as a placeholder for any of the dependent variables, such as u_i, e, and k. Γ_ϕ and s_ϕ represent the associated 'diffusion' and 'source' coefficients, which can be deduced from the parent equations.

For an arbitrary time-varying volume, V, bounded by a moving closed surface, S, equation 2.22 can be rewritten in the following manner:

$$\frac{d}{dt}\int_V \rho \phi dV + \int_S \left(\rho \bar{u}_r \phi - \Gamma_\phi grad\rho \right)\cdot d\vec{S} = \int_V s_\phi dV \qquad [2.23]$$

where $\vec{S}$ is a surface vector and $\bar{u}_r$ turns into the relative velocity vector between the fluid and the surface. Furthermore, with respect to a computational cell with volume V_p and discrete faces S_j, equation 2.23 turns into the following form:

$$\frac{d}{dt}\sum_{V_p} \rho \phi dV + \sum_j \sum_{S_j} \left(\rho \bar{u}_r \phi - \Gamma_\phi grad\rho \right)\cdot d\vec{S} = \sum_V s_\phi dV \qquad [2.24]$$

For clarification purposes, refer to figure 2.10 on the next page which illustrates a typical hexahedral computational cell with its neighbor cell and their centered nodes.
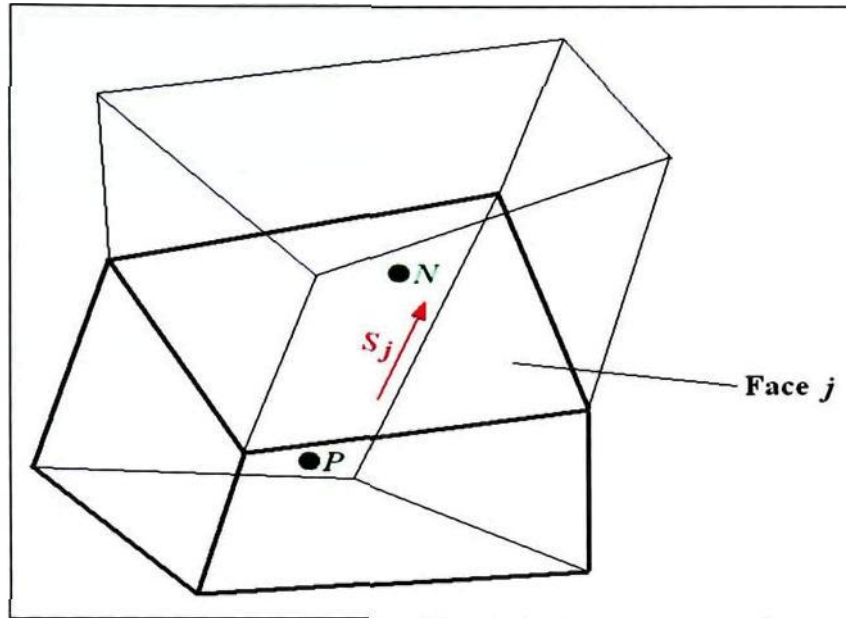
Figure 2.10: **Sketch of two adjacent hexahedral cells with their respective center nodes N and P**

After stating special forms of the conservation equations favorable for the FV discretization scheme, it is now necessary to introduce the approximations. Thus, the first term on the left-hand side of equation 2.24 is approximated in the following manner:

$$\frac{d}{dt} \int_{V_P} \rho \phi dV \approx \frac{\left(\rho \phi V\right)_P^n - \left(\rho \phi V\right)_P^o}{\delta t} \qquad [2.25]$$

In equation 2.25, the superscripts n and o refer to 'old' and 'new' time levels, respectively, which are separated by the time interval δt.

The second term on the left-hand side of equation 2.24 is approximated with the expression in equation 2.26. The latter is separated into contributions due to convection and diffusion, which are denoted by C_j and D_j, respectively.

33

$$\sum_{j}\sum_{S_j}\left(\rho\bar{u}_r\rho - -_{\phi}grad\rho\right)\!\cdot d\vec{S} - \sum_{j}\left(\rho\bar{u}_r\rho\cdot\vec{S}\right)_{j} - \sum_{j}\left(-_{\phi}\overline{grad\rho}\cdot\vec{S}\right)_{j} - \sum_{j}C_{j} - \sum_{j}D_{j} \qquad [2.26]$$

Finally, the term on the right-hand side of equation 2.24 is approximated with the following expression:

$$\int_{V}S_{\phi}dV \approx s_1 \approx s_2\phi_P \qquad [2.27]$$

Equation 2.27 may contain components representing sources, sinks and additional flux terms of the transported property.

STAR-CD gives the user the choice between two temporal discretization schemes, a first-order accurate fully implicit and a second-order accurate Crank-Nicholson scheme. For this investigation, the fully implicit scheme was used because it allows bigger time steps than the Crank-Nicholson scheme without the risk of generating unbounded extrema [7]. The bigger time steps, in turn, help reducing the computational requirements and computing times. In addition, as opposed to the explicit approach, this scheme avoids stability-related time step restrictions, which is advantageous in the case of small mesh spacing and high velocity and diffusion rates. The fully implicit scheme calculates fluxes prevailing over time from the new time-level values of the variable. Figure 2.11 below illustrates the inner working of this practice. Overall, the fully implicit scheme excels in efficiency because of its ability to deal with relatively bigger time steps; however the time steps should not be chosen too big in order to avoid temporal

approximation errors in transient problems and instabilities due to non-linearity in steady-state problems [7]. For the particular values of the time steps for the transient solutions in this study refer to the analysis section in chapter 3.
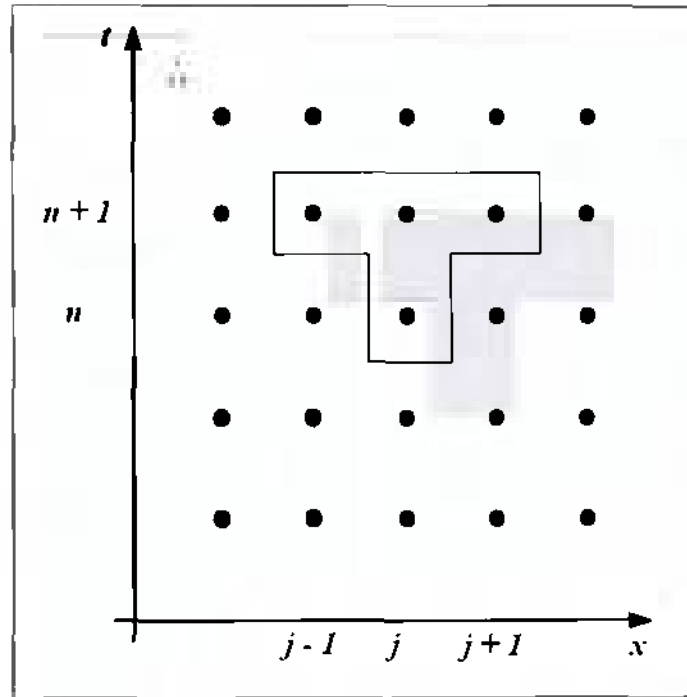
Figure 2.11: Illustration of fully implicit scheme

In the case of spatial discretization. STAR-CD offers either low-order or higher-order discretization schemes. For this study. a higher-order spatial discretization scheme called the monotone advection and reconstruction scheme (MARS) was applied to the *momentum conservation equations (equations 2.7) and the upwind differencing scheme* (UD). a low-order scheme. was used for the solution of the transport equations of turbulence kinetic energy and turbulence dissipation rate (equations 2.17 and 2.22) [7].

The MARS is a multidimensional second-order accurate differencing scheme that first conducts a reconstruction and then an advection of the dependent variables. During

reconstruction, the scheme computes monotone gradients using a multidimensional Total Variation Diminishing (TVD) scheme, and, during advection, the scheme uses reconstructed cell-face properties to calculate the face fluxes for all properties that underwent advection. This is accomplished by applying a monotone and bounded advection scheme. The advantages of this scheme are that it does not rely on any problem related parameters to work properly and that it can be applied to any problem and mesh types created by pro-STAR [7]. In addition, MARS has a feature which allows the user to compromise between accuracy and convergence rate, which turned out especially useful during this analysis.

The UD scheme is a first-order scheme that simply selects the nearest upwind neighbor value for the dependent variable, ϕ. The following expression describes the scheme:

$$C_j^{UD} = F_j \begin{matrix} \geq \phi_P, F_j \geq 0 \\ \geq \\ \geq \phi_{N+}, F_j < 0 \end{matrix}$$

[2.28]

For a node labeling convention suitable for expression 2.28, refer to figure 2.12 at the top of the next page. This simple scheme was chosen in order to increase the simulation's efficiency and to preserve the physical bounds on the dependent variable under all conditions.
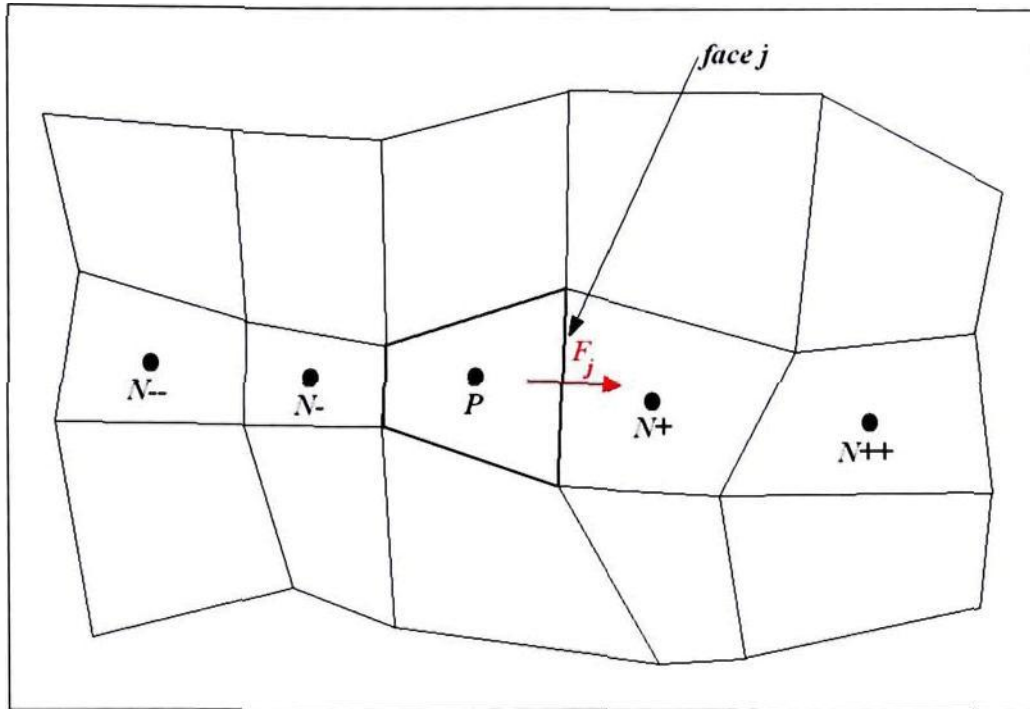
Figure 2.12: Illustration of the nomenclature used in the UD scheme

Before closing this section, it is necessary to present the final equations of the FV approach. First, however, the discretized form of the continuity equation needs to be defined. It runs as follows.

$$\frac{(\rho V)^{'} - (\rho V)^{''}}{\delta t} + \sum F_j = 0 \qquad\qquad [2.29]$$

For the fully implicit-scheme the F_j terms are at time level n + 1.

Then, by invoking the discretized continuity equation given above and by inserting all the various approximation terms into equation 2.24, the result, in its most compact form is given by the equation 2.30 on the next page.

$$A_p \phi_P^{n} = \sum_m A_m \phi_m^{n} + s_1 + B_P \phi_P^{o} \qquad [2.30]$$

where A_m effects of convection and/or diffusion

$\sum_m$ - summation over all neighbor nodes used in the flux discretization

B_P $(\rho V)^o / \rho t$

and

$$A_P \equiv \sum_m A_m + s_2 + B_P \qquad [2.31]$$

Equation 2.30 exists for every computational cell in the domain. Furthermore, the number of the equation sets depends on the number of dependent variables. The ways these sets of equations are solved are described in section 2.2.8., which presents the solution algorithm options in STAR-CD.

2.2.8. Boundary Conditions in STAR-CD

Boundary conditions specify the physical situation at the limits of the computational domain. STAR-CD has a variety of built-in options for the most useful boundary conditions. Furthermore, STAR-CD enables the user to apply boundary conditions to individual cell faces or an entire surface of the computational domain. This section introduces those specific boundary conditions that found application in this

investigation. Details about the specific values of inlet velocity components etc. are presented in the analysis, chapter 3.

The first boundary condition is the inlet, or free, boundary condition. It can be defined either by specifying the inlet flow or by declaring its stagnation conditions. For this particular analysis, the inlet conditions were specified by defining the inlet flow velocity components, the boundary pressures and the prescribed temperatures. In the case of incompressible flow, which is assumed in this investigation, the distributions of all variables except pressure are prescribed at the centers of the boundary cell faces [7]. The pressure is extrapolated from the solution domain interior. Furthermore, the inlet boundary condition was chosen to be located at the upstream face of the computational domain. For a clarification, please refer to figure 2.13 at the end of this section.

Another essential type of boundary condition that found application in this analysis is the outlet boundary. In general, this type of boundary condition is suitable for locations where the flow is outwards-directed everywhere, but otherwise the conditions are unknown. In this particular investigation, the outlet boundary condition was chosen to be located on the downstream face of the computational domain. STAR-CD identifies the unknown flow conditions in two steps. First, the distributions of variables on the outlet plane are evaluated by extrapolation from upstream, and then the velocities are adjusted, such that the outlet flow rate satisfies overall continuity. If inflow occurs at the outlet boundary, difficulties may occur [7]. That is why the author chose to extend the computational domain far enough downstream to avoid an interference of potential recirculation zones in the wake of the wing with the outlet boundary.

Except for the upstream and downstream faces, all other faces of the computational domain were defined as symmetry boundaries in this analysis. STAR-CD in this case assumes that the flow inside the computational domain resembles a virtual flow field outside the boundary. In other words, the symmetry boundary acts like a mirror for the flow. Ideally, the flow should be parallel to this sort of boundary to avoid complications in the calculations [7]. Therefore, the computational domain was generously expanded in the directions perpendicular to the symmetry boundaries.

The surfaces of the airfoil or wing in this analysis were modeled by an impermeable wall boundary. At this boundary, STAR-CD offers the option to either define it as a no-slip or slip surface for the flow. For this analysis the former was chosen. In addition, STAR-CD offers the user the choice of different near-wall turbulence models. These are described in more detail in the next section. Again, for a clarification of the location of the different boundaries, see figure 2.13 below.
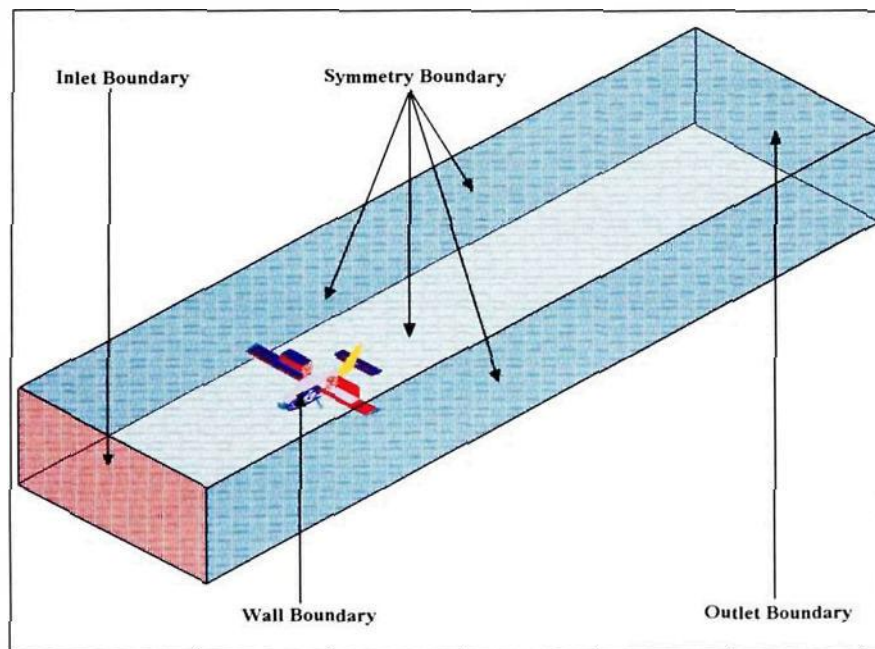
Figure 2.13: Sketch of computational domain with boundary condition location

2.2.9. Turbulent Wall Boundary Conditions

Due to the fact that turbulent flow is expected in this analysis, especially at high flap deflection angles, an appropriate treatment of the flow at the wall boundaries is required. STAR-CD offers several options to model the no-slip condition on walls and to account for boundary layers. These options include a 'two-layer'/low Reynolds number approach, a wall function approach and a hybrid wall boundary condition. For this analysis the second option was selected.

The wall function approach provides boundary conditions for the computational domain if the centroid of a near-wall cell lies within the logarithmic region of the boundary layer. According to the STAR-CD methodology, this is accomplished on the basis of assumed distributions of velocity, temperature and turbulence parameters across the boundary layer. The assumptions of this model state that the variations in the flow parameters are predominantly normal to the wall and hence one-dimensional, that the effects of pressure gradients and body forces are negligible leading to uniform shear stress in the layer, and that the shear stress and velocity vectors are aligned and unidirectional throughout the layer. Furthermore, it is assumed that a balance exists between turbulence energy production and dissipation and that the variation of turbulence length scale is linear. The following equations describe the velocity distribution in the boundary layer:

$$u^+ = \begin{cases} y^+ & , y^+ \leq y_m^+ \\ \dfrac{1}{\kappa}\ln\left(Ey^+\right) & , y^+ > y_m^+ \end{cases} \qquad [2.32]$$

41

where u^+ $\left(u - u_{w}\right)/u_{\tau}$

u — tangential fluid velocity

u_{w} — tangential wall velocity

u_{τ} — $\left(\tau_{w}/\tau\right)^{1/2}$

τ_{w} — wall shear stress

y^+ — $\rho u_{\tau} y / \mu \approx \rho C_{\mu}^{1/4} k^{1/2} y / \mu$

E — empirical coefficient

τ — von Karman constant

Furthermore, y_{m}^{+} satisfies the following equality:

$$y_{m}^{+} - \frac{1}{\kappa} \ln\left(E y_{m}^{+}\right) = 0 \qquad \qquad [2.33]$$

The numerical values of E and τ are shown in table 2.1 on page 25. The value of E = 9.0 corresponds to an aerodynamically smooth wall.

The wall function approach to the modeling of the boundary layer was chosen because it has the advantage of avoiding the need for a fine mesh at any wall boundary [7]. This, in turn, reduces the necessary computational requirements and computing time of the case under investigation. Ultimately, as mentioned before, next to the primary goal of this study to investigate the dynamic effects of flap deflection, computational efficiency was also a major concern.

42

Closely connected to the modeling of the boundary layer is the computation of wall forces. Specifically for this study, it was necessary to calculate the shear and pressure force on the surface of the wing and the airplane in order to compute the stability characteristics, such as lift, drag and moment coefficients, as well as the location of the center of pressure. STAR-CD allows the user to use specific functions to compute shear and pressure forces at the wall, which are based on the following mathematical models:

$$\overline{F}_s = \tau_w A_b \frac{\overline{v}_{par}}{\left|\overline{v}_{par}\right|}$$
[2.34]

and

$$\overline{F}_p = p_b A_b \overline{n}_b$$
[2.35]

where $\quad A_b \quad$ is a wall cell face area

$\overline{v}_{par}$ - is the velocity vector component parallel to the wall at the center of a near-wall cell

$\overline{n}_b$ - is the outward-pointing unit vector normal to the wall

The total force is subsequently computed by a simple vector addition:

$$\overline{F}_t = \overline{F}_s + \overline{F}_p$$
[2.36]

This concludes the discussion of the turbulent wall boundary conditions. The next section is the last in the introduction to the STAR-CD methodology and contains information regarding the solution algorithms used in this analysis.

2.2.10. Solution Algorithms

STAR-CD uses implicit methods to solve the algebraic FV equations 2.29 and 2.30 resulting from the discretization practices described in section 2.2.6. These implicit methods require the solution of simultaneous algebraic equation sets. This might turn into a disadvantage due to the often high complexity of the systems, but STAR-CD offers the user three implicit algorithms, which incorporate efficient, almost invariably iterative methods for solving these equation sets [7]. These three methods are variants of the so-called SIMPLE, PISO and SIMPISO methods, whereas the latter is a hybrid of the former two methods, as the name implies.

The SIMPLE and SIMPISO methods are used only for steady-state solutions, and the PISO method is applicable to both steady-state and transient calculations. For this specific study, the SIMPLE method was used to conduct the steady-state calculations. In addition, the PISO method was obviously used to compute the transient solution of the flowfield. In the past, the PISO method proved to be more efficient than iterative methods in the case of transient calculations [7]. For further details about the sequence of steady-state and transient calculations, refer to chapter 3, which gives a detailed description of the analysis part of this investigation. The following paragraphs describe the inner workings of both the PISO and the SIMPLE method.

The SIMPLE method is a subset of the PISO method, and, hence, the latter is described first. In addition, first the general working equations of the PISO method are introduced. These are suitable for a fixed Cartesian mesh aligned with the Cartesian velocity directions. To start with, the FV momentum equation, extracted from equation 2.30, runs as follows:

$$A_P u_{i,P}^n = H\left(u_{i,m}^n\right) + B_P^o u_{i,P}^o + s_1 + D_P\left(p_{N+}^n - p_{N-}^n\right) \qquad [2.37]$$

where $\qquad D_P \qquad$ - is a geometric coefficient

and

$$H\left(u_{i,m}\right) \equiv \sum_m A_m u_{i,m} \qquad [2.38]$$

In addition, the last term in equation 2.37 is the FV approximation to the pressure gradient, $\partial p / \partial x_i$. Furthermore, the continuity equation, 2.29 in section 2.2.6., is rewritten as follows:

$$B_P^n - B_P^o + \sum_j \left(\rho^n u_j^n S_j\right) = 0 \qquad [2.39]$$

where $\qquad u_j \qquad$ - velocities normal to the cell faces

$\qquad\qquad\quad S_j \qquad$ - are the corresponding face areas

For a clarification of the nomenclature, see figure 2.14 at the top of the next page.

.
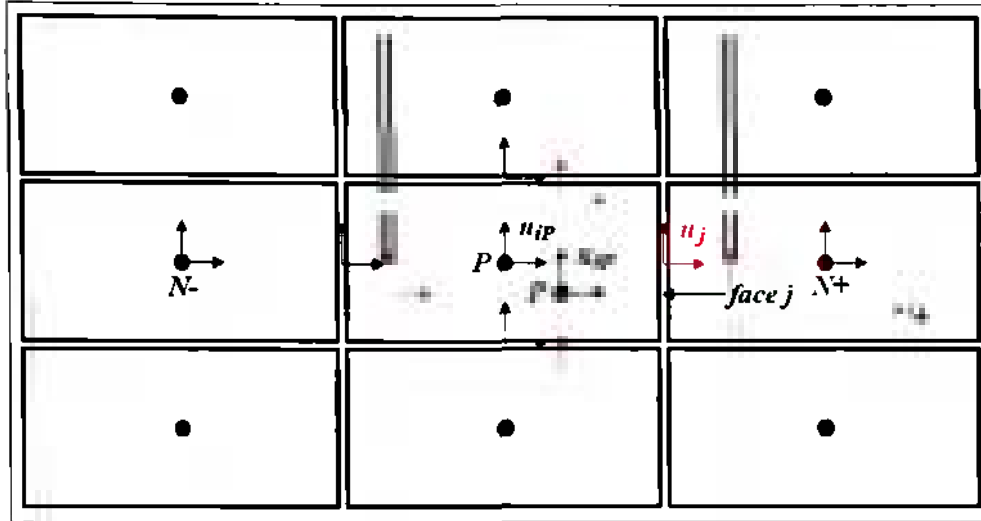
Figure 2.14: **Illustration of variables and notation used in the PISO algorithm for a Cartesian mesh**

In equation 2.39, the face velocities, u_j, are expressed in terms of the nodal velocities, u_{iP}, and the neighboring pressure. The former is necessary to calculate the mass fluxes, and the latter allows the formulation of a suitable pressure equation. For that purpose a cell-face momentum equation is formed based on equation 2.37:

$$\overline{A_P}u_j^n = \overline{H\left(u_{i,m}^n\right)} + \overline{B_P^o}u_{i,P}^n + \overline{s_i} + \overline{D_P}\left(p_P^n - p_{N+}^n\right) \qquad [2.40]$$

In equation 2.40, the over bars emphasize that the nodal momentum coefficients appearing under them are averaged. Furthermore, substituting equation 2.40 into the PISO form of the momentum equation, 2.39, yields the following pressure equation:

$$A_P p_P^n = \sum A_m p_m^n + s_1 \qquad [2.41]$$

where s_1 - function of nodal velocity fields u_i^n and u_i^o and other quantities

46

Now that the working equations of the PISO algorithm have been introduced, it makes sense to present the solution sequence employed by STAR-CD. It should be noted that the sequence starts from initial values of the dependent variable, ϕ^o, and advances through a time increment, δt, in a sequence of steps.

First, a predictor stage takes place, in which equation 2.37 in the following operator-split form is solved for the provisional nodal velocity field, $u_i^{(1)}$:

$$A_P u_{i,P}^{(1)} = H\left(u_{i,m}^{(1)}\right) + B_P^o u_{i,P}^o + s_1 + D_P \left(p_{N+}^{(0)} - p_{N-}^{(0)}\right)$$

[2.42]

The $p^{(0)}$ terms in equation 2.42 correspond to the pressure field at the start of the time step. Subsequently, the provisional face velocities, $u_j^{(1)}$, are computed through equation 2.40.

Following the predictor stage, a first corrector stage takes place, in which equation 2.42 is iterated in the following manner

$$A_P u_{i,P}^{(2)} = H\left(u_{i,m}^{(1)}\right) + B_P^o u_{i,P}^o + s_1 + D_P \left(p_{N+}^{(1)} - p_{N-}^{(1)}\right)$$

[2.43]

Again, equation 2.40 is applied to calculate the corresponding face velocities. The pressure equation, 2.41, in this case runs as follows:

$$A_P p_P^{(1)} = \sum_m A_m p_m^{(1)} + s_1$$

[2.44]

47

The resulting solution is an approximation to the original equations 2.37 and 2.39.

In the third and final step, further corrector stages are conducted in the same manner as in the first two steps. The equations in general form are:

$$A_P u_{i,P}^{(q+1)} = H\left(u_{i,m}^{(q)}\right) + B_P^o u_{i,P}^o + s_1 + D_P \left(p_{N+}^{(q)} - p_{N-}^{(q)}\right)$$

[2.45]

and

$$A_P p_P^{(q)} = \sum_m A_m p_m^{(q)} + s_1$$

[2.46]

where q - the corrector level (i.e. $q = 1, 2, \ldots$)

The solutions of successive corrector levels are better approximations to the original equations. STAR-CD determines the necessity for corrector stages after internally evaluating the measure of the splitting error. This enhances the accuracy and reliability of the algorithm [7].

The above description is based on Cartesian mesh geometry. In the more general case, which is often the case in STAR-CD, additional pressure gradient terms in the momentum equations complicate the pressure calculation, and the cell face mass fluxes depend on all three Cartesian velocity components. This means that the PISO algorithm presented above had to be modified substantially.

As mentioned in the introductory paragraph of this section, the SIMPLE algorithm was used for steady state calculations in this analysis. The major difference between the PISO and the SIMPLE algorithm is that the latter employs only one corrector stage. The implementation of the SIMPLE algorithm has similar features as the PISO

48

algorithm, and, otherwise, is based on the same general equations [7]. Therefore, the discussion of the solution algorithms ends at this point, which simultaneously concludes the introduction of the main features of STAR-CD.

In the subsequent sections, the focus shifts to the implementation and generation of the mesh geometry and features which were necessary to conduct this analysis. The previous discussion should have provided enough information to substantially facilitate an understanding of the rationale behind the methods.

2.3. Geometry Implementation and Mesh Generation

This section has the purpose to introduce the reader to the methodology developed to model a variable mesh geometry that allows the transient simulation of the effects of flap deflection on the aerodynamic and stability and control characteristics of a wing. The following subsections provide a detailed insight into the meshing strategy and how the geometric capabilities of STAR-CD are employed. Furthermore, wherever necessary and appropriate, an explanation is given of why specific geometries and mesh characteristics were chosen.

2.3.1. Window Structure and Semi-Automation in STAR-CD

STAR-CD offers two user-interface options: a command window and a graphical-user-interface (GUI), also called STARGUIde. Both options enable the user to access every feature offered by STAR-CD. In this analysis the command window was primarily

used for mesh generation and post-processing, and the GUI was used for the analysis and the definition of analysis parameters. Figure 2.15 below shows a picture of a typical STAR-CD window structure used in this analysis. It shows four different windows: the plot screen, the panel and the mentioned command window as well as STARGUIde. The plot screen visualizes the mesh geometry and the results. Figure 2.15 also shows that the use of at least two screens or, in the case of LINUX, the use of multiple work spaces, facilitates the handling of STAR-CD tremendously. Fortunately, the gas turbine laboratory at Embry-Riddle Aeronautical University offered a workstation that contained a LINUX operating system and that consisted of two 19-inch monitors, which were ideal for the use of STAR-CD and consequently accelerated the progress in this investigation.
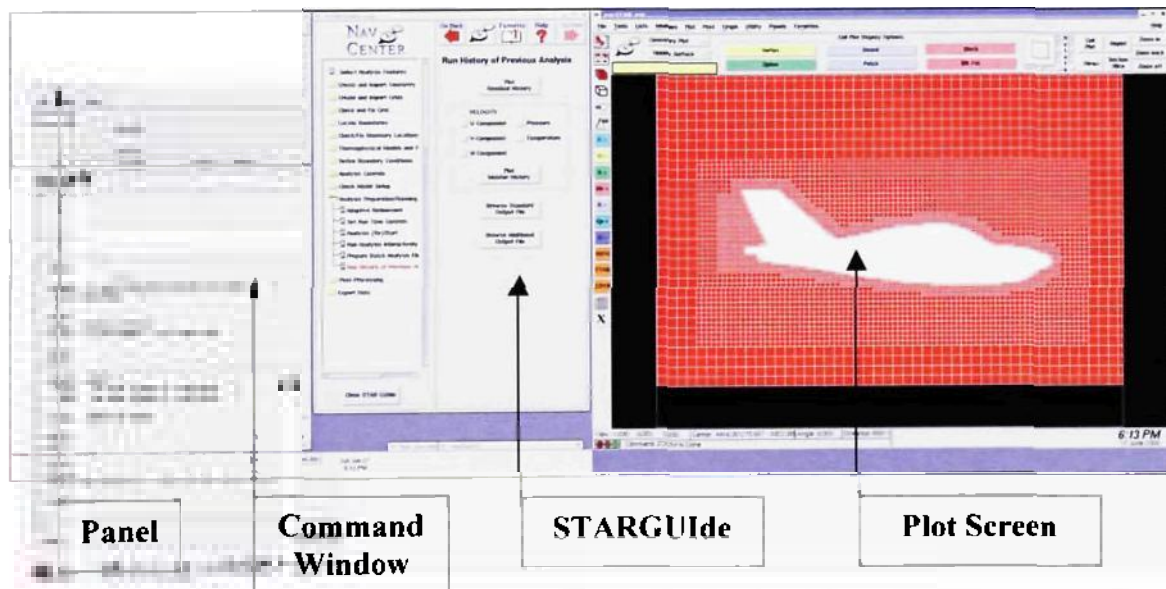
Figure 2.15: Picture of a typical STAR-CD window structure

50

The feature that deserves special attention is the panel because it allows the user to define customized command buttons, which, in turn, enables a semi-automation of the mesh generation process. It was mentioned in the previous paragraph and is located at the top left corner of figure 2.15. The panel contains several command buttons which can be defined by the user. The command buttons, in turn, can contain a user-specified number and order of STAR-CD commands that are automatically executed. In addition, the user can use the *ifile*-command to link the command button to an input file, which contains a script consisting of a batch of STAR-CD commands. This was especially useful in this investigation because it facilitated the development of scripts that automatically create large parts of the computational domain. That way, it was possible to create the entire mesh geometry by pushing a few command buttons on a panel, which made the mesh generation process semi-automatic. Also, this feature facilitated the search for and correction of bugs in the mesh generation scripts.

As indicated in the previous paragraph, the creation of mesh generation scripts was central to the mesh generation process. The following subsections focus on the purpose and inner workings of each script and describe the relationship among them. Before that, however, a brief description and explanation of the mesh geometry is given.

2.3.2. Two- and Three-Dimensional Geometry

The overall analysis in this study is divided into two parts: a two- and a three-dimensional analysis. The two-dimensional (2D) case was conducted first to prove the feasibility of modeling the process of flap deflection with STAR-CD. Then the three-dimensional (3D) case was performed to prove the ability of the basic mesh and analysis

concepts, developed in the 2D case, to adapt to an arbitrary plain flap and aircraft model if necessary. Overall, both cases together have the goal to present the successful development of a methodology that is based on commercial CFD software, which has the ability to fully capture both the aerodynamics and the related stability and control phenomena that occur during flap deflection.

Due to the fact that this analysis has the goal to investigate the effects of the process of flap deflection, a transient study was required. This, in turn, meant that the computational mesh in both the 2D and the 3D case needed to offer the ability to adapt to a changing geometry caused by the deflection of a plain flap. In other words, the implementation of a moving mesh was required for this analysis.

2.3.2.1. The 2D Case

For the 2D case, it was decided to use the NACA 0012 airfoil, which is a symmetric airfoil from the NACA four-digit family of wing sections [8]. The first two digits indicate that the airfoil does not have any camber and is indeed symmetric. The last two digits imply that the thickness of the airfoil consists of 12% of its chord. A scaled sketch of the airfoil is shown in figure 2.16 on the next page.

This airfoil was chosen because its parameters at zero angle of attack are well known. More specifically, a symmetrical airfoil at zero angle of attack does not produce any lift, as indicated by classical thin airfoil theory in section 2.1.1. on page 8. Furthermore, it was mentioned in section 2.1.2., on page 12, that the center of pressure for a symmetric airfoil at zero angle of attack is located at the quarter chord. So, if the

angle of attack of the airfoil is held constant at zero during the flap deflection process, the variations of the airfoil's lift coefficient and location of the center of pressure are easily identifiable. Also, the mentioned variations can be regarded as a result of the flap deflection process alone.

In addition to the benefits mentioned above, a symmetric airfoil facilitates the verification of the computational results. The theory of wing sections offers data regarding the value of the drag coefficient for a NACA 0012 airfoil at zero angle of attack. This, in addition to the known initial values for the lift coefficient and the location of the center of pressure, allows a holistic verification of the accuracy of the computational results for the NACA 0012 airfoil at zero angle of attack and no flap deflection.
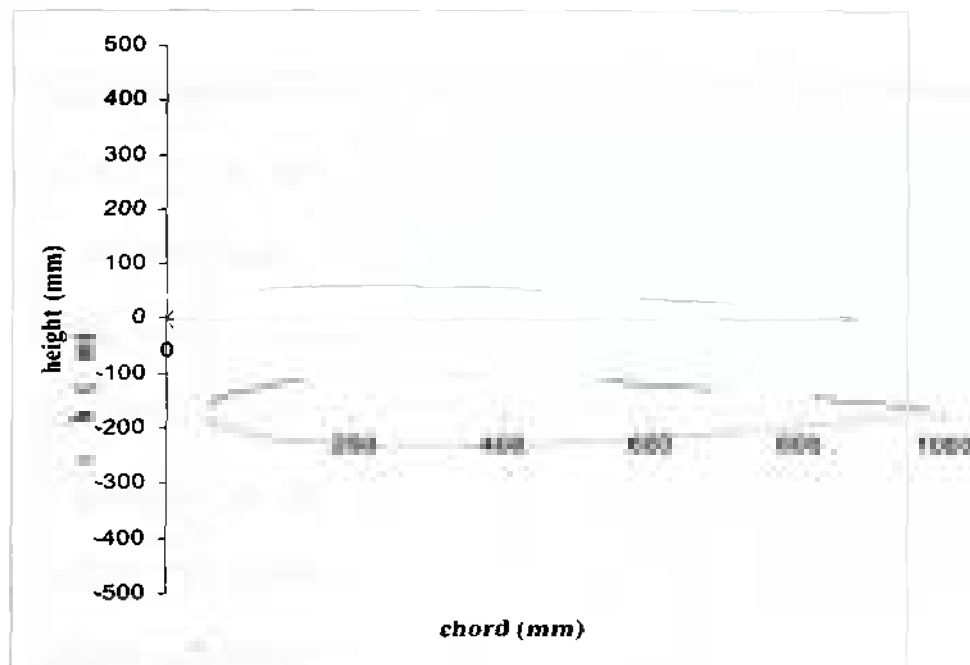
Figure 2.16: Scaled sketch of NACA 0012 airfoil

53

The 2D plain flap was modeled as a movable trailing edge section of the airfoil and was hinged at a point on the camber/chord line that is located 75% of the chord downstream of the leading edge. That figure was chosen somewhat arbitrarily, whereas it was made sure that the hinge point lies between 70% and 80% of the chord downstream of the leading edge, which seems to be the most common range for plain trailing edge flaps [9]. For a sketch of a plain trailing edge flap on an arbitrary airfoil, refer to figure 2.2 on page 10. The geometrical implementation of the plain trailing edge flap and its deflection in the computational mesh is explained in further detail in subsection 2.3.3.

2.3.2.2. The 3D Case

For the 3D case, it was decided to take the flap model from the 2D case, extend it into a 3D flap and attach it to the 3D model of a general aviation aircraft. This model was provided by Dr. Hany Nakhla, the thesis advisor and chairman of the thesis committee. The general aviation aircraft is called the FX-210 and was designed and built by Four Winds Aircraft, which is located in New Smyrna Beach [10]. A plot of the 3D model generated in STAR-CD is shown in figure 2.17 at the end of this subsection.

The geometry of the wing was prescribed by the 3D aircraft model. The dimensions of the flap, however, were chosen somewhat arbitrarily because no specific data on the type and dimensions of the actual flap used on the FX-210 aircraft were available. Nevertheless, the strategy behind choosing the dimensions for the 3D plain trailing edge flap followed the same rationale as in the 2D case. The hinge point for the flap was chosen to lie on the camber line about 75% of the chord downstream of the trailing edge. Furthermore, the span of the flap was chosen to be about 2.2 m, which

corresponds to about 37% of the entire half-span of the airplane. That estimate was based on observations made by evaluating other similar aircraft designs, such as the Cessna single engine aircraft family. The flaps on all aircraft of that family have flap spans that range from 30% to 40% of the half-span of the respective wing. For more precise measurements and rendering of the shape of the flap, refer to subsection 2.3.4.
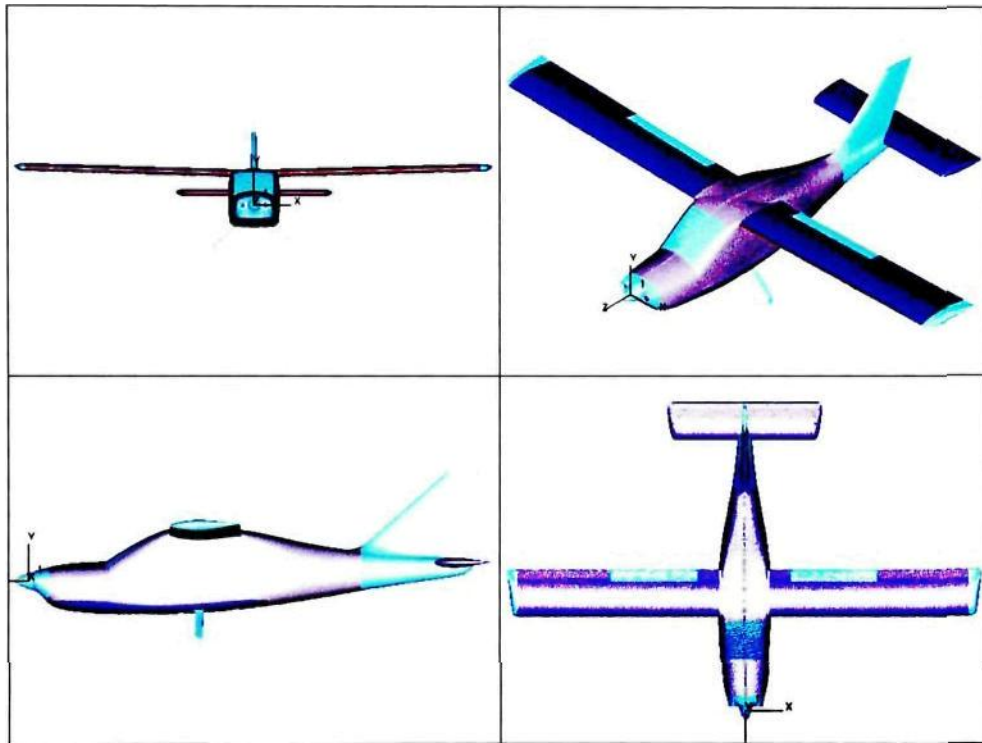
Figure 2.17: Plots of the Four Winds FX-210

2.3.3. Mesh Generation for the 2D Case

As mentioned in the previous subsection, the meshes in this study were generated using the panel feature of STAR-CD in conjunction with a series of input files that contain a batch of STAR-CD commands. This subsection gives a detailed description of the scripts and outlines the process of mesh generation step by step.

55

2.3.3.1. Airfoil Profile

The first and most crucial script that is used in this mesh generation process is called *Airfoil_V_NACA_0012.inp*. The complete script can be viewed in appendix A. Its purpose is to define the profile of the NACA 0012 airfoil. This is done by defining 19 vertices numbered 101 through 119 for the top surface and 19 vertices numbered 201 through 219 for the bottom surface. The exact coordinates for the vertices were taken from [8].

For this study, one vertex for each the top and the bottom surface was added in order to have two vertices at the chord location of the hinge point. The vertex numbers for these extra points are 115 and 215, respectively. According to the previous subsection the hinge point is located 75% of the chord downstream of the leading edge. For this geometry, a chord of one meter was chosen, which means that the x-coordinate for these extra points is 0.75 m or 750 mm. Note that the global unit length for all scripts is millimeters. The y-coordinate was found by interpolation, in which the neighbor vertices 114, 116 and 214, 216 were used as reference points. A plot of the vertices and the profile of the NACA 0012 airfoil is shown in figure 2.18 at the top of the next page.
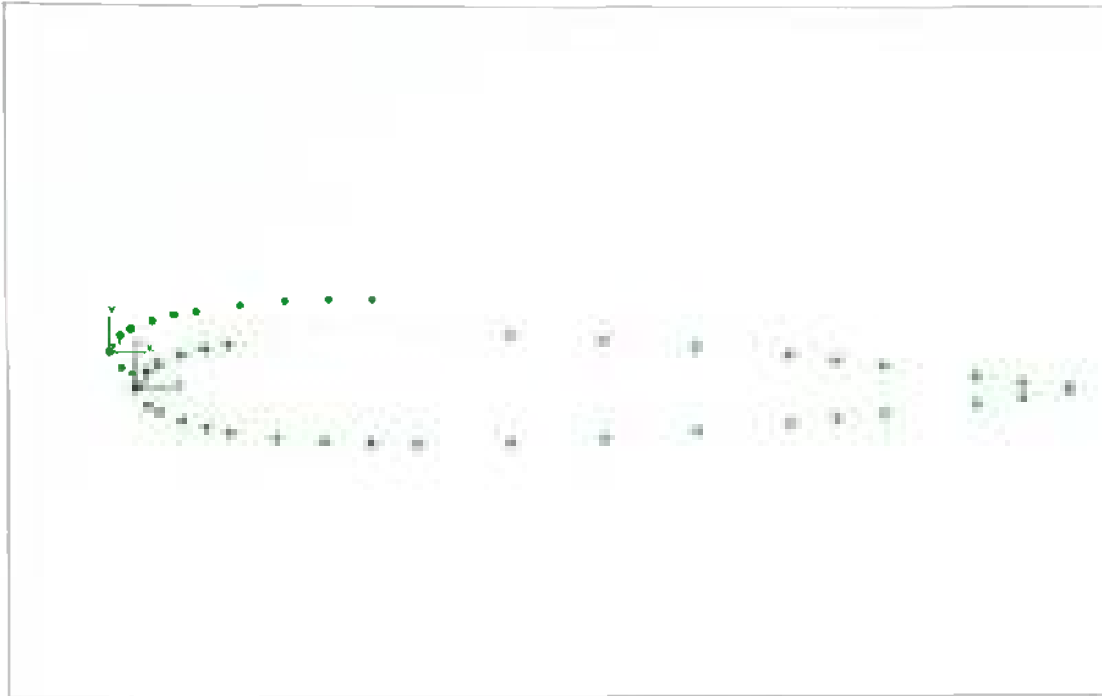
Figure 2.18: Plot of the airfoil profile vertices and their numbering

2 3 3.2 Definition and Filling of the Computational Domain

The script that fills the major part of the computational domain with shells is called *Section_NACA_0012_moving_flap imp* and can also be viewed in appendix A The filling of the computational mesh is accomplished with patches. According to the STAR-CD methodology, patches consist of smoothly-curving surfaces defined by splines along their edges and quadrilateral shells in-between. The user can define the splines and the density and distribution of the shells.

This script can work with any airfoil profile without any further changes to it, as long as the profile of the airfoil is defined by 19 vertices for each top and bottom surface. If an airfoil profile is defined by more or less vertices, this script can still be used; however, certain parameters need to be adjusted. The author also wants to point out that *Section_NACA_0012_moving_flap imp* is based on a script created by Dr. Nakhla, which

57

was modified substantially by the author in order to adapt the script to this specific analysis.

The first two and a half pages of this script consist of parameter definitions. More specifically, first the coordinate parameters for the domain boundary vertices are defined, and then the parameters for the identification of the airfoil profile vertices are specified. These would require modifications if a different number or a different numbering strategy for the airfoil profile vertices is used. Regarding the boundary vertices, it should be noted that the parameters were set, such that the upstream vertices of the domain boundary are located 10 chord lengths ahead of the airfoil's leading edge and the downstream boundary vertices are positioned 65 chord lengths behind the airfoil's leading edge. The top and the bottom boundary vertices were placed 20 chord lengths above and below the chord line of the airfoil, respectively. The reasons for the size of the computational domain are outlined in subsection 2.2.8. on pages 38 and 39. Subsequently, patch parameters are defined, which specify the number of shells in the x- and y-direction and their distribution. The patch parameters are important for the final section of this script, which creates the patches. This concludes the parameter definitions section of the script, and it should be kept in mind that so far no vertices or patches have been created.

Following the parameter definitions, the script contains a calculation section which computes the maximum thickness of the airfoil and places a vertex with vertex number 1000 at the chord-wise location of the maximum thickness. The main importance of this section is that it computes further parameters, such as dm and $dm2$, which are functions of the airfoil's profile dimensions and are important for the subsequent mesh

generation process. In other words, it is a continuation of the parameter definitions section.

The next section creates splines along the 38 airfoil profile vertices. This is accomplished along the top surface of the airfoil by defining spline 1 from the leading edge (vertex 101) to the flap hinge vertex (vertex 115) and spline 3 from the flap hinge vertex (vertex 115) to the trailing edge (vertex 119). Refer to figure 2.18 on page 57 for a clarification of the vertex locations. For the bottom surface. spline 2 and 4 are generated in a similar manner. Subsequently, splines 1 and 2 are merged into spline 2 and splines 3 and 4 are merged into spline 3. For a clarification of the spline generation process, refer to figure 2.19 below.

Figure 2.19: Plot of splines 1 and 3 at the airfoil surface

After the generation of the splines along the top and bottom surface of the airfoil, a second set of splines is created. These are offset from the first set, such that it marks a continuous layer of a certain thickness around the airfoil. This is accomplished by creating a copy set of the airfoil profile vertices and by offsetting it in the y-direction. More specifically, the copy set of the airfoil profile vertices of the top surface are moved in the positive y-direction, and the airfoil profile vertices of the bottom surface are moved in the negative y-direction. In addition, the vertex numbers of the copied vertex set are offset by 200. With that in mind, it should be noted that the two leading edge points of the copied vertex set 301 and 401, as well as the neighbor vertex of each, 302 and 402, respectively, are offset upstream. The two trailing edge points of the copied vertex set, 319 and 419, are also offset in the x-direction, however in the downstream direction. The horizontal offsets are accomplished in order to ensure that the distance between the offset layer and the airfoil is continuous around the entire airfoil. At the end of this section of the script, the original set of splines around the airfoil is also copied and fitted to the copied airfoil vertex set. It should be noted that this layer is referred to as the boundary layer in the script, although its primary purpose is not to mark the boundary layer sections of the mesh, but to create a section around the plain trailing edge flap that allows the limitation of the mesh movement to this section only. Figures 2.20 (a) and (b) on the next page show the two sets of vertices and the two sets of splines, respectively.
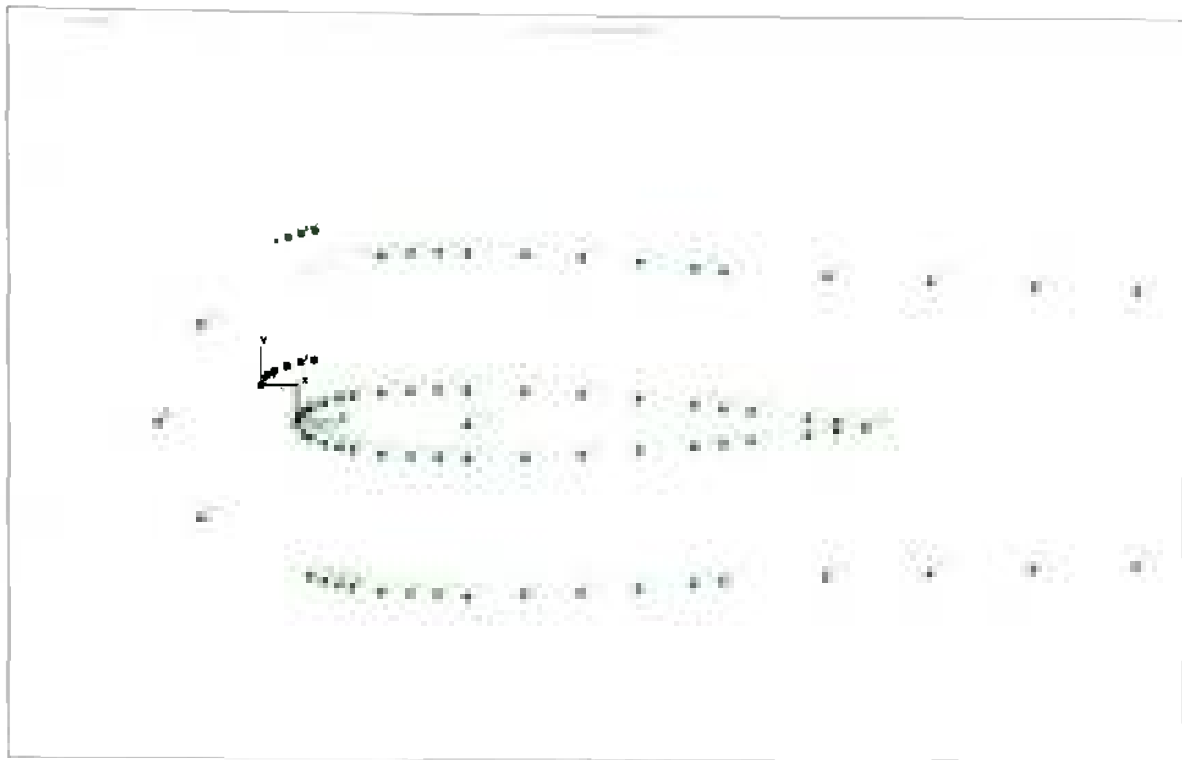
(a)
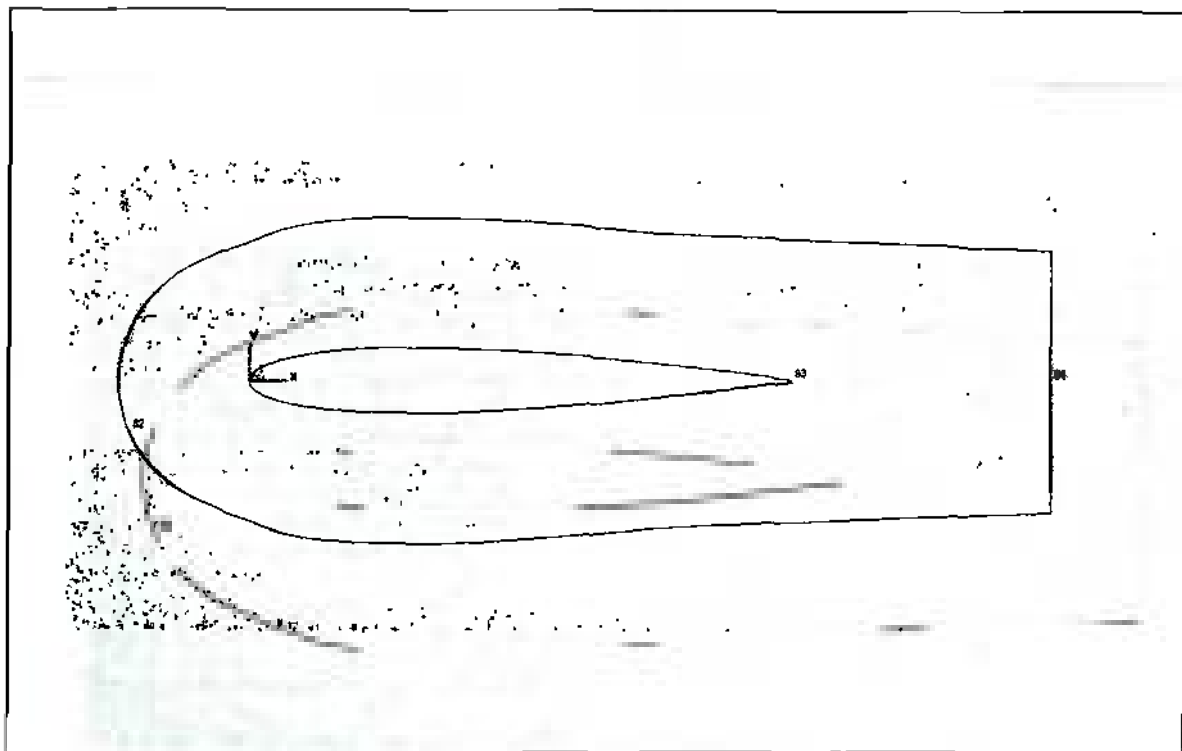
(b)

Figure 2.20: Plots of the airfoil and boundary layer (a) vertex sets and (b) spline sets

61

The remainder of this script is dedicated to the generation of patches to fill the computational domain with shells. However, before the patches are actually created, a few more operations are accomplished by the script. First, it defines a number of vertices along the border of the computational domain based on parameters defined at the very beginning of the script. These vertices are defined because the patches themselves are quadrilateral and, hence, require four corner vertices for their definition. Figure 2.21 below contains a plot of all vertices that have been created in this script so far: the airfoil profile and boundary vertices, as well as the domain boundary vertices.
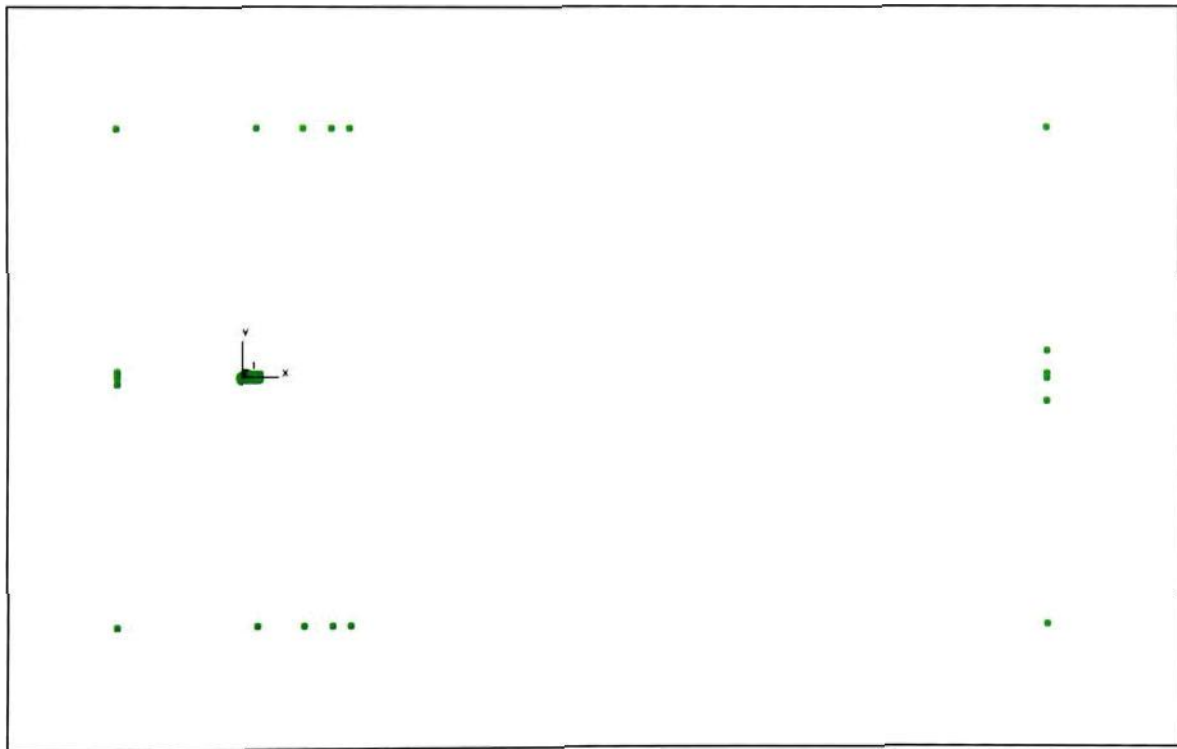
Figure 2.21: Plot of all airfoil profile, boundary layer and domain boundary vertices

Furthermore, the highest vertex number is identified and saved in a parameter called *aa*. This is necessary because the patches create vertices automatically along with the shells, and the new vertices are numbered automatically. In order to avoid overwriting and deleting previously created cells, the automatic vertex numbering is set to start at a number that is one greater than the maximum vertex number that was already defined. Finally, saving the newly created vertex numbers in parameters is the last task that is accomplished by the script before patch generation begins.

Patch generation is accomplished in three major sections: the outer mesh, the boundary layer and the inside of the airfoil. These major sections are further subdivided into subsections or so-called shell tables for visualization and reference purposes during subsequent mesh generation steps. For now, it is important to remember that all adjacent patches that belong to the same subsection share the same color. All patches can be viewed in figure 2.22 at the end of this paragraph. Please note that the plot in figure 2.22 is zoomed in to the vicinity of the airfoil in order to visualize the details in this area. The patches that are shown in this figure and that seem to extend beyond the plot simply extend to the border of the computational domain. Also note that the section around the plain trailing edge flap is missing. In fact, this section is bounded by the two sets of splines that were created earlier in this script, which shows that these splines do serve a purpose. The missing section is filled in another script that is explained in the next subsection.
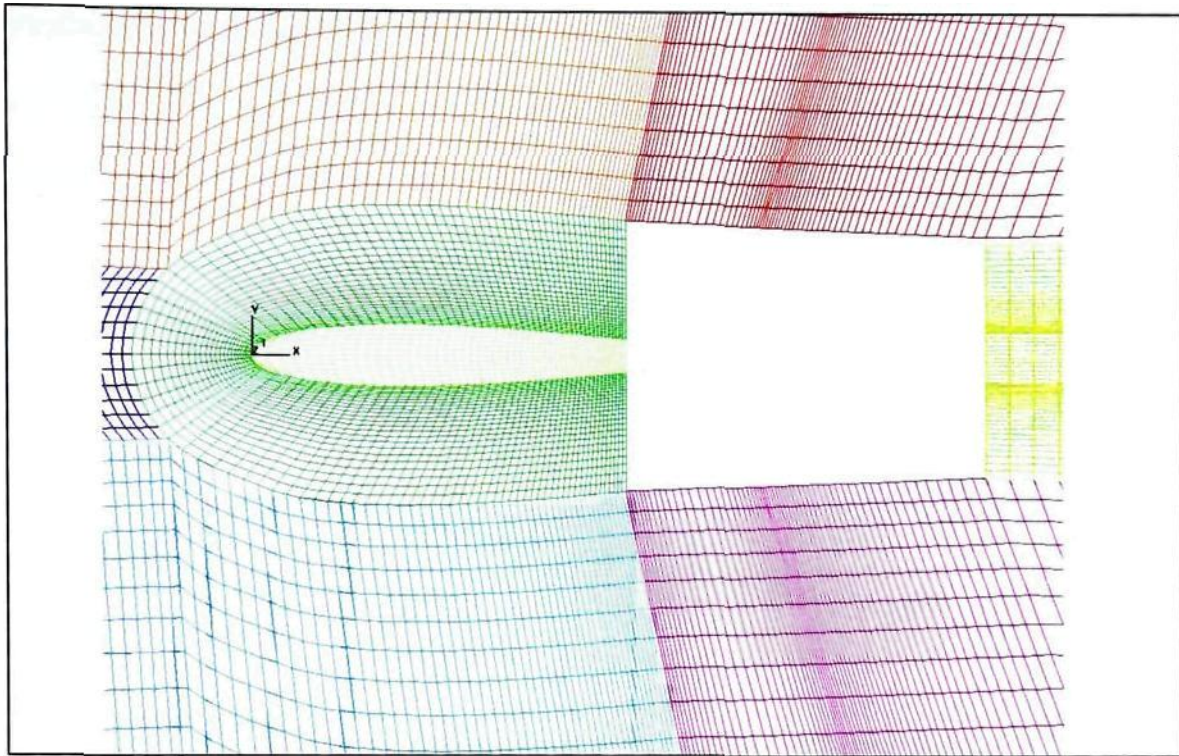
Figure 2.22: Plot of all patches except for the trailing edge flap section

2.3.3.3. Definition and Filling of the Trailing Edge Flap Section

Creating the patches for the trailing edge flap section requires special attention because the vertex filling needs to be accompanied by a structured numbering strategy. The script that accomplished this task is called *Section_Moving_Flap.inp* and can also be viewed in appendix A. The filling of the section in the vicinity of the airfoil starts with the definition and placement of two vertices at the hinge location of the flap (vertices 42500 and 42700) and two vertices at the trailing edge of the airfoil (vertices 42525 and 42725). These vertices are located at the top and bottom surface of the airfoil's flap, respectively, and coincide with vertices 115 and 215 at the hinge location and 119 and 219 at the trailing edge from the original vertex set. Refer to figure 2.23 at the end of this paragraph for a clarification of the vertex numbering in this script. For this section, the

64

numbering scheme has large values in order to avoid any risk of overwriting and deleting any vertices that have been created in previous scripts. The next step in the script creates vertices which are located along the border of this section of the mesh. Just like in the previous script, these vertices function as corner points for the quadrilateral patches.
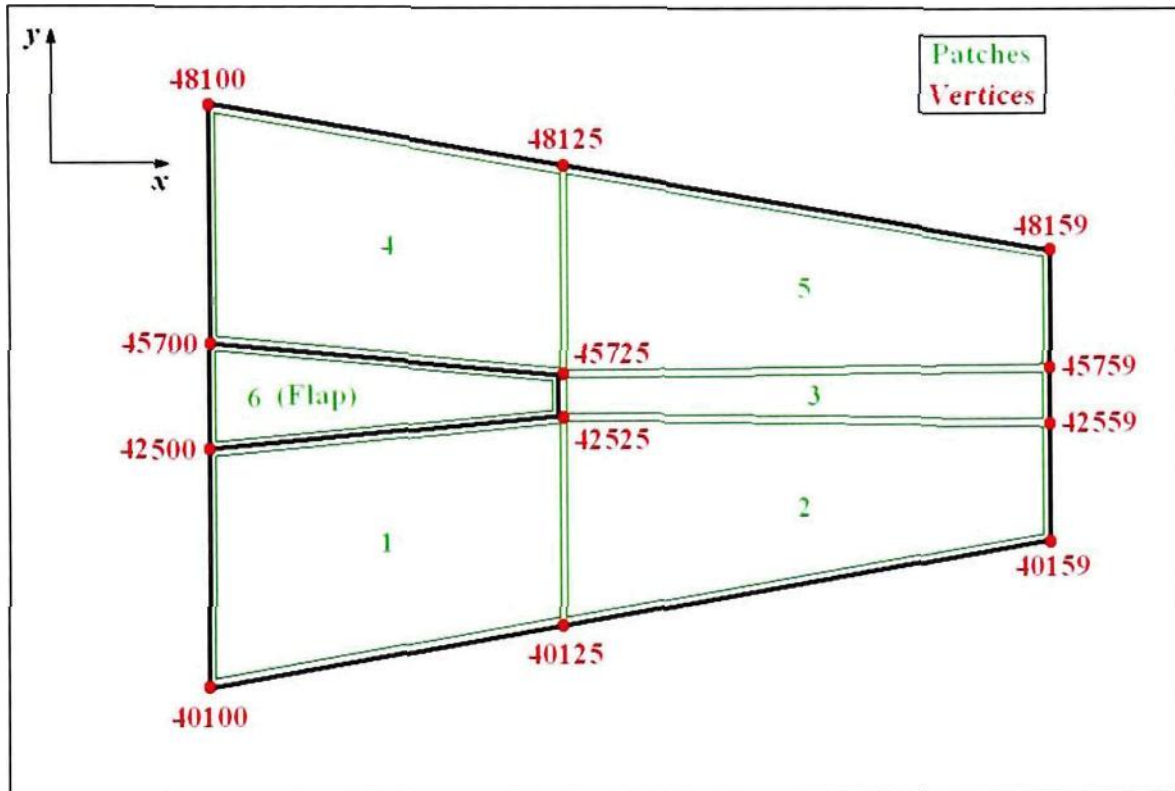
Figure 2.23: **Sketch of trailing edge flap section including corner vertex and patch numbering**

Figure 2.23 also indicates that the vertex/shell filling in this section consists of six patches. These are divided into two subsections: one for the flap and the other for the remainder of this section of the computational domain. The former contains one patch, and the latter consists of five patches. This organization of the patches is necessary for the development of computational cells based on the patches generated in this and the

previous script Furthermore, the vertex numbering in the patches is organized such that the vertices in each row in the trailing edge flap section is numbered from one till 59 and the numbering of each row is offset by 100 from its neighbor rows. The finished patches can be viewed in figure 2 24 at the end of this paragraph. Figure 2 24 contains only those patches that belong to the trailing edge flap section in order to visualize the details in this section. The next few paragraphs focus on the generation of cells based on the patches that have been created in this and the previous script and explain why the organization of patches in shell-tables and the structured cell numbering in this script are important.
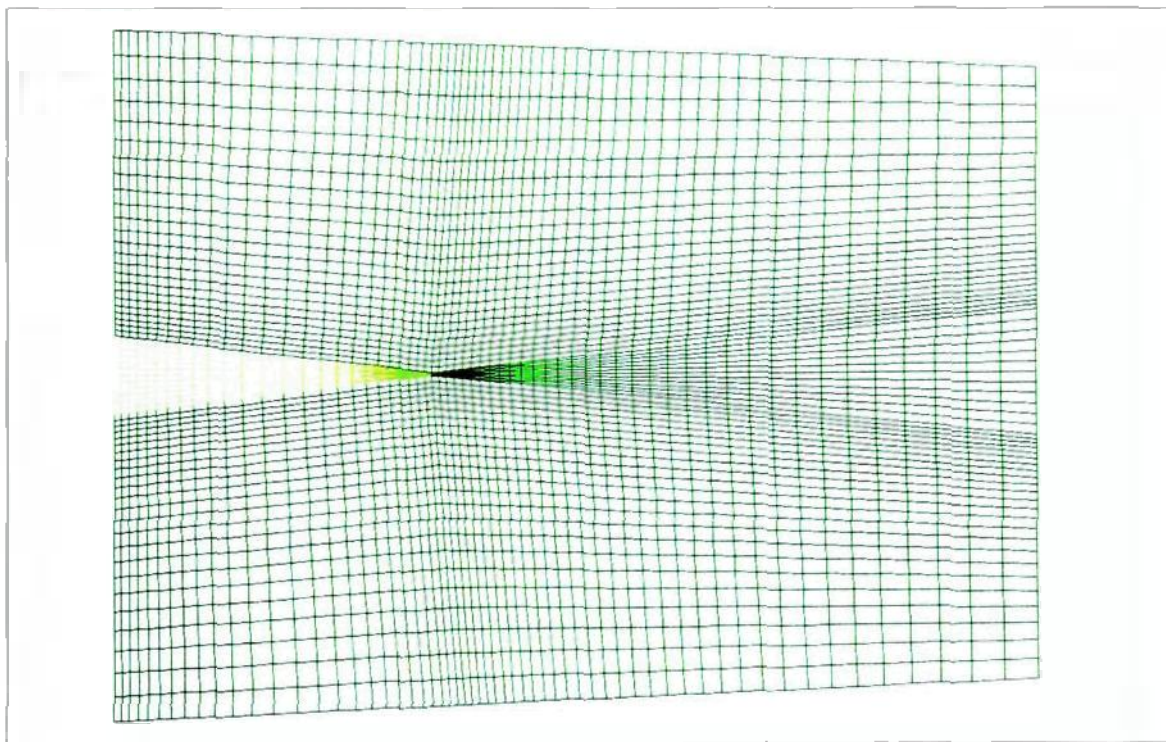
Figure 2.24: Plot of patches in trailing edge flap section

2.3.3.4. Extrusion and Cell Creation

This part of the mesh generation process is accomplished with a script called *Fluid_Gen_x_2D.inp*, which can be viewed in appendix A. However, before this script is executed, the *merge*-command of STAR-CD is used to merge all existing redundant vertices. Furthermore, a feature of this command is used that allows preserving the larger vertex number of the coinciding vertices. These are especially prevalent at the interface of the trailing edge flap section and the remainder of the computational domain. This step is necessary because redundant vertices with different vertex numbers can cause distortions in the mesh during the deflection of the flap.

After the *merge*-command has been executed, the script extrudes the shells created by the patches in the previous scripts into cells. This is necessary because as mentioned in subsection 2.2.7. on page 31, STAR-CD uses the FV method for discretizing the mathematical models. In other words, in order to conduct a 2D analysis in STAR-CD, it is necessary to extrude the 2D plane into a 3D mesh that is one cell-layer thick. This is accomplished with the *vcextrude*-command, which in this specific case is set up, such that it extrudes groups of cell sets. This is beneficial because STAR-CD distinguishes between solid and fluid cells. The latter allow mass fluxes, whereas the former are impermeable to all fluids and gases. In other words, solid cells are perceived by STAR-CD as cavities in the computational domain. For this specific analysis, this means that all shells within the airfoil need to be extruded as solid cells, and all remaining cells should be extruded as fluid cells. In the *Fluid_Gen_x_2D.inp* script this is accomplished by first extruding all shells belonging to shell-tables 5 through 55, except for shell table 15, as fluid cells, and then by extruding all shells in shell-table 15 as solid

cells. The parameter section at the beginning of the script indicates that the thickness of the extrusion layer, *LG1*, amounts to 50 mm and that the number of cell layers in the extrusion direction, *ny11*, is one. Besides, the offset in the numbering of the vertices in the newly created layer corresponds to the total number of vertices in one plane of the mesh. This is ensured by the re-computation of the parameter *aa*.

This concludes the description of this script and it should be noted that the mesh generation process for the 2D analysis has been successfully completed. Figure 2.25 below shows a zoomed-in plot of all fluid cells in the vicinity of the airfoil. In addition, the plot is angled in order to visualize the 3D character of the mesh. The next and final script that is described as part of this subsection realizes the motion of the mesh.
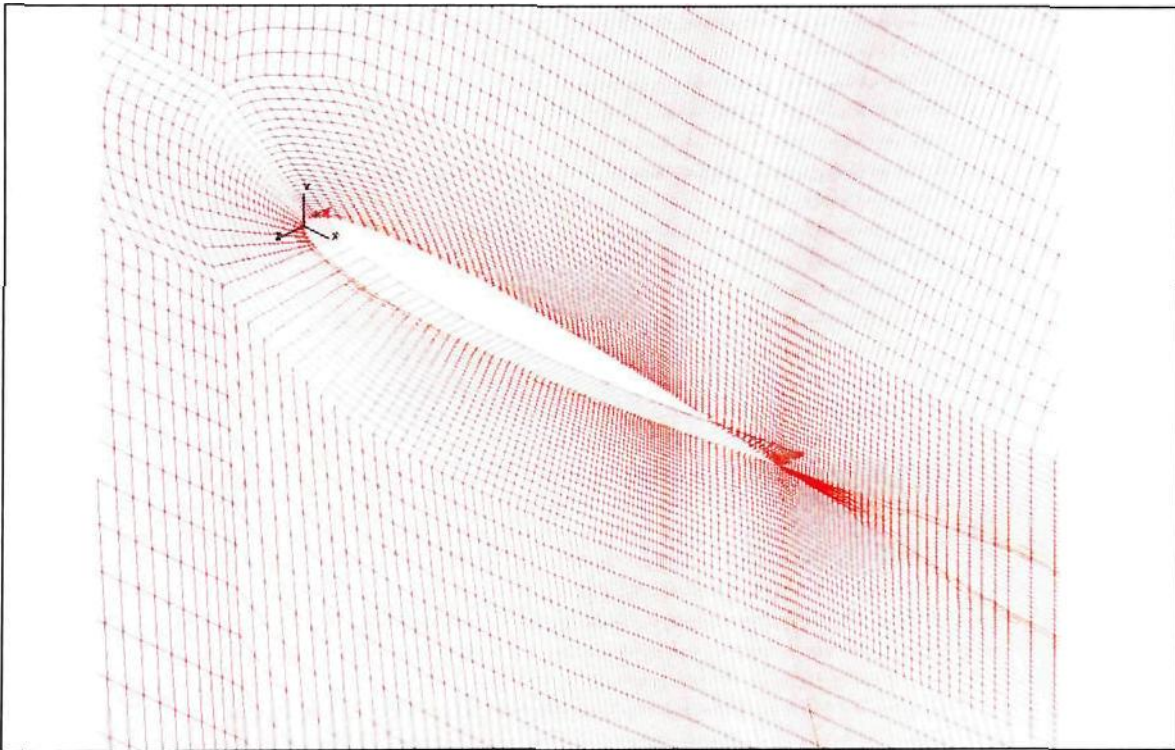
Figure 2.25: Isometric plot of the completed 3D mesh for the 2D analysis

2.3.3.5. 2D Flap Deflection and Moving Mesh

The deflection of the flap is accomplished by two scripts, *Section_Rotation_+.inp* and *Section_Rotation_.inp*. The two scripts are identical, but deflect the flap in opposite directions. In fact, the only difference between the two scripts is the sign in front of the deflection angle, and therefore only *Section_Rotation_.inp* is added to appendix A. Furthermore, these scripts necessitate the generation of a new local coordinate system at the hinge point of the plain trailing edge flap. This coordinate system is cylindrical in nature, and its center is located on the chord line 75% of the chord downstream from the leading edge. The rotation axis in this coordinate system is the z-axis and is perpendicular to the plane of the airfoil.

The first step that is taken by the script is the rotation of the two airfoil trailing edge vertices 42525 and 45725 about the trailing edge flap hinge point. For clarification of the exact location of the vertices, refer to figure 2.23 on page 65. The rotation is accomplished with STAR-CD's *vgenerate*-command and with respect to coordinate system six, which is the newly created cylindrical coordinate system introduced in the previous paragraph.

Subsequently, the *vfill*-command is used to redistribute all vertices in the trailing edge flap section of the mesh. The *vfill*-command in STAR-CD allows the user to fill a certain amount of cells between two predefined vertices. In addition, this command offers the ability to modify the numbering of the newly created vertices, to vary the fill ratio and to specify how many times this command is repeated and with what vertex number offset. For the purposes of this analysis, the *vfill*-command was first used to redistribute the vertices between the vertex above the hinge point (vertex 45700) and the trailing edge

vertex on the top surface of the flap (vertex 45725). Then, in a similar fashion, all vertices in the patch above the top surface of the airfoil were redistributed, by applying the *vfill*-command to each column of vertices. The redistribution of the vertices in patch 1 above the flap and patch 6 within the flap was accomplished similarly. Finally, the script redistributes the vertices in patches 2, 3 and 5 behind the trailing edge of the flap by applying the *vfill*-command to the vertex rows between vertices on the upstream and the downstream side of the patches. Throughout this process, the commands have been simultaneously applied to the second vertex layer which was created during the cell generation process.

This concludes the description of the script that moves the mesh in order to account for the deflection of the flap. Figures 2.26 (a) and (b) on the next page show the mesh in the trailing edge flap section and in the vicinity of the airfoil, respectively, at four different flap deflection angles. The script described in this section enables the user to manually manipulate the mesh. For the actual analysis, however, the deflection process was automated using a slightly modified version of this scrip. Further details on that script and the analysis set-up can be found in chapter 3, which focuses on the analysis.
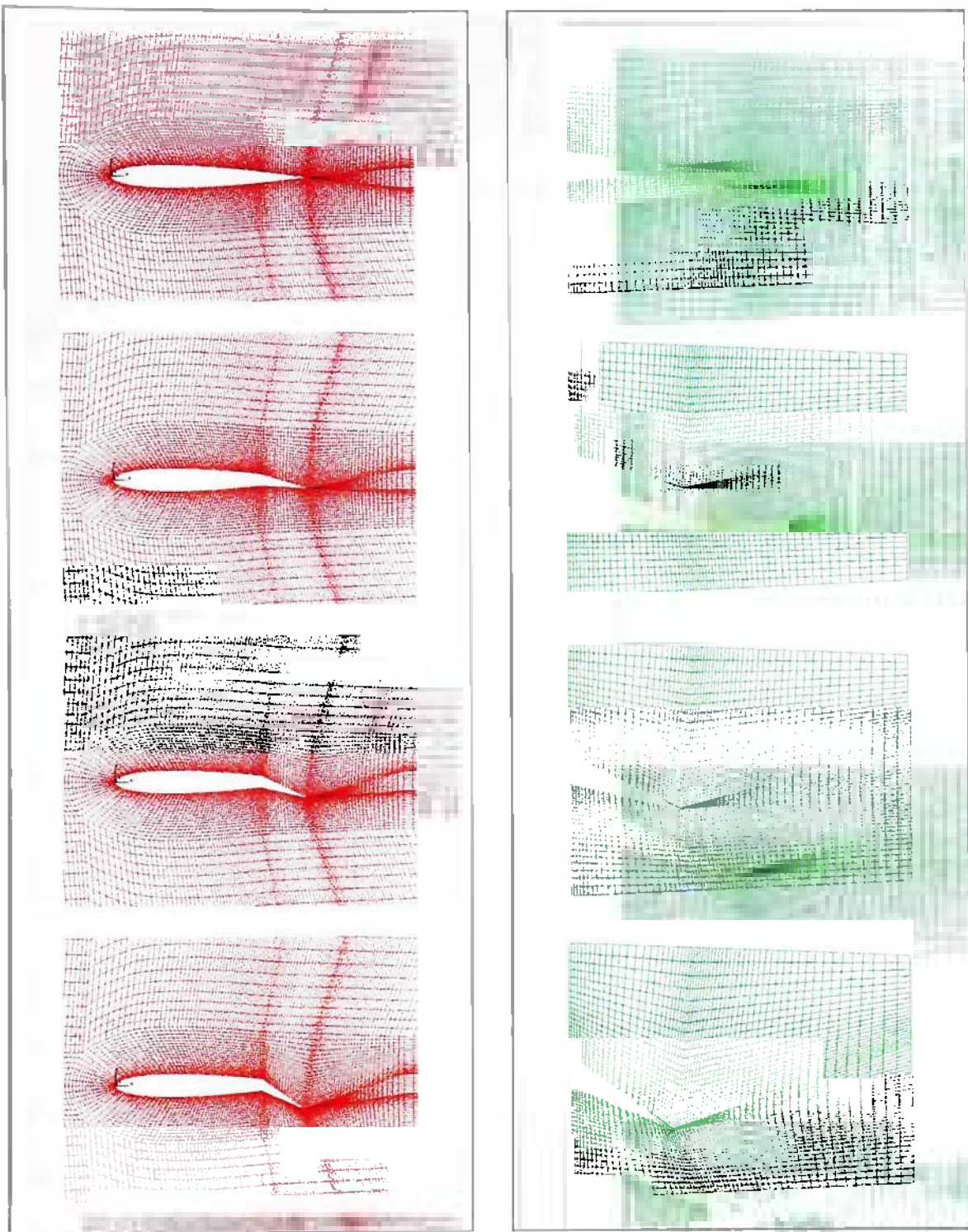
Figure 2.26: Plot of the mesh (a) in the vicinity of the airfoil and (b) within the trailing edge flap section at flap deflection angles of 0°, 10°, 20° and 30° from top to bottom

2.3.4. Mesh Generation for the 3D Case

This subsection focuses on the mesh generation process for the 3D flap and its integration into the 3D model of the Four Winds FX-210. For a plot of the 3D model, review figure 2.17 on page 55. Like in the 2D case, STAR-CD's panel and a number of scripts were used to generate the mesh for the 3D trailing edge flap section in order to semi-automate the process. Each script is described in more detail in the following paragraphs.

2.3.4.1. Meshing Strategy for the 3D Trailing Edge Flap Section

The mesh generation process in the 3D case focuses on the modeling of the 3D trailing edge flap section because the 3D model of the Four Winds Aircraft FX-210 was already provided. More specifically, in this process the mesh of the 3D flap section was created in its own file, stored in a database and then imported into the 3D aircraft model once it was completed. This meshing strategy allowed the use of basic concepts developed in the mesh generation process of the 2D trailing edge flap section, which were outlined and illustrated in subsections 2.3.3.3. and 2.3.3.4. Furthermore, developing the 3D flap model in its own file facilitated the development and debugging of the mesh generation scripts and avoided negative effects on the mesh of the 3D aircraft model. This meshing strategy, however, required the knowledge of the shape and exact dimensions of the 3D trailing edge flap section because once it was imported into the airplane's 3D model, it needed to fit onto the wing perfectly.

Before actually retrieving the exact dimensions of the 3D trailing edge flap section, it was necessary to specify the span-wise location of the flap edges. This was

necessary because it turned out that the wing of the FX-210 has a slightly positive dihedral, meaning that the wing tips are higher than the roots. So, if the span-wise location of the flap changed, the y-coordinates of the dimensions of the flap would also vary. A flap span of 2176 mm was chosen, as indicated in subsection 2.3.2.2. on page 54. The inboard flap edge was positioned 1152 mm from the geometrical center of the airplane, which indicates that the flap is located on the inboard half of the airplane's half-span. This is generally standard for any kind of flap on an airplane's wing.

With the knowledge of the exact dimensions and location of the flap it was possible to retrieve the contour of the plain trailing edge flap from the wing of the 3D aircraft model. These dimensions were subsequently used to start developing the mesh of the 3D plain trailing edge flap section. Figure 2.27 at the top of the next page shows a plot of the contour of the airfoil, which was used on the FX-210. The remainder of this subsection describes the inner workings of the set of scripts used to develop the mesh for the 3D trailing edge flap section.
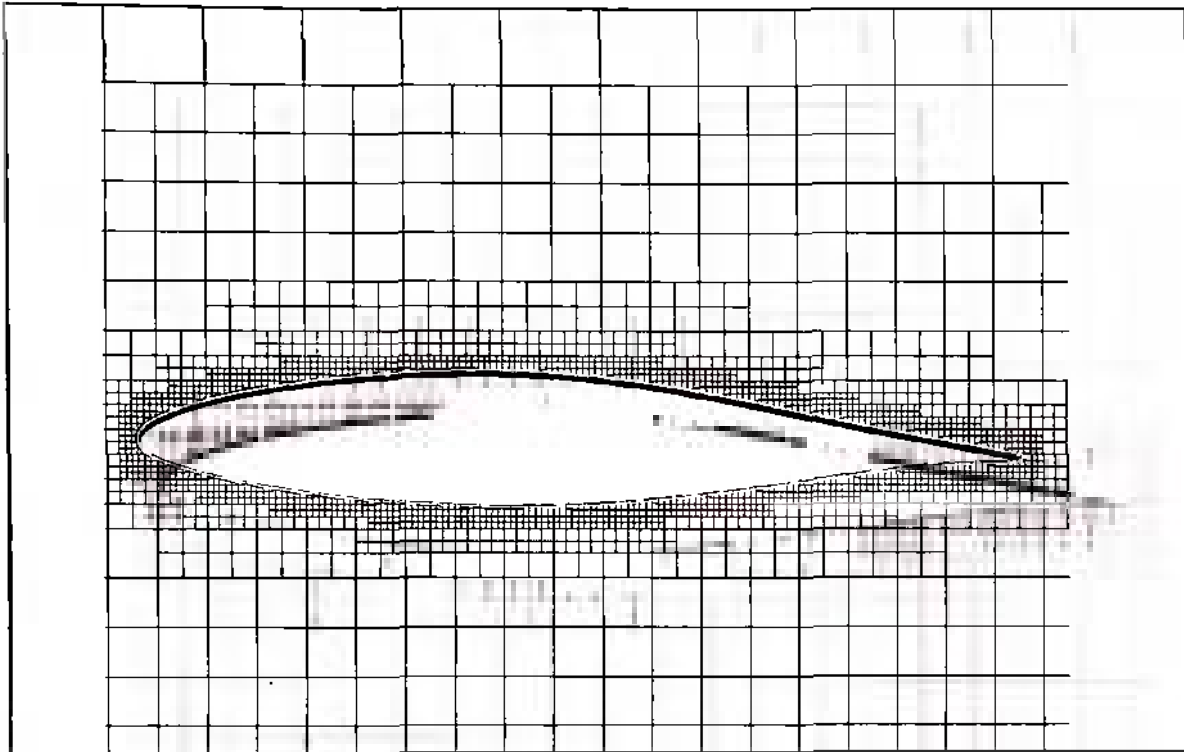
Figure 2.27: Plot of the wing profile used on the Four Winds FX-210

2.3.4.2. Development of the 3D Plain Trailing Edge Flap Section

The entire mesh of the 3D trailing edge flap section was produced with two scripts: *Mesh_of_3D_Flap_Left_d.inp* and *Mesh_of_3D_Flap_Right_d.inp*. The former creates the left wing and the latter creates the right wing with respect to the upstream direction. In fact, the two scripts are completely symmetric in the sense that the *x*-coordinates of the vertices have opposite signs in the two scripts. In addition, the vertex numbering has an offset of one million in order to avoid any deletions or overwriting of vertices. Due to the similarities in the scripts, only *Mesh_of_3D_Flap_Left_d.inp* is added to appendix A and is described in more detail in the following paragraphs.

74

Generally speaking, the script mentioned above had to overcome the challenge of perfectly matching the geometry of the airplane's wing. As mentioned earlier, the wing of the FX-210 has a positive dihedral and a slightly irregular trailing edge, which means that the cross section at each span-wise location of the airplane's wing is unique. In order to solve this problem, two planes of shells needed to be specified to a high degree of accuracy at each span-wise end of the 3D trailing edge flap section. In addition, two intermediate planes of shells needed to be defined in order to model a small gap between the flap and the wing at each span-wise end. This gap also needed to allow sufficient space for the generation of several cell layers that ensure continuity between the flap and the trailing edge section of the wing during flap deflection. This caused a problem for the cell creation process because STAR-CD's pre-processor pro-STAR does not offer a command or tool that directly fills cells in-between two geometrically dissimilar planes of shells. For a clarification of this situation, refer to the 2D sketch in figure 2.28 below. Note that this sketch is not drawn to scale.
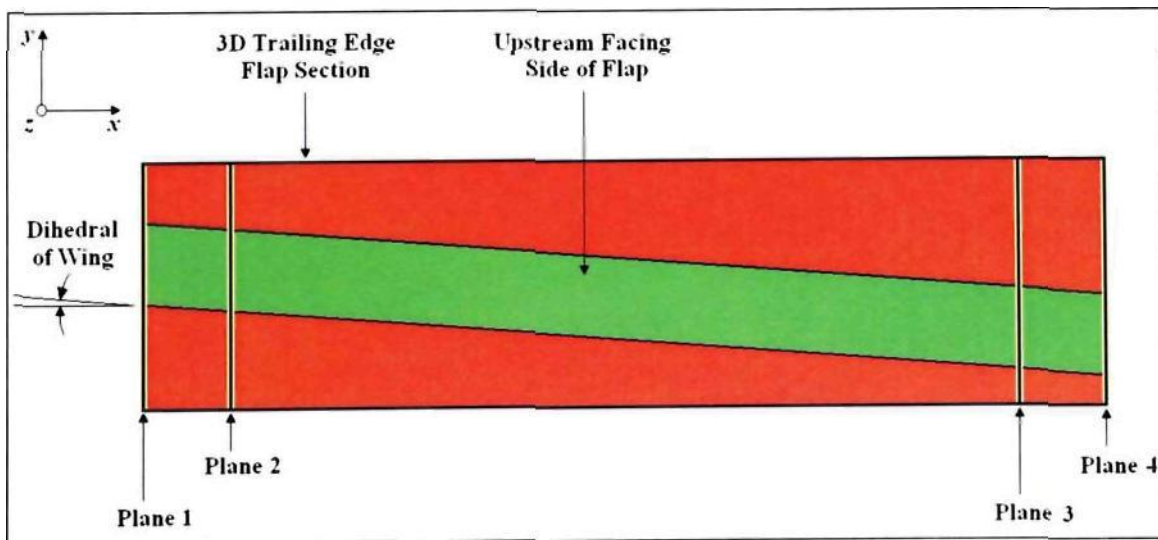
Figure 2.28: **Sketch of the upstream facing side of the 3D trailing flap section indicating the location of planes 1 through 4 and the dihedral of the airplane's wing**

75

The challenges described above were overcome by dividing the script up into five parts. The first part starts with the definition of the geometry of plane 1, which represents the outboard face of the hexahedral 3D trailing edge flap section. This is done by defining a number of vertices along the upper and lower surface of the plain trailing edge flap and along the boundary of the flap section. The former are the basis for a spline which is subsequently created, and the latter serve as corner vertices for the patches, which are created at a later point in the script. A plot of the vertices just created can be viewed in figure 2.29 (a). Figure 2.29 (b), furthermore, shows a sketch of the patch corner vertices and the patch structure applicable to this plane. Overall, it is obvious that the mesh generation process in this mesh is similar to the 2D case.
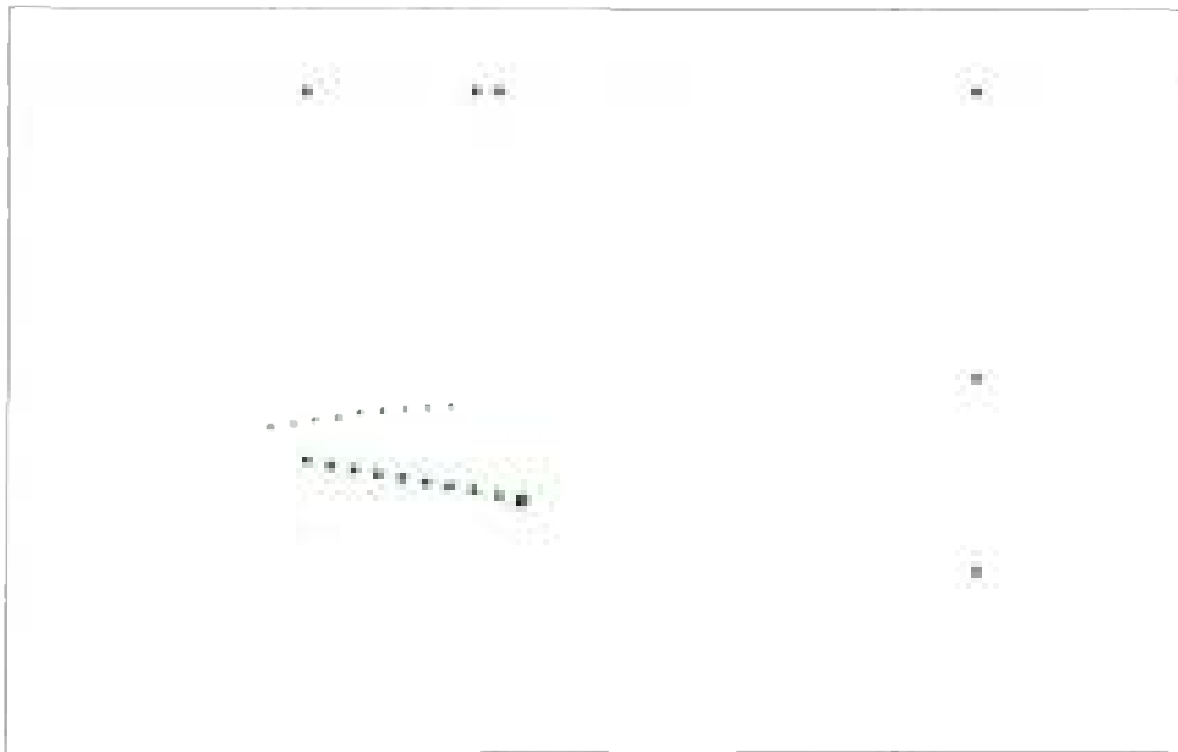
(a)
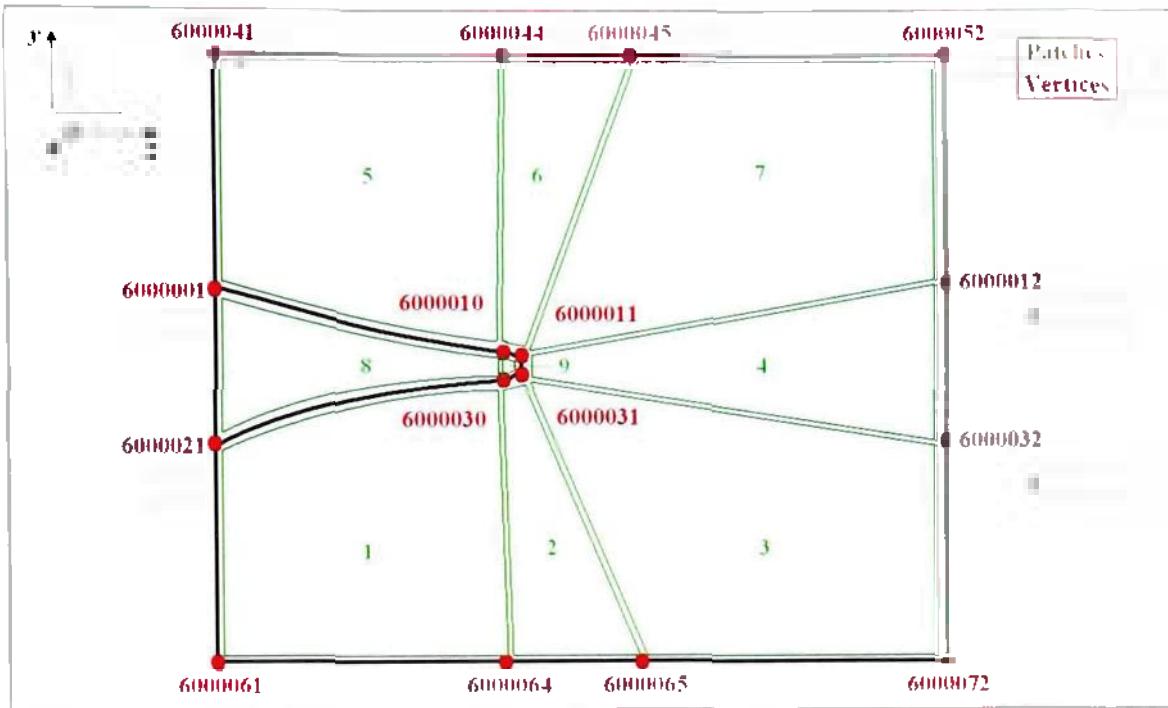
(b)

Figure 2.29: (a) Plot of the flap surface and the section boundary vertices; (b) Sketch of the patch structure in the 3D trailing edge flap section

After all necessary vertices have been generated successfully; a set of two splines is created along the top and the bottom surface of the trailing edge flap. More specifically, spline 1 is generated along the top surface, and spline 2 is fitted along the bottom surface. These splines are important for the generation of the patches because they ensure a smooth fitting of the patches to the surface of the flaps. Figure 2.30 at the top of the next page shows the splines mentioned above and the flap surface vertices whose generation was described in the previous paragraph.
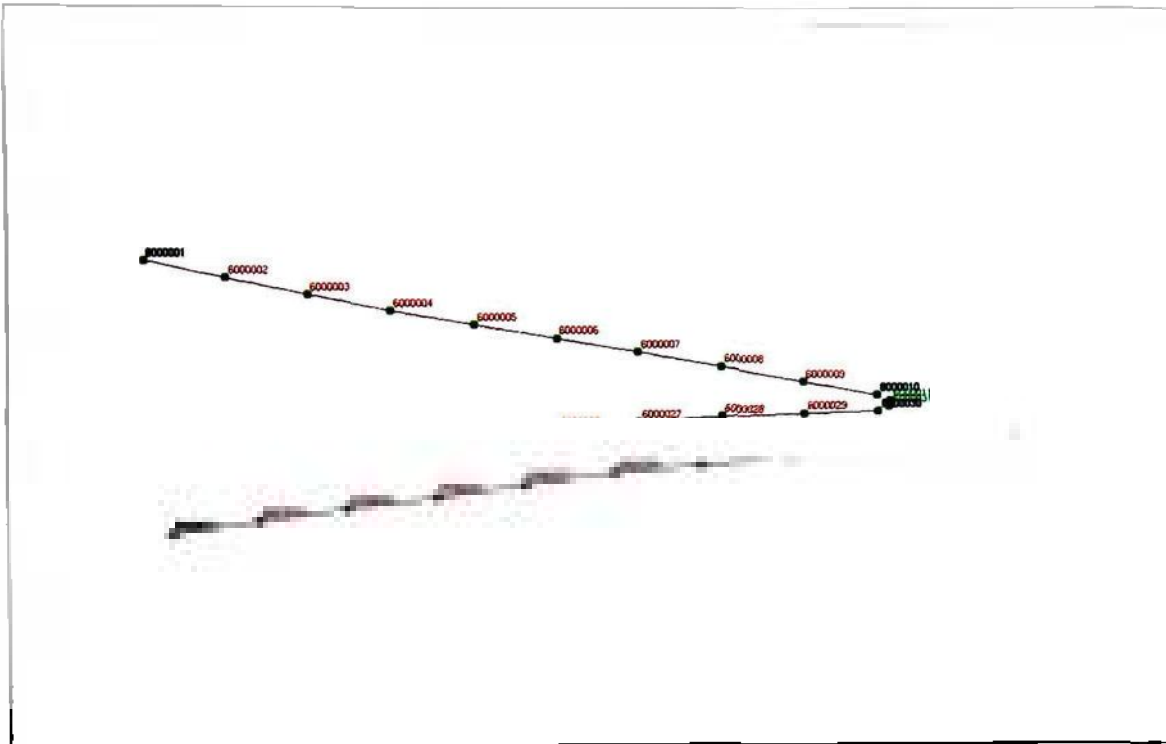
Figure 2.30: Plot of the flap surface splines and vertices

The next step in this part of the script generates the patches according to the sketch in figure 2.29 (b). There are a total of nine patches. The first seven are created in a different shell table than the last two. This distinction serves the sole purpose of facilitating the separate generation of fluid and solid cells during the extrusion process. But before describing the extrusion of the shells into fluid and solid cells, see figure 2.31 on the next page, which shows the finished patches and hence the complete first shell plane of the 3D trailing edge section. This figure also includes the flap surface splines and vertices, as well as the section boundary vertices.
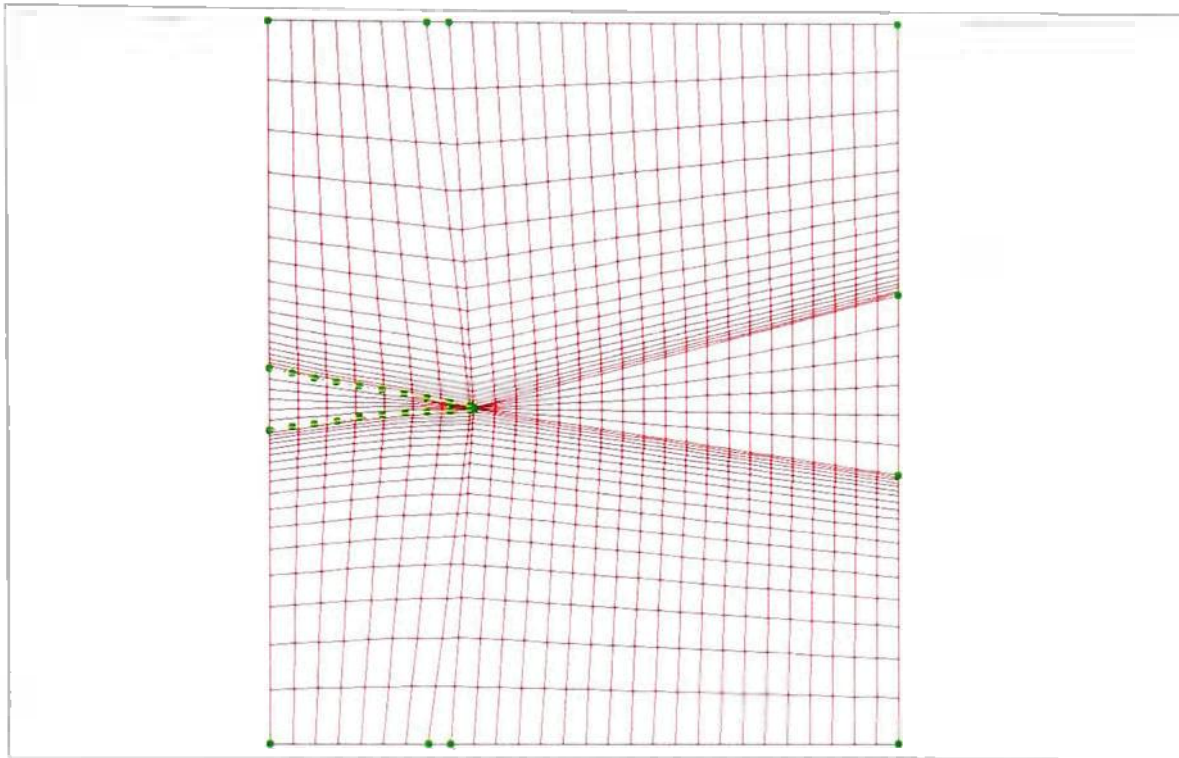
Figure 2.31: Plot of the patches on plane one of the 3D trailing edge flap section along with flap surface vertices and splines and section boundary vertices

After the patches have been completed, the script extrudes the shells into fluid and solid cells More specifically, the shells forming the flap are extruded into solid cells and the shells filling the domain around the flap are extruded into fluid cells The extrusion is accomplished using the *vcextrude*-command, just like in the 2D case. As mentioned in section 2.3.3.4. on page 67, this command generates the vertices of the created cells automatically. In this specific case the vertices in each new cell layer have a numbering offset of 10,000. This allows a high degree of continuity in the vertex numbering because the adjacent vertices in different neighbor layers have an identical vertex number with the exception of the first two to three leading digits. It should also be noted that the extrusion distance and the number of cell layers in the extrusion were chosen such that each cell

layer has a thickness which is a scalar multiple of 8 mm. This was important for the coupling process that took place when the entire 3D trailing edge flap section was joined with the mesh of the airplane's 3D model. Figure 2.32 below shows a 3D plot of the finished extrusion in this part of the mesh.
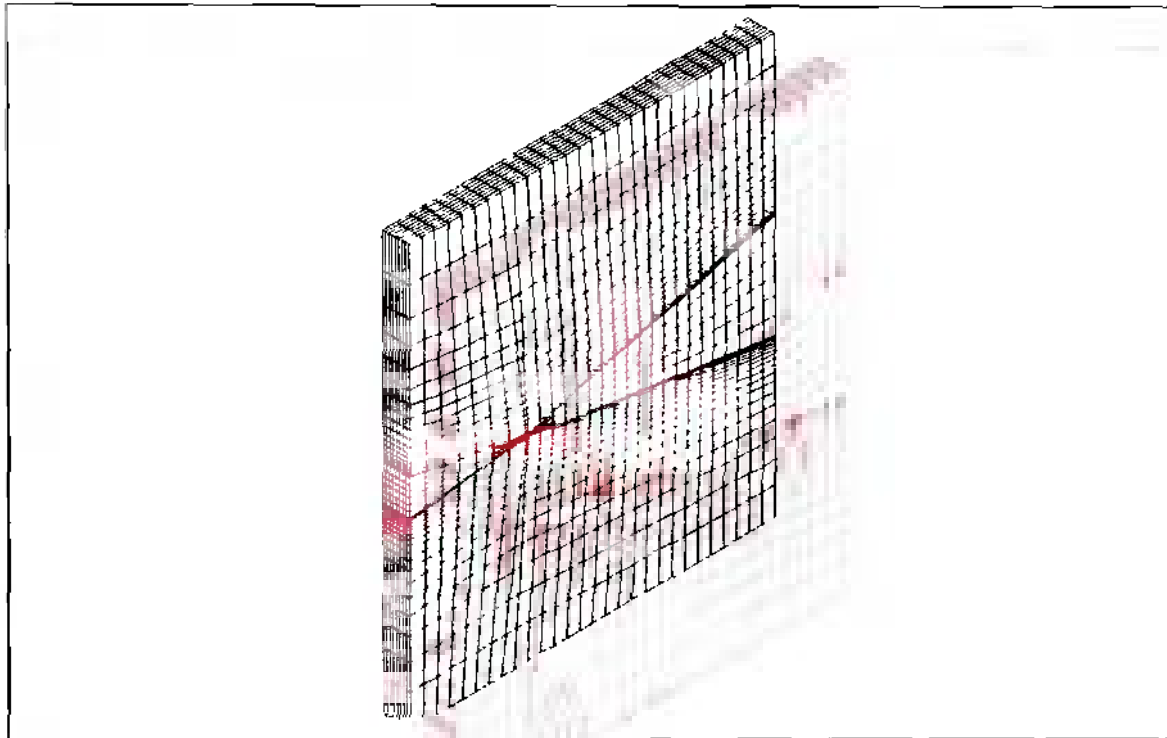
Figure 2.32: Plot of the extrusion of shell plane 1

The following two parts of *Mesh_of_3D_Flap_Left_d.inp* continue the mesh generation process by each generating an additional plane of shells, planes 2 and 3, respectively, and by each extruding the respective plane of shells in an identical manner as in part one of the script. It should be noted, however, that the three planes of shells that have been created by the script so far are geometrically dissimilar. This is due to the fact that the flap in each of the three planes is shifted in the negative y-direction to account for

the positive dihedral of the 3D aircraft model. Remember that the extrusion in this script takes place in the direction from the wing tip towards the centerline of the aircraft, and as the extrusion continues in this direction the flap will drop to lower y-coordinates Figure 2.33 below shows a zoomed-in plot of planes 1, 2 and 3 and visualizes the downward shift of the flap.
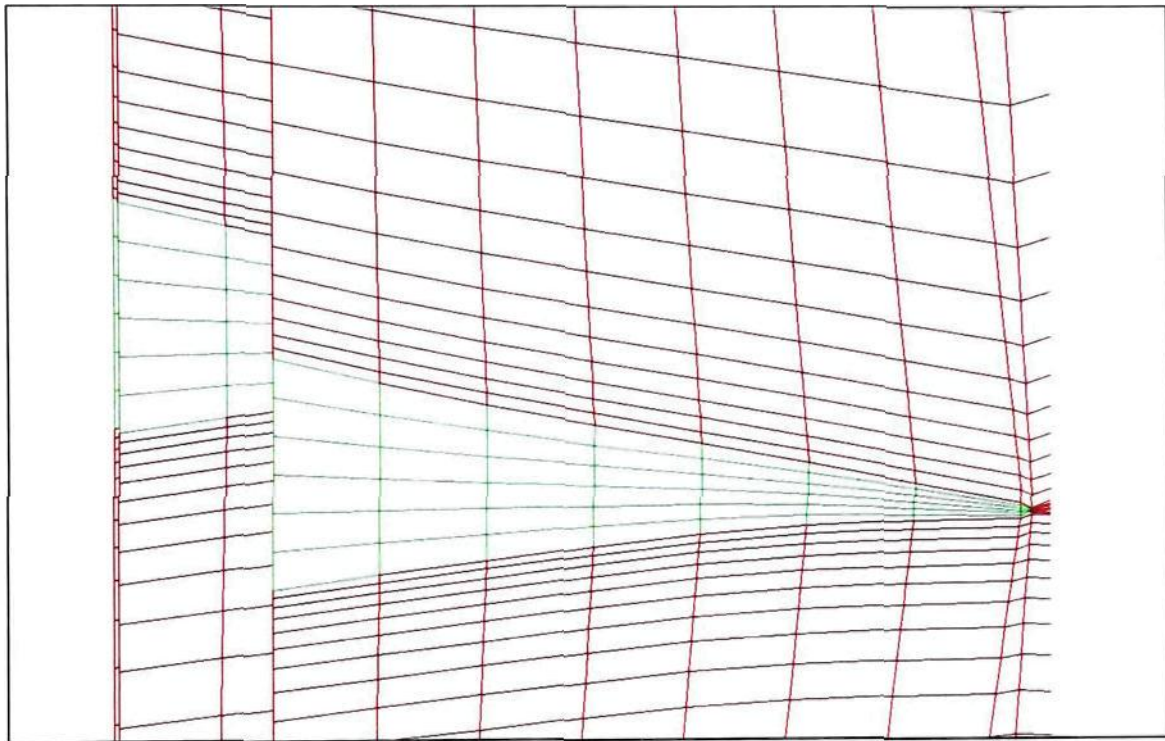
Figure 2.33: **Plot of planes 1, 2 and 3 in a tilted view to visualize the downward shift of the flap due to the positive dihedral of the wing**

The fourth part in the script creates a fourth plane of shells that represents the inboard face of the hexahedral 3D trailing edge flap section This part of the script creates this plane in an identical manner as the previous three parts It should be noted that the numbering of the vertices in planes 2, 3 and 4 has been chosen such that the vertices in the last layer of the extrusion of the previous shell plane are overwritten. In other words,

81

planes 2, 3 and 4 replace the last vertex layer of the previous extrusion. This causes discontinuities in the mesh as shown in figure 2.34 below. This figure shows a downstream view of the 3D trailing edge flap section.
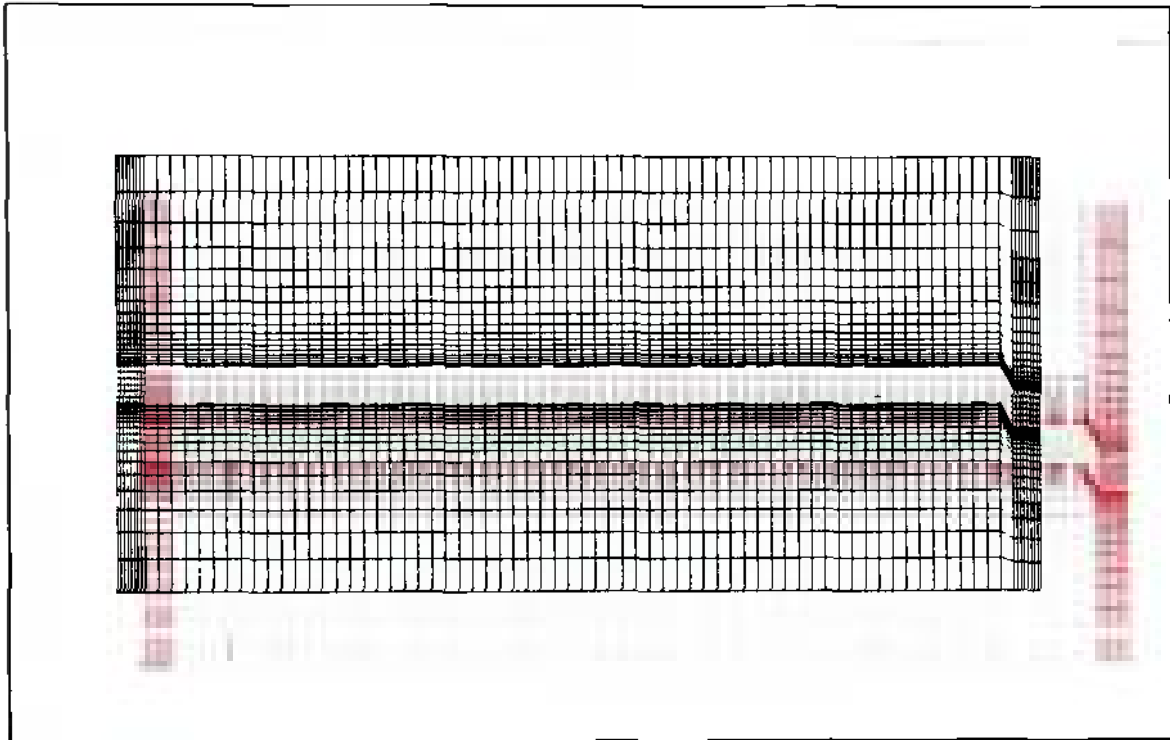
Figure 2.34: Plot of the upstream facing side of the 3D trailing edge flap section showing the discontinuities in the cell layers to the left of planes 2, 3 and 4

The final part in this mesh generation script removes the discontinuities in the mesh that can be seen in figure 2.34. This is accomplished with the *vfill*-command, which has been used in the 2D case to redistribute all vertices in the 2D trailing edge flap as explained in subsection 2.3.3.5. on page 69. More specifically, in this case the *vfill*-command is used to redistribute all vertices in-between each of the four planes. For example, the *vfill*-command is used to evenly redistribute all vertices between vertex 6000101 and 6800101. The former is located in plane 1, and the latter is part of plane 2 in

the 3D trailing edge flap section. By the use of loops, which are initiated with *define noexecute and terminated with *end, the redistribution is expanded over each row of vertices in-between each of the four planes. This part of both Mesh_of_3D Flap_ Left_d imp and Mesh_of_3D_Flap_Left_d.inp concludes the generation of the 3D trailing edge flap section, which can be viewed in an isometric plot in figure 2 35 (a) below In addition, figure 2.35 (b) shows an isometric plot of the flap alone.
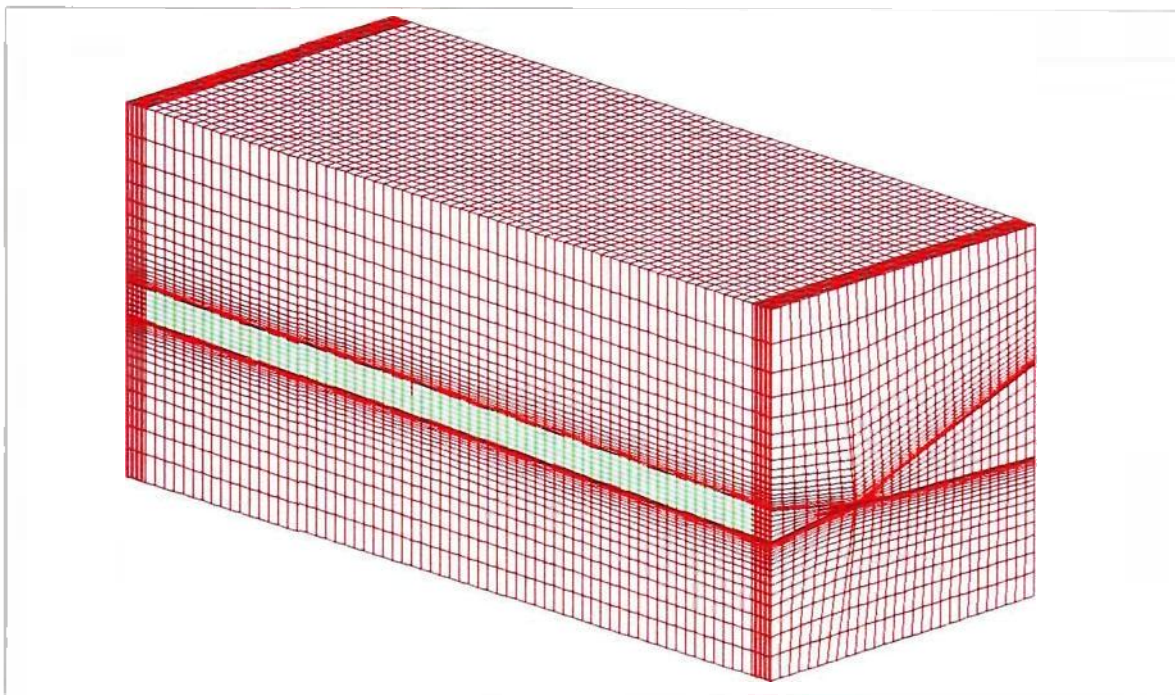
(a)
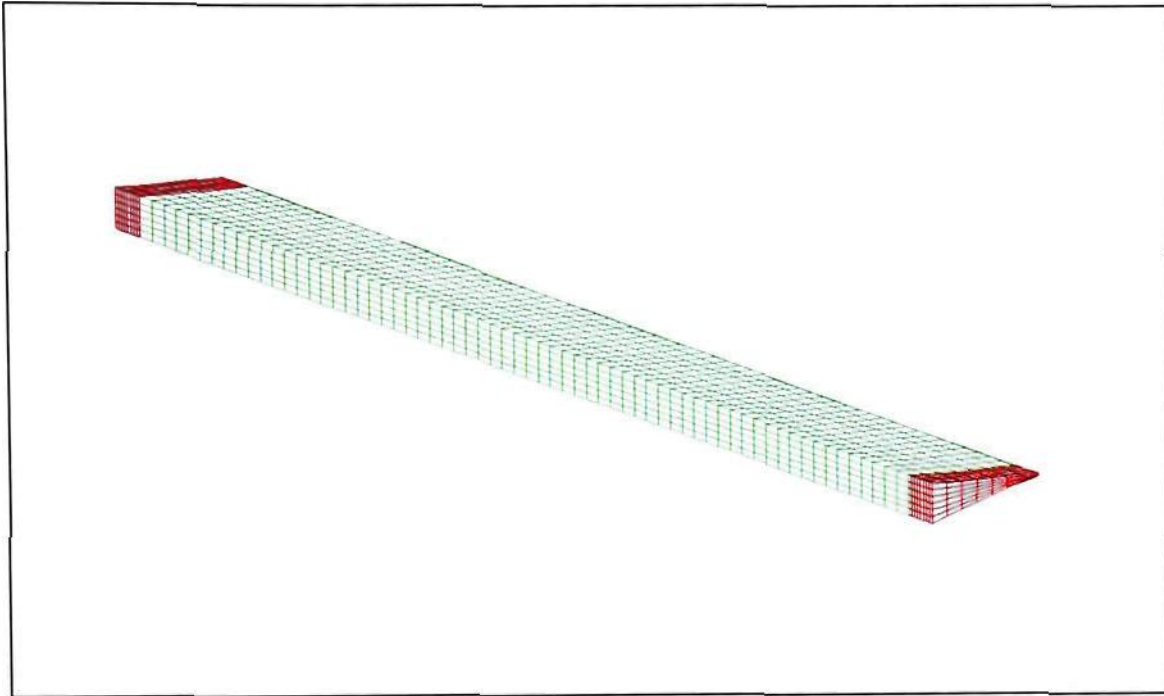
(b)

Figure 2.35: **Isometric plot of (a) the finished 3D trailing edge flap section and (b) the 3D flap**

2.3.4.3 3D Flap Deflection and Moving Mesh

Flap deflection in the 3D case is accomplished with two scripts: *Rotation_of_3D_Flap_2.inp* and *Rotation_of_3D_Flap+2.inp*. The former can be viewed in appendix A. Just like in the 2D case these two scripts are identical. They each deflect the flap in opposite directions. Their inner workings are also similar to their 2D counterparts regarding the fundamental meshing strategy. Another similarity to the 2D case is the fact that it was necessary to define two local cylindrical coordinate systems for each flap These coordinate systems needed to be located at the hinge points of the flap section in order to allow a rotation of the flap vertices in planes 2 and 3 about the hinge point of the flap. These local coordinate systems are visualized in figure 2.36 on the next page.
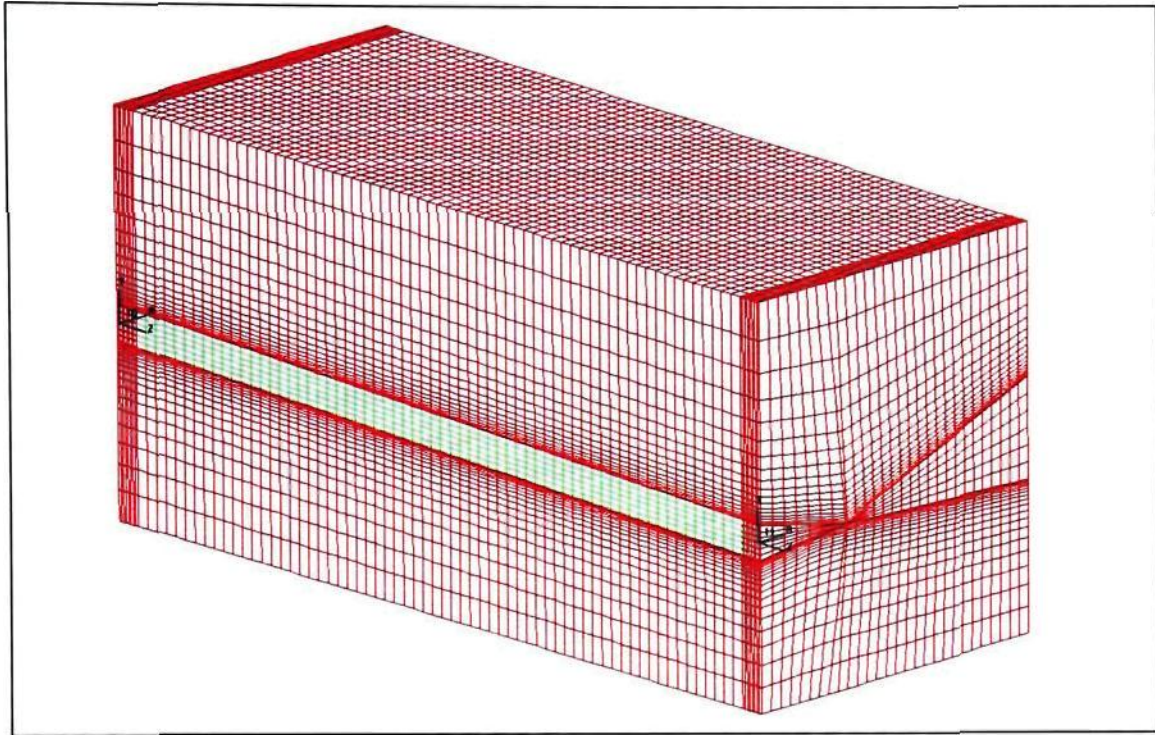
Figure 2.36: Plot of the 3D trailing edge flap section with local coordinate systems at the flap hinge points

The first step in both scripts is the definition of the deflection angle, which in the script is referred to *delta*. The user can vary this value, and it is automatically applied to the entire script because parameter declarations in STAR-CD are global. Subsequently, the scripts rotate all vertices on the top and the bottom surface of the flap in order to preserve the shape of the flap's cross section. Furthermore, the flap vertices only in planes 2 and 3 are affected because the respective vertices in planes 1 and 4 cannot be moved. This is due to the fact that they will have to match the shape of the trailing edge section of the wing in the FX-210 model once this trailing edge flap section is inserted into the mesh of the aircraft model. As previously mentioned, the cell layers between planes 1 and 2 and planes 3 and 4 act as transition zones between the deflected flap and the fixed wing. This situation is depicted in figure 2.37 (b) at the end of this section. This

figure contains a series of zoomed-in plots showing the transition zone between planes 3 and 4 during flap deflection.

The vertex redistribution in the 3D trailing edge flap section takes place in two major parts. In the first part, the *vfill*-command is used to redistribute all vertices in planes 2 and 3. More, specifically this is accomplished by refilling the vertex rows at the top and the bottom of patch 4 or between vertices 6000011 and 6000012, as well as vertices 6000031 and 6000032, respectively. Subsequently, all vertex columns in planes 2 and 3 are redistributed. In the second part of this vertex redistribution process, all vertices in-between planes 1 and 2, 2 and 3, and 3 and 4 are refilled on a row-by-row basis in the spanwise direction. For plots of the 3D flap during the deflection process, refer to figures 2.37 (a) and (b). The former shows the complete flap, and the latter contains zoomed-in plots of the transition region.

This concludes the description of the 3D flap deflection process and the respective scripts, *Rotation_of_3D_Flap_2.inp* and *Rotation_of_3D_Flap+2.inp*. The next subsection focuses on a description of the integration of the 3D trailing edge flap section into the FX-210 aircraft model.
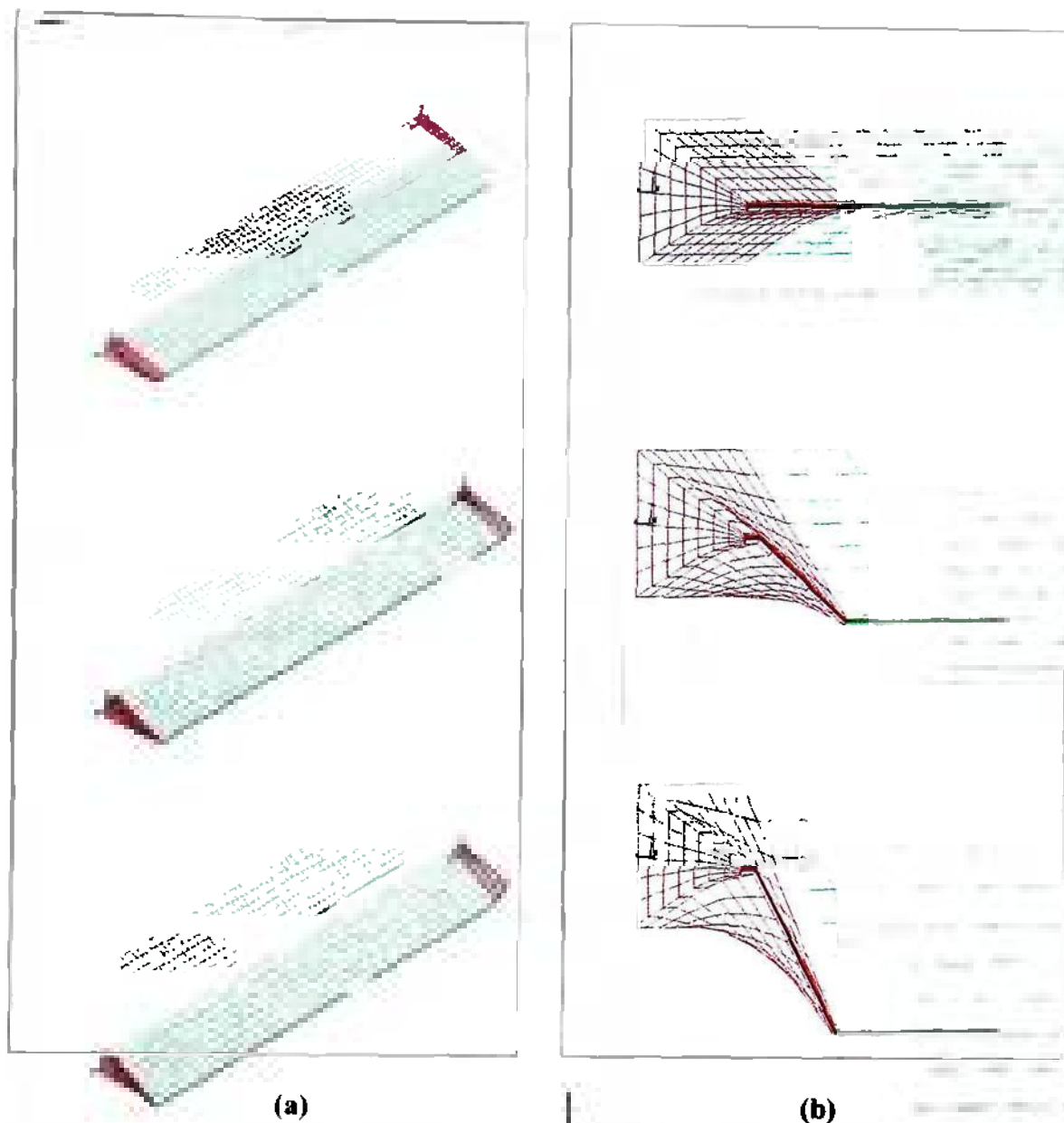
Figure 2.37: Plot of (a) the entire 3D flap and (b) the transition zone in a zoomed-in view at flap deflection angles of 0°, 10° and 20°

2.3.4.4. Integration of Flap Sections into FX-210 Aircraft Model

As mentioned in subsection 2.3.4.1. on page 72. after both 3D trailing edge flap sections have been successfully created. they were stored in a database and inserted into the FX-210 airplane model. More specifically. first the 3D trailing edge flap model was

87

opened in STAR-CD's advanced pro-processing module pro-am, which was mentioned in section 2.2.6, on page 28. In pro-am, the 3D trailing edge flap sections were stored in a database, which was subsequently copied into the file of the FX-210 aircraft model. In this model, all those cells were deleted that occupied the spaces where the 3D trailing edge flap sections were pasted. After that has been accomplished the 3D trailing edge flap sections were inserted into the airplane's model by loading the respective database. This completes the insertion process of the flap sections into the FX-210 aircraft model. However, it does not complete the overall integration process because the cell *distribution on each of the six faces of the 3D trailing edge flap sections does not* correspond to the cell distribution on the respective faces of the FX-210 aircraft model. Figure 2.38 below visualizes the issue by showing the cell distribution within and around the 3D trailing edge flap section.
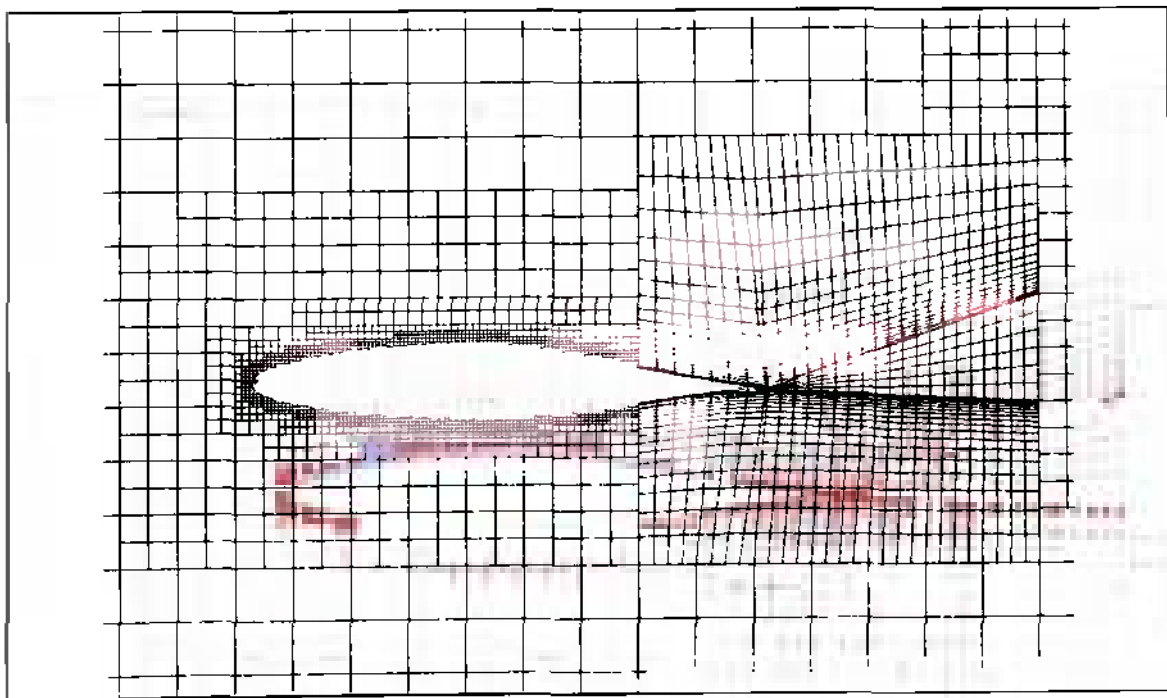
Figure 2.38: Plot of cell distribution inside and around 3D trailing edge flap section

The issue presented at the end of the previous paragraph was solved with a feature offered by STAR-CD called arbitrary mesh interfaces. As mentioned in section 2.2.6. on pages 28 through 30, this feature allows the user to join cell blocks containing different cell structures, such as the 3D trailing edge flap sections and the FX-210 aircraft model. Furthermore, an arbitrary connectivity was established between the cells of the 3D trailing edge flap sections and the FX-210 aircraft model. This was necessary because the cell-spacing and cell-face shape between the two blocks are not matching, which can be well observed in figure 2.38 on the previous page. The integration process and the successful creation of arbitrary mesh interfaces are completed with the definition of cell couples. These consist of a group of cells which are divided into a master cell and several slave cells. In this specific case, the master cells were chosen to be on the face of the FX-210 aircraft model because these are generally bigger than those on the face of the 3D trailing edge flap section. The face with the coarser mesh and, hence, larger cells should be the master side in order to increase computational efficiency of the analysis [7]. The successful creation of all necessary cell couples ensures the proper communication between all cells adjacent to the interface between the airplane model and the 3D trailing edge flap sections and concludes the integration process. Figure 2.39 at the top of the next page shows a plot of the FX-210 aircraft model with the two integrated 3D trailing edge flap sections, one for each wing.
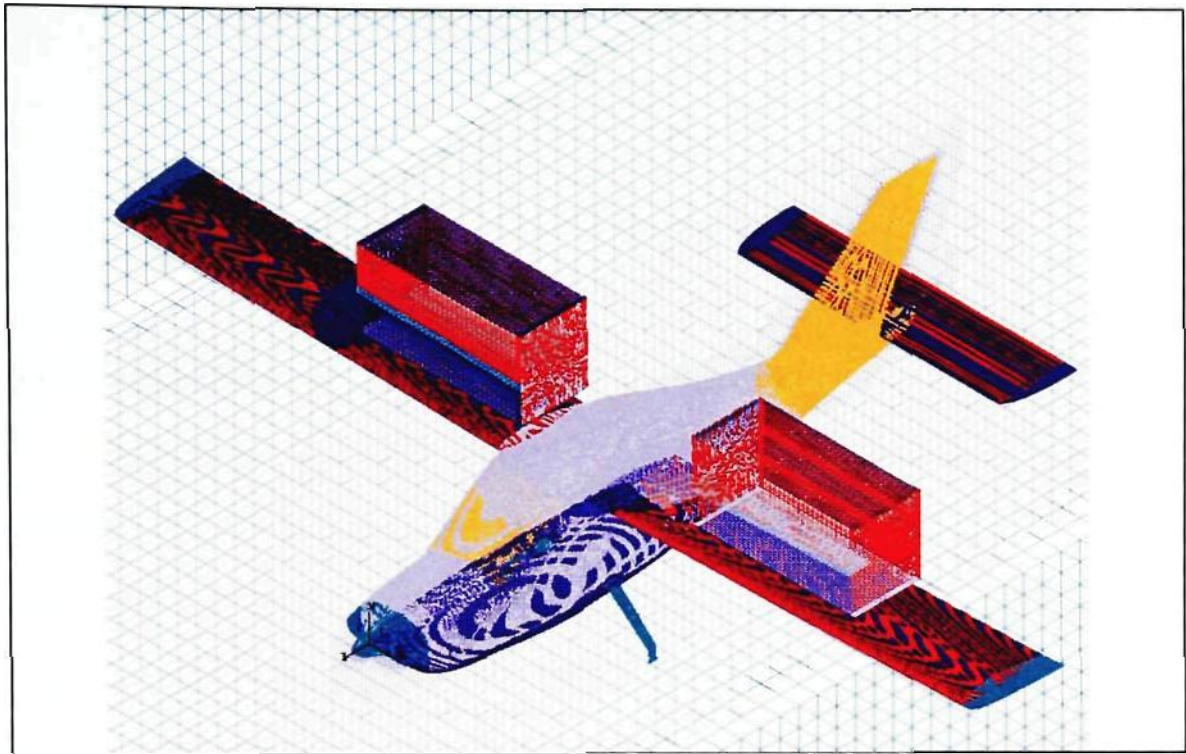
Figure 2.39: Plot of FX-210 with integrated 3D trailing edge flap sections

This concludes the description of the 3D mesh generation process. Furthermore, it completes the description of the methodology utilized to show the viability of using STAR-CD for an investigation of the dynamic effects of flap deflection on the wing's aerodynamic and stability and control characteristics. In the next chapter, the procedure and parameter settings used during the various CFD simulations are described in further detail.

3. ANALYSIS

3.1. Analysis of the 2D Case

This section of chapter 3 has the goal to describe the procedure followed in the analysis of the 2D case. More specifically, in this subsection the author describes the sequence of the steady-state and the different transient cases that have been studied. Initial conditions and several additional parameters are introduced and their specification is explained. Furthermore, this section contains a brief explanation of how the motion of the mesh was set up in STAR-CD using the appropriate scripts whose development and inner workings have been described in subsection 2.3.3.5. on page 69.

3.1.1. 2D Steady-State Analysis

Before the transient analysis was initiated, a converged steady-state solution needed to be generated, which would serve as the initial condition for the various transient cases. Converged in this context means that the values of all dependent variables, such as the velocity components U and V (in the x- and y-direction, respectively), as well as the pressure and the mass flow, needed to approach a steady-state value. In addition, acceptable residual values for the same flowfield parameters needed to be on the order of 10^{-2} to 10^{-3}, preferably. The monitoring location in the computational domain from which these flowfield parameters were taken was chosen arbitrarily with the limitation that it needed to be in proximity to the

91

NACA 0012 airfoil, where the flow was assumed to achieve convergence slower as compared to the rest of the computational domain.

The run time for the steady state analysis was set to 2000 iterations, and the simulation was automatically stopped if a residual tolerance of 10^{-5} was reached. Furthermore, as mentioned in subsection 2.2.10. on page 44, the SIMPLE algorithm was chosen for the steady-state analysis. Table 3.1 below shows the standard parameter settings suggested by STAR-CD [11]. It should be noted that the pressure relaxation factor has been decreased to 0.005 in order to overcome stability issues in the solution.

Table 3.1: Default parameter settings for the SIMPLE algorithm

Parameter	Variable				
	Velocity	*Pressure*	*Turbulence*	*Enthalpy*	*Mass Fraction*
Solver Tolerance	0.1	0.05	0.1	0.1	0.1
Sweep Limit	100	1000	100	100	100
Relaxation Factor	0.7	0.3	0.7	0.95	1

The inlet velocity components U and V have been chosen to be 100 m/s and 0 m/s, respectively. This means that the velocity is only in the x-direction, which furthermore ensures that the angle of attack of the airfoil is zero. This, in turn, facilitates the analysis because it rules out any effects of the angle of attack on the lift, drag, and moment coefficient of the airfoil, as well as on the location of the center of pressure. Furthermore, under standard sea-level conditions, which means at a pressure of $P = 101.325$ kPa and a temperature of $T = 293.15$ K, the airflow can be assumed to be incompressible because the Mach number, M, under these conditions is less than 0.3.

This is based on the assumptions that the ratio of specific heats for air, γ, equals 1.400 and that the specific gas constant for air, R, amounts to 287 J/kg·K. The following calculation backs up the assumption that the flow is incompressible:

$$a = \sqrt{\gamma R T} \tag{3.1}$$

$$a = \sqrt{1.400 \left(287.0 \frac{\text{J}}{\text{kg K}}\right) (293.15 \text{K})}$$

$$a \approx 343.2 \, \text{m}/\text{s}$$

$$M = \frac{V_x}{a} \tag{3.2}$$

$$M = \frac{\left(100 \, \text{m}/\text{s}\right)}{\left(343.2 \, \text{m}/\text{s}\right)}$$

$$\boxed{M \approx 0.291}$$

Based on the above assumption that the flow is incompressible, the density of the flow was chosen to be constant as mentioned in subsection 2.2.3. on page 22, and its value was set to 1.205 kg/m³. This eliminated one of the dependent variables and contributed to an increase in computational efficiency.

For the sake of completeness, it should be mentioned that the default values for the turbulence kinetic energy and its dissipation rate have not been changed. STAR-CD defines the initial turbulent kinetic energy, k, at the inlet boundary to be 0.00375 m^2/s^2

and its dissipation rate, ε, to amount to 0.0377 m²/s³. This concludes the description of the set up of the 2D steady-state analysis, which was subsequently used as the initial condition for the various transient cases.

3.1.2. 2D Transient Analysis

The most prevalent difference between the transient and the steady-state analysis is the fact that the converged steady-state solution that was previously generated served as a field of initial values. Furthermore, a different solution algorithm was used, namely the PISO algorithm. The inner workings of that algorithm were described in subsection 2.2.10. on page 44, and table 3.2 below shows the default parameter settings for the PISO algorithm [11]. The pressure correction relaxation factor in this case was reduced to 0.001.

Table 3.2: Default parameter settings for the PISO algorithm

Parameter	Variable				
	Velocity	*Pressure*	*Turbulence*	*Enthalpy*	*Mass Fraction*
Solver Tolerance	0.01	0.001	0.01	0.01	0.01
Sweep Limit	100	1000	100	100	100
Corrector Limit = 20					
Pressure Correction Relaxation Factor = 1.0					
Corrector Step Tolerance = 0.25					

The inlet velocity was kept at 100 m/s exclusively in the x-direction, which means that the flow was again assumed to be incompressible with a constant density of 1.205 kg/m³ according to standard sea-level conditions. Also, the turbulence kinetic energy and the respective dissipation rate were kept the same as in the steady-state analysis, namely at 0.00375 m²/s² and 0.0377 m²/s³, respectively.

94

The motion of the mesh necessary to accommodate the deflection of the plain trailing edge flap was modeled using the *mvgrid*-feature in STAR-CD. This feature allows the user to either apply a user-subroutine called *NEWXYZ*, which contains appropriate FORTRAN code to move the mesh, or to use the *EVENTS* command module. For this specific transient analysis the *EVENTS* command module was used because it allows the user to specify a certain number of time-dependent events which contain a batch of STAR-CD commands that cause the mesh to move, such as the flap rotation scripts that were presented in subsection 2.3.3.5. on page 69. The batch of STAR-CD commands needs to be stored as a *cgrd*-file, which in this transient analysis is almost identical to the flap rotation scripts *Section_Rotation_+.inp* and *Section_Rotation_.inp*. A sample *cgrd*-file used in the transient analysis called *rotate_2b.cgrd* is presented in appendix A. This specific *cgrd*-file is merely a sample file because several transient cases with different flap rotation rates have been conducted.

The transient analysis was conducted at several different deflection rates in order to conduct a more holistic analysis of the dynamic effects of flap deflection on the aerodynamic and stability and control characteristics of the airfoil and to show the adaptability of this methodology. First, a more conservative variation of the flap deflection rate was considered, which led to the choice of deflection rates of 10°/s, 20°/s and 40°/s. During these three transient cases, the flap was deflected at the respective rates to a maximum deflection angle of 30°. This means that the run time for each case was set to 3s, 1.5s and 0.75s for the 10°/s, 20°/s and 40°/s trial, respectively. Furthermore, the time steps, δt, were set to 0.01s for the 10°/s and 20°/s trials, and the 40°/s trial had a time step setting of 0.005s. Due to the fact that STAR-CD runs the *cgrd*-file mentioned above

95

during each time step, the deflection angles defined in the file had to be adjusted accordingly. More specifically, the deflection angle setting for the 10°/s, 20°/s and 40°/s trial were 0.1°, 0.2° and 0.2°, respectively. The latter two deflection angle settings could be kept the same because the time step in the 40°/s trial is half as long as compared to the 20°/s trial. This implies that the deflection takes place twice as quickly. Table 3.3 below summarizes the settings outlined above.

Table 3.3: Settings for the transient cases with deflections rates of 10°/s, 20°/s and 40°/s

Case #	Deflection Rate [deg/s]	Time Step [s]	Deflection Angle per Time Step [deg]	Run Time [s]
1	10	0.01	0.1	3
2	20	0.01	0.2	1.5
3	40	0.005	0.2	0.75

After the above three cases were completed, it was decided to increase the flap deflection rate by an order of magnitude. Consequently, a fourth case was conducted with a flap deflection rate of 200°/s, whereas the maximum deflection angle remained at 30°. In addition, the time step was decreased from 0.005s in the 40°/s case to 0.001s in the 200°/s case. This meant that the deflection angle per time step, which needed to be entered into the cgrd-file, remained at 0.2°. In other words, it was possible to use the same cgrd-file as in the 40°/s. The run time for this case was extended beyond 0.15s that are necessary to allow the flap to deflect to 30°, so that the unsteady development of the flow could be captured. More specifically, the run time was increased to 1s. In order to

allow a frame-by-frame qualitative and degree-by-degree quantitative comparison, the 20°/s case had to be repeated with an appropriate extension of its runtime. In fact, this additional fifth case had an extended run time of 10s. All other analysis parameters remained the same as shown in table 3.4 below.

Table 3.4:   Settings for the transient cases with deflections rates of 200°/s and 20°/s

Case #	Deflection Rate [deg/s]	Time Step [s]	Deflection Angle per Time Step [deg]	Run Time [s]
4	200	0.001	0.2	1
5	20	0.01	0.2	10

There are two further transient cases (6 and 7) that were conducted in the 2D analysis. Case 6 was run at 200°/s and case 7 was run at 20°/s, and each case consists of two full flap deflection and retraction cycles. In other words, in both cases 6 and 7 the flap was first deflected to 30°, then retracted to 0°, and again deflected to 30° and retracted back to 0°. It was decided to conduct these cases in order to quantitatively capture the dynamic effects of flap retraction on the stability and control characteristics of the NACA 0012 airfoil and to ensure that it was possible to reproduce these effects. In addition, these cases further emphasize the adaptability of this methodology. All analysis parameters remained the same as in the previous cases except for the run time, which was set to 0.7s in case 6 and to 7s in case 7. These run times allow two full flap deflection and retraction cycles, which take 0.6s and 6s, respectively, as well as an additional 0.1s and 1s, which serve as a stabilization period to allow the flow to return to its initial condition. Table 3.5 at the top of the next page summarizes the analysis settings for cases 6 and 7.

Table 3.5: Settings for the transient cases with two full deflection/retraction cycles at rates of 200°/s and 20°/s

Case #	Deflection Rate [deg/s]	Time Step [s]	Deflection Angle per Time Step [deg]	Run Time [s]
6	200	0.001	0.2	0.7
7	20	0.01	0.2	7

3.1.3. 2D Post-Processing

The post-processing was conducted once all cases (1 through 7) have been completed successfully and consists of two parts: a qualitative and a quantitative one. The next few paragraphs describe each part in more detail and simultaneously outline what to expect in the next chapter, which presents the results.

The qualitative part of the post-processing produced plots of the distribution of several dependent variables in the vicinity of the airfoil. More specifically, the dependent variables that were plotted are the pressure coefficient and the velocity, both as a scalar in a contour-plot and as a vector in a vector-plot. The pressure coefficient was calculated based on the local and freestream velocity by using the following formula [3]:

$$C_p = 1 - \left(\frac{V}{V_\infty}\right)^2 \qquad [3.3]$$

Both the velocity vector and its magnitude were normalized by expressing them in terms of the inlet or freestream condition. For example, the normalized velocity magnitude was

computed by dividing each local velocity magnitude by its counterpart at the inlet. This is also expressed by equation 3.4 below:

$$\left|\vec{V}\right|_{norm} = \frac{\left|\vec{V}\right|_{local}}{\left|\vec{V}\right|_{inlet}} = \frac{\left|\vec{V}\right|_{local}}{\left|\vec{V_\infty}\right|} = \frac{\left|\vec{V}\right|_{local}}{\left(100\,m/s\right)}$$ [3.4]

It should be noted that the qualitative part of the post-processing was conducted to fulfill the primary purpose of visualizing the dynamic effects of flap deflection on the aerodynamic characteristics of the airfoil. Furthermore, it was used to show the effects of the variation of the flap deflection rate on the flowfield. Therefore, it was merely applied to cases 1 through 5 and was not used in cases 6 and 7 in order not to repeat results.

Just like in the mesh generation process, the qualitative analysis was accomplished by using a script. In this case, the script was called *Post_1_Qualitative.inp*, and it can be viewed in appendix A. This script is subdivided into three major parts. The first part defines the size and the zoom of the plot and simultaneously loads the appropriate *pstt*-file. This file contains the solution of the transient simulation and consists of both geometry data for the moving mesh and flowfield data. Each case has its own *pstt*-file. The second part of the *Post_1_Qualitative.inp* script contains a loop which repeatedly loads geometry and flowfield data for each time step in a chronological order and simultaneously dumps the plots as *gif*-files into the current directory. The third and final part of this script represents a library as it contains pieces of the script that load different dependent variables. That means that these pieces can be substituted into parts one and two of the script in order to produce plots of different dependent variables in the

99

flowfield. Overall, *Post_1_Qualitative.inp* semi-automates the post-processing process, just like the scripts in the mesh generation process.

The quantitative part of the post-processing complements the qualitative part by extracting data to visualize the dynamic effects of flap deflection on the stability and control characteristics of the NACA 0012 airfoil. More specifically, the stability and control characteristics that are subject to the quantitative post-processing are the section lift coefficient, c_l, section drag coefficient, c_d, and section moment coefficient about the quarter chord, $c_{m,c/4}$, as well as the relative location of the center of pressure, x_{cp}/c. Furthermore, all of these variables are expressed as functions of the flap deflection angle, δ, as can be seen in the next chapter. This has been done in order to facilitate a direct comparison of the data from the 200°/s and 20°/s cases. Furthermore, the quantitative part of the post-processing has been applied to cases 4 and 5 in order to show the development of the stability and control parameters during the flap deflection process and after the flap has reached its maximum deflection angle of 30°. Then the quantitative analysis has been extended to cases 6 and 7 in order to investigate the development of the stability and control parameters during both flap deflection and retraction.

Just like in the qualitative part of the post-processing, the quantitative part has been accomplished by using a script, namely *Post_2_Quantitative.inp*, which is also shown in appendix A. Contrary to *Post_1_Qualitative.inp*, this script does not produce plots, but creates a *txt*-file that contains data for the total lift, total drag and the respective moment about the leading edge for each time step in the flap deflection process. The script can be viewed in appendix A and consists of two steps. In the first step, the script loads the airfoil surface cells into a cell set and then uses the *getnv*-command to read the

total force data for each cell in this set. This is first done in the y-direction for lift-data and then in the x-direction for drag-data. It should be noted that STAR-CD computes the total force acting on each shell by using the static pressure. For more information regarding the force calculation, refer to equations 2.34 through 2.36 in subsection 2.2.9. on page 43. Simultaneously, the script calculates the moments, m_x and m_y, due to the lift and drag forces acting on each airfoil surface cell, respectively, according to the following equations:

$$m_x = d \cdot y \qquad\qquad [3.5]$$

$$m_y = l \cdot x \qquad\qquad [3.6]$$

In equation 3.5, d is the drag force acting on each surface cell, and y is the vertical distance between the centroid of the respective cell and the leading edge or chord line. In equation 3.6, l is the lift force acting on each surface cell, and x is the horizontal distance between the centroid of the respective cell and the leading edge.

At the end of the first step, the script defines two sets of virtual vertices, one for all data from the analysis in the x-direction and the other for all data from the analysis in the y-direction. The vertex sets are considered virtual because the x-, y- and z-coordinates represent time, the total forces and moments about the leading edge for the entire airfoil, respectively. It should also be noted that the first vertex set contains data from the analysis in the y-direction, and the second vertex set contains data from the analysis in the

101

x-direction. The total forces and moments for the airfoil have been computed using the following equations, where the sum is over all airfoil surface cells, *i*:

$$L = \sum_i l_i \qquad\qquad\qquad [3.7]$$

$$M_x = \sum_i m_{x,i} \qquad\qquad\qquad [3.8]$$

Finally, the second step of the script uses the *ofile*-command to write the vertices and their virtual coordinates to a *txt*-file. The latter was then used for further manipulation, which is described in more detail in the next chapter when the data is actually presented.

3.2. Analysis of the 3D Case

Overall, the analysis of the 3D case is similar to the 2D case, with the biggest difference being the complexity of the analysis itself. The higher complexity in the 3D case translated into longer computing times that resulted in a limitation of the scope of the analysis. Again, a steady-state analysis was conducted first, which then served as a field of initial conditions for the transient analysis. The following two subsections describe the set up of the steady-state and the transient analysis in more detail.

However, before continuing with a detailed description of the 3D analysis, it should be noted that in order to realize the simulation of the flow with a single processor, the size of the mesh of the 3D model was reduced by 50%. This was accomplished by cutting the mesh into two halves along the symmetry plane of the aircraft and by

subsequently deleting one half. Due to the fact that the model is perfectly symmetric, it was concluded that this reduction of the mesh would not affect the quality of the solution. After the reduction of the computational domain, the symmetry plane acted as a boundary and was consequently turned into a symmetry boundary, which is described in more detail in subsection 2.2.8. on page 40. This modification to the mesh reduced the number of cells by 50% to about $2.38 \cdot 10^6$. For a plot of the reduced 3D aircraft model refer to figure 3.1 below.
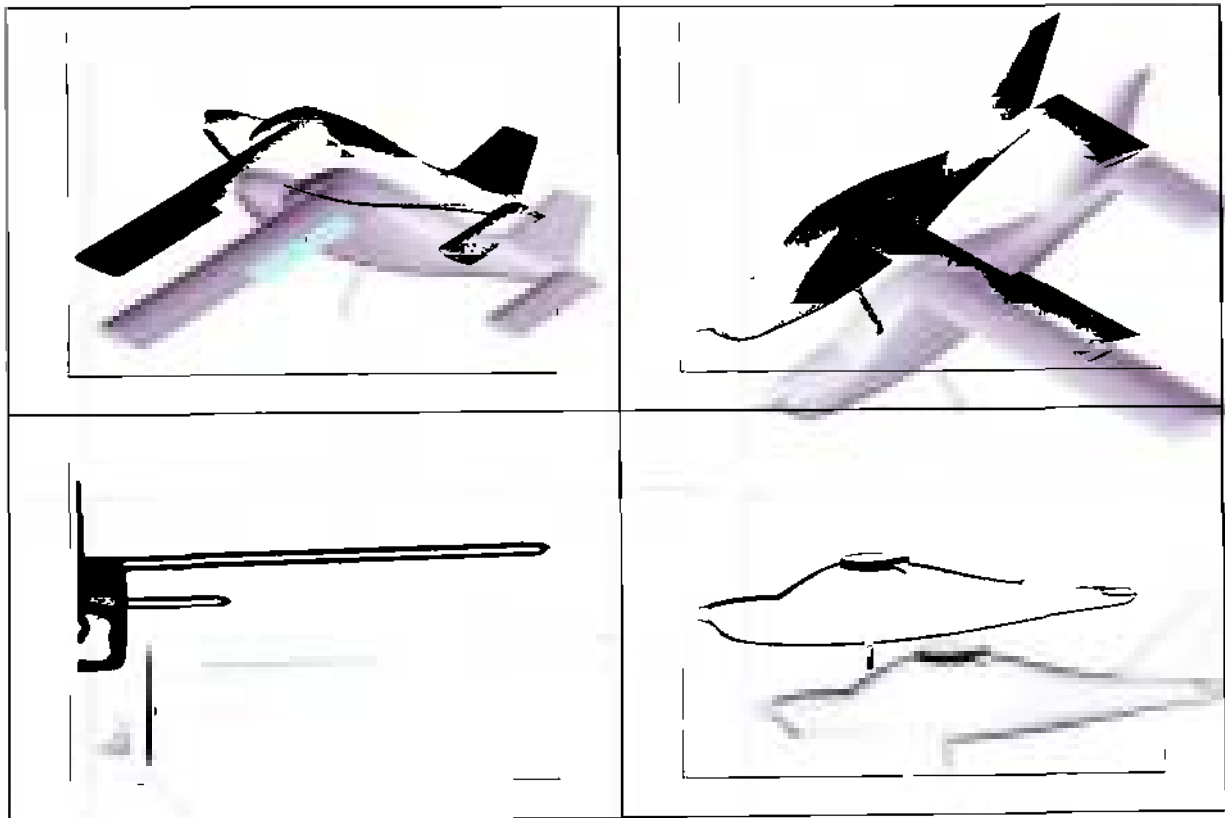
Figure 3.1: Plots of the reduced 3D model of the Four Winds FX-210

3.2.1. 3D Steady-State Analysis

Just like in the 2D case, a converged steady-state solution needed to be generated first. The criterion for convergence in the 3D case was a maximum variation of the velocity components of the flow of 5% in the monitoring cell. This cell was located close to the wing and fuselage of the 3D aircraft model because it is an area where a convergence of the flowfield was assumed to occur relatively late as compared to the rest of the computational domain. In addition, the residual values of the dependent variables needed to be on the order of 10^{-2} to 10^{-3} in order to fulfill the stability criterion for a converged steady-state solution. The run time for the 3D steady-state analysis was set to 1000 iterations, whereas the SIMPLE solution algorithm was used again. The parameter settings for the SIMPLE algorithm are the same as in the 2D steady-state case (see table 3.1 on 92).

The initial conditions at the inlet boundary were defined in a similar manner to the 2D case. The inlet or freestream velocity was chosen such that the angle of attack of the aircraft was zero in order to avoid any effects of a non-zero angle of attack on the stability and control characteristics of the airplane. This meant that the U and the V inlet velocity components were zero, and the W inlet velocity component was set to -100 m/s. Furthermore, the remaining boundary conditions were not defined according to standard sea-level conditions because it was determined that the simulation would be more authentic if the simulation was set up such that the airplane flies at an altitude of 900m. The temperature and the density of the air at the inlet of the computational domain were found by using the U.S. Standard Atmosphere 1976 model. This model rendered an air temperature of 282.2 K and a density of 1.121 kg/m^3 [12]. This meant that the speed of

sound, a, and the Mach number, M, according to equations 3.1 and 3.2, respectively, were:

$$a = \sqrt{\gamma R T} = \sqrt{1.400 \left(287.0 \frac{\text{J}}{\text{kg K}}\right)(282.2 \text{K})}$$

$$a \approx 336.7 \frac{\text{m}}{\text{s}}$$

$$M = \frac{V_x}{a} = \frac{\left(100 \frac{\text{m}}{\text{s}}\right)}{\left(336.7 \frac{\text{m}}{\text{s}}\right)}$$

$$\boxed{M \approx 0.297}$$

Although, the Mach number is still less than 0.3, which would justify an incompressible treatment of this case, it was chosen not to run this simulation with a constant density. Instead, STAR-CD's compressible flow solver was used, which calculates the density as a function of pressure and temperature. For a more detailed explanation of the compressible flow solver, refer to subsection 2.2.3. on page 21.

To complete the description of the 3D steady-state analysis, it should be mentioned that the default initial values of the turbulent kinetic energy and its dissipation rate have been changed. The default values can be viewed at the top of page 92. For this part of the analysis, the turbulent kinetic energy, k, has been changed to 1.35 m^2/s^2, and its dissipation rate, ε, has been replaced by 0.184 m^2/s^3.

3.2.2. 3D Transient Analysis

Like the 3D steady-state analysis, the transient part has many similarities to its 2D counterpart. One of these similarities is the use of the PISO algorithm and related parameter settings. A more detailed description of the former is given in subsection 2.2.10. on page 44, and a summary of the latter can be viewed in table 3.2 on page 94. It should be noted however, that the pressure correction relaxation factor has been increased from 0.001 to 0.05 in the 2D case.

Another similarity shared by the 2D and the 3D transient cases is the fact that the inlet boundary conditions have been kept the same as in the respective steady-state cases. More specifically, the inlet velocity was kept at 100 m/s strictly in the negative z-direction, and the air temperature and density were kept at 282.2 K and 1.121 kg/m^3, respectively. Also, the turbulent kinetic energy and its dissipation rate were kept the same as in the 3D steady-state case at 1.35 m^2/s^2 and 0.184 m^2/s^3, respectively.

The implementation of the motion of the mesh in the 3D trailing edge flap section is another commonality of the 3D transient case with its 2D counterpart. Again, STAR-CD's *mvgrid*-feature in combination with the *EVENTS* command module was used to load a *cgrd*-file called *rotate_3D_flap_2c.cgrd*, which is added to appendix A at the end of this thesis. Again, just like in the 2D case, the *cgrd*-file is a slightly modified version of the 3D flap rotation script called *Rotation_of_3D_Flap_2.inp* which is explained in further detail in subsection 2.3.4.3 on page 84.

As mentioned in the introductory paragraph to this section, the 3D transient analysis does not have the variety of cases as its 2D counterpart. For the most part, this is due to the complexity of the geometry of the 3D aircraft model and the resulting long

computing times. In fact, only one case was conducted for the 3D analysis, during which the flap was deflected at a rate of 20°/s for one second, so that the maximum flap deflection angle in this analysis was 20°. A deflection rate of 20°/s has been chosen because it was the case that has been investigated most in the 2D analysis. In addition, it represents a fairly realistic estimation for the deflection rate on real general aviation aircraft.

It should also be noted that a change has been added to the geometry of the 3D trailing edge flap section. More specifically, this change affects the transition zone between the flap and the wing, which is depicted in figure 3.2 at the end of this subsection. The cells in the transition zone, which is marked red in figure 3.2, has been turned into solid cells, which means that STAR-CD perceives them as a cavity in the computational mesh, just like the flap, the wing and the rest of the FX-210 aircraft model. This has been done in order to avoid any complications that could occur during the computation due to highly skewed fluid cells. Internal angles between adjacent cell walls and warp angles on cell faces should not exceed 45° [11]. Figure 3.2 shows that some of the cells in this transition region are in the vicinity of these guidelines, and that is why it was decided to avoid possible complications by turning the affected cells into solid cells.
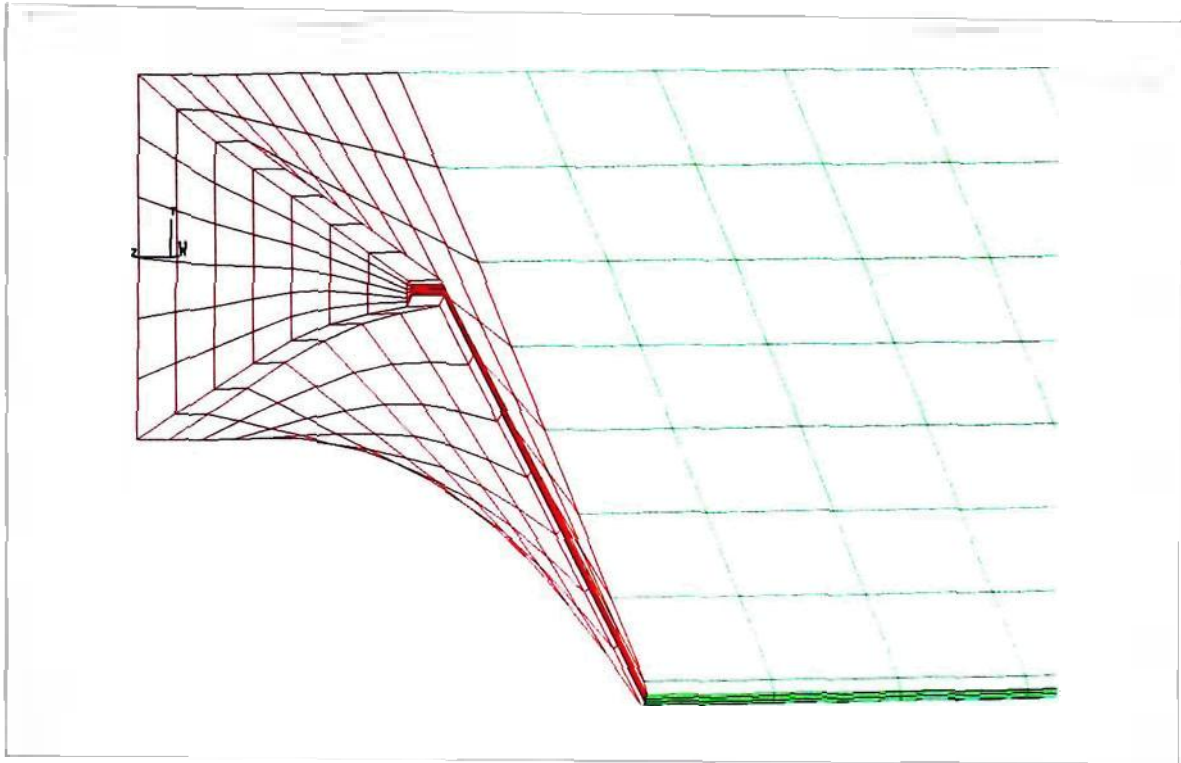
Figure 3.2: Zoomed-in plot of transition zone from 3D flap to wing

3.2.3. 3D Post-Processing

As mentioned earlier, due to the complexity of the simulation the scope of the 3D analysis is limited. Similarly to the 2D analysis, the post-processing of the 3D case is also divided into a qualitative and a quantitative part. In the qualitative part, the distribution of the velocity magnitude across the surface of the aircraft model is visualized at several steps of the flap deflection process. That way the dynamic effects of flap deflection on the flowfield in the vicinity of the aircraft were captured. These plots were produced manually as opposed to the semi-automatic procedure used in the 2D case because the small number of plots required in this case did not justify the laborious modification of the 2D post-processing scripts.

The quantitative analysis, on the other hand, utilized the *Post_2_Quantitative.inp* script from the 2D analysis to trace the development of the effects of flap deflection on the stability and control characteristics on the various components of the aircraft. More specifically, the 3D quantitative analysis traces the development of the lift, drag and moment coefficient, as well as the location of the center of pressure, for the fuselage, the horizontal tail and the wing as functions of the flap deflection angle. For that purpose, the script only needed to be slightly modified, but in its general character it remained unchanged. Overall, the 3D quantitative analysis has a similar character as its 2D counterpart.

This concludes chapter 3, and all necessary information for an understanding of the rationale behind the presentation of the results was covered. The next chapter contains all relevant results that have been gathered during this analysis, and it should be noted that the outline in which the results are presented resembles the one described in this chapter.

4. RESULTS

4.1. Results of the 2D Analysis

This section of chapter 4 presents all the results that have been collected during the 2D analysis of this investigation. As outlined in the previous chapter, first the results from the 2D steady-state analysis are presented and then the results from the various 2D transient cases are present. Wherever necessary, this section explains any treatments or calculations that were made in order to present the results in an appropriate and meaningful manner.

4.1.1. Results of the 2D Steady-State Analysis

Before the actual results are presented, proof is given that the 2D steady-state analysis is indeed converged and meets the stability criteria presented in subsection 3.1.1. on page 91. As a reminder, the author considered the steady-state solution as converged, if the residuals are on an order of magnitude of 10^{-2} to 10^{-3} or less and the dependent variables have approached a steady-state value. For that purpose, figures 4.1 (a) through (c) on the next page show the development of the velocity components U and V, as well as the static pressure P, at the monitoring location as a function of the iteration number. In addition, figure 4.1 (d) and (e) on page 112 consist of plots that trace the development of the residuals as functions of the iteration number. The monitoring location is located at a point close to the leading edge of the airfoil.

MONITORED VALUES FOR FLUID 1

U MON. FOR FLUID 1

(a)

MONITORED VALUES FOR FLUID 1

V MON FOR FLUID 1

(b)

MONITORED VALUES FOR FLUID 1

P MON FOR FLUID 1

(c)

(d)

(e)
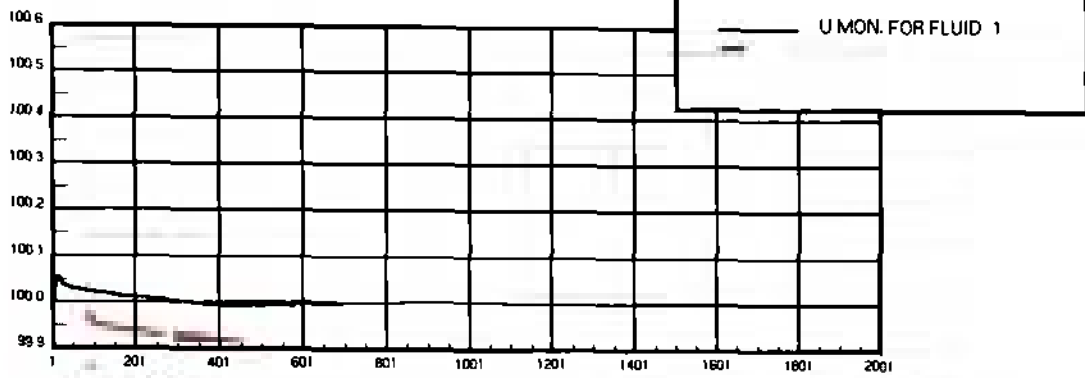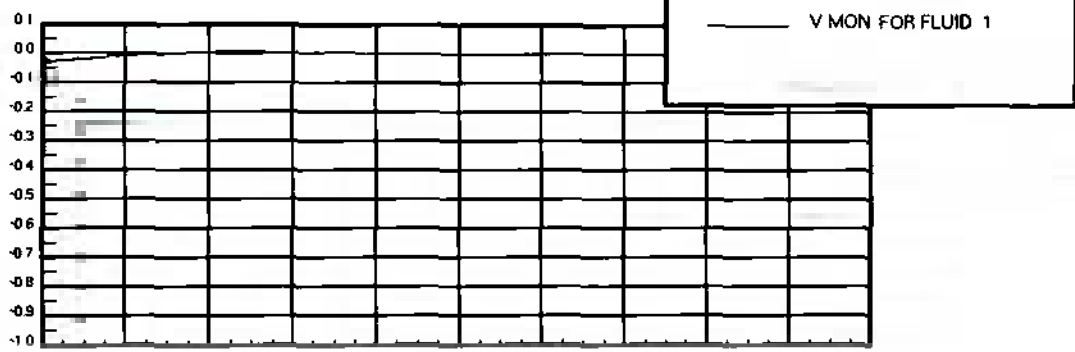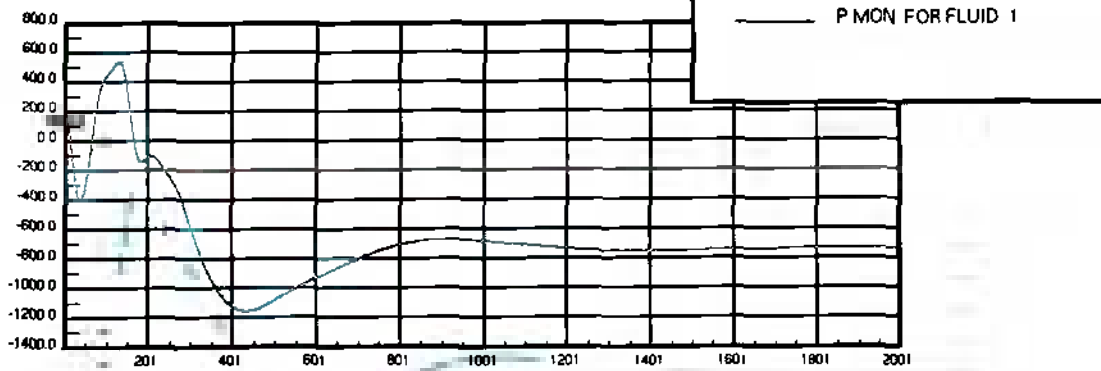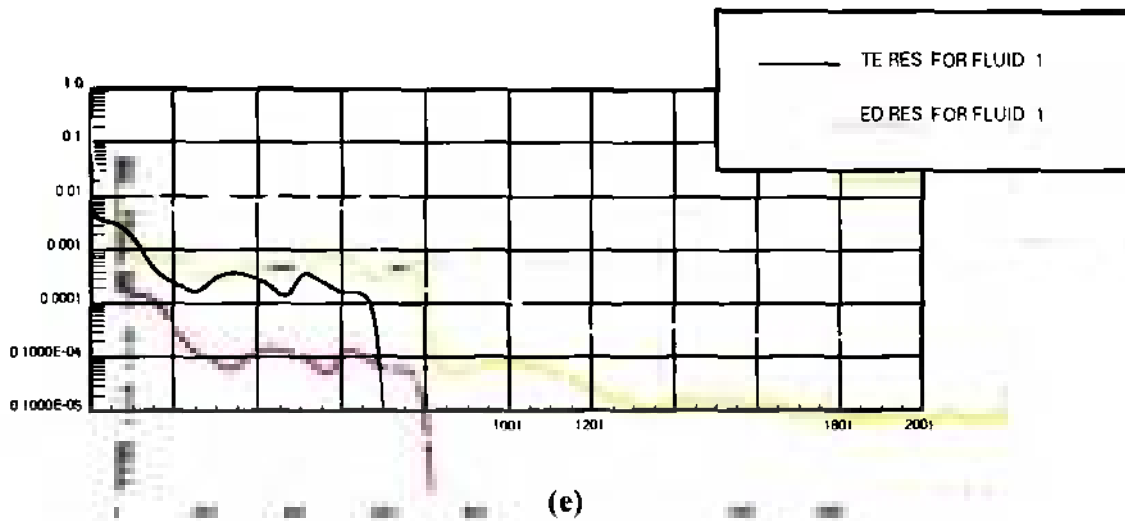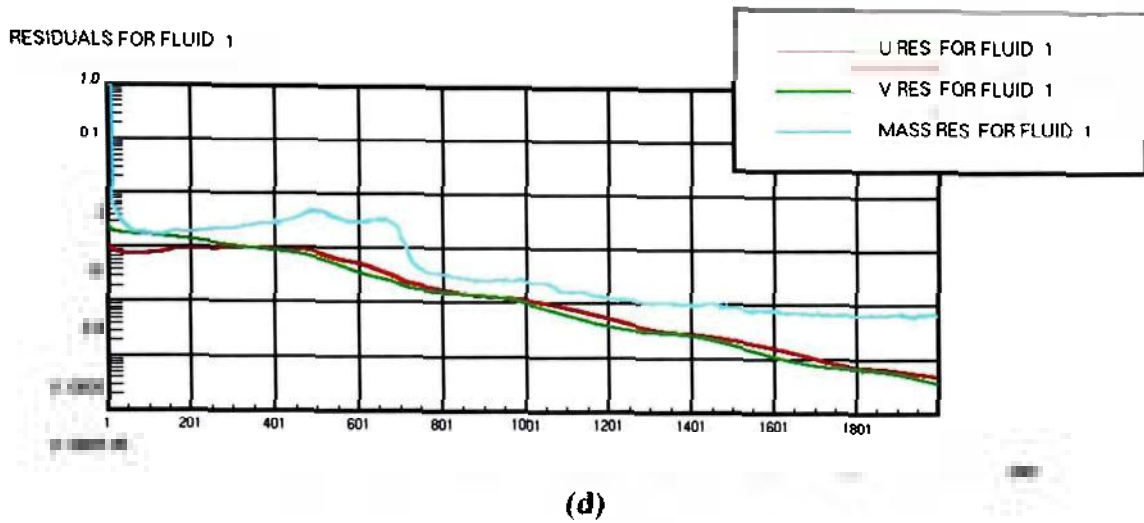
Figure 4.1: Plot of the monitoring values of (a) U in m/s, (b) V in m/s and (c) P in Pascals as functions of the iteration number; plot of the residuals of (d) U, V, and *Mass*, as well as of (e) the turbulent kinetic energy, *TE*, and its dissipation rate, *ED*, as a function of the iteration number

Figures 4.1 (a) through (c) indeed show that the velocity components U and V, as well as the static pressure P, at the monitoring location approached steady-state values, which is a good indicator that the 2D steady-state solution has converged after 2000 iterations. It should be noted that the monitoring values are differences to the respective values at a reference cell which has been defined at the inlet boundary of the computational domain. This explains why, for instance, the monitoring value for the pressure is negative. Furthermore, figures 4.1 (d) and (e) show that the residual values of the velocity components U and V, as well as of the massflow, $MASS$, turbulent kinetic energy, TE, and its dissipation rate, ED, decline continuously, which is another indicator for the stability of the 2D steady-state solution. Besides, after 2000 iterations all residuals are well below the stability criterion stated earlier, so that it can be legitimately concluded that the 2D steady-state analysis is converged and represents a valid basis for the various 2D transient cases.

Now, that the validity of the 2D steady-state has been confirmed, the actual flowfield solution of the 2D steady-state analysis is presented. This is done in three plots that have all been produced with a script called *Post_1_Qualitative.inp*, which is explained in more detail in subsection 3.1.3. on page 98. Figures 4.2 (a) through (c) on the next page show a distribution of the relative velocity, the pressure coefficient and the normalized velocity vector, respectively. It should be noted that the former two are contour plots and the latter is a vector plot. In addition, the vector plot is zoomed-in to the region around the trailing edge flap of the airfoil in order to show the details in that region. In order to provide continuity, the same views have been adopted for both the steady-state and the transient results.
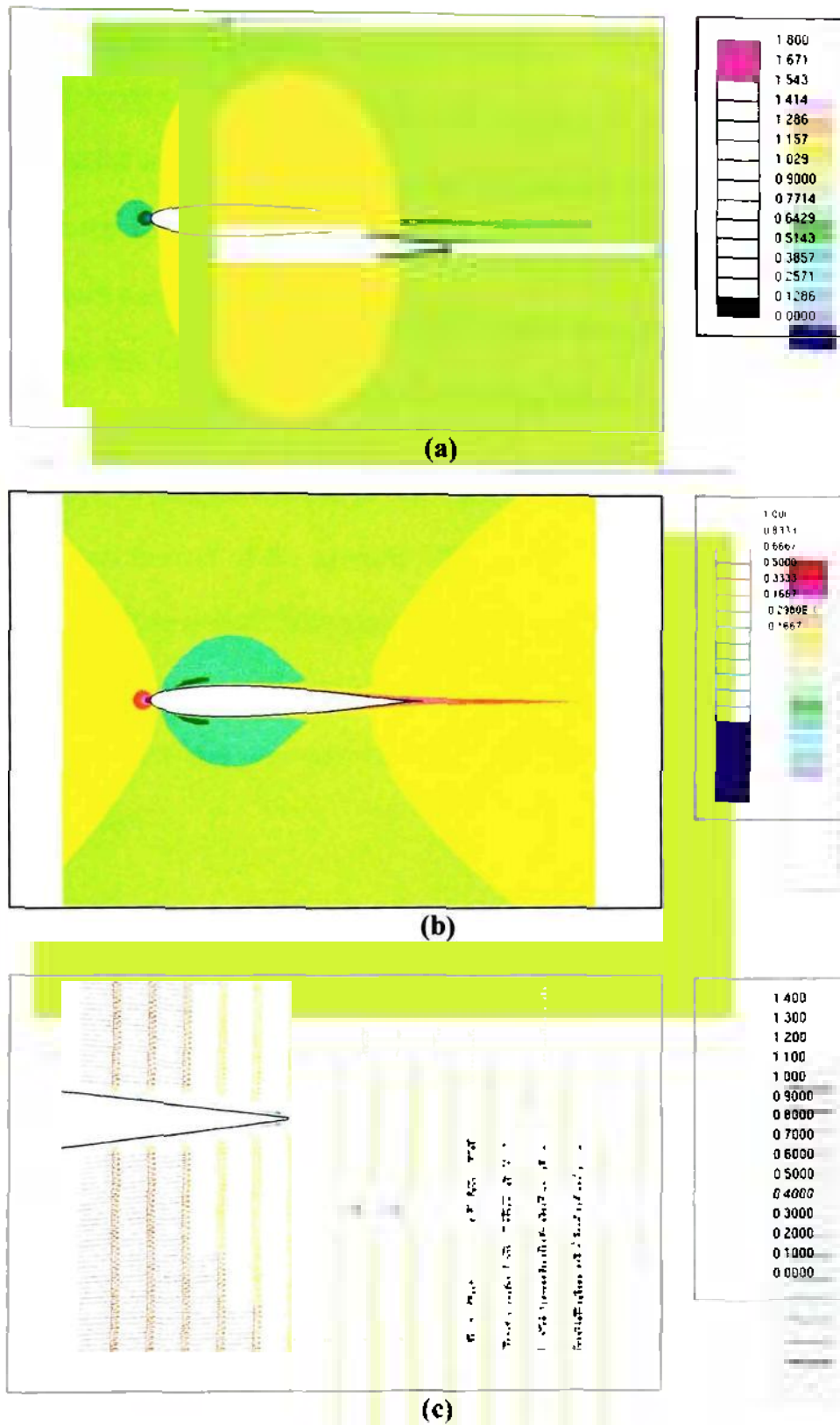
Figure 4.2: Plot of the distribution of the (a) velocity magnitude, (b) pressure coefficient and (c) normalized velocity vector

The most conspicuous characteristic in all three plots of figure 4.2 is the high degree of symmetry in the flowfield. This is certainly expected from the flow around a symmetric airfoil at zero angle of attack. In addition, this indicates that this airfoil does not produce any lift due to the identical velocity and pressure distributions over the top and the bottom surface of the airfoil. All of this corresponds well to initial expectations and the theory that has been presented in subsection 2.1.1. on page 7. Besides, this result emphasizes the importance of choosing a symmetrical airfoil at zero angle of attack as a basis for this investigation because the initial symmetric flowfield facilitates the qualitative identification of the dynamic effects of flap deflection on the aerodynamic characteristics of the airfoil. With the confidence that the result of the 2D steady-state analysis is indeed well converged and that it corresponds well to the theory presented in chapter 2, the author now proceeds with the presentation of the results from the various 2D transient cases.

4.1.2. Results of the 2D Transient Analysis

As indicated in subsection 3.1.2. on page 94, the 2D transient analysis consists of seven cases in total. Due to the structure of the analysis and for the purpose of presenting the results in a meaningful way, these seven cases have been divided into three groups. In the first group, cases 1, 2 and 3 are compared qualitatively, and in the second group cases 4 and 5 are compared both qualitatively and quantitatively. Finally, the third group quantitatively compares cases 6 and 7. The following three subsections present the results and conduct the respective comparison for each group.

4.1.2.1. Qualitative Comparison of the Results of Cases 1, 2 and 3

Table 3.3 on page 96 showed that in cases 1, 2 and 3 the flap has been deflected at 10°/s, 20°/s and 40°/s, respectively. The results for these cases are shown similarly to the 2D steady-state case: in a contour plot of the relative velocity and the pressure coefficient distribution in the vicinity of the airfoil and in a vector plot of the velocity vector in the vicinity of the plain trailing edge flap. Furthermore, for each case and type of plot, the result is presented at a flap deflection of 0°, 10°, 20° and 30° in order to show the dynamic effects of flap deflection on the flowfield and to realize a qualitative comparison of the three cases.

Figures 4.3 (a) through (c) on the next page contain plots of the relative velocity distribution in the vicinity of the airfoil for deflection angles of 0°, 10°, 20° and 30° for the 10°/s, 20°/s and 40°/s cases, respectively. Figures 4.4 (a) through (c) show plots of the pressure coefficient distribution in the vicinity of the airfoil in the same manner as figures 4.3 (a) through (c). Finally, figures 4.5 (a) through (c) present the relative velocity distribution in the vicinity of the plain trailing edge flap in vector form in the same structure as the previous figures. Figures 4.4 and 4.5 can be viewed on pages 118 and 119, respectively.

t = 0s; δ = 0°

t = 0s; δ = 0°

t = 0s; δ = 0°

t = 1s; δ = 10°

t = 0.5s; δ = 10°

t = 0.25s; δ = 10°

t = 2s; δ = 20°

t = 1.0s; δ = 20°

t = 0.50s; δ = 20°

t = 3s; δ = 30°

t = 1.5s; δ = 30°

t = 0.75s; δ = 30°

(a)

(b)

(c)
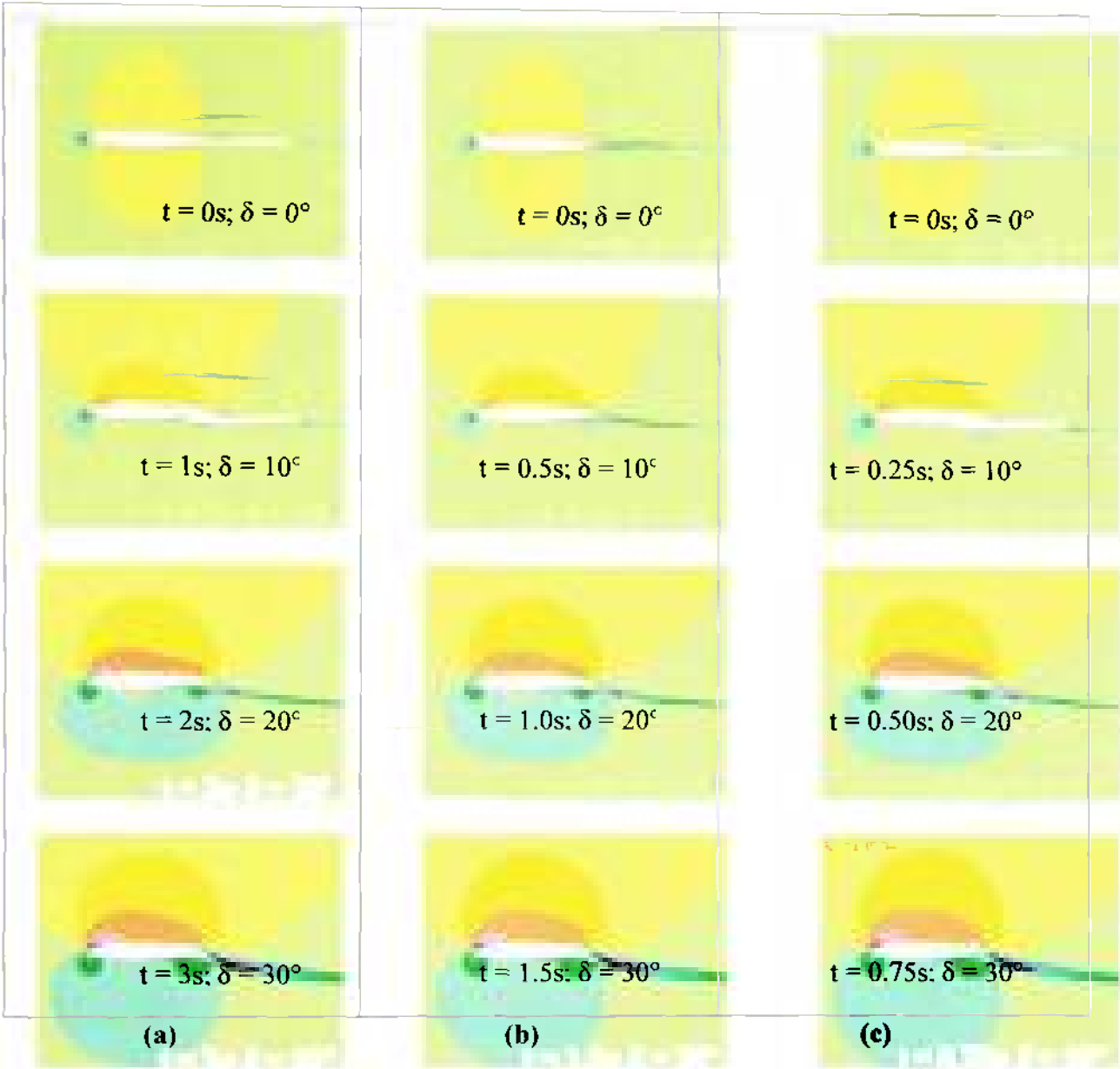
Figure 4.3: Plot of the relative velocity distribution in the vicinity of the airfoil during the process of flap deflection at (a) 10°/s, (b) 20°/s and (c) 40°/s

1 800
1 671
1 543
1 414
1 286
1 157
1 029
0 9000
0 7714
0 6429
0 5143
0 3857
0 2571
0 1286
0 0000

t = 0s; δ = 0°   t = 0s; δ = 0°   t = 0s; δ = 0°

t = 1s; δ = 10°   t = 0.5s; δ = 10°   t = 0.25s; δ = 10°

t = 2s; δ = 20°   t = 1.0s; δ = 20°   t = 0.50s; δ = 20°

t = 3s; δ = 30°   t = 1.5s; δ = 30°   t = 0.75s; δ = 30°

(a)   (b)   (c)
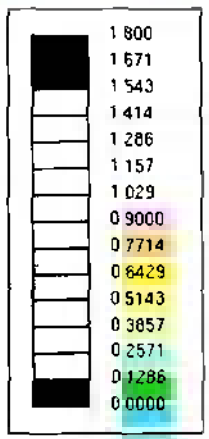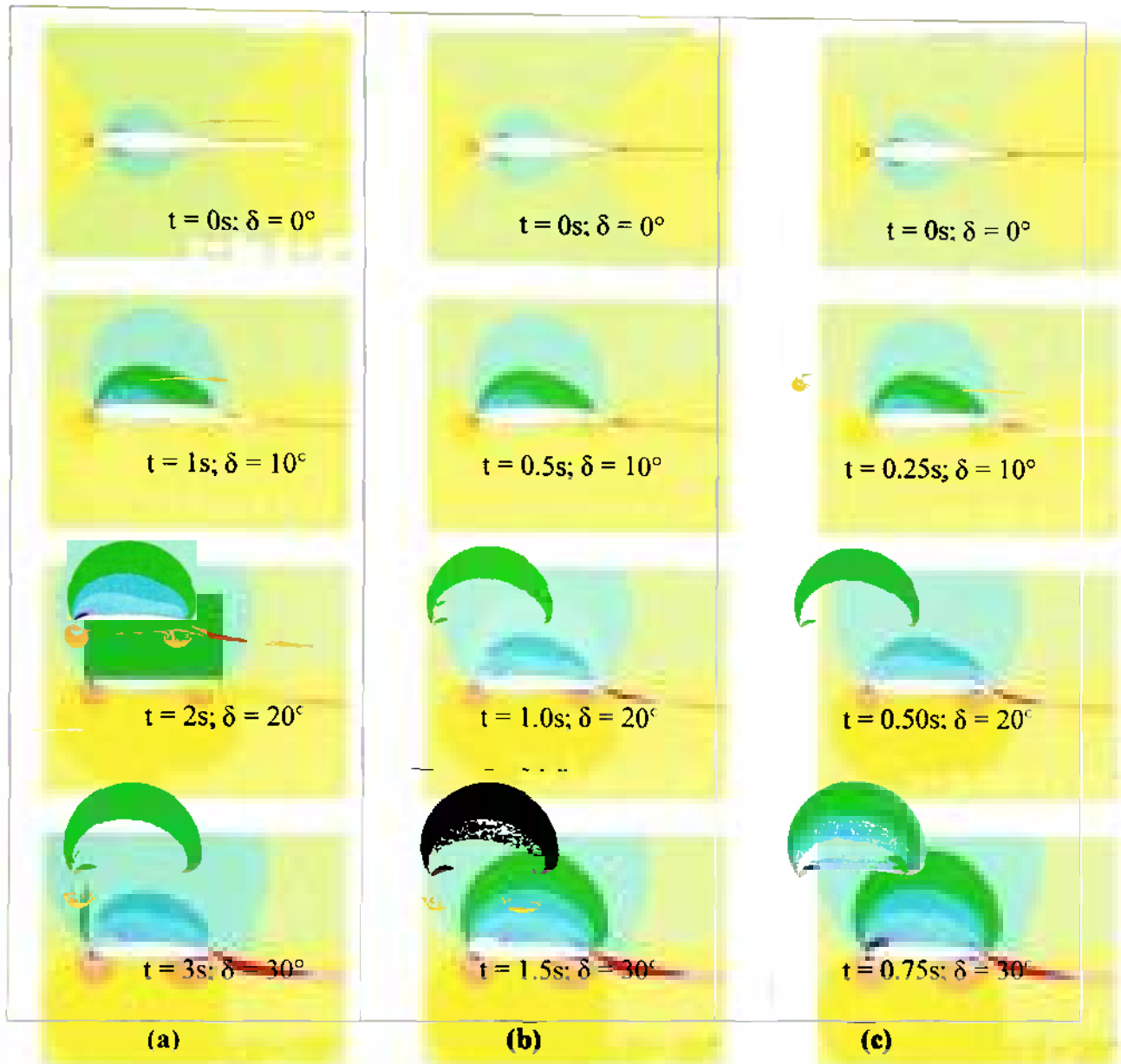
Figure 4.4: Plot of the pressure coefficient distribution in the vicinity of the airfoil during the process of flap deflection at (a) 10°/s, (b) 20°/s and (c) 40°/s

118
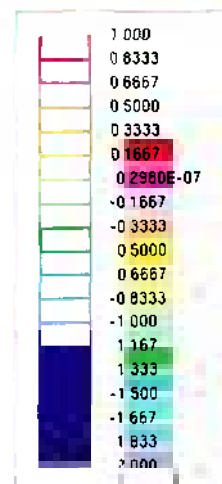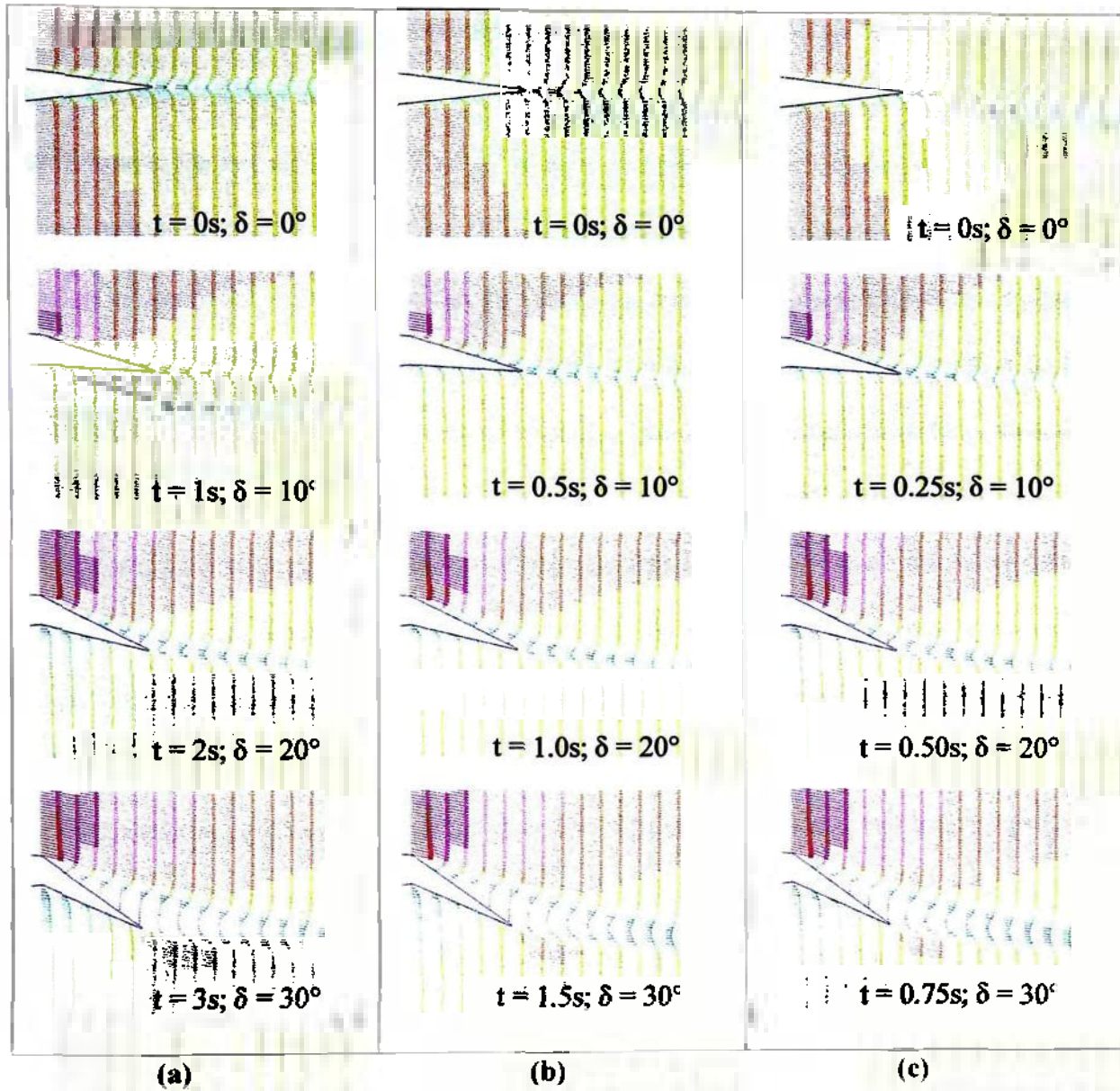
Figure 4.5: Plot of the normalized velocity vector distribution in the vicinity of the airfoil during the process of flap deflection at (a) 10°/s, (b) 20°/s and (c) 40°/s
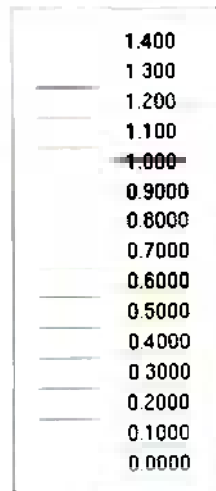
The plots in figure 4.3 (a) on page 117 show that the flowfield loses its symmetry once the plain trailing edge flap starts to deflect downwards. In fact, the velocity of the airflow over the top surface of the airfoil starts to increase, and the velocity of the airflow over the bottom surface starts to decrease. Furthermore, it is possible to observe that the region of increased velocity over the top surface of the airfoil grows downstream to the upstream edge of the flap. Over the bottom surface of the airfoil the airflow develops two isolated regions of substantially reduced velocity. One of them is the stagnation point at the leading edge, which slowly moves downstream along the bottom surface of the airfoil during flap deflection, and the other is at the upstream edge of the flap. It should also be noted that starting at a flap deflection angle of $\delta = 20°$ a region of low velocity starts to develop at the flaps trailing edge. It can be regarded as a separation bubble which grows during flap deflection and eventually covers the entire top surface of the trailing edge flap at the maximum deflection angle of $\delta = 30°$. Simultaneously, the separation bubble extends downstream beyond the trailing edge of the flap by about a quarter of the airfoil's chord. When comparing figures 4.3 (a) through (c), it turns out that no substantial qualitative differences exist between the three cases.

The plots in figure 4.4 (a) on page 118 correspond well to those in figure 4.3 (a). The pressure coefficient distribution also shows that the flow field starts to lose its symmetry once flap deflection commences. Generally speaking, the magnitude of the pressure distribution over the top surface decreases and increases over the bottom surface of the airfoil. This shows that the airfoil starts to create lift once the deflection process starts. More specifically, a region of lower pressure coefficient extends over the top surface starting at the leading edge of the airfoil and growing downstream to the upstream

120

edge of the flap. This is similar to the development of the relative velocity distribution in figure 4.3 (a). Starting at a flap deflection angle of $\delta = 20°$, the pressure coefficient distribution resolves two distinct regions of low values, one in the vicinity of the airfoil's leading edge and the other at the upstream edge of the flap. Over the bottom surface, one can observe an analogical development, whereas in this case the two regions contain high pressure. This also corresponds well to the results shown in figure 4.3 (a). Furthermore, the separation bubble mentioned in the previous paragraph is also well visible in figure 4.4 (a). It is marked by a region of high pressure that develops at the flap's trailing edge at a flap deflection angle of $\delta = 20°$ and grows upstream until it eventually covers the entire top surface of the flap. Finally, a comparison of the plots of figures 4.4 (a) through (c) again shows that no major differences exist between the flow fields of the three deflection cases.

The plots in figure 4.5 (a) are zoomed-in to the region around the plain trailing edge flap and visualize the development of the normalized velocity vector distribution during the flap deflection process. Just like the previous two results, the plots in figure 4.5 (a) also show the loss of symmetry in the flowfield and the increase and decrease of the velocity magnitudes over the top and bottom surface of the flap, respectively. Another similarity is the observation that at a flap deflection angle of $\delta = 20°$ the region of reduced velocity magnitude downstream of the flap's trailing edge starts to grow. Figures 4.5 (a) through (c), however, actually visualize that the velocity profile shows larger gradients within the separation bubble. The larger velocity gradients eventually cause the flow to recirculate at a deflection angle of $\delta = 30°$. This is indicated by small upstream oriented velocity vectors within the separation bubble in the last plot of figure 4.5 (a).

This recirculation zone, in turn, is an indicator for increased pressure drag as indicated in subsection 2.1.2 on page 12. Furthermore, a qualitative comparison of figures 4.5 (a) through (c) again shows that no major differences exist among the flowfields of the three cases.

4.1.2.2. Qualitative and Quantitative Comparison of the Results of Cases 4 and 5

Table 3.4 on page 97 shows that in cases 5 and 6 a flap deflection rate of 200°/s and 20°/s was chosen, respectively. In addition to qualitative results, this section also presents quantitative results. The former is presented in an identical manner as in the previous subsection, and the latter consists of four graphs that show the development of the section lift, drag and moment coefficient about the quarter chord, as well as the motion of the center of pressure. All four parameters are expressed in terms of the flap deflection angle, δ, in order to facilitate the comparison of the results from the 200°/s and 20°/s case.

Figures 4.6 (a) and (b) on the next page contain plots of the relative velocity distribution in the vicinity of the airfoil for the 200°/s and 20°/s cases, respectively. Figures 4.7 (a) and (b) show plots of the pressure coefficient distribution in the vicinity of the airfoil for the two cases. Finally, figures 4.8 (a) and (b) present the relative velocity distribution in the vicinity of the plain trailing edge flap in vector form. Figures 4.7 and 4.8 can be viewed on pages 124 and 125, respectively.

122

The colorbar values read (top to bottom): 1 800, 1 671, 1 543, 1 414, 1 286, 1 157, 1 029, 0 9000, 0 7714, 0 6429, 0 5143, 0 3857, 0 2571, 0 1286, 0 0000

Left column (a): t = 0s; δ = 0°; t = 0.05s; δ = 10°; t = 0.10s; δ = 20°; t = 0.15s; δ = 30°

Right column (b): t = 0s; δ = 0°; t = 0.5s; δ = 10°; t = 1.0s; δ = 20°; t = 1.5s; δ = 30°

(a)

(b)
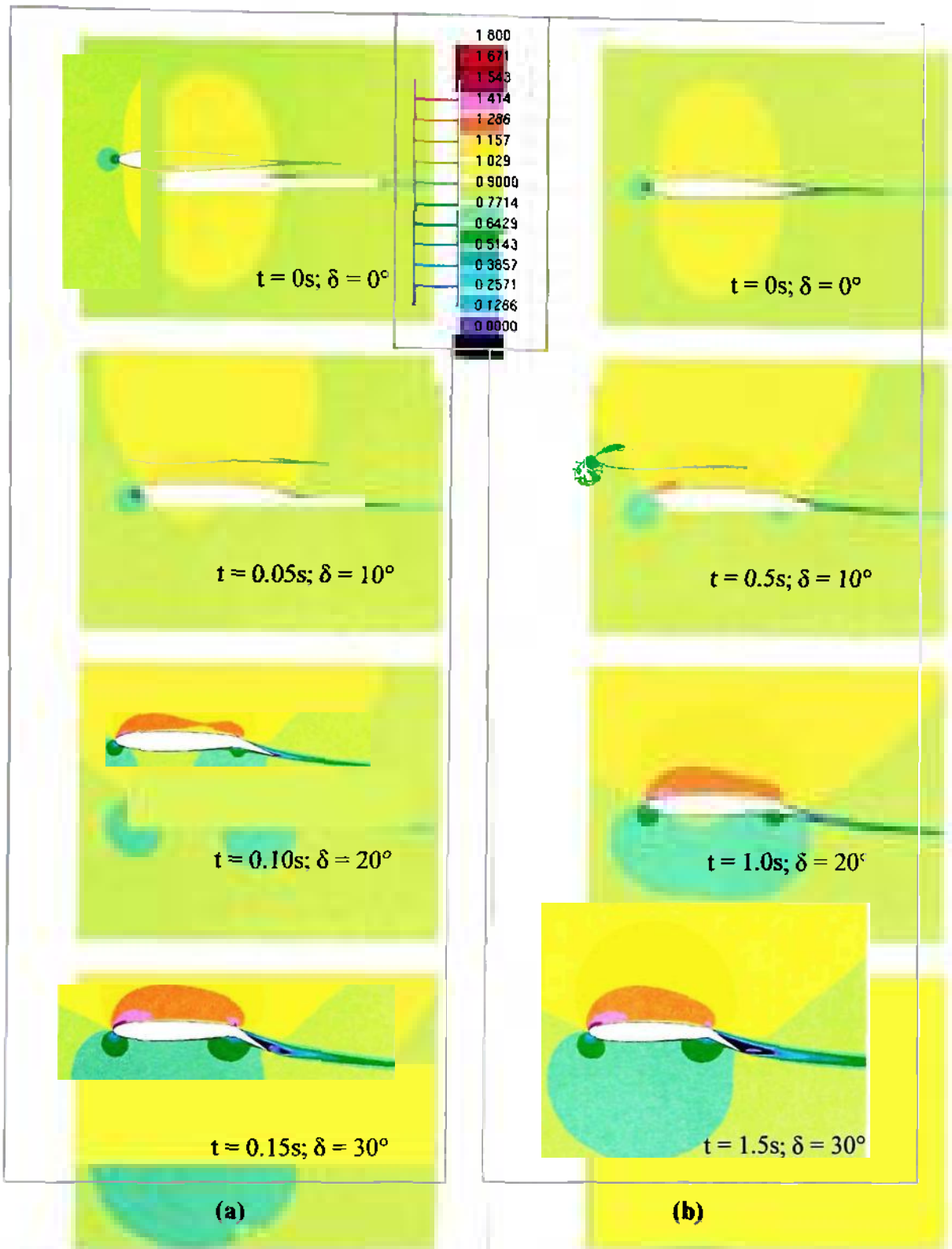
Figure 4.6: Plot of the relative velocity distribution in the vicinity of the airfoil during the process of flap deflection at (a) 200°/s and (b) 20°/s
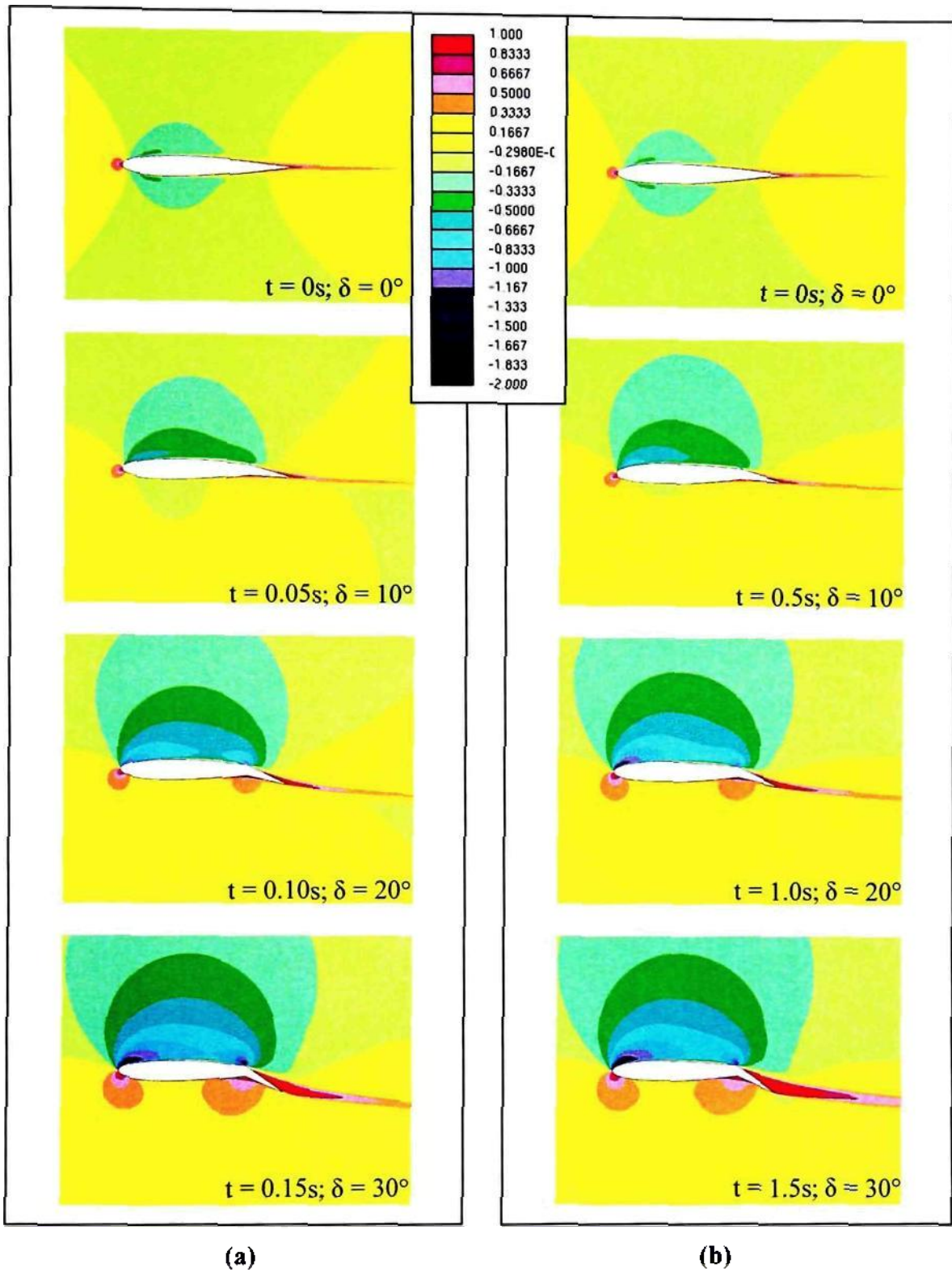
Figure 4.7: Plot of the pressure coefficient distribution in the vicinity of the airfoil during the process of flap deflection at (a) 200°/s and (b) 20°/s
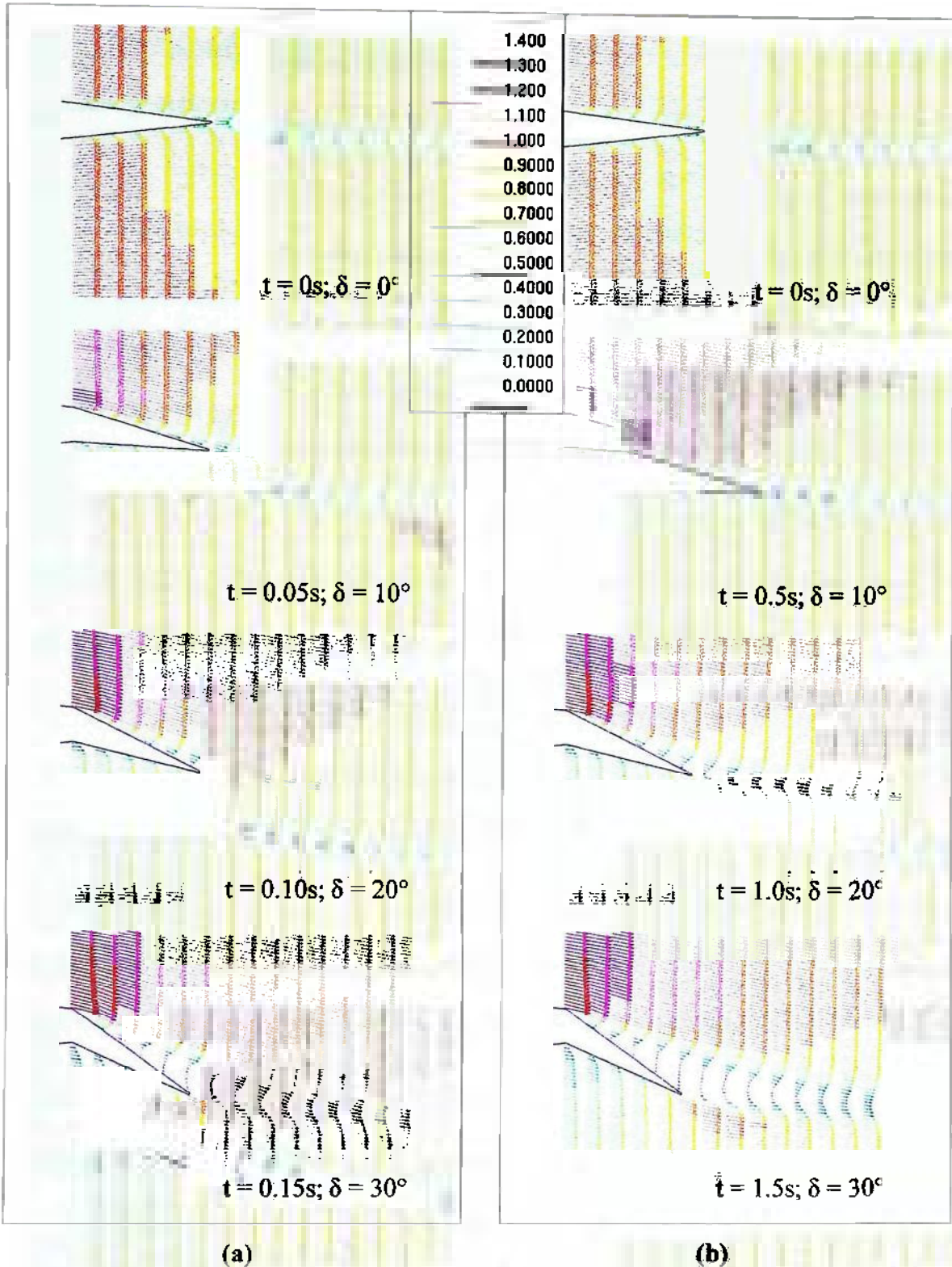
Figure 4.8: Plot of the normalized velocity vector distribution in the vicinity of the trailing edge flap during the process of flap deflection at (a) 200°/s and (b) 20°/s

125

The plots in figures 4.6 (a) and (b) on page 123 show a similar development of the flowfield as seen in figures 4.3 through 4.5, which is expected because except for the runtime case 5 presented in figure 4.6 (b) and case 2 presented in figure 4.3 (b) are practically the same. Therefore, emphasis is put on the comparison of the respective plots in parts (a) and (b) of figure 4.6. When comparing the development of the relative velocity distribution during the flap deflection process, it turns out that the development in the 200°/s case seems to lag behind its counterpart in the 20°/s case. For instance, at a deflection angle of δ = 20°, the two regions with a relative velocity of at least 1.286 barely connect with each other in figure (a). In figure (b), on the other hand, these two regions have already merged into a single region. Furthermore, at a deflection angle of δ = 30° the separation zone in figure (a) is not as well developed as in figure (b).

The same general observations can be made in terms of the pressure coefficient distribution and the normalized velocity vector distribution in figures 4.7 and 4.8 on pages 124 and 125, respectively. In addition, figure 4.8 (a) shows that at a flap deflection angle of δ = 30°, the velocity profile within the separation region on the top surface of the flap has larger gradients as its counterpart in figure 4.8 (b). Overall, it is observable that the recirculation zone in the bottom plot of figure 4.8 (a) is more compact, but stronger in comparison to the one in the bottom plot of figure 4.8 (b).

After having shown and described the qualitative results of cases 4 and 5, the quantitative results are presented. These are based on an output file that was produced by the *Post_2_Quantitative.inp* script which is described in subsection 3.1.3. on page 99. The output file for cases 4 and 5 were named *center_of_pressure_location_0_30_ in_200.txt* and *center_of_pressure_location_0_30_in_20.txt*, respectively, and are both

126

shown in appendix B. These output files contain two sets of virtual vertices, whose x-, y- and z-coordinate represent the time, force and moment about the leading edge due to the force, respectively. Furthermore, the first vertex set represents data for the lift, and the second vertex set contains the drag data for the airfoil. Note that all numbers are given in SI-units.

In order to present the results from the output file as graphs of the force and moment coefficients as functions of the flap deflection angle, further calculations needed to be accomplished. The lift and drag coefficients of the airfoil, c_l and c_d, were calculated using the following equations:

$$c_l = \frac{L}{\frac{1}{2}\rho_\infty V_\infty^2 S}$$
[4.1]

$$c_d = \frac{D}{\frac{1}{2}\infty_\infty V_\infty^2 S}$$
[4.2]

In equations 4.1 and 4.2, ρ_∞ and V_∞ are the freestream density and velocity and amount to 1.205 kg/m³ and 100 m/s, respectively. Furthermore, L and D are the lift and drag force of the wing section, respectively. S is the planform area, which is the product of the airfoil's chord, c, and its span, s. The chord of the airfoil effectively changes due to the deflection of the flap, so that equation 4.3 below was used for its calculation:

$$c = \sqrt{\lceil(0.75m)+(0.25m)\cos\delta\rceil^2 + \lceil(0.25m)\sin\delta\rceil^2}$$
[4.3]

127

In equation 4.3 on the previous page, 0.75 m represents the chord of the wing without the flap, and the 0.25 m represents the chord of the flap For a clarification of the rationale behind equation 4.3, refer to figure 4.9 below.
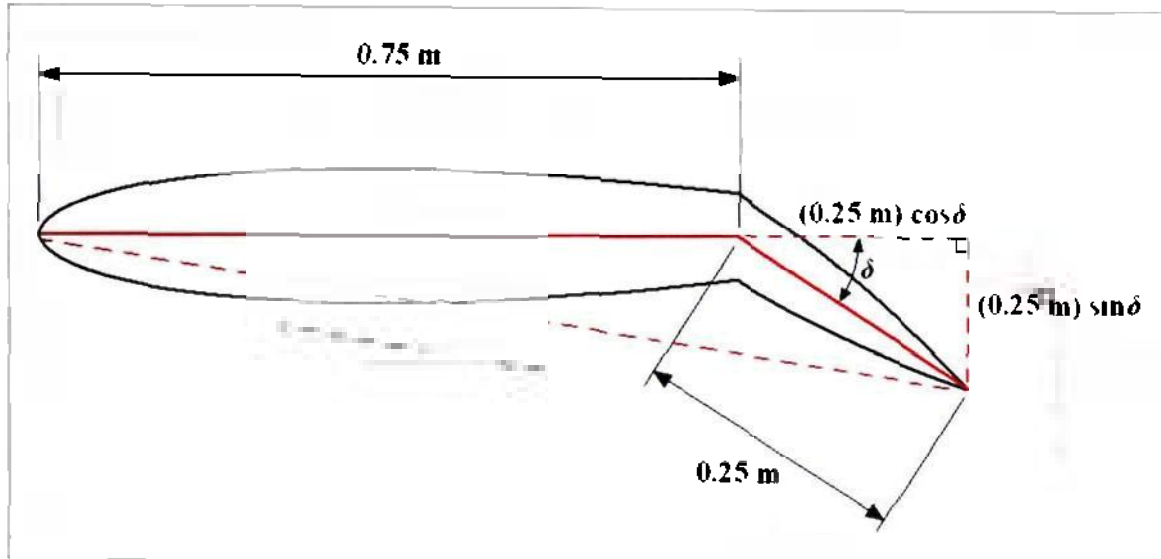
Figure 4.9: Sketch of the airfoil and its chord during flap deflection

As mentioned above, the airfoil's span, s, is necessary for the computation of the lift and drag coefficients. Under normal circumstances, an airfoil is 2D only. However, STAR-CD requires a computational domain that is at least one cell layer thick [11], so that the 2D mesh was extruded by 0.05 m as described in subsection 2.3.3.4. on page 67. This, in turn, means that the span of the airfoil in equations 4 1 and 4.2 amounts to s = 0.05 m

The moment coefficient about the quarter chord was calculated by equation 4.4 shown at the top of the next page, which is based on equation 2 4 in subsection 2.1.2. on page 12:

$$c_{m,c/4} = \frac{-M_{LE} + c/4\,L}{\frac{1}{2}\rho_x V_x^2 Sc}$$

[4.4]

In equation 4.4, M_{LE} is the sum of the moments in the first and the second vertex set, so that the effect of both the lift and the drag is accounted for.

Finally, the location of the center of pressure has been computed by dividing the moment due to lift about the leading edge by the lift force. This gives the horizontal distance of the center of pressure from the leading edge of the airfoil. Subsequently, the result was divided by the cord, c, in order to non-dimensionalize this value. Equation 4.5 below summarizes the steps taken to compute the relative location of the center of pressure with respect to the leading edge, x_{cp}/c:

$$\frac{x_{cp}}{c} = \frac{M}{Lc}$$

[4.5]

Now, that all calculations have been clarified, the results for the quantitative analysis of cases 4 and 5 are presented. Figures 4.10 (a) through (d) on the next two pages show graphs of the lift, drag, and moment coefficients about the quarter chord, as well as the relative position of the center of pressure, as functions of the flap deflection angle during the flap deflection process. Note that all graphs contain two curves, one for case 4 and the other for case 5.

(a)

(b)

(c)

130
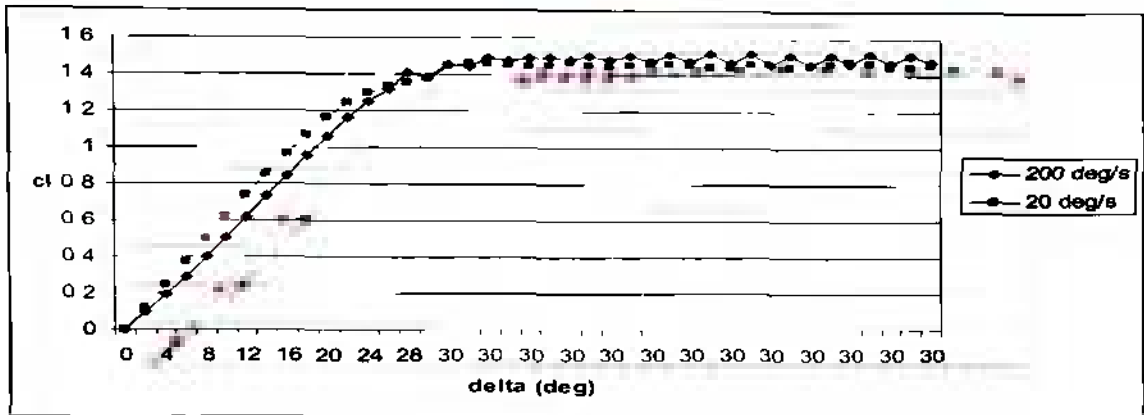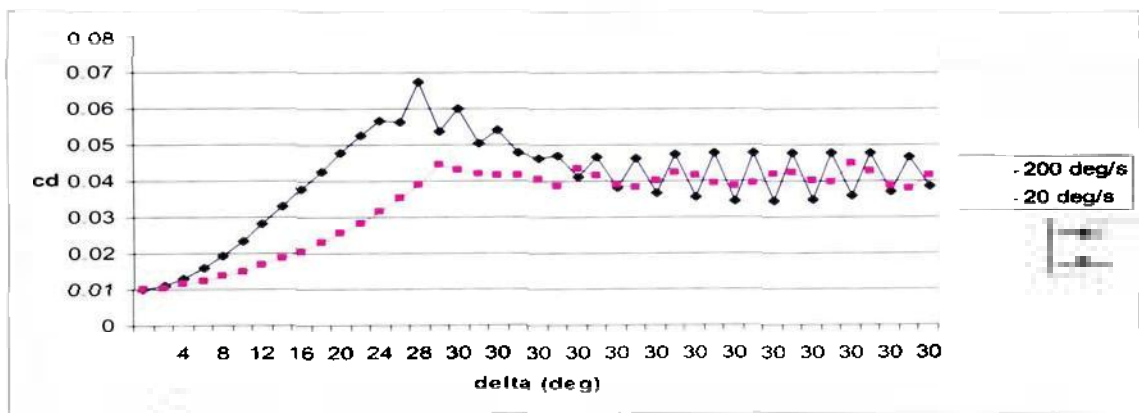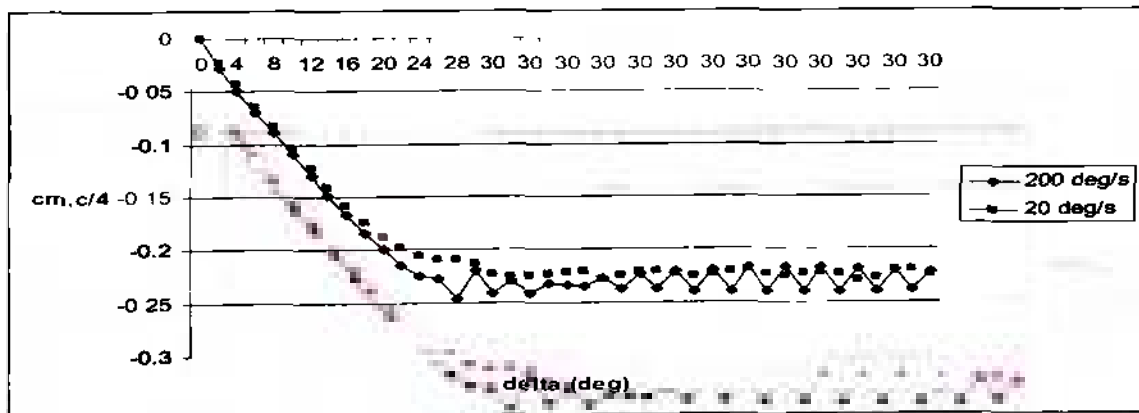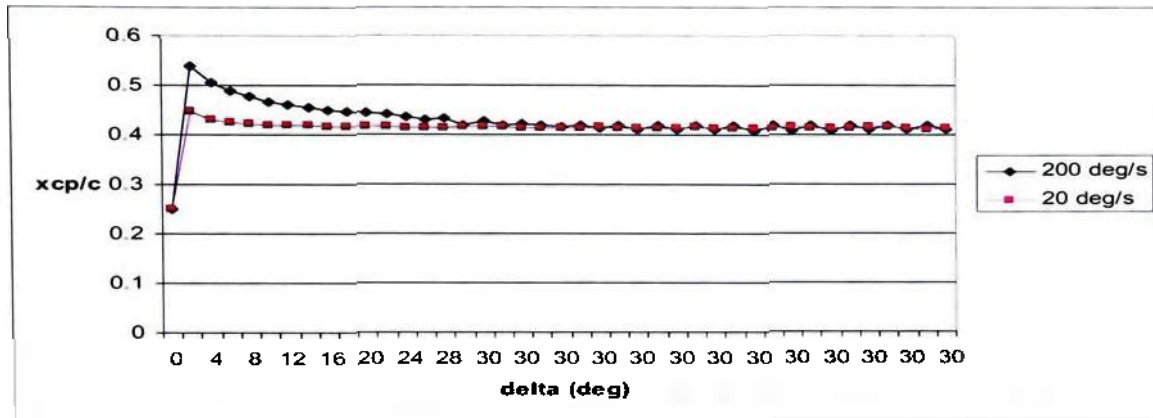
(d)

Figure 4.10: Graphs of the section (a) lift coefficient c_l, (b) drag coefficient c_d, and (c) moment coefficient about the quarter chord $c_{m,c/4}$, as well as of the (d) relative location of the center of pressure x_{cp}/c, as functions of the flap deflection angle δ

Figure 4.10 (a) shows that in both cases the section lift coefficient increases during the process of flap deflection. More specifically, it can be observed that in the case of a flap deflection rate of 200°/s, the section lift coefficient initially increases at a slightly slower rate than in the case of a deflection rate of 20°/s. This causes the section lift coefficient curve in the 200°/s case to lag behind the one in the 20°/s case by a flap deflection angle of about 2° Ultimately, the section lift coefficient in the 200°/s case overtakes its counterpart from the 20°/s case as the flap deflection angle approaches 30° and both curves start to level off The steady-state values for both curves indicate that in the 200°/s case the airfoil produces slightly more lift than in the 20° s case More specifically, the final lift coefficient for the 200°/s case is $c_l \approx 1.50$, and the respective value for the 10°/s case is $c_l \approx 1.45$.

131

Figure 4.10 (b) shows the section drag coefficient curves which indicate that in the 200°/s case the drag increases at a much faster rate and reaches a much higher maximum value than in the 20°/s case. In fact, the trend line indicates that the maximum value for the section drag coefficient in the 200°/s case is $c_d \approx 0.056$. In the 20°/s case the drag coefficient reaches a maximum value of $c_d \approx 0.043$. Furthermore, in the 200°/s case this maximum section drag coefficient is already reached at a flap deflection angle of 28°. In the 20°/s case this maximum section drag coefficient is reached a little later into the flap deflection process at $\delta = 29°$. After the flap has been deflected to 30° for a while, the section drag coefficient in both cases tends to approach a steady-state value of $c_d \approx 0.04$, and the oscillations about this value is greater in the 200°/s case than in the 20°/s case.

The development of the section moment coefficient about the quarter chord for both cases 4 and 5 is depicted in figure 4.10 (c). The section moment coefficient for the 200°/s case initially decreases at a slightly smaller rate than its counterpart in the 20°/s case. As the flap deflection angle approaches 30°, the section moment coefficient in the 200°/s case decreases further than its counterpart in the 20°/s case, and subsequently both values level off at steady-state values, which amount to about -0.2 and -0.225 for the 20°/s and 200°/s case, respectively. Overall, it is legitimate to say that the section moment coefficients behave similarly to the section lift coefficients, whereas the trends are in opposite directions. Also note that the section moment coefficient about the quarter chord is always negative in both cases, which by convention indicates that the airfoil experiences a greater nose-down pitching moment as the flap deflects.

Finally, figure 4.10 (d) shows the relative movement of the center of pressure during flap deflection. It is interesting to note that in both cases the center of pressure

132

moves aft of its initial position immediately after the flap deflection process started and then slowly moves towards the leading edge of the airfoil. As a reminder, it was mentioned in subsection 2.1.2. on page 13 that the center of pressure for a symmetric airfoil at zero angle of attack and with no flap deflection is located at the quarter chord. In the 200°/s case, the center of pressure moves aft to 54% of the chord immediately after the flap deflection process started and then proceeds towards the leading edge of the airfoil in order to reach its final position at about 41.5% of the chord at a flap deflection angle of 30°. The center of pressure in the 20°/s case behaves similarly. It initially moves aft to only 45% of the chord, which is less than in the 200°/s case. Its steady-state location at a deflection angle of 30°, however, is the same as in the 200°/s case, that is to say 42% of the chord.

In summary, this quantitative analysis showed that in the 200°/s case the increase in lift and nose-down pitching moment about the quarter chord is slightly delayed as compared to the 20°/s case. Also, in the 200°/s case the drag production is higher and the movement of the center of pressure is greater during the process of flap deflection. On the other hand, the steady-state values for each of the stability and control parameters seem to be similar in both cases 2 and 5.

4.1.2.3. Quantitative Comparison of the Results of Cases 6 and 7

This subsection presents the results from cases 6 and 7, which consist of two full flap deflection and retraction cycles at 200°/s and 20°/s, respectively. This quantitative analysis has been conducted in an identical way as in the previous two cases, and the results are based on the two output files *center_of_pressure_ location_200_2_cycle.txt*

and *center_of_pressure_location_20_2_cycle.txt*, both of which can be viewed in appendix B. Figures 4.11 (a) through (d) below show graphs of the section lift, drag, and moment coefficient about the quarter chord, as well as the relative position of the center of pressure as functions of the flap deflection angle during two full flap deflection and retraction cycles.
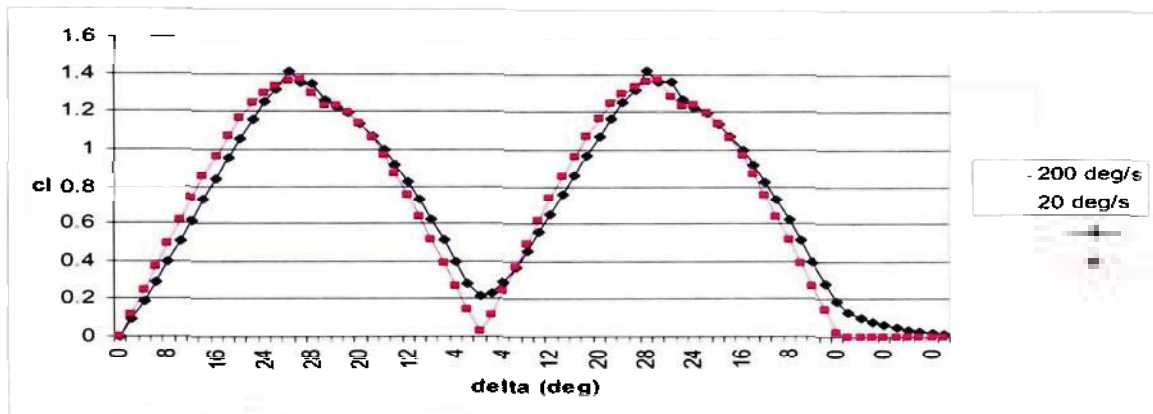
(a)
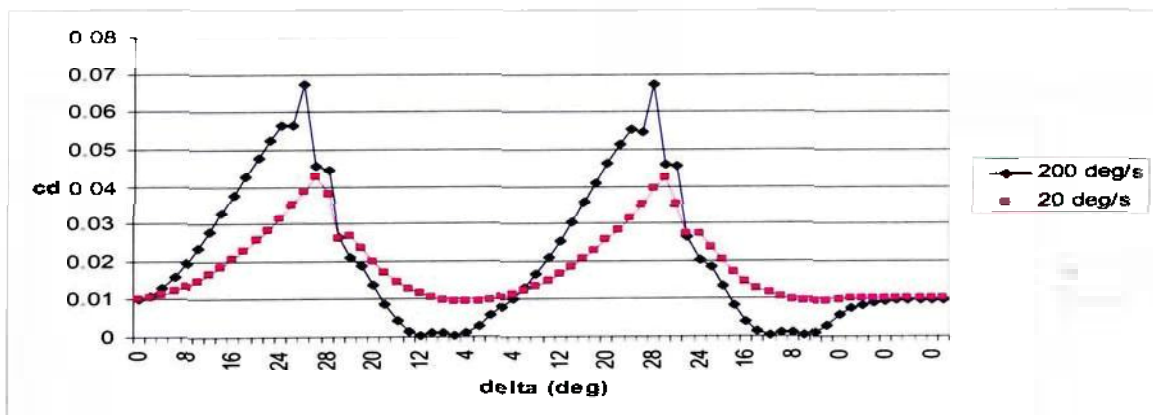
(b)
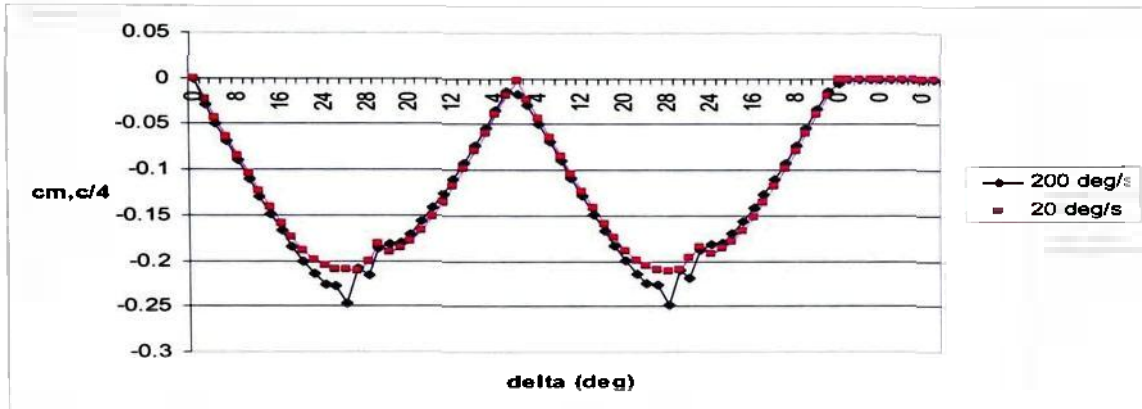
(c)
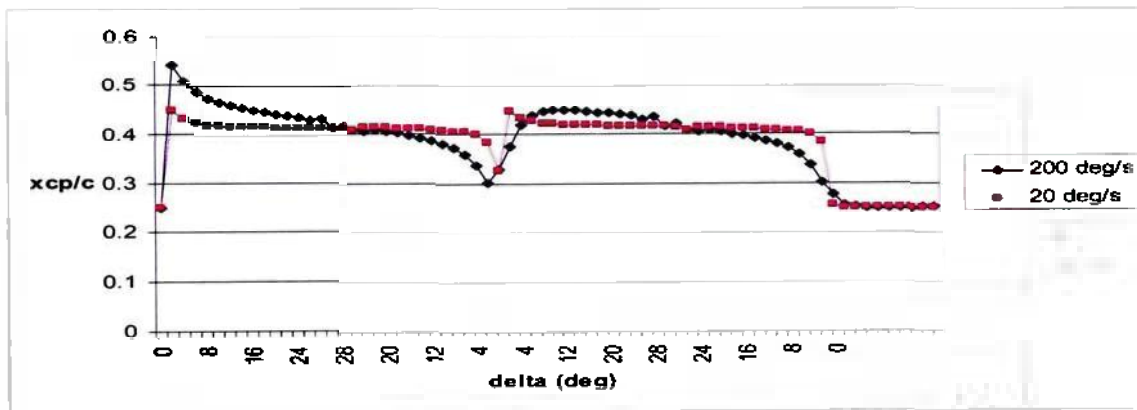
(d)

Figure 4.11: Graphs of the section (a) lift coefficient c_l, (b) drag coefficient c_d, and (c) moment coefficient about the quarter chord $c_{m,c/4}$, as well as of the (d) relative location of the center of pressure x_{cp}/c, as functions of the flap deflection angle δ during two full flap deflection and retraction cycles

Figure 4.11 (a) shows a similar behavior of the section lift coefficient during the flap deflection process as figure 4.10 (a). Furthermore, during the flap retraction process the section lift coefficient for the 200°/s case continues to lag behind its counterpart for the 20°/s case because in the former case the section lift coefficient decreases at a slower

135

rate than in the latter case. In fact, this causes the section lift coefficient in the 200°/s case to fail to return to its initial value of zero as the flap returns to a deflection angle of $\delta = 0°$ after the first full flap deflection and retraction cycle. The second cycle looks identical to the first with the slight difference that the section lift coefficient for the 200°/s case does return to zero after a few more time steps past the end of the second cycle.

The development of the section drag coefficient during flap deflection for cases 6 and 7, which is depicted in figure 4.11 (b), shows many similarities to its counterpart in cases 4 and 5, which are depicted in figure 4.10 (b). During the flap retraction process, on the other hand, the section drag coefficients for the 200°/s and the 20°/s case behave quite differently. In the former case, the section drag coefficient drops much more quickly from its maximum value of 0.68 and drops well below its initial value of 0.01 to about 0. This means, that as the flap retracts and approaches a deflection angle of $\delta = 0°$, the airfoil produces less drag than it would at a zero flap deflection angle. In fact, between a flap deflection angle of about 12° and 0°, the airfoil produces close to zero drag. The second flap deflection and retraction cycle shows an identical development of the section drag coefficient with the difference that in this case it does return to its initial value a few time steps after the end of the flap deflection and retraction process.

Figure 4.11 (c) shows the development of the section moment coefficient during two full flap deflection and retraction cycles. Overall, it shows characteristics which are analogous to those of the development of the section lift coefficient in figure 4.11 (a), whereas the trend goes in the opposite direction. Furthermore, the curves for the 200°/s and the 20°/s case are very close to each other just like in figure 4.10 (c).

Finally, figure 4.11 (d) traces the movement of the center of pressure in both cases 6 and 7. The curves for the flap deflection process in the first cycle are very similar to their counterparts in cases 4 and 5. Furthermore, during the flap retraction process of the first cycle, the center of pressure keeps moving towards the leading edge of the airfoil. This happens at a faster pace in the 200°/s case than in the 20°/s case. This continues until the flap is fully retracted and the center of pressure has reached a distance to the leading edge of 30% and 33% of the chord in cases 6 and 7, respectively. In the second flap deflection and retraction cycle, the center of pressure undergoes a similar motion. It should be noted, however, that in the 200°/s case it does not reach the maximum distance to the leading edge of 54% of the chord in the previous cycle. Furthermore, after the second cycle has been completed, the center of pressure returns to its initial location at the quarter chord in both cases 6 and 7. In addition, the location of the center of pressure in the 20°/s case varies less than in the 200°/s case.

In summary, the quantitative analysis of cases 6 and 7 showed similar results as the quantitative analysis for cases 4 and 5. For instance, these cases showed again that the development of the section lift and moment coefficient is delayed in the 200°/s case as compared to the 20°/s case. Furthermore, in case 6 much more drag was produced during the flap deflection process. During the last part of the flap retraction process, however, the airfoil experienced no drag. Finally, the center of pressure in the 20°/s case travels less than in the 200°/s case.

4.1.3. Comparison of 2D Results with Theoretical, Experimental and Empirical Data

This subsection has the primary purpose of comparing the results of the 2D analysis with suitable theoretical, experimental and empirical data from the literature in order to show the validity of the results from this analysis and to evaluate the success of this methodology.

4.1.3.1. Comparison of 2D Results with Theoretical Data

Subsection 2.1.2. starting on page 10 explains several effects of the deflection of a plain flap on the aerodynamic characteristics of an airfoil. One such effect is the increase of the section lift coefficient, which agrees well with the respective results from the 2D analysis shown in figures 4.10 (a) and 4.11 (a). These figures clearly show that the section lift coefficient increases substantially as the flap deflection angle increases. Furthermore, the 2D analysis correctly finds that at a flap deflection angle of $\delta = 0°$, the symmetric airfoil does not produce any lift.

Furthermore, on page 12 of subsection 2.1.2. it was mentioned that flap deflection increases both components of parasite drag: the skin friction and the pressure drag. Figures 4.10 (b) and 4.11 (b) both show that a substantial increase of the parasite drag is indeed noticeable. Furthermore, figures 4.6 and 4.7 show that a separation bubble starts to form over the top surface of the trailing edge flap at a deflection angle of $\delta = 20°$. This indicates that the pressure drag as explained in [3] does not start to contribute to parasite drag until the last third of the flap deflection process. Therefore, this implies that the 2D analysis does account for both components of the parasite drag.

Subsection 2.1.2 also states that the nose-down pitching moment experienced by the airfoil increases and that the center of pressure moves aft of its initial position at the quarter chord during flap deflection. Both of these phenomena were also observed in the quantitative results of the 2D analysis. Both figures 4.10 (c) and 4.11 (c) showed that the nose-down pitching moment indeed does increase. Furthermore, figure 4.10 (d) shows that throughout the flap deflection process the center of pressure is located aft of its initial position, and figure 4.11 (d) indicates that the center of pressure remains aft of its initial position even during flap retraction. However, it is surprising that while located aft of the quarter chord, the center of pressure slightly moves forward during the two full deflection and retraction processes.

4.1.3.2. Comparison of 2D Results with Experimental Data

A search for experimental data for a comparison with the results of the 2D analysis proved difficult because of the specific nature of this analysis. For example, [8] does contain experimental data for the NACA 0012 airfoil. However, none of it deals with the deflection of a plain trailing edge flap, so that only the initial condition of the simulation could be compared to its experimental counterpart. The initial condition in this case refers to the airfoil at zero angle of attack and with a flap deflection angle of $\delta = 0°$. In [8], experimental data for the section lift, drag and moment coefficient about the quarter chord for the NACA 0012 airfoil is presented. It indicates that both the lift and the moment coefficient about the quarter chord are zero at a zero angle of attack and at a flap deflection angle of $\delta = 0°$. Furthermore, the drag coefficient is indicated to be 0.01 for a Reynolds number of $Re = 6.0 \cdot 10^6$ and a standard surface roughness.

These experimental numbers all agree well with the results of the 2D analysis because it showed that the airfoil indeed produces zero lift and does not experience any pitching moment at a flap deflection angle of $\delta = 0°$. In addition, under these conditions the airfoil produces a section drag coefficient of $c_d \approx 0.01$. The proof that the 2D analysis is run at a Reynolds number of about $6.0 \cdot 10^6$ is given by the following calculation based on the definition of the Reynolds number in equation 4.6:

$$Re = \frac{\rho_x V_x c}{\mu_x}$$ [4.6]

$$Re = \frac{\left(1.205 \, ^{kg}\!\big/\!_{m^3}\right)\!\left(100 \, ^{m}\!\big/\!_{s}\right)\!\left(1m\right)}{\left(1.82 \cdot 10^{-5} \, ^{Ns}\!\big/\!_{m^2}\right)}$$

$$\boxed{Re = 6.62 \cdot 10^6}$$

The comparison of the results of the 2D analysis with experimental data is summarized in table 4.1 below.

Table 4.1: Comparison of the results from the 2D analysis with experimental data found in Theory of Wing Sections

Parameter	2D Analysis	Experimental
c_l	0	0
c_m	0	0
c_d	0.01	0.01

140

4.1.3.3. Comparison of 2D Results with Empirical Data

The empirical data that was used in this comparison originates from [9]. More specifically, a purely empirical expression was found in that reference that defines the lift increment due to flap deflection in terms of the wing's lift-curve slope and the relative chord of the flap. This expression is shown as equation 16.17 on page 491 of [9], and is presented below as equation 4.7. This empirical expression is designed for the estimation of the efficiency of a plain trailing edge flap on a finite 3D wing.

$$\frac{1}{C_{L_\alpha}}\frac{\partial C_L}{\partial \delta_f} = 1.576\left(\frac{c_f}{c}\right)^3 - 3.458\left(\frac{c_f}{c}\right)^2 + 2.882\left(\frac{c_f}{c}\right)$$ [4.7]

In equation 4.7, C_{L_α} is the wing's lift-curve slope, $\dfrac{\partial C_L}{\partial \delta_f}$ is the lift increment due to flap deflection and c_f/c is the relative chord of the flap. For the purpose of this comparison, equation 4.7 was solved for the lift increment due to flap deflection, and the wing parameters were replaced by airfoil parameters. This resulted in equation 4.8 below:

$$\frac{\partial c_l}{\partial \delta_f} = c_{l_\alpha}\left[1.576\left[\frac{c_f}{c}\right]^3 - 3.458\left[\frac{c_f}{c}\right]^2 + 2.882\left[\frac{c_f}{c}\right]\right]$$ [4.8]

The airfoil lift curve slope was chosen to be $c_{l_\alpha} = 2\pi$ according to equation 2.2. on page 8. Furthermore, the ratio of the flap chord to the airfoil chord equals 0.25. This led to the result that $\dfrac{\partial c_l}{\partial \delta_f} = 3.32/rad$. Due to the fact that this empirical result takes into account

141

3D effects such as downwash and induced angle of attack, which were both explained in subsection 2.1.3. on page 14, it should be kept in mind that the true value for the lift increment due to flap deflection should be higher than the one computed with equation 4.8.

For the 2D analysis, the lift increment is simply plotted as a function of the flap deflection angle in figures 4.10 (a) and 4.11 (a). In order to compare it to the value computed with equation 4.8, the slope of the nearly linear part of the section lift coefficient curve of the 20°/s case was computed.

$$\frac{\partial c_l}{\partial \delta_f} \partial \frac{\partial c_l}{\partial \delta_f} \tag{4.9}$$

$$\frac{\partial c_l}{\partial \delta_f} \partial \frac{1.07}{0.314 \text{rad}}$$

$$\boxed{\frac{\partial c_l}{\partial \delta_f} \partial \frac{3.41}{\text{rad}}}$$

As shown in the above calculation the lift increment in this 2D analysis amounts to 3.41/rad, which results in an error of 2.71% as compared to the empirical value of 3.32/rad. This %-error is rather small, and the fact that the value from the 2D analysis is slightly greater than the empirical value corresponds well to the fact that the empirical result is based on the assumption that the wing is 3D and finite.

Furthermore, [9] contains another empirical result for the location of the center of pressure for a lift increment due to flaps. This data is actually taken from the results of the United States Air Force Digital Datcom, a software that computes stability and

control derivatives for a given airplane geometry. Furthermore, this data is presented in the form of a graph in figure 16.9 on page 493 of [9], which plots the relative location of the center of pressure as a function of the flap-chord ratio. The relative location of the center of pressure in this case is calculated with respect to the mean aerodynamic chord MAC. This, however, does not affect the applicability of this data because the MAC in the 2D analysis is unity because the 2D wing does not have any sweep or taper. So, for a flap-chord ratio of 0.25, the curve for the plain flap in figure 16.9 indicates a relative location of the center of pressure of about 42.6% of the airfoil's chord. This compares well to the average value for the relative location of the center of pressure in the 2D analysis, which amounts to about 41.5% of the airfoil's chord, as indicated in subsection 4.1.2.2. on page 133.

4.2. Results of the 3D Analysis

In this subsection, the results are presented in a similar manner as in the previous subsection. First, the 3D steady-state results are presented, and it is shown that this solution is indeed converged. Then, the 3D transient solution is presented in order to show the effects of flap deflection on the different components of the aircraft, which is done in a similar manner as in the 2D transient analysis by tracing the development of the stability and control characteristics during the flap deflection process.

4.2.1. Results of the 3D Steady-State Analysis

Just like in the 2D case, the degree to which the steady-state solution is converged is assessed before the actual result is presented. Furthermore, the same stability criteria as

in the 2D analysis were applied to the 3D analysis. Subsection 3.2.1. on page 104 stated that the 3D steady-state solution is considered converged if the dependent variables in the monitoring cell approach a steady-state value or if they do not vary more the 5%. In addition, it was stated that the residuals should be on the order of 10^{-2} to 10^{-3} in order to fulfill the stability criterion for a converged steady-state solution.

Figures 4.12 (a) through (e) below show the monitoring values for the velocity components U, V, W, the static pressure P and the temperature T as functions of the iteration number, respectively. Furthermore, figures 4.12 (f) and (g) show plots of the residual values for the dependent variables just mentioned, as well as for the mass flow, turbulent kinetic energy and its dissipation rate as functions of the iteration number. Just like in the 2D case, the monitoring cell is located close to the leading edge of the aircraft's wing, where the steady-state solution is assumed to approach convergence rather slowly.

(a)

144
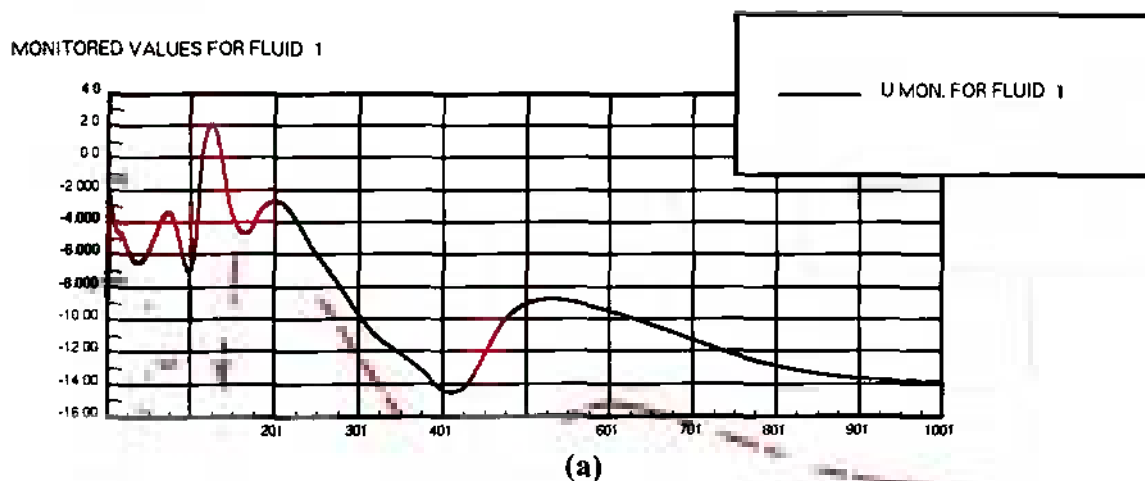
MONITORED VALUES FOR FLUID 1

(b)
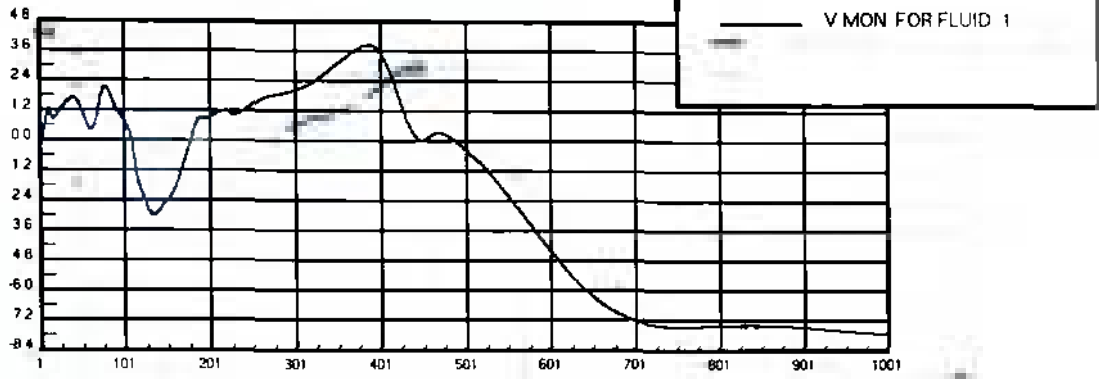
MONITORED VALUES FOR FLUID 1
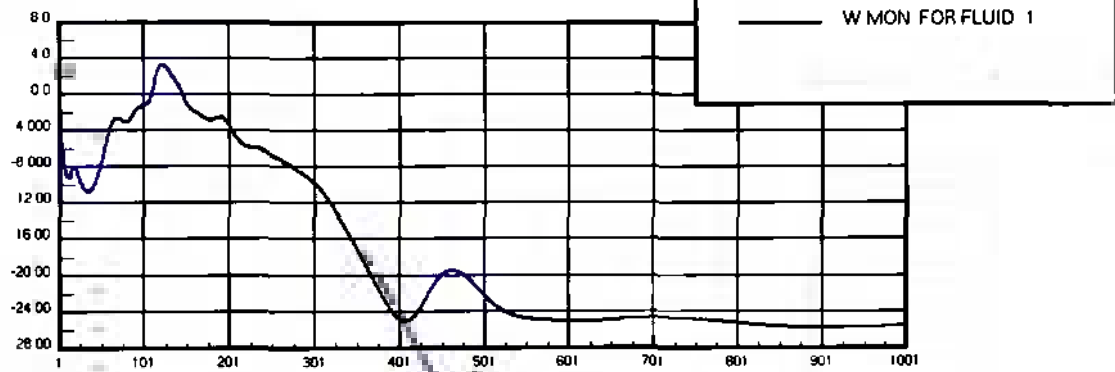
(c)

MONITORED VALUES FOR FLUID 1

(d)

145

(e)

(f)

(g)
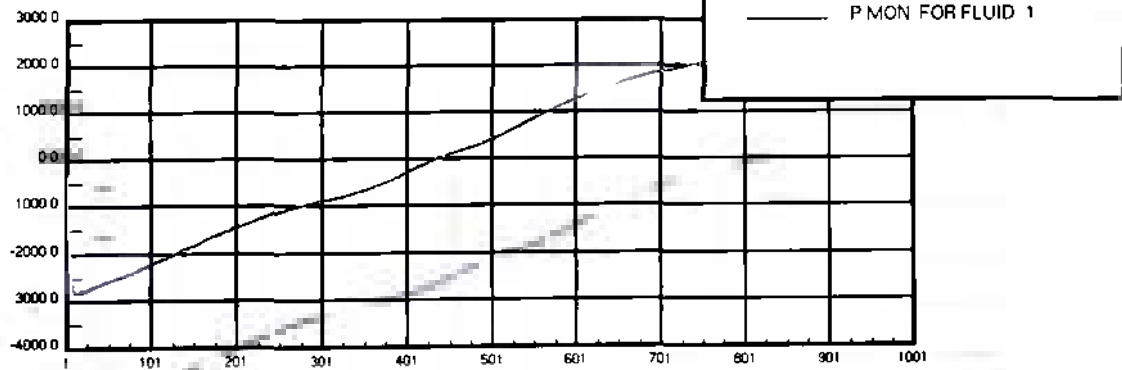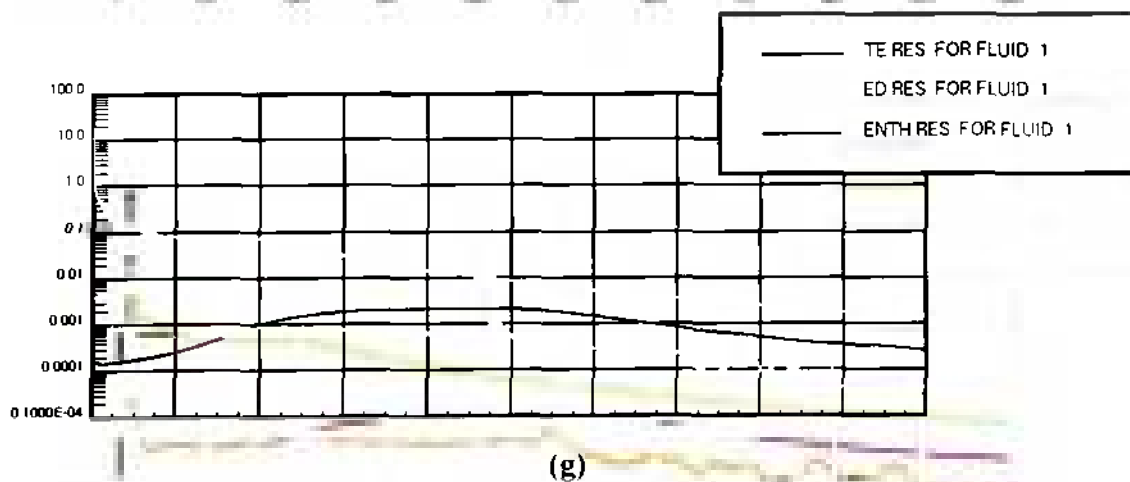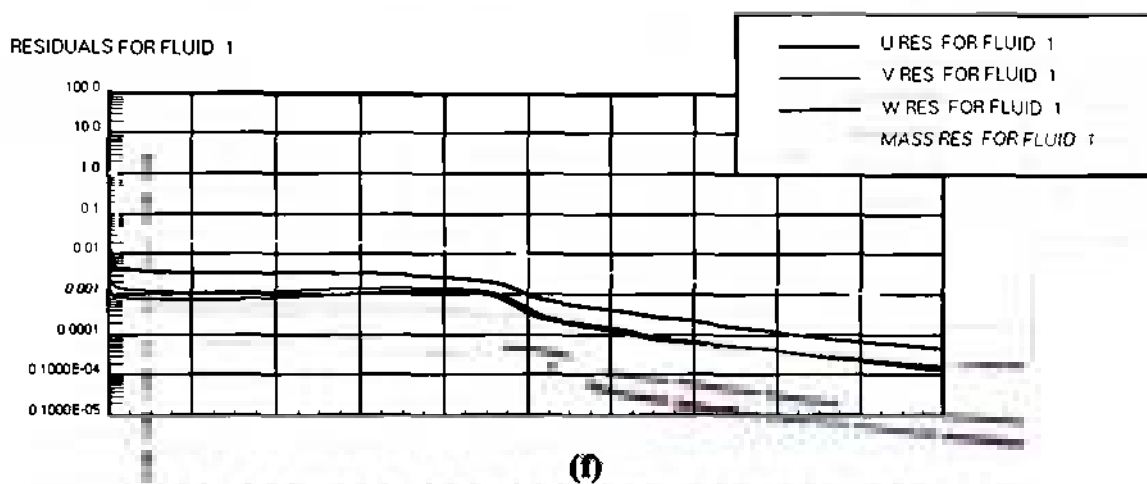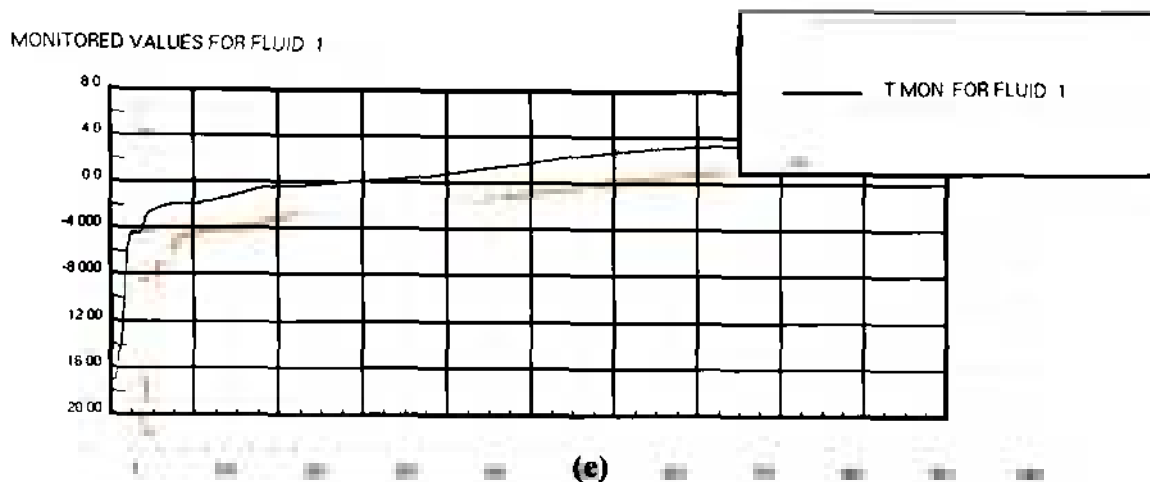
Figure 4.12: Plot of the monitoring values of (a) U in m/s, (b) V in m/s, (c) W in m/s, (d) P in Pa and (e) T in K as functions of the iteration number; plot of the residuals of (d) U, V, W and *Mass*, as well as of (e) the turbulent kinetic energy, *TE*, (f) its dissipation rate, *ED*, and (g) the enthalpy, **ENTH** as functions of the iteration number

146

The plots in figures 4.12 (b) and (c) show that the velocity components V and W have approached steady-state values after about 750 iterations. Furthermore, the plots in figures 4.12 (d) and (e) do not show any drastic changes in the development of the static pressure and temperature at the monitoring location. The velocity component V, which is depicted in figure 4.12 (a) seems to have just approached a steady-state value at iteration number 1000. Finally, the values of the residuals of the dependent variables at the monitoring location have decreased below the 10^{-2} mark, and many of the residuals of the dependent variables have even decreased below the 10^{-3} mark. This means that overall it is legitimate to conclude that the 3D steady-state solution has satisfied the stability criteria set in subsection 3.2.1. on page 104 and that it is converged. It also means that the 3D steady-state solution can be used as a basis for the 3D transient analysis.

After having shown that the 3D steady-state solution is converged, it is now possible to present the flow solution. Due to the fact that the analysis contains a 3D model, it was necessary to show the model from different angles. Figures 4.13 (a) through (d) show the velocity magnitude distribution across the surface of the 3D model of the Four Winds FX-210 aircraft. More specifically, Figures 4.13 (a) through (d) show the 3D model in a front, side, top and isometric view, respectively.

147

(a)

138 4
128 6
116 8
109 0
99 18
89 37
79 57
69 77
59 96
50 16
40 36
30 55
20 75
10 95
1 145

(b)

138 4	
128 6	
118 8	
109 0	
99 18	
89 37	
79 57	
69 77	
59 96	
50 16	
40 36	
30 55	
20 75	
10 95	
1 145	

(c)

(d)
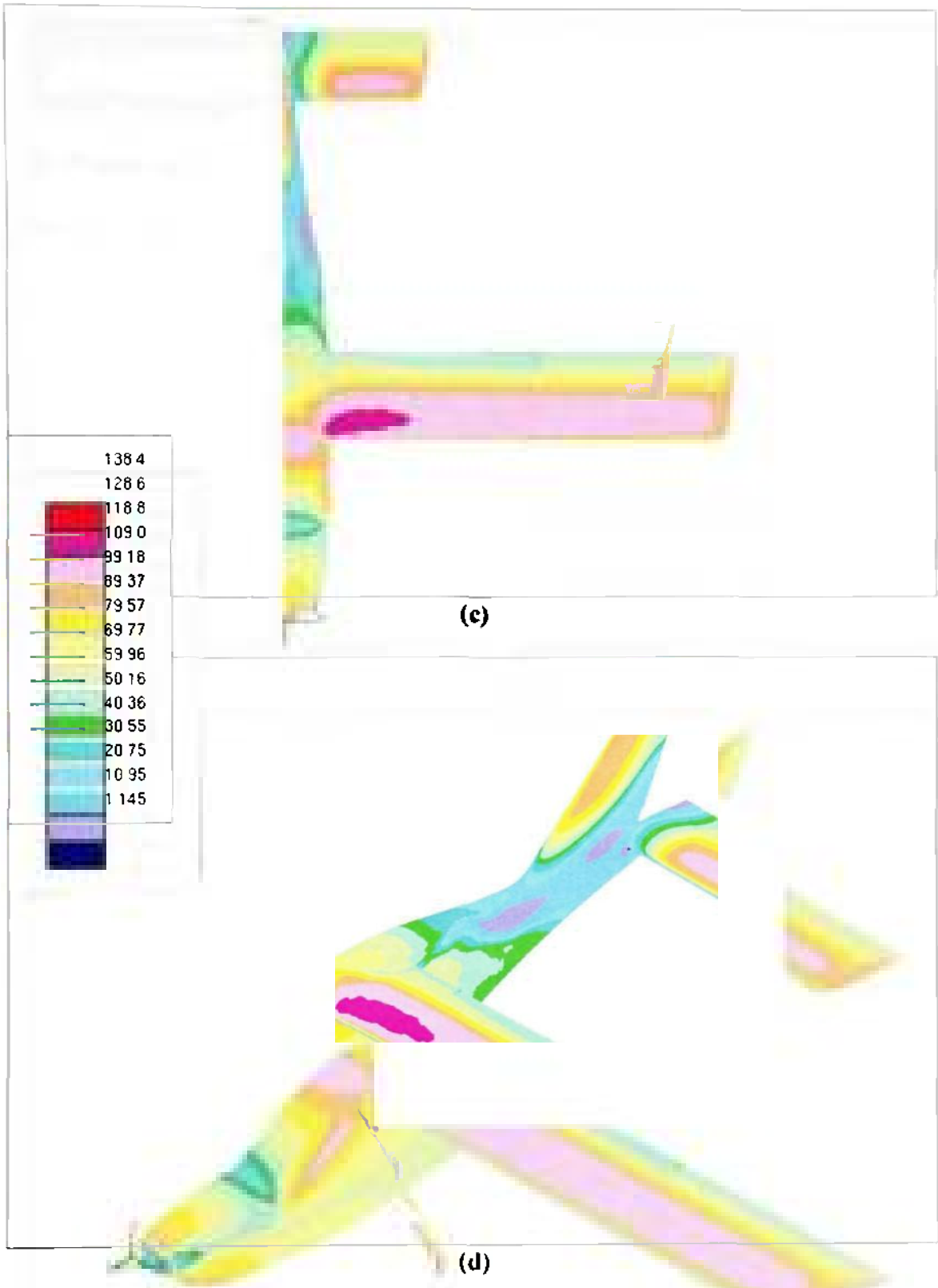
Figure 4.13: Plot of (a) front, (b) side, (c) top and (d) isometric view of the velocity magnitude distribution across the surface of the FX-210 aircraft model; the unit for the velocity magnitude is m/s

149

The result of the 3D steady-state analysis in figures 4.13 (a) through (d) shows several interesting characteristics. For example, Figure 4.13 (c) shows that the velocity distribution across the wing contains a region of high velocity in the vicinity of the wing root. This indicates that the lift distribution across the wing is higher towards the wing root. Furthermore, figures 4.12 (b) through (d) all show that the velocity distribution across the tail of the aircraft is low, and in some parts the airflow even seems to be close to stationary. This indicates that as the airflow passes the widest cross section of the airplane, it starts to experience an adverse pressure gradient that is seemingly strong enough to cause the flow to separate. Finally, figure 4.13 (c) shows that the solution for the flow through the 3D trailing edge flap section blends with the rest of the solution, which indicates that the integration of the moving flap section has been successful.

The author wants to note that the small irregularities in the flowfield in the region of the 3D trailing edge flap section were caused during the plot generation process. More specifically, the plots in figure 4.13 visualize the distribution of the velocity magnitude two cell layers above the actual skin of the aircraft. Furthermore, since the mesh of 3D trailing edge flap section has a different geometric structure, the distribution of the velocity magnitude is given at different distances from the surface of the aircraft. This explains why the velocity magnitude distribution in the 3D trailing edge flap section does not blend perfectly with the rest of the aircraft model in figure 4.13.

4.2.2. Results of the 3D Transient Analysis

During the 3D analysis, the author encountered several problems, which ultimately led to the failure to produce a solution. The simulation stopped in every

attempt due to an issue with the development of the densities. More specifically, the *run*-file of the 3D transient analysis, which summarizes the input data and numerical statistics, indicated that it found negative densities at more than a hundred cells. Furthermore, the *info*-file, which contains STAR warning messages and additional statistical information, stated the specific cell numbers where the error was found, the author plotted some of those cells in order to see whether the geometry of the mesh is erroneous at these locations. However, the author found that the cells were regular hexahedra without excessive aspect ratios, skewing or warping. Also, the fact that the cells, where the negative densities were found, are spread across the entire computational domain indicates that the issue is global and not specific to a certain region of the mesh. Furthermore, the built-in mesh checking tool of STAR-CD passed the mesh without any errors prior to writing the geometry file for the transient analysis. Besides, the steady-state analysis, whose results were presented in the previous subsection, ran without major problems, and it produced meaningful results as shown in figures 4.13 (a) through (d) on pages 148 and 149. This leads to the conclusion that the mesh is not the source of the failure.

A more thorough investigation of the *info*-file followed with the result that in each iteration step the code does go through the maximum number of corrector stages specified by the user, namely 50. The reason for this seems to be the fact that the simulation fails to achieve convergence for the U, V and W momentum equation due to out of bounds values for the enthalpy as indicated in the *info*-file. The development of the rates of change of the dependent variables can be viewed in figures 4.14 (a) and (b) on the next page.
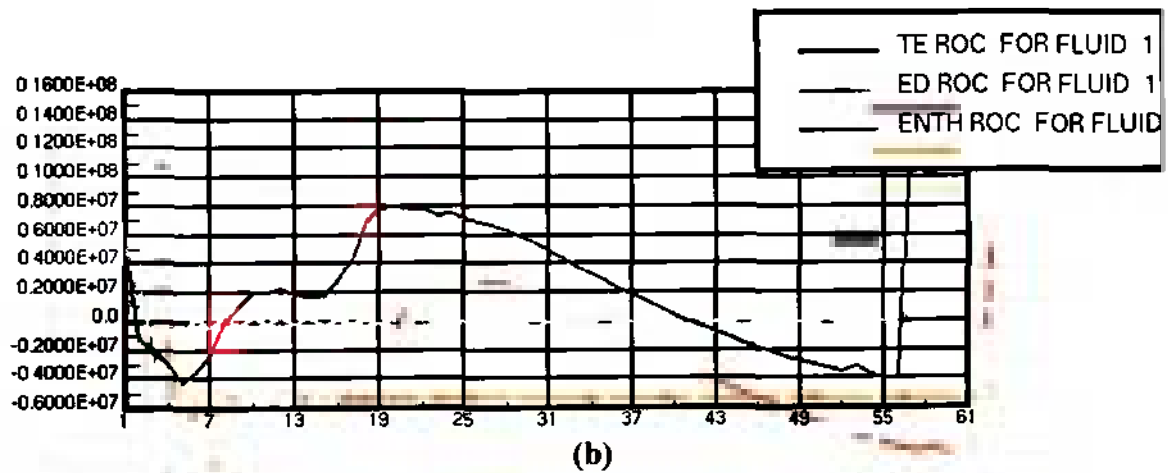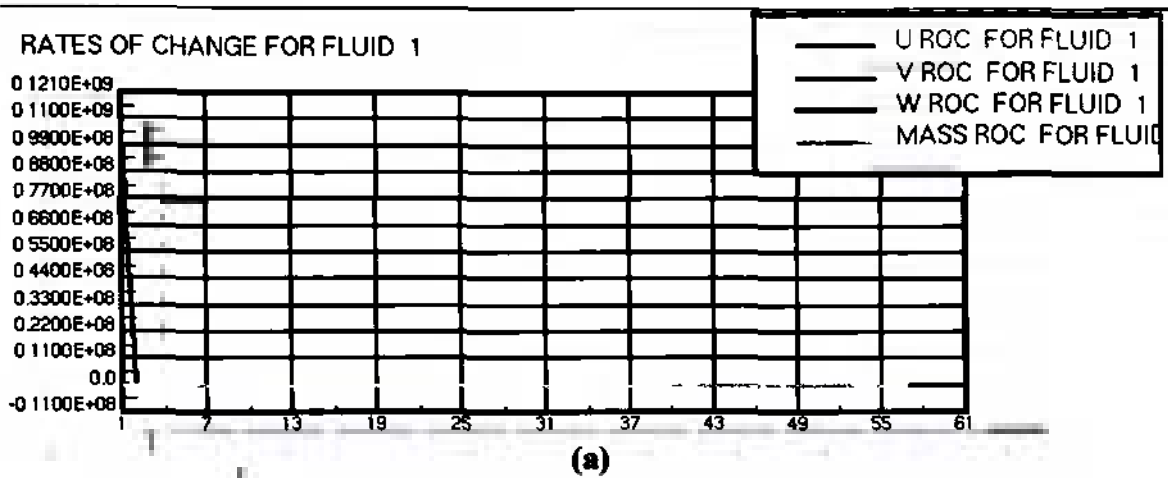
Figure 4.14: Plot of the rates of change of (a) the velocity components *U*, *V*, *W* and the mass flow, as well as of (b) the turbulent kinetic energy, *TE*, its dissipation rate, *ED*, and the enthalpy, *ENTH*

Figure 4.14 shows that the rates of change of all dependent variables are converged except for the enthalpy, *ENTH* When interpreting the above figure it should be noted that the flap deflection in this case was set to start after 50 time steps. This explains why the rates of change of most dependent variables are about zero. Nevertheless, it can be observed that regardless of when the deflection of the flap commences, the enthalpy does not reach a steady-state value.

152

In order to fix the issue, the author attempted to vary the pressure correction under-relaxation factor and to increase the number of corrector stages, which are also referred to as sweeps. However, a variation of the pressure correction under-relaxation factor from its initial values of 0.05 as mentioned in subsection 3.2.2. on page 106 did not have the desired effect of eliminating the issue regarding the enthalpy. Increasing the number of sweeps did not improve the situation either. In fact, it made it worse in the sense that the computing time increased. More specifically, doubling the number of sweeps increased the computing time for each time step proportionally.

In another attempt to solve the problem, the author decreased the time step of the simulation by an order of magnitude from 0.01s to 0.001s, although the initial time step already satisfies the operability criterion, which states that the time step is typically within fifty times of the smallest characteristic time step, $\delta t \approx 50 \; \delta t_c$ [11]. δt_c can be calculated using equation 4.10 below:

$$\delta t_c = \frac{\delta L}{U} \qquad\qquad [4.10]$$

In equation 4.10, δL is the mean mesh dimension and U is the characteristic velocity. For this analysis, the former was computed from the overall volume of the computational domain, which amounts to 4730 m^3, and the number of fluid cells, which is equal to 2.38 $\cdot$ 10^6. This led to mean mesh dimension of 0.126 m. The characteristic velocity was assumed to be the inlet velocity which amounts to 100 m/s. This means that the smallest characteristic time for the 3D transient analysis is 1.26 $\cdot$ 10^{-3}s, so that a time step of 0.01 indeed does fall within the operability criterion of 6.30 $\cdot$ 10^{-2}s.

153

Nevertheless, an observation of the first 36 time steps of the simulation indicated that the new time step size of 0.001s does not lead to the results that were hoped for. The simulation still relies on using the maximum number of sweeps, which means that the computing time increased by a factor of ten because every time step still takes the same amount of time as in the case of the smaller time step size of 0.01s. Furthermore, the *info-file* still contains warning messages that state that the there is an equation of state imbalance. This indicates that once the deflection of the flap begins at time step 100, it will again be possible to observe a spike in the rate of change of the enthalpy variable.

This concludes the summary of the problems encountered in the 3D transient analysis, and the author currently continues to work on a solution to the issues described above. For further recommendations regarding the 3D analysis refer to chapter 6 that contains suggestions for future work.

5. CONCLUSIONS

5.1. Conclusions from the 2D Analysis

The 2D analysis had the goal to prove the feasibility of modeling the flap deflection process with STAR-CD. This goal was achieved, and a good number of qualitative and quantitative results regarding the dynamic effects of flap deflection on the aerodynamic and stability and control characteristics of an airfoil were produced. These are listed below.

The qualitative investigation showed that flap deflection increases the velocity magnitude and decreases the static pressure distribution over the top surface of the airfoil. Furthermore, the effects on the flowfield over the bottom surface of the airfoil are the opposite. The qualitative results also indicated that flow separation can be caused by flap deflections with large angles. This was indicated by a separation bubble that started to develop at a flap deflection angle of about 20°, which subsequently grew until it covered almost the entire top surface of the flap at a deflection angle of about 30°.

The qualitative analysis also showed that a moderate variation of the flap deflection rate does not have any effects on the flowfield characteristics. An increase of the flap deflection rate by an order of magnitude, on the other hand, does have an effect on the velocity and pressure coefficient distribution in the vicinity of the airfoil, namely a delay of the development of the phenomena described in the previous paragraph. Furthermore, an increase of the deflection rate by an order of magnitude caused the

155

separation bubble to be more compact. The velocity gradients in this separation bubble became larger. This indicates that the flow in this area became more turbulent with the increase in flap deflection rate.

The 2D quantitative analysis showed the effects of flap deflection and retraction on the stability and control parameters of the airfoil. More specifically, this part of the analysis led to the conclusion that flap deflection increases the lift, drag and nose-down pitching moment of an airfoil and causes the center of pressure to move aft of its initial position at the quarter chord, whereas its motion is not uniform and not proportional to the flap deflection process.

The 2D quantitative analysis also verified the observation from the qualitative analysis that the development of the effects of flap deflection is delayed in the case of an increased flap deflection rate of 200°/s. Another rather surprising solution from that case was the fact that the drag becomes almost zero during the final part of the flap retraction process, which actually means that it effectively produced thrust that neutralized the airfoil's drag.

Overall, the results and conclusions from the 2D qualitative and quantitative analysis agree well with conceptual data found in the literature. They also show good agreement with empirical and experimental data, although not many opportunities exist for a holistic comparison in these two cases due to the specific nature of this analysis. Nevertheless, it is safe to say that the 2D analysis was successful in showing that STAR-CD and the methodology presented in this work can be used to model the process of flap deflection and to capture both aerodynamic as well as stability and control phenomena during this process.

5.2. Conclusions from the 3D Analysis

As mentioned in subsection 2.3.2. on page 51, the 3D analysis had the goal to prove that the methodology that was developed and proven in the 2D analysis has the ability to adapt to an arbitrary plain flap and aircraft model if necessary. As seen in the results section this part of the analysis has only been partly achieved.

The 3D analysis rendered only a steady-state analysis, which did not provide any indications regarding the effects of flap deflection on the aerodynamic and stability and control characteristics of the aircraft. Nevertheless, the steady-state solution showed that the mesh generation process has been successful and that the integration of the moving trailing edge flap section worked. Some of the findings which were made in the attempts to run the 3D transient analysis led to the conclusion that the issue lies in the set-up of the case and not in the geometry of the mesh.

As stated above the failure of the 3D transient analysis means that the objective of the 3D analysis and this overall investigation was only partially fulfilled. It was proven that STAR-CD can be used to develop a methodology that has the ability to fully capture both the aerodynamics and the related stability and control phenomena that occur during flap deflection of a 2D flap. The 3D transient case still needs to be investigated, but the results from the 3D steady-state analysis give hope that this is merely a matter of finding the right set up for the investigation. A working 3D analysis would prove the adaptability of this methodology, which in turn opens a new range of applications.

6. RECOMMENDATIONS AND FUTURE WORK

In order to successfully complete the 3D transient analysis, the author currently tries to reduce the time step δt. In the mean time, it is recommended to attempt to run the 3D transient case on multiple parallel processors in order to substantially reduce the computing time necessary to complete this analysis. This is important because as noted in subsection 4.2.2. on page 154, a reduction in the time step size substantially lengthens the computing time for the simulation.

Once the 3D case has been run successfully, and it has been proven that the methodology developed in this work has the ability to adapt to different geometrical situations; it can be applied to a wide variety of cases. For example, due to the fact that this methodology allows the deflection of a plain flap in both the downward as well as the upward direction, it can be applied to the simulation of other control surfaces, such as ailerons or rudders.

An extension of the application of this methodology to other control surfaces on the aircraft has the potential to allow the transient simulations of entire flight maneuvers, such as turns. These, for instance, consist of both roll and yaw and hence would require the simulation of both ailerons and vertical stabilizer. Furthermore, the results of such an analysis can be linked to an optimization algorithm, which would make this methodology an important and capable link in the preliminary aerodynamic design process of an airplane.

REFERENCES

1. Tinoco, Edward. "The Changing Role of Computational Fluid Dynamics in Aircraft Development." AIAA-98-2512, 1998.

2. Idahosa, Uyi. <u>An Automated Optimal Design of a Fan Blade Using an Integrated CFD/MDO Computer Environment</u>. Thesis. Daytona Beach: Embry-Riddle Aeronautical University, 2005.

3. Anderson, John. <u>Fundamentals of Aerodynamics</u>. New York: McGraw Hill, 2001.

4. Streett, C. "Numerical Simulation of a Flap-Edge Flowfield." AIAA-98-2226, 1998.

5. Joslin, R., Warren Baker, Eric Paterson, L. Peltier. "Aerodynamic Prediction of a NACA0015-Flap Flow Control Configuration." AIAA-2002-0410, January 2002

6. Grismer, M., D. Kinsey, D. Grismer. "Hinge Moment Predictions Using CFD." AIAA-2000-4325, August 2000.

7. <u>Methodology, STAR-CD, Version 3.20</u>. New York: CD-adapco Group, 2004.

8. Abbott, Ira, Albert von Doenhoff. <u>Theory of Wing Sections</u>. New York: Dover Publications, Inc., 1959.

9. Raymer, Daniel. <u>Aircraft Design: A Conceptual Approach</u>. Reston: American Institute of Aeronautics and Astronautics, Inc., 1999.

10. Todd. "FX-210." New Smyrna Beach: Four Winds Aircraft, 2005. <http://www.fourwindsaircraft.com/fx210.html>

11. <u>User Guide, STAR-CD, Version 3.20</u>. New York: CD-adapco Group, 2004.

12. "1976 Atmosphere Calculator." Digital Dutch, 2003. <http://www.digitaldutch.com/atmoscalc/>

13. Wilcox, David. <u>Turbulence Modeling for CFD</u>. La Cañada: DCW Industries, Inc., 1998.

14. Davidson, Lars. "An Introduction to Turbulence Models." Goteborg: Chalmers University of Technology, 2003. <http://www.tfd.chalmers.se/~lada/postscript_files/kompendium_turb.pdf>

APPENDIX A

STAR-CD INPUT FILES

Content:

Appendix A.1: *Airfoil_V_NACA_0012.inp* – **Input file containing coordinates for NACA 0012 airfoil profile vertices**

```
!!!!!!!!!!!!!!!!!!!!!!!!!!!!!!!!!!!!!!!!!!!!!!!!!!!!!!!!!!
!!!!Airfoil Vertices        !!!!!!!!!!!!!!!!!!!!!!!!!!!!!!!
!!!!NACA 0012               !!!!!!!!!!!!!!!!!!!!!!!!!!!!!!!
!!!!Alexander Moerchel      !!!!!!!!!!!!!!!!!!!!!!!!!!!!!!!
!!!!Created: 01/15/2006     !!!!!!!!!!!!!!!!!!!!!!!!!!!!!!!
!!!!Last Update: 01/15/2006       !!!!!!!!!!!!!!!!!!!!!!!!!!
!!!!!!!!!!!!!!!!!!!!!!!!!!!!!!!!!!!!!!!!!!!!!!!!!!!!!!!!!!


csys 1


!!!!Upper Surface !!!!!!!!!!!!!!!!!!!!!!!!!!!!!!!!!!!!!!!!!

v 101 0 0 0
v 102 12.5 18.94 0
v 103 25.0 26.15 0
v 104 50.0 35.55 0
v 105 75.0 42.00 0
v 106 100.0 46.83 0
v 107 150.0 53.45 0
v 108 200.0 57.37 0
v 109 250.0 59.41 0
v 110 300.0 60.02 0
v 111 400.0 58.03 0
v 112 500.0 52.94 0
v 113 600.0 45.63 0
v 114 700.0 36.64 0
v 115 750.0 31.44 0
v 116 800.0 26.23 0
v 117 900.0 14.48 0
v 118 950.0 8.07 0
v 119 1000.0 1.26 0


!!!!Lower Surface !!!!!!!!!!!!!!!!!!!!!!!!!!!!!!!!!!!!!!!!

v 201 0 0 0
v 202 12.5 -18.94 0
v 203 25.0 -26.15 0
v 204 50.0 -35.55 0
v 205 75.0 -42.00 0
v 206 100.0 -46.83 0
v 207 150.0 -53.45 0
v 208 200.0 -57.37 0
v 209 250.0 -59.41 0
v 210 300.0 -60.02 0
v 211 400.0 -58.03 0
v 212 500.0 -52.94 0
v 213 600.0 -45.63 0
v 214 700.0 -36.64 0
v 215 750.0 -31.44 0
v 216 800.0 -26.23 0
v 217 900.0 -14.48 0
v 218 950.0 -8.07 0
v 219 1000.0 -1.26 0

!!!!!!!!!!!!!!!!!!!!!!!!!!!!!!!!!!!!!!!!!!!!!!!!!!!!!!!!!!
```

Appendix A.2: *Section_NACA_0012_moving_flap.inp* – Input file creating shells for the computational domain except for the 2D flap section

```
!!!!!!!!!!!!!!!!!!!!!!!!!!!!!!!!!!!!!!!!!!!!!!!!!!!!!!!!!!!!!!!!!!!!!!!!!!!!!!!!
!!!!Mesh Generation        !!!!!!!!!!!!!!!!!!!!!!!!!!!!!!
!!!!NACA 0012              !!!!!!!!!!!!!!!!!!!!!!!!!!!!!!!
!!!!Alexander Moerchel     !!!!!!!!!!!!!!!!!!!!!!!!!!!!!!!
!!!!Created: 02/07/06      !!!!!!!!!!!!!!!!!!!!!!!!!!!!!!!
!!!!Last Update: 03/06/06  !!!!!!!!!!!!!!!!!!!!!!!!!!!!!!!
!!!!!!!!!!!!!!!!!!!!!!!!!!!!!!!!!!!!!!!!!!!!!!!!!!!!!!!!!!!!!!!!!!!!!!!!!!!!!!!!


!!!!!!!!!!!!!!!!!!!!!!!!!!!!!!!!!!!!!!!!!!!!!!!!!!!!!!!!!!!!!!!!!!!!!!!!!!!!!!!!
!!!!Input File of Airfoil Vertices       !!!!!!!!!!!!!!!!!!!!!!!!!!!!
!!!!!!!!!!!!!!!!!!!!!!!!!!!!!!!!!!!!!!!!!!!!!!!!!!!!!!!!!!!!!!!!!!!!!!!!!!!!!!!!


ifile Airfoil_V_NACA_0012.inp


!!!!!!!!!!!!!!!!!!!!!!!!!!!!!!!!!!!!!!!!!!!!!!!!!!!!!!!!!!!!!!!!!!!!!!!!!!!!!!!!
!!!!Input Parameters       !!!!!!!!!!!!!!!!!!!!!!!!!!!!!!!!!!!!
!!!!!!!!!!!!!!!!!!!!!!!!!!!!!!!!!!!!!!!!!!!!!!!!!!!!!!!!!!!!!!!!!!!!!!!!!!!!!!!!

!!!!Corners of Outside Domain !!!!!!!!!!!!!!!!!!!!!!!!!!!!
*set xx1 -10000 ! -1800
*set xx5 20000 ! 2800
*set yy1 -20000 ! -500
*set yy5 20000 ! 500

!!!!Intermediate Outside Domain Points !!!!!!!!!!!!!!!!!
*set dxx xx5 - xx1
*set ddxx dxx / 4
*set xx2 1.5 * ddxx + xx1
*set xx3 2 * ddxx + xx1
*set xx4 2.5 * ddxx + xx1
*set xx5 10 * ddxx + xx1
*set xx6 2.3 * ddxx + xx1
*set dyy yy5 - yy1
*set ddyy dyy / 4
*set yy2 1.95 * ddyy + yy1
*set yy22 1.8 * ddyy + yy1
*set yy3 2 * ddyy + yy1
*set yy4 2.05 * ddyy + yy1
*set yy42 2.2 * ddyy + yy1
*set yy6 1.995 * ddyy + yy1
*set yy7 2.005 * ddyy + yy1
*set yy8 1.98 * ddyy + yy1
*set yy9 2.02 * ddyy + yy1

!!!!Vertex Data !!!!!!!!!!!!!!!!!!!!!!!!!!!!!!!!!!!!!!!!!!
*set nvs1 101      ! V start - upper surface
*set nvs2 201      ! V start - lower surface
*set nv1 19        ! Number of vertices
*set nvf1 115      ! V Flap upper Surface
*set nvf2 215      ! V Flap Lower surface
*set of2 200       ! Vertex offset Intermediate
*set of3 100       ! Vertex offset Intermediate
*set a1 2          ! offset in Upper Section
*set a2 -2                  ! offset in Lower section
*set a3 4          ! x-offset of BL Trailing Edge

!!!!Parameters for Patch !!!!!!!!!!!!!!!!!!!!!!!!!!!!!!!!!
*set RY1 1.07      ! Relaxation factor - Near Body 0.9
```

162

```
*set NY1 24        ! number y - Near Surface
*set NXN 6         ! number X - Nose
*set RXN 1.0       ! Relaxation Factor - Nose -1.05
*set NXBU 50       ! number X - Upper Body
*set RXBU 0.97     ! Relaxation factor - Upper Body -1.05
*set NXBL NXBU     ! number X - Lower Body
*set RXBL RXBU     ! Relaxation factor - Lower body
*set NXFU 54       ! number X - Flap upper
*set RXFU 1.0      ! Relaxation factor - Upper Flap -1.05
*set NXFL NXFU     ! number X - Flap lower
*set RXFL RXFU     ! Relaxation factor - Lower Flap
*set RXF1 -1.1     ! Relaxation factor - First B.L. Flap Section
*set RXF2 1.05     ! Relaxation factor - Second B.L. Flap Section
*set NXT 2 * NXN             ! number X - B.L. Trailing Edge
*set NXTD 80       !number X - Trailing Edge
*set RXT -1.05     ! Relaxation factor - Trailing Edge
*set fx1 0.95      ! Relaxation factor X direction
*set fy1 0.95      ! Relaxation factor Y direction
*set RXUA 1.0      ! Relaxation factor X direction for airfoil
*set RYAU 0.95     ! Relaxation factor Y direction for airfoil
*set RYAL 1 / RYAU         !Relaxation factor Y direction for airfoil


!!!!!!!!!!!!!!!!!!!!!!!!!!!!!!!!!!!!!!!!!!!!!!!!!!!!!!!!!!!


*set RXUS 0.93     ! relaxation factor - Upstream 0.97
*set NXUS 50       ! number X - upstream
*set NYU 50        ! number Y Upper zone
*set RYU 1 / 0.93  ! relaxation factor - Upper zone 1.08
*set RYUA 1.9      ! relaxation factor - Airfoil
*set NYL 50        ! number Y lower zone
*set RYL 0.93      ! relaxation factor - Lower Zone 0.93
*set NXDS 100      ! number X - Downstream
*set RXDS 1.041    ! relaxation factor - Downstream 1.02



!!!!!!!!!!!!!!!!!!!!!!!!!!!!!!!!!!!!!!!!!!!!!!!!!!!!!!!!!!!!!!!
!!!!Calculation Section        !!!!!!!!!!!!!!!!!!!!!!!!!!!!
!!!!!!!!!!!!!!!!!!!!!!!!!!!!!!!!!!!!!!!!!!!!!!!!!!!!!!!!!!!!!!!

!!!!Finding the Coordinates of the Vertices !!!!!!!!!!!
*get mix,x,nvs1
*get max,x,nvs2

!!!!Finding Maximum Thickness and Place Center !!!!!!!!!
*get ds1 dist nvs1, nvs1 + nv1 - 1
*define noexecute
*set v1 x1
*get d1 dy, v1, v1 + nvs2 - nvs1
*if d1 GT dm
*set dm d1
*set dm2 dm / 1.333
*set vm v1
*endif
*end
*set dm 0
*set x1 101,1
*loop 1, nv1 - 1
*get y1 y vm
*get y2 y vm + 100
*get x1 x vm
*set y3 y1 + y2
*set y3 y3 / 2
csys 1
v 1000 x1,y3,0
```

163

```
vlocal 20 cyli 1000,x,nvs1,y,vm
vlocal 21 cart 1000,x,nvs1,y,vm

!!!!Create Splines for Airfoil !!!!!!!!!!!!!!!!!!!!!!!!!!
*set ne1 nvs1 + nv1    1
*set ne2 nvs2 + nv1    1
*set nvs12 nvs1 + 1
*set nvs22 nvs2 + 1
spl, 1, vrange, nvs1, nvf1, 1
spl, 2, vrange, nvs2, nvf2, 1
splmodify, 1, join, 2
spldelete, 2
spl, 3, vrange, nvf1, ne1, 1
spl, 4, vrange, nvf2, ne2, 1
splmodify, 3, join, 4
spldelete, 4
splmodify, 3, modify, ne1, -1 * ne1
splmodify, 3, modify, ne2, -1 * ne2

!!!!Create Splines for Boundary Layer!!!!!!!!!!!!!!!!!!
csys 1
vgen 2,of2,nvs1,ne1,1,,a1 * dm
vgen 2,of2,nvs2,ne2,1,,a2 * dm
vgen 2,of2,nvs1,nvs2,nvs2 - nvs1,a2 * dm,0,0
vgen 2,of2,nvs12,nvs12,0,a2 * dm2,150,0
vgen 2,of2,nvs22,nvs22,0,a2 * dm2,-150,0
*set te1 ne1 + of2
*set te2 ne2 + of2
*set tvf1 nvf1 + of2
*set tvf2 nvf2 + of2
vset news vlist te1
vgen 2,0,vset,,,dm * a3
vfill nvf1 + of2,te1,te1 - tvf1    1,tvf1 + 1,1,1
vset news vlist te2
vgen 2,0,vset,,,dm * a3
vfill nvf2 + of2,te2,te2 - tvf2 - 1,tvf2 + 1,1,1
splgen 2,1,1,3,2,of2

!!!!Outer Domain Patch !!!!!!!!!!!!!!!!!!!!!!!!!!!!!!!!!!!

!!Vertex Definitions
v 11 xx1 yy1 0
v 12 xx2 yy1 0
v 13 xx3 yy1 0
v 14 xx4 yy1 0
v 15 xx5 yy1 0
v 16 xx6 yy1 0
v 21 xx1 yy2 0
v 25 xx5 yy22 0
v 31 xx1 yy3 0
v 36 1480.16 yy6 0
v 37 1480.16 yy7 0
v 38 xx5 yy8 0
v 39 xx5 yy9 0
v 41 xx1 yy4 0
v 45 xx5 yy42 0
v 51 xx1 yy5 0
v 52 xx2 yy5 0
v 53 xx3 yy5 0
v 54 xx4 yy5 0
v 55 xx5 yy5 0
v 56 xx6 yy5 0
v 60 1020.43 -260.342 0
v 70 1020.43 260.342 0
```

```
!!Caculation of Maximum Vertex Number
*get a mxve
*set aa a + 1

!!Calculation of Patch Parameters
*set vo11 11
*set vo12 12
*set vo13 13
*set vo14 14
*set vo15 15
*set vo16 16
*set vo21 21
*set vo25 25
*set vo31 31
*set vo36 36
*set vo37 37
*set vo38 38
*set vo39 39
*set vo41 41
*set vo45 45
*set vo51 51
*set vo52 52
*set vo53 53
*set vo54 54
*set vo55 55
*set vo56 56
*set vo60 60
*set vo70 70

!!Creation of Outer Mesh Patches

ctab 7 shell,4
patch vo21 402 301 vo31,NXUS,NXN,,,,,,,,,RXUS 1 / RXN
patch vo31 301 302 vo41,NXUS,NXN,,,,,,,,RXUS,RXN

ctab 8 shell,5
patch vo11 vo12 402 vo21,NXUS,NYL,,,,,,,,,RXUS,RYL
patch vo12 vo13 415 402,NXBL,NYL,,,,,,,,,RXBU,RYL

ctab 9 shell,6
patch vo13 vo16 vo60 415,25,NYL,,,,,,,,,RXF1,RYL
patch vo16 vo14 419 vo60,34,NYL,,,,,,,,,RXF2,RYL
patch vo14 vo15 vo25,419,NXDS,NYL,,,,,,,,RXDS,RYL

ctab 10 shell,7
patch vo37 vo39 vo45 319,NXDS,24,,,,,,,,,RXDS,RY1
patch vo36 vo38 vo39 vo37,NXDS,12,,,,,,,,RXDS,1
patch 419 vo25 vo38 vo36,NXDS,24,,,,,,,,RXDS,1 / RY1

ctab 11 shell,8
patch vo41 302 vo52 vo51,NXUS,NYU,,,,,,,,RXUS,RYU
patch 302 315 vo53 vo52,NXBU,NYU,,,,,,,,RXBU,RYU




ctab 12 shell,9
patch 315 vo70 vo56 vo53,25,NYU,,,,,,,,,RXF1,RYU
patch vo70 319 vo54 vo56,34,NYU,,,,,,,,RXF2,RYU
patch 319 vo45 vo55 vo54,NXDS,NYU,,,,,,,,RXDS,RYU

!!Creation of Boundary Layer Patches

ctab 5 shell,3
```

```
patch 101 103 302 301, NXN,NY1,.........RXN,RY1
patch 103 115 315 302,NXBU,NY1.........RXBU,RY1
patch 215 203 402 415,NXBL,NY1.........1 / RXBU,RY1
patch 203 101 301 402, NXN,NY1.........1 / RXN, RY1

!!Creation of Patches Inside of Airfoil
vfil 115,215,1,515
vfil 119,219,1,519
ctab 15 shell,27
patch 101,515,115,103,NXBU,NXN.........RXBU,RXN
patch 203 215 515 101,NXBL,NXN.........RXBU,1 / RXN
!patch 515 519 119 115,NXFU,NXN.........RXUA,RXN
!patch 215 219 519 515,NXFU,NXN.........RXUA,1 / RXN

!!!!Refining the Final Plot!!!!!!!!!!!!!!!!!!!!!!!!!!!!
!cset news shell
!vset news cset
!vmerge vset,,,001
axis z
view 0 0 -1
angl -90
!cset all
!cplo
!ccom all
!y
!vcom all
!y
!repl
!!!!!!!!!!!!!!!!!!!!!!!!!!!!!!!!!!!!!!!!!!!!!!!!!!!!!!!!!!!
!!!!!!!!!!!!!!!!!!!!!!!!!!!!!!!!!!!!!!!!!!!!!!!!!!!!!!!!!!!
```

Appendix A.3: *Section_Moving_Flap.inp* – Input file creating shells for the mesh within the 2D trailing edge flap section

```
!!!!!!!!!!!!!!!!!!!!!!!!!!!!!!!!!!!!!!!!!!!!!!!!!!!!!!!!!
!!!!Moving Flap          !!!!!!!!!!!!!!!!!!!!!!!!!!!!!
!!!!NACA 0012            !!!!!!!!!!!!!!!!!!!!!!!!!!!!!
!!!!Alexander Moerchel   !!!!!!!!!!!!!!!!!!!!!!!!!!!!!
!!!!Created: 02/07/06    !!!!!!!!!!!!!!!!!!!!!!!!!!!!!
!!!!Last Update: 03/06/06   !!!!!!!!!!!!!!!!!!!!!!!!!!!!!
!!!!!!!!!!!!!!!!!!!!!!!!!!!!!!!!!!!!!!!!!!!!!!!!!!!!!!!!!


csys 1



!!!!Flap Vertices!!!!!!!!!!!!!!!!!!!!!!!!!!!!!!!!!!!!!!!!


!Upper Surface
v 42500 750 -31.44 0
v 42525 1000.00 -1.26000 0

!Lower Surface
v 45700 750 31.44 0
v 45725 1000.00 1.26000 0



!!!!Moving Flap Section Domain!!!!!!!!!!!!!!!!!!!!!!


!Upper Surface Vertices
v 40100 750 -271.52 0
v 40159 1480.16 -241.34 0

!Lower Surface Vertices
v 48100 750 271.52 0
v 48159 1480.16 241.34 0

!B.L. Trailing Edge Vertices
!v 42559 1480.16 -45.2714 0
!v 45759 1480.16 45.2714 0



!!!!Creating Patches!!!!!!!!!!!!!!!!!!!!!!!!!!!!!!!!!!!!


ctab 6 shell,3
patch 40100,vo60,42525,42500,25,24,1,100,40100,,,,,RXF1,1 / RY1
patch vo60,40159,vo36,42525,34,24,1,100,40125,,,,,RXF2,1 / RY1
patch 42525,vo36,vo37,45725,34,12,1,100,42525,,,,,RXF2,-RXN
patch 45700,45725,vo70,48100,25,24,1,100,45700,,,,,RXF1,RY1
patch 45725,vo37,48159,vo70,34,24,1,100,45725,,,,,RXF2,RY1

ctab 15 shell,27
patch 42500,42525,45725,45700,25,12,1,100,42500,,,,,RXF1,-RXN



!!!!!!!!!!!!!!!!!!!!!!!!!!!!!!!!!!!!!!!!!!!!!!!!!!!!!!!!


repl

!!!!!!!!!!!!!!!!!!!!!!!!!!!!!!!!!!!!!!!!!!!!!!!!!!!!!!!!!
!!!!!!!!!!!!!!!!!!!!!!!!!!!!!!!!!!!!!!!!!!!!!!!!!!!!!!!!!
```

Appendix A.4: *Fluid_Gen_x_2D.inp* – Input file extruding shells of entire computational domain into solid and fluid cells

```
!!!!!!!!!!!!!!!!!!!!!!!!!!!!!!!!!!!!!!!!!!!!!!!!!!!!!!!!!!!
!!!!Fluid Cell Generation     !!!!!!!!!!!!!!!!!!!!!!!!!!!!!
!!!!NACA 0012                  !!!!!!!!!!!!!!!!!!!!!!!!!!!!!
!!!!Alexander Moerchel         !!!!!!!!!!!!!!!!!!!!!!!!!!!!!
!!!!Created: 02/15/06          !!!!!!!!!!!!!!!!!!!!!!!!!!!!!
!!!!Last Update: 02/18/06      !!!!!!!!!!!!!!!!!!!!!!!!!!!!!
!!!!!!!!!!!!!!!!!!!!!!!!!!!!!!!!!!!!!!!!!!!!!!!!!!!!!!!!!!!!


!!!!!!!!!!!!!!!!!!!!!!!!!!!!!!!!!!!!!!!!!!!!!!!!!!!!!!!!!!!!
!!!!Input Parameters          !!!!!!!!!!!!!!!!!!!!!!!!!!!!!
!!!!!!!!!!!!!!!!!!!!!!!!!!!!!!!!!!!!!!!!!!!!!!!!!!!!!!!!!!!!

*set ny11 1 ! Number of Cells in x-Radial Direction
*set LG1 50 ! Wing Span


!!!!!!!!!!!!!!!!!!!!!!!!!!!!!!!!!!!!!!!!!!!!!!!!!!!!!!!!!!!!
!!!!Calculation Section         !!!!!!!!!!!!!!!!!!!!!!!!!!!!
!!!!!!!!!!!!!!!!!!!!!!!!!!!!!!!!!!!!!!!!!!!!!!!!!!!!!!!!!!!!

!!!!Extrusion of Initial Mesh !!!!!!!!!!!!!!!!!!!!!!!!!!!!

!!Parameters
*get a mxve
*set aa a + 1
*set lz1 LG1 / ny11
*set nve2 ny11 + 1 * aa

!!Extrusion of Mesh
csys 21
ctab 1,fluid,2
cset news type 5 55
cset dele type 15
vcextrude,ny11,aa,cset,,,local,,,lz1
cset news type 15
ctab 70,solid
vcextrude,ny11,aa,cset,,,local,,,lz1
cset news shell
vset news cset
vmerge vset,,,001

cset all
cplo

!!!!!!!!!!!!!!!!!!!!!!!!!!!!!!!!!!!!!!!!!!!!!!!!!!!!!!!!!!!!!
!!!!!!!!!!!!!!!!!!!!!!!!!!!!!!!!!!!!!!!!!!!!!!!!!!!!!!!!!!!!!
```

168

Appendix A.5: *Section_Rotation_-.inp* – Input file rotating 2D flap

```
!!!!!!!!!!!!!!!!!!!!!!!!!!!!!!!!!!!!!!!!!!!!!!!!!!!!!!!!!!!!!!
!!!!Moving Flap          !!!!!!!!!!!!!!!!!!!!!!!!!!!!!!
!!!!NACA 0012            !!!!!!!!!!!!!!!!!!!!!!!!!!!!!!
!!!!Alexander Moerchel   !!!!!!!!!!!!!!!!!!!!!!!!!!!!!!
!!!!Created: 02/08/06    !!!!!!!!!!!!!!!!!!!!!!!!!!!!!!
!!!!Last Update: 03/06/06  !!!!!!!!!!!!!!!!!!!!!!!!!!!!!
!!!!!!!!!!!!!!!!!!!!!!!!!!!!!!!!!!!!!!!!!!!!!!!!!!!!!!!!!!!!!!

*define noexecute

!!!!Rotation of Flap!!!!!!!!!!!!!!!!!!!!!!!!!!!!!!!!!!!!!!!!

csys 6
vgen,2,0,42525,42525 + aa,aa,0,th,0,1
vgen,2,0,45725,45725 + aa,aa,0,th,0,1

!!!!Repeting the Mesh Filling!!!!!!!!!!!!!!!!!!!!!!!!!!!!

csys 1

!Upper Surface
vfill,42500,42525,24,42501,1,2,aa,RXF1
vfill,40100,42500,23,40200,100,26,1,1 / RY1
vfill,40100 + aa,42500 + aa,23,40200 + aa,100,26,1,1 / RY1

!Lower Surface
vfill,45700,45725,24,45701,1,2,aa,RXF1
vfill,45700,48100,23,45800,100,26,1,RY1
vfill,45700 + aa,48100 + aa,23,45800 + aa,100,26,1,RY1

!Flap
vfill,42500,45700,11,42600,100,26,1,RXN
vfill,42500 + aa,45700 + aa,11,42600 + aa,100,26,1,RXN

!Downstream Section
vfill,40125,40159,33,40126,1,36,100,RXF2
vfill,40125 + aa,40159 + aa,33,40126 + aa,1,36,100,RXF2
vfill,45725,45759,33,45726,1,24,100,RXF2
vfill,45725 + aa,45759 + aa,33,45726 + aa,1,24,100,RXF2

!!!!!!!!!!!!!!!!!!!!!!!!!!!!!!!!!!!!!!!!!!!!!!!!!!!!!!!!!!!!!

repl
*end
*set th 2
*loop 1

!!!!!!!!!!!!!!!!!!!!!!!!!!!!!!!!!!!!!!!!!!!!!!!!!!!!!!!!!!!!!!
!!!!!!!!!!!!!!!!!!!!!!!!!!!!!!!!!!!!!!!!!!!!!!!!!!!!!!!!!!!!!!
```

Appendix A.6: *rotate_2b.cgrd* – *cgrd*-file rotating 2D flap during transient analysis

!!Rotation of Flap

*set aa 48160

local 5,cylindrical,750,0,0,0,0,0

csys 5

vgen,2,0,42525,42525 + aa,aa,0,-0.2,0,1
vgen,2,0,45725,45725 + aa,aa,0,-0.2,0,1

!!Repeting the Mesh Filling

csys 1

!!Upper Surface
vfill,42500,42525,24,42501,1,2,aa,-1.1
vfill,40100,42500,23,40200,100,26,1,1 / 1.07
vfill,40100 + aa,42500 + aa,23,40200 + aa,100,26,1,1 / 1.07

!!Lower Surface
vfill,45700,45725,24,45701,1,2,aa,-1.1
vfill,45700,48100,23,45800,100,26,1,1.07
vfill,45700 + aa,48100 + aa,23,45800 + aa,100,26,1,1.07

!!Flap
vfill,42500,45700,11,42600,100,26,1,1.0
vfill,42500 + aa,45700 + aa,11,42600 + aa,100,26,1,1.0

!!Downstream Section
vfill,40125,40159,33,40126,1,36,100,1.05
vfill,40125 + aa,40159 + aa,33,40126 + aa,1,36,100,1.05
vfill,45725,45759,33,45726,1,24,100,1.05
vfill,45725 + aa,45759 + aa,33,45726 + aa,1,24,100,1.05

Appendix A.7: *Mesh_of_3D_Flap_Left_d.inp* – Input file creating 3D trailing edge flap section for the left wing

```
!!!!!!!!!!!!!!!!!!!!!!!!!!!!!!!!!!!!!!!!!!!!!!!!!!!!!!!!!!!!!
!!!!Mesh of 3D Flap      !!!!!!!!!!!!!!!!!!!!!!!!!!!!!!!!!
!!!!Left                 !!!!!!!!!!!!!!!!!!!!!!!!!!!!!!!!!
!!!!Alexander Moerchel   !!!!!!!!!!!!!!!!!!!!!!!!!!!!!!!!!
!!!!Created: 05/01/06    !!!!!!!!!!!!!!!!!!!!!!!!!!!!!!!!!
!!!!Last Update: 05/01/06  !!!!!!!!!!!!!!!!!!!!!!!!!!!!!!!!
!!!!!!!!!!!!!!!!!!!!!!!!!!!!!!!!!!!!!!!!!!!!!!!!!!!!!!!!!!!!!

csys 1

!!Right Wing!!!!!!!!!!!!!!!!!!!!!!!!!!!!!!!!!!!!!!!!!!!!!!!!

!!Plane 1

!Upper Flap Surface
v 7000001 3328 892.215 -3200
v 7000002 3328 885.453 -3231.51
v 7000003 3328 879.082 -3263.06
v 7000004 3328 873.272 -3294.82
v 7000005 3328 867.753 -3327.28
v 7000006 3328 862.444 -3359.17
v 7000007 3328 857.087 -3390.81
v 7000008 3328 851.474 -3423.21
v 7000009 3328 845.876 -3455.08
v 7000010 3328 840.704 -3484.07
v 7000011 3328 838.692 -3489.08
v 7000012 3328 1000 -4096

!Lower Flap Surface
v 7000021 3328 805.002 -3200
v 7000022 3328 809.684 -3231.29
v 7000023 3328 814.136 -3263.14
v 7000024 3328 818.713 -3295.64
v 7000025 3328 823.090 -3327.08
v 7000026 3328 827.200 -3359.67
v 7000027 3328 830.244 -3391.51
v 7000028 3328 832.269 -3423.73
v 7000029 3328 833.632 -3455.73
v 7000030 3328 834.511 -3484.73
v 7000031 3328 836.348 -3489.04
v 7000032 3328 744 -4096
v 7000041 3328 1384 -3200
v 7000044 3328 1384 -3424
v 7000045 3328 1384 -3456
v 7000052 3328 1384 -4096
v 7000061 3328 360 -3200
v 7000064 3328 360 -3424
v 7000065 3328 360 -3456
v 7000072 3328 360 -4096

!Splines
spl 11 vrange 7000001 7000010 1
spl 12 vrange 7000021 7000030 1

!Patches

ctab 24,shell,2
patch 7000061,7000064,7000030,7000021,7,18,1,50,7000101........1 / 1.2
patch 7000064,7000065,7000031,7000030,1,18,1,50,7000108........1 / 1.2
patch 7000065,7000072,7000032,7000031,20,18,1,50,7000109........1 / 1.2
```

171

```
patch 7000031,7000032,7000012,7000011,20,6,1,100,7001009
patch 7000001,7000010,7000044,7000041,7,18,1,50,7001601.......1,2
patch 7000010,7000011,7000045,7000044,1,18,1,50,7001608.......1,2
patch 7000011,7000012,7000052,7000045,20,18,1,50,7001609.......1,2


ctab 25,shell,2
patch 7000021,7000030,7000010,7000001,7,6,1,100,7001001
patch 7000030,7000031,7000011,7000010,1,6,1,100,7001008


!Extrusion from Plane 1 to Plane 2
*set of1 10000
*set nx12 8
*set distance 3328 - 3264
*set dt12 distance / nx12
ctab 32,fluid,2
cset news type 24
vcextrude,nx12,of1,cset,,,local,-dt12,0,0
ctab 33,fluid,2
cset news type 25
vcextrude,nx12,of1,cset,,,local,-dt12,0,0


!!Plane 2

!Upper Surface
v 7080001 3264 890.447 -3200
v 7080002 3264 883.672 -3231.14
v 7080003 3264 877.136 -3263.45
v 7080004 3264 871.336 -3295.13
v 7080005 3264 865.910 -3326.96
v 7080006 3264 860.495 -3359.40
v 7080007 3264 855.106 -3391.15
v 7080008 3264 849.605 -3422.87
v 7080009 3264 843.933 -3455.06
v 7080010 3264 838.648 -3484.62
v 7080011 3264 836.826 -3489.35
v 7080012 3264 1000 -4096


!Lower Surface
v 7080021 3264 803.201 -3200
v 7080022 3264 807.821 -3231.29
v 7080023 3264 812.314 -3263.39
v 7080024 3264 816.780 -3295.32
v 7080025 3264 821.226 -3327.33
v 7080026 3264 825.277 -3359.47
v 7080027 3264 828.339 -3391.64
v 7080028 3264 830.336 -3423.64
v 7080029 3264 831.688 -3455.60
v 7080030 3264 832.524 -3485.33
v 7080031 3264 834.202 -3489.31
v 7080032 3264 744 -4096
v 7080041 3264 1384 -3200
v 7080044 3264 1384 -3424
v 7080045 3264 1384 -3456
v 7080052 3264 1384 -4096
v 7080061 3264 360 -3200
v 7080064 3264 360 -3424
v 7080065 3264 360 -3456
v 7080072 3264 360 -4096


!Splines
spl 13 vrange 7080001 7080010 1
spl 14 vrange 7080021 7080030 1


!Patches
```

ctab 26,shell,2
patch 7080061,7080064,7080030,7080021,7,18,1,50,7080101,.......1 / 1.2
patch 7080064,7080065,7080031,7080030,1,18,1,50,7080108,.......1 / 1.2
patch 7080065,7080072,7080032,7080031,20,18,1,50,7080109,.......1 / 1.2
patch 7080031,7080032,7080012,7080011,20,6,1,100,7081009
patch 7080001,7080010,7080044,7080041,7,18,1,50,7081601,.......1.2
patch 7080010,7080011,7080045,7080044,1,18,1,50,7081608,.......1.2
patch 7080011,7080012,7080052,7080045,20,18,1,50,7081609,.......1.2

ctab 27,shell,3
patch 7080021,7080030,7080010,7080001,7,6,1,100,7081001
patch 7080030,7080031,7080011,7080010,1,6,1,100,7081008

!Extrusion from Plane 2 to Plane 3
*set ofl 10000
*set nx23 64
*set distance 3264 - 1216
*set dt23 distance / nx23

ctab 34,fluid,2
cset news type 26
vcextrude,nx23,ofl,cset,,,local,-dt23,0,0
ctab 35,solid,3
cset news type 27
vcextrude,nx23,ofl,cset,,,local,-dt23,0,0

!!Plane 3

!Upper Surface
v 7720001 1216 831.309 -3200
v 7720002 1216 824.234 -3230.93
v 7720003 1216 817.434 -3262.65
v 7720004 1216 811.116 -3295.06
v 7720005 1216 805.228 -3327.48
v 7720006 1216 799.605 -3359.11
v 7720007 1216 793.848 -3390.87
v 7720008 1216 787.895 -3423.23
v 7720009 1216 781.914 -3455.02
v 7720010 1216 776.270 -3484.99
v 7720011 1216 774.265 -3489.03
v 7720012 1216 1000 -4096

!Lower Surface
v 7720021 1216 744.015 -3200
v 7720022 1216 748.316 -3231.43
v 7720023 1216 752.452 -3263.36
v 7720024 1216 756.612 -3295.42
v 7720025 1216 760.671 -3327.42
v 7720026 1216 764.368 -3359.58
v 7720027 1216 767.017 -3391.53
v 7720028 1216 768.684 -3423.80
v 7720029 1216 769.701 -3455.70
v 7720030 1216 770.230 -3484.66
v 7720031 1216 771.851 -3488.93
v 7720032 1216 744 -4096
v 7720041 1216 1384 -3200
v 7720044 1216 1384 -3424
v 7720045 1216 1384 -3456
v 7720052 1216 1384 -4096
v 7720061 1216 360 -3200
v 7720064 1216 360 -3424
v 7720065 1216 360 -3456
v 7720072 1216 360 -4096

!Splines
spl 15 vrange 7720001 7720010 1
spl 16 vrange 7720021 7720030 1

!Patches

ctab 28.shell.2
patch 7720061.7720064.7720030.7720021.7.18.1.50.7720101........1 / 1.2
patch 7720064.7720065.7720031.7720030.1.18.1.50.7720108........1 / 1.2
patch 7720065.7720072.7720032.7720031.20.18.1.50.7720109........1 / 1.2
patch 7720031.7720032.7720012.7720011.20.6.1.100.7721009
patch 7720001.7720010.7720044.7720041.7.18.1.50.7721601........1.2
patch 7720010.7720011.7720045.7720044.1.18.1.50.7721608........1.2
patch 7720011.7720012.7720052.7720045.20.18.1.50.7721609........1.2

ctab 29.shell.2
patch 7720021.7720030.7720010.7720001.7.6.1.100.7721001
patch 7720030.7720031.7720011.7720010.1.6.1.100.7721008

!Extrusion from Plane 3 to Plane 4
*set ofl 10000
*set nx34 8
*set distance 1216 - 1152
*set dt34 distance / nx34

ctab 36.fluid.2
cset news type 28
vcextrude.nx34.ofl.cset...local.-dt34.0.0
ctab 37.fluid.2
cset news type 29
vcextrude.nx34.ofl.cset...local.-dt34.0.0

!!Plane 4

!Upper Surface
v 7800001 1152 829.355 -3200
v 7800002 1152 822.377 -3230.93
v 7800003 1152 815.492 -3263
v 7800004 1152 809.303 -3294.73
v 7800005 1152 803.405 -3327.16
v 7800006 1152 797.626 -3359.56
v 7800007 1152 791.891 -3391.1
v 7800008 1152 786.042 -3422.89
v 7800009 1152 779.957 -3455.16
v 7800010 1152 774.561 -3483.8
v 7800011 1152 773.495 -3488.65
v 7800012 1152 1000 -4096

!Lower Surface
v 7800021 1152 742.141 -3200
v 7800022 1152 746.488 -3231.67
v 7800023 1152 750.540 -3263.15
v 7800024 1152 754.761 -3295.66
v 7800025 1152 758.746 -3327.21
v 7800026 1152 762.488 -3359.78
v 7800027 1152 765.129 -3391.65
v 7800028 1152 766.757 -3423.73
v 7800029 1152 767.760 -3455.74
v 7800030 1152 768.308 -3483.89
v 7800031 1152 770.827 -3489.21
v 7800032 1152 744 -4096
v 7800041 1152 1384 -3200
v 7800044 1152 1384 -3424

```
v 7800045 1152 1384 -3456
v 7800052 1152 1384 -4096
v 7800061 1152 360 -3200
v 7800064 1152 360 -3424
v 7800065 1152 360 -3456
v 7800072 1152 360 -4096

!Splines
spl 17 vrange 7800001 7800010 1
spl 18 vrange 7800021 7800030 1

!Patches
ctab 30.shell.2
patch 7800061.7800064.7800030.7800021.7.18.1.50.7800101........1 / 1.2
patch 7800064.7800065.7800031.7800030.1.18.1.50.7800108........1 / 1.2
patch 7800065.7800072.7800032.7800031.20.18.1.50.7800109........1 / 1.2
patch 7800031.7800032.7800012.7800011.20.6.1.100.7801009
patch 7800001.7800010.7800044.7800041.7.18.1.50.7801601........1.2
patch 7800010.7800011.7800045.7800044.1.18.1.50.7801608........1.2
patch 7800011.7800012.7800052.7800045.20.18.1.50.7801609........1.2
ctab 31.shell.2
patch 7800021.7800030.7800010.7800001.7.6.1.100.7801001
patch 7800030.7800031.7800011.7800010.1.6.1.100.7801008

!!Filling Vertices between Plane 1 and Plane 2
*set inc 0
*define noexecute
vfill.7000101 + inc.7080101 + inc.7.7010101 + inc.of1.29.1
*set inc inc + 50
*end
*loop 0.48.1

!!Filling Vertices between Plane 2 and Plane 3
*set inc 0
*define noexecute
vfill.7080101 + inc.7720101 + inc.63.7090101 + inc.of1.29.1
*set inc inc + 50
*end
*loop 0.48.1

!!Filling Vertices between Plane 3 and Plane 4
*set inc 0
*define noexecute
vfill.7720101 + inc.7800101 + inc.7.7730101 + inc.of1.29.1
*set inc inc + 50
*end
*loop 0.48.1
!!Visualization
cset all
cplo

!!!!!!!!!!!!!!!!!!!!!!!!!!!!!!!!!!!!!!!!!!!!!!!!!!!!!!!!!!!!!!!!!!!!!
!!!!!!!!!!!!!!!!!!!!!!!!!!!!!!!!!!!!!!!!!!!!!!!!!!!!!!!!!!!!!!!!!!!!!
```

Appendix A.8: *Rotation_of_3D_Flap_2.inp* – Input file rotating 3D flap

```
!!!!!!!!!!!!!!!!!!!!!!!!!!!!!!!!!!!!!!!!!!!!!!!!!!!!!!!!!!!!!!!!!!!!
!!!!Mesh of 3D Flap        !!!!!!!!!!!!!!!!!!!!!!!!!!!!!!!
!!!!Flap Rotation          !!!!!!!!!!!!!!!!!!!!!!!!!!!!!!!
!!!!Alexander Moerchel     !!!!!!!!!!!!!!!!!!!!!!!!!!!!!!!
!!!!Created: 04/25/06      !!!!!!!!!!!!!!!!!!!!!!!!!!!!!!!
!!!!Last Update: 05/01/06  !!!!!!!!!!!!!!!!!!!!!!!!!!!!!!!
!!!!!!!!!!!!!!!!!!!!!!!!!!!!!!!!!!!!!!!!!!!!!!!!!!!!!!!!!!!!!!!!!!!!

*set delta -2

!!Right Wing!!!!!!!!!!!!!!!!!!!!!!!!!!!!!!!!!!!!!!!!!!!!!

!!Rotation of Side 1 Flap Vertices

!Plane 2
csys 10
vgen 2,0,6081003,6081009,1,,delta
vgen 2,0,6081603,6081609,1,,delta

!Plane 3
csys 11
vgen 2,0,6721003,6721009,1,,delta
vgen 2,0,6721603,6721609,1,,delta

!!Refilling Vertices
csys 1

!Plane 2
vfill 6081001,6081003,1,6081002,,2,600
vfill 6081009,6081029,19,6081010,1,2,600
vfill 6080102,6081002,17,6080152,50,27,1,1 / 1.2
vfill 6081002,6081602,5,6081102,100,27,1
vfill 6081602,6082502,17,6081652,50,27,1,1,2

!Plane 3
vfill 6721001,6721003,1,6721002,,2,600
vfill 6721009,6721029,19,6721010,1,2,600
vfill 6720102,6721002,17,6720152,50,27,1,1 / 1.2
vfill 6721002,6721602,5,6721102,100,27,1
vfill 6721602,6722502,17,6721652,50,27,1,1,2

!!Filling Vertices between Plane 1 and Plane 2

*set inc 0
*define noexecute
vfill,6010101 + inc,6080101 + inc,6,6020101 + inc,of1,29,1
*set inc inc + 50
*end
*loop 0,18,1

*set inc 0
*define noexecute
vfill,6011001 + inc,6081001 + inc,6,6021001 + inc,of1,29,1
*set inc inc + 100
*end
*loop 0,6,1

*set inc 0
*define noexecute
vfill,6011601 + inc,6081601 + inc,6,6021601 + inc,of1,29,1
*set inc inc + 50
```

*end
*loop 0.18.1

!!Filling Vertices between Plane 2 and Plane 3

*set inc 0
*define noexecute
vfill,6080101 + inc,6720101 + inc,63,6090101 + inc,of1,29,1
*set inc inc + 50
*end
*loop 0.18.1

*set inc 0
*define noexecute
vfill,6081001 + inc,6721001 + inc,63,6091001 + inc,of1,29,1
*set inc inc + 100
*end
*loop 0.6.1

*set inc 0
*define noexecute
vfill,6081601 + inc,6721601 + inc,63,6091601 + inc,of1,29,1
*set inc inc + 50
*end
*loop 0.18.1

!!Filling Vertices between Plane 3 and Plane 4

*set inc 0
*define noexecute
vfill,6720101 + inc,6790101 + inc,6,6730101 + inc,of1,29,1
*set inc inc + 50
*end
*loop 0.18.1

*set inc 0
*define noexecute
vfill,6721001 + inc,6791001 + inc,6,6731001 + inc,of1,29,1
*set inc inc + 100
*end
*loop 0.6.1

*set inc 0
*define noexecute
vfill,6721601 + inc,6791601 + inc,6,6731601 + inc,of1,29,1
*set inc inc + 50
*end
*loop 0.18.1

*set delta -2

!!Left Wing!!!

!!Rotation of Side 1 Flap Vertices

!Plane 2
csys 12
vgen 2,0,7081003,7081009,1,,delta
vgen 2,0,7081603,7081609,1,,delta

!Plane 3
csys 13
vgen 2,0,7721003,7721009,1,,delta

177

vgen 2,0,7721603,7721609,1,,delta

!!Refilling Vertices
csys 1

!Plane 2
vfill 7081001,7081003,1,7081002,,2,600
vfill 7081009,7081029,19,7081010,1,2,600
vfill 7080102,7081002,17,7080152,50,27,1,1 / 1.2
vfill 7081002,7081602,5,7081102,100,27,1
vfill 7081602,7082502,17,7081652,50,27,1,1.2

!Plane 3
vfill 7721001,7721003,1,7721002,,2,600
vfill 7721009,7721029,19,7721010,1,2,600
vfill 7720102,7721002,17,7720152,50,27,1,1 / 1.2
vfill 7721002,7721602,5,7721102,100,27,1
vfill 7721602,7722502,17,7721652,50,27,1,1.2

!!Filling Vertices between Plane 1 and Plane 2

*set inc 0
*define noexecute
vfill,7010101 + inc,7080101 + inc,6,7020101 + inc,of1,29,1
*set inc inc + 50
*end
*loop 0,18,1

*set inc 0
*define noexecute
vfill,7011001 + inc,7081001 + inc,6,7021001 + inc,of1,29,1
*set inc inc + 100
*end
*loop 0,6,1

*set inc 0
*define noexecute
vfill,7011601 + inc,7081601 + inc,6,7021601 + inc,of1,29,1
*set inc inc + 50
*end
*loop 0,18,1

!!Filling Vertices between Plane 2 and Plane 3

*set inc 0
*define noexecute
vfill,7080101 + inc,7720101 + inc,63,7090101 + inc,of1,29,1
*set inc inc + 50
*end
*loop 0,18,1
*set inc 0
*define noexecute
vfill,7081001 + inc,7721001 + inc,63,7091001 + inc,of1,29,1
*set inc inc + 100
*end
*loop 0,6,1

*set inc 0
*define noexecute
vfill,7081601 + inc,7721601 + inc,63,7091601 + inc,of1,29,1
*set inc inc + 50
*end
*loop 0,18,1

"Filling Vertices between Plane 3 and Plane 4

```
*set inc 0
*define noexecute
vfill,7720101 + inc,7790101 + inc,6 7730101 + inc,ofl,29,1
*set inc inc + 50
*end
*loop 0,18,1

*set inc 0
*define noexecute
vfill,7721001 + inc,7791001 + inc,6,7731001 + inc,ofl,29,1
*set inc inc + 100
*end
*loop 0,6,1

*set inc 0
*define noexecute
vfill,7721601 + inc,7791601 + inc,6,7731601 + inc,ofl,29,1
*set inc inc + 50
*end
*loop 0,18,1
```

"Visualization

repl

!!
!!

Appendix A.9: *rotate_3D_flap_2c.cgrd* – *cgrd*-file rotating 3D flap during transient analysis

```
!!Rotation of 3D Flap

csys 1
local 12.cylindrical.3320.848.385.-3200.0.0.90

csys 1
local 13.cylindrical.1160.785.987.-3200.0.0.90

!!Plane 2
csys 12
vgen 2.0.7081003.7081009.1..-0.1
vgen 2.0.7081603.7081609.1..-0.1

!!Plane 3
csys 13
vgen 2.0.7721003.7721009.1..-0.1
vgen 2.0.7721603.7721609.1..-0.1

!!Refilling Vertices
csys 1

!!Plane 2
vfill 7081001.7081003.1.7081002..2.600
vfill 7081009.7081029.19.7081010.1.2.600
vfill 7080102.7081002.17.7080152.50.27.1.1 / 1.2
vfill 7081002.7081602.5.7081102.100.27.1
vfill 7081602.7082502.17.7081652.50.27.1.1.2

!!Plane 3
vfill 7721001.7721003.1.7721002..2.600
vfill 7721009.7721029.19.7721010.1.2.600
vfill 7720102.7721002.17.7720152.50.27.1.1 / 1.2
vfill 7721002.7721602.5.7721102.100.27.1
vfill 7721602.7722502.17.7721652.50.27.1.1.2

!!Filling Vertices between Plane 1 and Plane 2

*set inc 0
*define noexecute
vfill.7010101 + inc.7080101 + inc.6.7020101 + inc.of1.29.1
*set inc inc + 50
*end
*loop 0.18.1

*set inc 0
*define noexecute
vfill.7011001 + inc.7081001 + inc.6.7021001 + inc.of1.29.1
*set inc inc + 100
*end
*loop 0.6.1

*set inc 0
*define noexecute
vfill.7011601 + inc.7081601 + inc.6.7021601 + inc.of1.29.1
*set inc inc + 50
*end
*loop 0.18.1

!!Filling Vertices between Plane 2 and Plane 3
```

```
*set inc 0
*define noexecute
vfill.7080101 + inc.7720101 + inc.63.7090101 + inc.ofl.29 1
*set inc inc + 50
*end
*loop 0.18.1


*set inc 0
*define noexecute
vfill.7081001 + inc.7721001 + inc.63.7091001 + inc.ofl.29 1
*set inc inc + 100
*end
*loop 0.6.1


*set inc 0
*define noexecute
vfill.7081601 + inc.7721601 + inc.63.7091601 + inc.ofl.29.1
*set inc inc + 50
*end
*loop 0.18.1
```

''Filling Vertices between Plane 3 and Plane 4

```
*set inc 0
*define noexecute
vfill.7720101 + inc.7790101 + inc.6.7730101 + inc.ofl.29 1
*set inc inc + 50
*end
*loop 0.18.1


*set inc 0
*define noexecute
vfill.7721001 + inc.7791001 + inc.6.7731001 + inc.ofl.29.1
*set inc inc + 100
*end
*loop 0.6.1


*set inc 0
*define noexecute
vfill.7721601 + inc.7791601 + inc.6.7731601 + inc.ofl.29.1
*set inc inc + 50
*end
*loop 0.18 1
```

IIIIIIIIIIIIIIIIIIIIIIIIIIIIIIIIIIIIIIIIIIIIIIIIIIIIIIIIIIIIIIII
IIIIIIIIIIIIIIIIIIIIIIIIIIIIIIIIIIIIIIIIIIIIIIIIIIIIIIIIIIIIIIII

181

Appendix A.10: *Post_1_Qualitative.inp* – Post-processing script for the qualitative analysis

```
!!!!!!!!!!!!!!!!!!!!!!!!!!!!!!!!!!!!!!!!!!!!!!!!!!!!!!!!!!!!!!!!!!!!!!!!!!!!
!!!!Mesh Generation          !!!!!!!!!!!!!!!!!!!!!!!!!!!!!!
!!!!NACA 0012                !!!!!!!!!!!!!!!!!!!!!!!!!!!!!!!
!!!!Alexander Moerchel       !!!!!!!!!!!!!!!!!!!!!!!!!!!!!!!
!!!!Created: 02/28/06        !!!!!!!!!!!!!!!!!!!!!!!!!!!!!!!
!!!!Last Update: 07/07/06    !!!!!!!!!!!!!!!!!!!!!!!!!!!!!!!
!!!!!!!!!!!!!!!!!!!!!!!!!!!!!!!!!!!!!!!!!!!!!!!!!!!!!!!!!!!!!!!!!!!!!!!!!!!!


!!!!!!!!!!!!!!!!!!!!!!!!!!!!!!!!!!!!!!!!!!!!!!!!!!!!!!!!!!!!!!!!!!!!!!!'
!!Set Up of the Plot Window        !!!!!!!!!!!!!!!!!!!!!!!!!!!!!!!
!!!!!!!!!!!!!!!!!!!!!!!!!!!!!!!!!!!!!!!!!!!!!!!!!!!!!!!!!!!!!!!!!!!!


plty sect
axis y
spoint 0 0 -20
snorm 0 0 1
view snorm
cset news fluid

angl 0
dist 100
center 1000 -60 0

popt vect
vescale 1.15
csca.14.user 0 1.4
ugrid on 15.80
getc all
oper getc vmag 4
oper smult 0.01.4.4

cplo
evfi conn
cset news fluid


!!!!!!!!!!!!!!!!!!!!!!!!!!!!!!!!!!!!!!!!!!!!!!!!!!!!!!!!!!!!!!!!!!
!!Loading Data for Successive Time Steps!!!!!!!!!!!!!
!!!!!!!!!!!!!!!!!!!!!!!!!!!!!!!!!!!!!!!!!!!!!!!!!!!!!!!!!!!!!!!!!!


*set tx1 0
*define noexecute
store itstep tx1
getc all
oper getc vmag 4
oper smult 0.01.4.4
popt vect
vescale 1.3
csca.14.user 0 1.4
ugrid on 15.80
repl
!scdump gif.n1
*set tx1 tx1 + 10
*end
*set n1.2.1
*loop 0.100.1
scdump off
!!!!!!!!!!!!!!!!!!!!!!!!!!!!!!!!!!!!!!!!!!!!!!!!!!!!!!!!!!!!!!!!
!!Command Library for Other Variables!!!!!!!!!!!!!!!!
```

182

Appendix A.11: *Post_2_Quantitative.inp* – Post-processing script for the quantitative analysis

```
!!!!!!!!!!!!!!!!!!!!!!!!!!!!!!!!!!!!!!!!!!!!!!!!!!!!!!!!!!!!!!!!!
!!!!Post-Processing        !!!!!!!!!!!!!!!!!!!!!!!!!!!!!
!!!!Quantitative Analysis  !!!!!!!!!!!!!!!!!!!!!!!!!!!!!
!!!!Alexander Moerchel      !!!!!!!!!!!!!!!!!!!!!!!!!!!!!
!!!!Created  03/14/06       !!!!!!!!!!!!!!!!!!!!!!!!!!!!!
!!!!Last Update  07/07/06   !!!!!!!!!!!!!!!!!!!!!!!!!!!!!
!!!!!!!!!!!!!!!!!!!!!!!!!!!!!!!!!!!!!!!!!!!!!!!!!!!!!!!!!!!!!!!!!


!!!!!!!!!!!!!!!!!!!!!!!!!!!!!!!!!!!!!!!!!!!!!!!!!!!!!!!!!!!!!!!
!!Loading Forces at Airfoil Surface   !!!!!!!!!!!!!!!!!
!!!!!!!!!!!!!!!!!!!!!!!!!!!!!!!!!!!!!!!!!!!!!!!!!!!!!!!!!!!!!!!


popt cont
getw sfty
cset news type 72
wplot

*get amxve
*set tx1 10
*set xs1 1
*define noexecute
store itstep tx1
*get t time
getw sfty
cset news type 72
wplot

csys 1
oper getw.x.1.2
oper getw.sfty.3.pstat
oper multip 2.3.4
*get Msy1.rtot.4
*get Fsy1.rtot.3

oper getw.y.1.2
oper getw.sftx.3.pstat
oper multip.2.3.4
*get Msx1.rtot.4
*get Fsx1.rtot.3

v a + 1000 + xs1.t.Fsy1.Msy1
v a + 2000 + xs1.t.Fsx1.Msx1

*set xs1 xs1 + 1
*set tx1 tx1 + 10
*end
*loop 0.69.1


!!!!!!!!!!!!!!!!!!!!!!!!!!!!!!!!!!!!!!!!!!!!!!!!!!!!!!!!!!!!!!!
!!Writing Data to TXT-File  !!!!!!!!!!!!!!!!!!!!!!!!!!!!!
!!!!!!!!!!!!!!!!!!!!!!!!!!!!!!!!!!!!!!!!!!!!!!!!!!!!!!!!!!!!!!!
vset news vrang a + 1000. a + 1001 + 69
vset add vrang a + 2000. a + 2001 + 69
ofile center_of_pressure_location txt
vlist a + 1000.a + 2001 + 69
close center_of_pressure_location txt
```

184

APPENDIX B

STAR-CD OUTPUT FILES

Content:

Appendix B.1: *center_of_pressure_location_0_30_ in_200.txt* – **Output file for case 4 of 2D transient analysis**

```
                    VERTEX LIST IN COORDINATE SYSTEM NO.   1
                      (* INDICATES VERTICES IN CURRENT VSET)

          VERTEX              X                Y                  Z
  *        97320      0.100000E-01        8.86476          5825.74
  *        97321      0.200000E-01        29.3785          15837.2
  *        97322      0.300000E-01        57.5078          29137.9
  *        97323      0.400000E-01        87.4525          42702.0
  *        97324      0.500000E-01        119.353          56756.1
  *        97325      0.600000E-01        152.176          70937.7
  *        97326      0.700000E-01        185.451          85089.9
  *        97327      0.800000E-01        219.358          99319.7
  *        97328      0.900000E-01        252.204          112870.
  *        97329      0.100000            284.402          125939.
  *        97330      0.110000            315.411          138317.
  *        97331      0.120000            344.550          149688.
  *        97332      0.130000            370.261          159263.
  *        97333      0.140000            388.549          164300.
  *        97334      0.150000            414.822          176313.
  *        97335      0.160000            406.463          166255.
  *        97336      0.170000            425.269          176958.
  *        97337      0.180000            424.150          173349.
  *        97338      0.190000            437.597          180243.
  *        97339      0.200000            433.281          176590.
  *        97340      0.210000            437.497          177955.
  *        97341      0.220000            438.463          178778.
  *        97342      0.230000            435.634          175625.
  *        97343      0.240000            441.326          179952.
  *        97344      0.250000            434.021          174088.
  *        97345      0.260000            442.319          180360.
  *        97346      0.270000            432.835          173152.
  *        97347      0.280000            444.152          181427.
  *        97348      0.290000            431.929          172487.
  *        97349      0.300000            445.123          181963.
  *        97350      0.310000            430.047          171345.
  *        97351      0.319999            445.045          181953.
  *        97352      0.329999            429.153          170897.
  *        97353      0.339999            444.451          181633.
  *        97354      0.349999            429.004          170974.
  *        97355      0.359999            444.589          181680.
  *        97356      0.369999            430.100          171828.
  *        97357      0.379999            444.835          181759.
  *        97358      0.389999            430.884          172458.
  *        97359      0.399998            443.699          181003.
  *        97360      0.409998            431.868          173281.
  *        97361      0.419998            443.226          180698.
  *        97362      0.429998            432.803          173960.
  *        97363      0.439998            442.294          179999.
  *        97364      0.449998            433.721          174677.
  *        97365      0.459998            441.620          179480.
  *        97366      0.469997            434.741          175425.
  *        97367      0.479997            440.232          178528.
  *        97368      0.489997            435.907          176253.
```

186

*	97369	0.499997	438.559	177385.
*	97370	0.509997	437.260	177266.
*	97371	0.519997	436.782	176208.
*	97372	0.529997	438.467	178046.
*	97373	0.539997	434.941	174937.
*	97374	0.549996	439.542	178771.
*	97375	0.559996	433.755	174074.
*	97376	0.569996	440.363	179295.
*	97377	0.579996	432.452	173210.
*	97378	0.589996	441.409	179960.
*	97379	0.599996	431.213	172402.
*	97380	0.609996	442.514	180696.
*	97381	0.619996	430.203	171766.
*	97382	0.629995	443.345	181181.
*	97383	0.639995	428.686	170849.
*	97384	0.649995	443.785	181444.
*	97385	0.659995	428.347	170645.
*	97386	0.669995	443.672	181320.
*	97387	0.679995	428.473	170847.
*	97388	0.689995	443.965	181444.
*	97389	0.699995	429.168	171397.
*	97390	0.709994	443.770	181277.
*	97391	0.719994	430.261	172225.
*	97392	0.729994	443.172	180814.
*	97393	0.739994	431.235	172985.
*	97394	0.749994	442.836	180562.
*	97395	0.759994	432.558	173899.
*	97396	0.769994	441.655	179650.
*	97397	0.779994	433.518	174608.
*	97398	0.789993	441.231	179290.
*	97399	0.799993	434.517	175332.
*	97400	0.809993	439.986	178392.
*	97401	0.819993	435.945	176311.
*	97402	0.829993	438.211	177196.
*	97403	0.839993	437.602	177492.
*	97404	0.849993	436.551	176017.
*	97405	0.859993	438.620	178140.
*	97406	0.869992	434.561	174685.
*	97407	0.879992	439.615	178818.
*	97408	0.889992	433.306	173782.
*	97409	0.899992	440.297	179256.
*	97410	0.909992	432.072	172982.
*	97411	0.919992	441.543	180058.
*	97412	0.929992	431.135	172365.
*	97413	0.939991	442.592	180738.
*	97414	0.949991	430.050	171668.
*	97415	0.959991	443.290	181137.
*	97416	0.969991	428.631	170805.
*	97417	0.979991	443.701	181377.
*	97418	0.989991	428.226	170577.
*	97419	1.00000	443.501	181206.
*	98320	0.100000E-01	3.01158	16.6680
*	98321	0.200000E-01	3.30632	30.3738
*	98322	0.300000E-01	3.90527	29.1502
*	98323	0.400000E-01	4.76931	10.8282
*	98324	0.500000E-01	5.82577	-22.8891
*	98325	0.600000E-01	7.05673	-72.4104

*	98326	0.700000E-01	8.39542	-139.244
*	98327	0.800000E-01	9.84530	-224.411
*	98328	0.900000E-01	11.3000	-328.419
*	98329	0.100000	12.7632	-453.632
*	98330	0.110000	14.2156	-601.186
*	98331	0.120000	15.5987	-772.983
*	98332	0.130000	16.7510	-973.691
*	98333	0.140000	16.6859	-1154.65
*	98334	0.150000	19.8038	-1551.92
*	98335	0.160000	15.7480	-1578.26
*	98336	0.170000	17.5962	-1709.27
*	98337	0.180000	14.7549	-1590.96
*	98338	0.190000	15.8941	-1708.45
*	98339	0.200000	14.0081	-1672.09
*	98340	0.210000	13.6044	-1676.37
*	98341	0.220000	13.8527	-1743.80
*	98342	0.230000	12.0462	-1642.90
*	98343	0.240000	13.6943	-1772.26
*	98344	0.250000	11.1582	-1622.62
*	98345	0.260000	13.6240	-1785.84
*	98346	0.270000	10.7245	-1610.89
*	98347	0.280000	13.8961	-1810.77
*	98348	0.290000	10.4325	-1602.54
*	98349	0.300000	14.0447	-1822.55
*	98350	0.310000	10.1330	-1594.41
*	98351	0.319999	14.0757	-1830.31
*	98352	0.329999	10.0731	-1594.21
*	98353	0.339999	14.0144	-1823.80
*	98354	0.349999	10.2017	-1604.05
*	98355	0.359999	13.9960	-1822.02
*	98356	0.369999	10.5715	-1624.83
*	98357	0.379999	14.0280	-1819.61
*	98358	0.389999	10.9017	-1651.02
*	98359	0.399998	13.7525	-1802.77
*	98360	0.409998	11.2573	-1674.41
*	98361	0.419998	13.6469	-1796.96
*	98362	0.429998	11.4896	-1688.49
*	98363	0.439998	13.3847	-1780.52
*	98364	0.449998	11.7674	-1700.40
*	98365	0.459998	13.1838	-1766.72
*	98366	0.469997	12.0329	-1715.09
*	98367	0.479997	12.8356	-1743.71
*	98368	0.489997	12.3507	-1731.84
*	98369	0.499997	12.4127	-1716.27
*	98370	0.509997	12.7385	-1755.96
*	98371	0.519997	12.0067	-1691.39
*	98372	0.529997	12.9861	-1766.60
*	98373	0.539997	11.5382	-1663.62
*	98374	0.549996	13.2265	-1777.43
*	98375	0.559996	11.2177	-1643.75
*	98376	0.569996	13.3632	-1783.43
*	98377	0.579996	10.9144	-1628.07
*	98378	0.589996	13.5899	-1794.20
*	98379	0.599996	10.6413	-1611.56
*	98380	0.609996	13.8598	-1809.60
*	98381	0.619996	10.4630	-1601.41
*	98382	0.629995	14.0153	-1816.90

188

*	98383	0.639995	10.2108	-1591.32
*	98384	0.649995	14.1038	-1821.85
*	98385	0.659995	10.1586	-1590.59
*	98386	0.669995	14.0207	-1816.84
*	98387	0.679995	10.3020	-1603.02
*	98388	0.689995	14.0446	-1817.36
*	98389	0.699995	10.5267	-1619.35
*	98390	0.709994	13.9742	-1812.90
*	98391	0.719994	10.9128	-1647.56
*	98392	0.729994	13.7763	-1799.99
*	98393	0.739994	11.2007	-1667.24
*	98394	0.749994	13.6876	-1795.80
*	98395	0.759994	11.5507	-1688.28
*	98396	0.769994	13.2879	-1772.83
*	98397	0.779994	11.7788	-1701.02
*	98398	0.789993	13.1468	-1764.21
*	98399	0.799993	12.0175	-1713.92
*	98400	0.809993	12.7845	-1741.00
*	98401	0.819993	12.3744	-1734.54
*	98402	0.829993	12.3623	-1713.72
*	98403	0.839993	12.8209	-1761.43
*	98404	0.849993	11.9211	-1687.56
*	98405	0.859993	12.9987	-1767.96
*	98406	0.869992	11.4492	-1659.61
*	98407	0.879992	13.2296	-1778.14
*	98408	0.889992	11.1038	-1638.73
*	98409	0.899992	13.3474	-1782.97
*	98410	0.909992	10.8480	-1624.67
*	98411	0.919992	13.6164	-1797.17
*	98412	0.929992	10.6237	-1611.50
*	98413	0.939991	13.8516	-1810.55
*	98414	0.949991	10.4228	-1600.84
*	98415	0.959991	13.9840	-1816.54
*	98416	0.969991	10.1806	-1591.88
*	98417	0.979991	14.0571	-1820.52
*	98418	0.989991	10.1378	-1591.61
*	98419	1.00000	13.9655	-1814.96

Appendix B.2: *center_of_pressure_location_0_30_ in_20.txt* – **Output file for case 5 of 2D transient analysis**

```
             VERTEX LIST IN COORDINATE SYSTEM NO.    1
              (*  INDICATES VERTICES IN CURRENT VSET)


           VERTEX              X               Y               Z
    *      97320        0.100000        2.25680        1252.85
    *      97321        0.200000        35.3328        15815.1
    *      97322        0.300000        73.0718        31509.8
    *      97323        0.400000        111.050        47185.6
    *      97324        0.500000        148.508        62571.9
    *      97325        0.600000        185.134        77587.8
    *      97326        0.700000        221.032        92270.0
    *      97327        0.800000        255.733        106385.
    *      97328        0.899999        288.746        119737.
    *      97329        0.999999        319.429        132025.
    *      97330        1.10000         346.984        142893.
    *      97331        1.20000         369.251        151473.
    *      97332        1.30000         384.796        157179.
    *      97333        1.40000         394.600        160631.
    *      97334        1.50000         399.932        162042.
    *      97335        1.60000         404.893        164000.
    *      97336        1.70000         423.663        171721.
    *      97337        1.80000         428.376        173374.
    *      97338        1.90000         427.754        172992.
    *      97339        2.00000         426.431        172457.
    *      97340        2.10000         425.060        171540.
    *      97341        2.20000         426.659        171711.
    *      97342        2.30000         430.382        174608.
    *      97343        2.40000         426.661        172572.
    *      97344        2.50000         424.512        170915.
    *      97345        2.60000         425.505        171153.
    *      97346        2.70000         428.459        172946.
    *      97347        2.80000         429.115        173779.
    *      97348        2.90000         425.663        172196.
    *      97349        3.00000         424.065        170916.
    *      97350        3.10000         423.980        170660.
    *      97351        3.20000         428.057        172552.
    *      97352        3.30000         428.979        173634.
    *      97353        3.40000         424.413        171741.
    *      97354        3.50000         425.453        171614.
    *      97355        3.60000         428.715        172864.
    *      97356        3.70000         432.462        175826.
    *      97357        3.80000         429.539        174050.
    *      97358        3.90000         423.118        170223.
    *      97359        4.00000         423.850        170288.
    *      97360        4.10000         428.497        173324.
    *      97361        4.20000         428.201        173244.
    *      97362        4.30000         425.355        171721.
    *      97363        4.40001         424.288        170773.
    *      97364        4.50001         428.259        172582.
    *      97365        4.60001         430.395        174547.
    *      97366        4.70001         425.414        171850.
    *      97367        4.80001         424.297        170672.
    *      97368        4.90002         426.099        171394.
```

*	97369	5.00002	430.643	174939.
*	97370	5.10002	429.041	173827.
*	97371	5.20002	427.062	172893.
*	97372	5.30003	422.954	169810.
*	97373	5.40003	426.723	171695.
*	97374	5.50003	429.506	174085.
*	97375	5.60003	426.170	172442.
*	97376	5.70004	423.578	170600.
*	97377	5.80004	424.094	170670.
*	97378	5.90004	426.218	171366.
*	97379	6.00004	430.785	174777.
*	97380	6.10004	427.538	173032.
*	97381	6.20005	422.881	169901.
*	97382	6.30005	427.809	172363.
*	97383	6.40005	429.409	173854.
*	97384	6.50005	428.039	173309.
*	97385	6.60006	423.361	170226.
*	97386	6.70006	424.088	170640.
*	97387	6.80006	425.419	171225.
*	97388	6.90006	427.915	172785.
*	97389	7.00007	426.168	172436.
*	97390	7.10007	424.424	171183.
*	97391	7.20007	423.715	170571.
*	97392	7.30007	428.534	173522.
*	97393	7.40007	425.459	172317.
*	97394	7.50008	426.252	171533.
*	97395	7.60008	428.213	172880.
*	97396	7.70008	428.874	173703.
*	97397	7.80008	425.346	171833.
*	97398	7.90009	424.234	170737.
*	97399	8.00009	428.093	173197.
*	97400	8.10009	427.884	173141.
*	97401	8.20009	425.845	172120.
*	97402	8.30009	425.789	171390.
*	97403	8.40010	427.802	172603.
*	97404	8.50010	430.342	174551.
*	97405	8.60010	427.159	172880.
*	97406	8.70010	420.230	168340.
*	97407	8.80011	425.719	171208.
*	97408	8.90011	428.433	172885.
*	97409	9.00011	430.899	174869.
*	97410	9.10011	425.824	172228.
*	97411	9.20012	423.432	170361.
*	97412	9.30012	426.812	171970.
*	97413	9.40012	430.450	174654.
*	97414	9.50012	427.217	172899.
*	97415	9.60012	421.668	169232.
*	97416	9.70013	428.445	172926.
*	97417	9.80013	430.605	174656.
*	97418	9.90013	427.283	172918.
*	97419	10.0000	421.853	169392.
*	98320	0.100000	2.99967	3.02452
*	98321	0.200000	3.16723	-15.3158
*	98322	0.300000	3.41404	-56.5761
*	98323	0.400000	3.71765	-105.221
*	98324	0.500000	4.06837	-162.166
*	98325	0.600000	4.48974	-228.076

191

*	98326	0.700000	4.96682	-306.006
*	98327	0.800000	5.52168	-397.919
*	98328	0.899999	6.13835	-503.470
*	98329	0.999999	6.85613	-625.296
*	98330	1.10000	7.61265	-763.680
*	98331	1.20000	8.40915	-918.863
*	98332	1.30000	9.29279	-1091.90
*	98333	1.40000	10.3937	-1292.38
*	98334	1.50000	11.4554	-1502.48
*	98335	1.60000	13.0775	-1749.45
*	98336	1.70000	12.6117	-1651.65
*	98337	1.80000	12.2884	-1665.20
*	98338	1.90000	12.1491	-1662.87
*	98339	2.00000	12.1584	-1657.42
*	98340	2.10000	11.8101	-1632.93
*	98341	2.20000	11.3250	-1607.28
*	98342	2.30000	12.7507	-1693.43
*	98343	2.40000	12.2327	-1654.09
*	98344	2.50000	11.3983	1602.10
*	98345	2.60000	11.2090	-1599.93
*	98346	2.70000	11.7930	-1641.94
*	98347	2.80000	12.4036	-1674.25
*	98348	2.90000	12.2137	-1656.27
*	98349	3.00000	11.5762	-1618.48
*	98350	3.10000	11.3457	-1604.01
*	98351	3.20000	11.5385	-1629.18
*	98352	3.30000	12.3050	-1669.28
*	98353	3.40000	12.3983	-1658.05
*	98354	3.50000	11.7299	-1629.60
*	98355	3.60000	11.6167	-1627.70
*	98356	3.70000	13.1626	-1719.96
*	98357	3.80000	12.5190	-1684.65
*	98358	3.90000	11.3406	-1596.51
*	98359	4.00000	11.0371	-1581.95
*	98360	4.10000	12.2095	-1659.37
*	98361	4.20000	12.2678	-1665.16
*	98362	4.30000	11.8482	-1635.52
*	98363	4.40001	11.3164	-1604.91
*	98364	4.50001	11.4931	-1627.80
*	98365	4.60001	12.6354	-1694.81
*	98366	4.70001	12.0252	-1641.46
*	98367	4.80001	11.2342	-1595.80
*	98368	4.90002	11.2516	-1602.01
*	98369	5.00002	13.0027	-1704.99
*	98370	5.10002	12.4880	-1680.94
*	98371	5.20002	12.3810	-1665.49
*	98372	5.30003	10.9404	-1570.69
*	98373	5.40003	11.1884	-1601.10
*	98374	5.50003	12.5805	-1687.69
*	98375	5.60003	12.2625	-1657.64
*	98376	5.70004	11.4682	-1609.74
*	98377	5.80004	11.3111	-1601.09
*	98378	5.90004	11.0686	-1598.33
*	98379	6.00004	12.7634	-1694.89
*	98380	6.10004	12.2936	-1664.27
*	98381	6.20005	11.0523	-1581.67
*	98382	6.30005	11.3811	-1615.59

192

*	98383	6.40005	12.3653	-1671.41
*	98384	6.50005	12.3848	-1672.79
*	98385	6.60006	11.2165	-1592.21
*	98386	6.70006	11.2946	-1595.40
*	98387	6.80006	11.2829	-1604.50
*	98388	6.90006	11.8065	-1640.61
*	98389	7.00007	12.2395	-1659.00
*	98390	7.10007	11.7102	-1629.41
*	98391	7.20007	11.3900	-1602.12
*	98392	7.30007	12.4205	-1668.48
*	98393	7.40007	12.4846	-1666.66
*	98394	7.50008	11.3196	-1598.09
*	98395	7.60008	11.7747	-1642.34
*	98396	7.70008	12.4259	-1677.28
*	98397	7.80008	12.0174	-1642.89
*	98398	7.90009	11.3225	-1601.70
*	98399	8.00009	12.2662	-1660.87
*	98400	8.10009	12.3067	-1666.91
*	98401	8.20009	12.0775	-1646.50
*	98402	8.30009	11.3195	-1603.35
*	98403	8.40010	11.6505	-1631.94
*	98404	8.50010	12.7065	-1692.92
*	98405	8.60010	12.3278	-1659.92
*	98406	8.70010	10.6501	-1562.28
*	98407	8.80011	11.1851	-1595.92
*	98408	8.90011	11.7368	-1639.75
*	98409	9.00011	12.7781	-1700.99
*	98410	9.10011	12.2442	-1653.92
*	98411	9.20012	11.2710	-1597.42
*	98412	9.30012	11.4931	-1622.98
*	98413	9.40012	12.7817	-1696.07
*	98414	9.50012	12.2896	-1663.71
*	98415	9.60012	10.8927	-1576.74
*	98416	9.70013	11.6908	-1634.73
*	98417	9.80013	12.7128	-1693.96
*	98418	9.90013	12.2794	-1660.89
*	98419	10.0000	10.9711	-1582.75

Appendix B.3: *center_of_pressure_ location_200_2_cycle.txt* – **Output file for case 6 of 2D transient analysis**

```
               VERTEX LIST IN COORDINATE SYSTEM NO.   1
                  (*  INDICATES VERTICES IN CURRENT VSET)

        VERTEX           X              Y                Z
  *     97320      0.100000E-01      8.86476         5825.74
  *     97321      0.200000E-01      29.3785         15837.2
  *     97322      0.300000E-01      57.5078         29137.9
  *     97323      0.400000E-01      87.4525         42702.0
  *     97324      0.500000E-01      119.353         56756.1
  *     97325      0.600000E-01      152.176         70937.7
  *     97326      0.700000E-01      185.451         85089.9
  *     97327      0.800000E-01      219.358         99319.7
  *     97328      0.900000E-01      252.204         112870.
  *     97329      0.100000          284.402         125939.
  *     97330      0.110000          315.411         138317.
  *     97331      0.120000          344.550         149688.
  *     97332      0.130000          370.261         159263.
  *     97333      0.140000          388.549         164300.
  *     97334      0.150000          414.822         176313.
  *     97335      0.160000          397.718         160614.
  *     97336      0.170000          397.304         162892.
  *     97337      0.180000          371.604         148110.
  *     97338      0.190000          362.692         144594.
  *     97339      0.200000          354.073         142323.
  *     97340      0.210000          338.510         135555.
  *     97341      0.220000          319.278         126729.
  *     97342      0.230000          297.703         116960.
  *     97343      0.240000          274.420         106819.
  *     97344      0.250000          248.166         95523.7
  *     97345      0.260000          218.887         82883.3
  *     97346      0.270000          187.465         69379.4
  *     97347      0.280000          154.317         55191.9
  *     97348      0.290000          119.368         40319.8
  *     97349      0.300000          84.4389         25454.5
  *     97350      0.310000          65.1585         21390.8
  *     97351      0.319999          69.8816         26155.5
  *     97352      0.329999          88.1900         36814.4
  *     97353      0.339999          111.301         48636.8
  *     97354      0.349999          137.852         61319.0
  *     97355      0.359999          166.422         74404.1
  *     97356      0.369999          196.356         87715.0
  *     97357      0.379999          227.604         101272.
  *     97358      0.389999          258.310         114290.
  *     97359      0.399998          288.854         126944.
  *     97360      0.409998          318.614         139011.
  *     97361      0.419998          346.892         150197.
  *     97362      0.429998          372.039         159578.
  *     97363      0.439998          388.446         163646.
  *     97364      0.449998          416.964         177177.
  *     97365      0.459998          399.500         161449.
  *     97366      0.469997          399.994         164297.
  *     97367      0.479997          373.511         148978.
  *     97368      0.489997          363.529         144655.
```

194

*	97369	0.499997	354.823	142436.
*	97370	0.509997	338.615	135379.
*	97371	0.519997	319.389	126659.
*	97372	0.529997	297.737	116903.
*	97373	0.539997	274.543	106839.
*	97374	0.549996	248.266	95545.8
*	97375	0.559996	218.973	82911.5
*	97376	0.569996	187.503	69388.6
*	97377	0.579996	154.305	55182.7
*	97378	0.589996	119.320	40290.8
*	97379	0.599996	84.4022	25444.9
*	97380	0.609996	56.2200	15520.1
*	97381	0.619996	40.2452	10229.3
*	97382	0.629995	30.7930	7754.39
*	97383	0.639995	23.9331	6005.77
*	97384	0.649995	18.7804	4713.95
*	97385	0.659995	14.6484	3672.35
*	97386	0.669995	11.3665	2850.77
*	97387	0.679995	8.73965	2191.82
*	97388	0.689995	6.66112	1673.92
*	97389	0.700000	5.05738	1274.15
*	98320	0.100000E-01	3.01158	16.6680
*	98321	0.200000E-01	3.30632	30.3738
*	98322	0.300000E-01	3.90527	29.1502
*	98323	0.400000E-01	4.76931	10.8282
*	98324	0.500000E-01	5.82577	-22.8891
*	98325	0.600000E-01	7.05673	-72.4104
*	98326	0.700000E-01	8.39542	-139.244
*	98327	0.800000E-01	9.84530	-224.411
*	98328	0.900000E-01	11.3000	-328.419
*	98329	0.100000	12.7632	-453.632
*	98330	0.110000	14.2156	-601.186
*	98331	0.120000	15.5987	-772.983
*	98332	0.130000	16.7510	-973.691
*	98333	0.140000	16.6859	-1154.65
*	98334	0.150000	19.8038	-1551.92
*	98335	0.160000	13.4186	-1453.77
*	98336	0.170000	13.1461	-1536.24
*	98337	0.180000	7.78396	-1204.06
*	98338	0.190000	6.20488	-1032.93
*	98339	0.200000	5.59652	-927.000
*	98340	0.210000	4.08823	-792.965
*	98341	0.220000	2.54363	-674.168
*	98342	0.230000	1.29257	-583.532
*	98343	0.240000	0.460721	-515.962
*	98344	0.250000	-0.555105E-01	-458.405
*	98345	0.260000	-0.346351	-408.365
*	98346	0.270000	-0.375111	-365.326
*	98347	0.280000	-0.159140	-327.719
*	98348	0.290000	0.294297	-293.993
*	98349	0.300000	0.926401	-263.121
*	98350	0.310000	1.76961	-198.182
*	98351	0.319999	2.41574	-137.083
*	98352	0.329999	3.09180	-100.754
*	98353	0.339999	3.97057	-91.0705
*	98354	0.349999	5.02573	-103.078
*	98355	0.359999	6.25416	-135.438

*	98356	0.369999	7.63957	-188.105
*	98357	0.379999	9.14584	-262.186
*	98358	0.389999	10.6900	-357.332
*	98359	0.399998	12.2437	-475.550
*	98360	0.409998	13.7620	-617.385
*	98361	0.419998	15.2476	-785.604
*	98362	0.429998	16.3895	-984.932
*	98363	0.439998	16.1660	-1145.53
*	98364	0.449998	19.8389	-1570.12
*	98365	0.459998	13.4777	-1471.10
*	98366	0.469997	13.4637	-1562.70
*	98367	0.479997	7.85695	-1216.46
*	98368	0.489997	5.99724	-1030.73
*	98369	0.499997	5.44301	-926.561
*	98370	0.509997	3.94008	-791.772
*	98371	0.519997	2.46186	-674.757
*	98372	0.529997	1.23323	-583.912
*	98373	0.539997	0.430640	-516.569
*	98374	0.549996	-0.711599E-01	-458.825
*	98375	0.559996	-0.353782	-408.603
*	98376	0.569996	-0.380241	-365.498
*	98377	0.579996	-0.162836	-327.764
*	98378	0.589996	0.298653	-294.059
*	98379	0.599996	0.918073	-262.899
*	98380	0.609996	1.75472	-214.828
*	98381	0.619996	2.27016	-166.930
*	98382	0.629995	2.55915	-129.247
*	98383	0.639995	2.74082	-101.055
*	98384	0.649995	2.83912	-79.1797
*	98385	0.659995	2.89923	-61.9120
*	98386	0.669995	2.94407	-48.0593
*	98387	0.679995	2.97145	-36.8967
*	98388	0.689995	2.98606	-28.0228
*	98389	0.700000	2.99636	-21.2030

Appendix B.4: *center_of_pressure_ location_20_2_cycle.txt* – Output file for case 7 of 2D transient analysis

```
VERTEX LIST IN COORDINATE SYSTEM NO.    1
   (* INDICATES VERTICES IN CURRENT VSET)
```

	VERTEX	X	Y	Z
*	97320	0.100000	2.25680	1252.85
*	97321	0.200000	35.3328	15815.1
*	97322	0.300000	73.0718	31509.8
*	97323	0.400000	111.050	47185.6
*	97324	0.500000	148.508	62571.9
*	97325	0.600000	185.134	77587.8
*	97326	0.700000	221.032	92270.0
*	97327	0.800000	255.733	106385.
*	97328	0.899999	288.746	119737.
*	97329	0.999999	319.429	132025.
*	97330	1.10000	346.984	142893.
*	97331	1.20000	369.251	151473.
*	97332	1.30000	384.796	157179.
*	97333	1.40000	394.600	160631.
*	97334	1.50000	399.932	162042.
*	97335	1.60000	402.002	162419.
*	97336	1.70000	381.890	154731.
*	97337	1.80000	362.674	144571.
*	97338	1.90000	364.778	147659.
*	97339	2.00000	355.077	144250.
*	97340	2.10000	338.964	137935.
*	97341	2.20000	317.260	129134.
*	97342	2.30000	290.043	118081.
*	97343	2.40000	259.389	105623.
*	97344	2.50000	226.139	92009.2
*	97345	2.60000	191.222	77684.6
*	97346	2.70000	155.220	62876.0
*	97347	2.80000	118.194	47613.3
*	97348	2.90000	80.6939	32126.0
*	97349	3.00000	42.5959	16345.5
*	97350	3.10000	8.11993	2652.55
*	97351	3.20000	35.8115	15931.4
*	97352	3.30000	73.1190	31521.2
*	97353	3.40000	111.038	47176.8
*	97354	3.50000	148.493	62565.4
*	97355	3.60000	185.112	77579.5
*	97356	3.70000	220.960	92244.7
*	97357	3.80000	255.748	106390.
*	97358	3.90000	288.737	119733.
*	97359	4.00000	319.420	132021.
*	97360	4.10000	346.986	142897.
*	97361	4.20000	369.237	151463.
*	97362	4.30000	384.742	157149.
*	97363	4.40001	394.526	160585.
*	97364	4.50001	401.267	162777.
*	97365	4.60001	401.592	162212.
*	97366	4.70001	377.807	152198.
*	97367	4.80001	364.382	145684.
*	97368	4.90002	365.806	148250.

*	97369	5.00002	354.675	144171.
*	97370	5.10002	339.131	138024.
*	97371	5.20002	317.309	129158.
*	97372	5.30003	290.039	118076.
*	97373	5.40003	259.315	105581.
*	97374	5.50003	226.126	92005.7
*	97375	5.60003	191.235	77689.4
*	97376	5.70004	155.219	62876.2
*	97377	5.80004	118.202	47617.4
*	97378	5.90004	80.7071	32131.4
*	97379	6.00004	42.6046	16350.6
*	97380	6.10004	6.44944	1641.76
*	97381	6.20005	0.925198	258.140
*	97382	6.30005	0.102413	30.8275
*	97383	6.40005	0.380600E-01	13.2606
*	97384	6.50005	0.902628E-02	1.16194
*	97385	6.60006	0.212480E-01	6.83707
*	97386	6.70006	0.511096E-02	1.47669
*	97387	6.80006	-0.814523E-03	0.569393E-01
*	97388	6.90006	-0.393937E-04	0.705550
*	97389	7.00000	0.407641E-02	1.37722
*	98320	0.100000	2.99967	3.02452
*	98321	0.200000	3.16723	-15.3158
*	98322	0.300000	3.41404	-56.5761
*	98323	0.400000	3.71765	-105.221
*	98324	0.500000	4.06837	-162.166
*	98325	0.600000	4.48974	-228.076
*	98326	0.700000	4.96682	306.006
*	98327	0.800000	5.52168	-397.919
*	98328	0.899999	6.13835	-503.470
*	98329	0.999999	6.85613	-625.296
*	98330	1.10000	7.61265	-763.680
*	98331	1.20000	8.40915	-918.863
*	98332	1.30000	9.29279	-1091.90
*	98333	1.40000	10.3937	-1292.38
*	98334	1.50000	11.4554	-1502.48
*	98335	1.60000	12.4888	-1724.43
*	98336	1.70000	11.1479	-1478.23
*	98337	1.80000	7.74119	-1136.01
*	98338	1.90000	7.90089	-1028.53
*	98339	2.00000	6.97376	-883.132
*	98340	2.10000	5.98137	-750.616
*	98341	2.20000	5.05747	-630.786
*	98342	2.30000	4.35652	-522.985
*	98343	2.40000	3.84162	-427.424
*	98344	2.50000	3.44486	-343.937
*	98345	2.60000	3.15940	-271.675
*	98346	2.70000	2.97640	-210.309
*	98347	2.80000	2.87845	157.363
*	98348	2.90000	2.83625	-110.766
*	98349	3.00000	2.87293	-68.9165
*	98350	3.10000	2.97862	-22.7633
*	98351	3.20000	3.15454	-17.4940
*	98352	3.30000	3.41025	-56.8347
*	98353	3.40000	3.71472	-105.312
*	98354	3.50000	4.06594	-162.255
*	98355	3.60000	4.48455	-228.060

*	98356	3.70000	4.96942	-305.846
*	98357	3.80000	5.52189	-397.979
*	98358	3.90000	6.13728	-503.438
*	98359	4.00000	6.85351	-625.148
*	98360	4.10000	7.61243	-763.704
*	98361	4.20000	8.40870	-918.822
*	98362	4.30000	9.29258	-1091.62
*	98363	4.40001	10.3797	-1291.75
*	98364	4.50001	11.6285	-1514.98
*	98365	4.60001	12.4514	-1721.82
*	98366	4.70001	10.3343	-1431.88
*	98367	4.80001	8.06286	-1152.71
*	98368	4.90002	8.03153	-1038.46
*	98369	5.00002	7.03917	-884.701
*	98370	5.10002	5.99076	-751.507
*	98371	5.20002	5.05487	-630.955
*	98372	5.30003	4.35923	-522.976
*	98373	5.40003	3.84250	-427.356
*	98374	5.50003	3.44413	-343.857
*	98375	5.60003	3.15959	-271.743
*	98376	5.70004	2.97595	-210.294
*	98377	5.80004	2.87485	-157.321
*	98378	5.90004	2.83847	-110.795
*	98379	6.00004	2.86888	-68.8812
*	98380	6.10004	2.97703	-26.6420
*	98381	6.20005	3.00558	-3.40872
*	98382	6.30005	3.00957	-0.322110
*	98383	6.40005	3.00826	-0.860853E-01
*	98384	6.50005	3.00658	-0.981071E-01
*	98385	6.60006	3.01166	-0.744616E-01
*	98386	6.70006	3.01527	-0.150748E-01
*	98387	6.80006	3.00946	0.203109E-01
*	98388	6.90006	3.01128	0.131297E-01
*	98389	7.00000	3.01365	-0.128146E-01